2016

Particulate inorganic carbon flux and sediment transport dynamics in karst: Significance to landscape evolution and the carbon cycle.

Randall Lee Paylor
Louisiana State University and Agricultural and Mechanical College

PARTICULATE INORGANIC CARBON FLUX AND SEDIMENT TRANSPORT DYNAMICS IN KARST: SIGNIFICANCE TO LANDSCAPE EVOLUTION AND THE CARBON CYCLE

A Dissertation

Submitted to the Graduate Faculty of
Louisiana State University and
Agricultural and Mechanical College
in the partial fulfillment of the
requirements for the degree of
Doctor of Philosophy

in

The Department of Geology and Geophysics

by
Randall Lee Paylor
B.S., Tennessee Technological University, 1990
M.S., Eastern Kentucky University, 2007
December 2016

ACKNOWLEDGEMENTS

This research would not have been possible without the generous support of many people and organizations. I would like to thank the National Science Foundation for the primary project funding covering equipment and research, as well as the Geological Society of America for equipment funds.

I want to thank my advisor, Dr. Carol Wicks for endless patience and support for these projects, Dr. Sam Bentley for the instruction and use of gamma analysis equipment, and Dr. Bentley and Dr. Clinton Willson for their excellent advice along the way.

I could not have completed this project without the generous extended access to the cave and accommodations at Sunnybrook Blowing Cave, KY granted by Charles and Lavonne Gibbs.

And many thanks to the Ozark Underground Lab at Tumbling Creek Cave, MO run by Tom and Cathy Aley for their support and lodging during field work, as well as the open access to Hidden River Cave, KY and assistance from David Foster. The initial work at Mammoth Cave would not have been completed without the help I received from the National Park Service and the Cave Research Foundation.

Assistance with the extensive field work was vital for these studies, and could not have been completed without help from numerous people including fellow researchers Ben Maas and Caroline Broderick, cavers Bill Walden, Mike Beavin and Jim Malone, and my unceasingly supportive family Valerie Donegan, John Gilliat and Barbara Stagg.

PREFACE

The dissertation chapters presented here are written for publishing in academic journals. Each chapter represents a different paper to be published. The chapters address particular aspects of the overall research into karst processes: hydrogeology and hydrochemistry, sediment transport and the carbon cycle, and related geomorphologic processes and effects. Each chapter has its own abstract, introduction, methods, results, discussion, conclusion, and reference sections. Some materials are partially duplicated between chapters in order for them to stand alone as separate journal submissions, but the purposes and conclusions of each chapter are unique.

TABLE OF CONTENTS

LIST OF FIGURES

LIST OF TABLES

DISSERTATION ABSTRACT

Research focused on three areas of karst hydrogeology and sediment transport that have been poorly studied in the past: the role of particulate inorganic carbon transport in calculating carbon sink rates in karst; rapid changes in surface vs. subsurface sediment mixing in karst conduits; and comparison of landscape denudation calculations using dissolved carbonate load vs. total dissolved/sediment load.

Carbonate bedrock weathering is a significant component of the atmospheric carbon sink. Particulate inorganic carbon (PIC) in bed and suspended sediment load of karst waters is frequently dismissed as insignificant for calculating denudation and carbon transport/sink rates, but PIC flux has not been adequately studied. PIC fluxes were quantified in fluviokarst settings using RFID-tagged cobbles and gravel to track subsurface bed load flux, along with remote loggers and lab analysis of sediment and water chemistry for suspended and dissolved loads. PIC contributed about 10.3 percent annually to total inorganic carbon removal and additional carbon sequestration at Blowing Cave basin.

Cosmogenic and fallout radionuclides ^{7}Be and ^{137}Cs were also utilized to develop a better understanding of rapid, short-term changes in sediment flux and transport through karst aquifers. The ratio of surface-derived sediment to stored and remobilized subsurface sediment in cave streams was estimated by tracking isotopic changes across storm runoff events. During a large storm event, approximately 34% of the total sediment flux during the 4-day runoff event originated from surface erosion.

Landscape denudation rates in karst settings have been calculated using a number of different methods. The most widely applied basin-wide method is measurement of dissolved carbonate load at base-level springs, calculating denudation using the area of exposed carbonate outcrop, and assuming other outcrop types are in equilibrium. In mixed carbonate/noncarbonate lithologies (which includes most fluviokarst settings), much of the landscape is also eroded by transport of sediments through conduits. The basin average rate of landscape denudation (aggregating both carbonate and non-carbonate areas) was 48.5 mm/ka, but denudation rates for carbonate and non-carbonate outcrop areas were not in equilibrium.

CHAPTER 1: DISSERTATION INTRODUCTION

Research for the dissertation focused on three areas of karst hydrogeology and sediment transport that have been poorly studied. Soluble bedrock underlies about one-fifth of the United States and world landmasses (Martin & White 2008) and rapid turbulent flow into and through well-developed conduits in these regions can transport water and materials in dynamic and unpredictable ways (Vesper et al. 2001). Surface water and groundwater are intimately linked in karst terrains, so better understanding of the rapid changes in sediment flux and transport through karst aquifers is needed to sort out a variety of related processes such as inorganic carbon transport, and sediment erosion.

One poorly studied problem is the assumption that mechanical removal of carbonate in karst basins is negligible in calculating inorganic carbon mass flux because chemical processes dominate the systems (White 1984; Palmer 2007). Nearly all past research on carbonate dissolution kinetics, carbon sink processes and geochemical fluxes in karst waters has focused on dissolved inorganic carbon (DIC) flux (e.g., Liu et al. 1997; Dreybrodt & Eisenlohr 2000; White 2000; Groves & Meiman 2001; Gombert 2002). Chemical loads typically dominate karst waters during low to moderate flow conditions, but some research has shown that the particulate inorganic carbon (PIC) in suspended and bed loads can be a major component of carbon mass flux under higher flow conditions during moderate to extreme storm events (Newson 1971; Herman et al. 2008), so dissertation study focused on these dynamics.

Another poorly studied processes in karst ground- and surface water interaction is the mixing of freshly-eroded surface material with reworked and remobilized sediment stored in subsurface stream conduits, and how the provenance of suspended load evolves during storm runoff events (Herman et al. 2006). Determining residence times of sediments within conduits and investigating the surface/subsurface sediment mixing ratios in karst storm runoff is difficult, but important for determining things like intensity of agricultural erosion or movement of surface contamination into the subsurface (Herman et al. 2008). One part of the dissertation study involved investigating storm sediment spikes in karst aquifers

using naturally-occurring cosmogenic and fallout radioactive isotopes that adhere strongly to sediments and soil in order to determine the ratios of surface sediment and remobilized subsurface sediment in suspended loads during runoff events.

A third poorly-understood process in karst research is the dynamic of landscape denudation in mixed carbonate and non-carbonate terrains like the fluviokarst settings of most of the eastern United States Interior Lowland Plateaus and Valley and Ridge provinces. Landscape denudation rates in karst settings have been calculated using a number of different methods by past researchers (e.g., Kaufmann 2003; Anthony & Granger 2007; Gabrovšek 2009). The most widely applied method of measuring carbonate solute exiting karst basins to determine mass of bedrock removal from drainage basins may be inappropriate for mixed bedrock settings. The total mass of all modes of bedrock removal was investigated in the fluviokarst basin of Blowing Cave for this research, and related to landscape denudation of different lithologies and the resulting geomorphology.

REFERENCES

Anthony, D.M. & Granger, D.E., 2007. An empirical stream power formulation for knickpoint retreat in Appalachian Plateau fluviokarst. *Journal of Hydrology*, 343(3–4), pp.117–126.

Dreybrodt, W. & Eisenlohr, L., 2000. Limestone dissolution rates in karst environments. In A. Klimchouk et al., eds. *Speleogenesis and Evolution of Karst Aquifers*. Huntsville, AL: National Speleological Socieity, pp. 136–148.

Gabrovšek, F., 2009. On concepts and methods for the estimation of dissolutional denudation rates in karst areas. *Geomorphology*, 106(1–2), pp.9–14.

Gombert, P., 2002. Role of karstic dissolution in global carbon cycle. *Global and Planetary Change*, 33(1–2), pp.177–184.

Groves, C. & Meiman, J., 2001. Inorganic Carbon Flux and Aquifer Evolution in the South Central Kentucky Karst. U.S. Geological Survey Karst Interest Group Proceedings, St. Petersburg, Florida , pp.99–105.

Herman, E.K. et al., 2006. Mineralogy of suspended sediment in three karst springs. *Hydrogeology Journal*, 15(2), pp.255–266.

Herman, E.K., Toran, L. & White, W.B., 2008. Threshold events in spring discharge: Evidence from sediment and continuous water level measurement. *Journal of Hydrology*, 351(1–2), pp.98–106.

Kaufmann, G., 2003. Karst landscape evolution. *Speleogenesis and Evolution of Karst Aquifers*, 1(3), 243-258.

Liu, Z., Zhao, J., 1997. Contribution of Carbonate Rock Weathering to the Atmospheric CO2 Sink, *Environmental Geology*, 39(9), pp.1053-1058.

Martin, J.B. & White, W.B., 2008. *Frontiers in Karst Research* J. B. Martin & W. B. White, eds., Karst Waters Institute, Special Publication 13, p.118.

Newson, M.D., 1971. A Model of subterranean limestone erosion in the British Isles based on hydrology. *Transactions of the Institute of British Geographers*, 54, pp.55–70.

Palmer, A.N., 2007. *Cave Geology*, Dayton, Ohio: Cave Books, p.445.

Vesper, D.J., Loop, C.M. & White, W.B., 2001. Contaminant transport in karst aquifers. *Materials Research*, 13–14(2), pp.101–111.

White, W.B., 2000. Dissolution of limestone from field observations. In A. B. Klimchouk et al., eds. *Speleogenesis and Evolution of Karst Aquifers*. Huntsville, AL: National Speleological Society, pp. 149–155.

White, W.B., 1984. Rate processes: chemical kinetics and karst landform development. *Zeitschrift fur Geomorphologie, Groundwater as a Geomorphic Agent*, pp.227–248.

CHAPTER 2: EVALUATION OF PARTICULATE INORGANIC CARBON FLUX IN KARST SEDIMENT TRANSPORT

ABSTRACT

Carbonate bedrock weathering has been recognized as a significant component of the atmospheric CO_2 sink. Studies of atmospheric carbon sink processes in karst terrains have focused primarily on dissolved inorganic carbon (DIC). Particulate inorganic carbon (PIC) in the sediment of karst waters is frequently considered insignificant to carbon transport/sink rates, because chemical processes are assumed to greatly dominate. PIC flux from carbonate terrains may be an important missing carbon cycle component because carbonate sediment continues to dissolve in undersaturated water downstream of sampling points.

PIC fluxes were quantified by measuring sediment load entrainment and transport in fluviokarst settings in Kentucky and Missouri. Knowledge gained from these sites can be extended to many other regions with similar settings and climate. Bed load transport in underground streams and surface overflow channels was tracked with RFID tagged cobbles and gravel. Water samples and in-situ data loggers were used to determine suspended sediment concentration and water chemistry, and the mass of PIC within suspended sediments was quantified by cation/anion analysis of dual filtered/unfiltered samples. The mass of PIC in the bed load was measured directly by representative sampling and streambed photographs. Total PIC flux was compared to dissolved inorganic carbon flux to determine the significance of each component of carbon removal.

Analysis of storm events at field sites indicated that PIC flux can be significant during peak storm flow. A storm above the threshold of bed transport with a 0.87-month return period produced a peak PIC flux of 13.9 g/s and a peak DIC flux of 147 g/s at 1.44 m^3/s flow. The largest storm had a return period of 7.7 months, a peak discharge of 4.57 m^3/s, and peak PIC flux of 621 g/s compared to a peak DIC flux of 353 g/s. Bed load transport was the most significant contribution to PIC flux at the BC site, exceeding the suspended flux by an order of magnitude during storm events. When calculated on an annual basis, PIC contributes about 10.3% to total inorganic carbon removal and additional carbon sequestration.

INTRODUCTION

Purpose and significance

Carbonate bedrock underlies about one-fifth of the United States (Fig. 2.1) and world landmasses. (Martin & White 2008). Researchers currently assume that mechanical removal of carbonate in karst basins is negligible in calculating inorganic carbon mass flux because chemical processes dominate the systems (White 1984; Palmer 2007). Nearly all past research on carbonate dissolution kinetics, carbon sink processes and geochemical fluxes in karst waters has focused on dissolved inorganic carbon (DIC) flux (e.g., Liu et al. 1997; Dreybrodt & Eisenlohr 2000; White 2000; Groves & Meiman 2001; Gombert 2002).

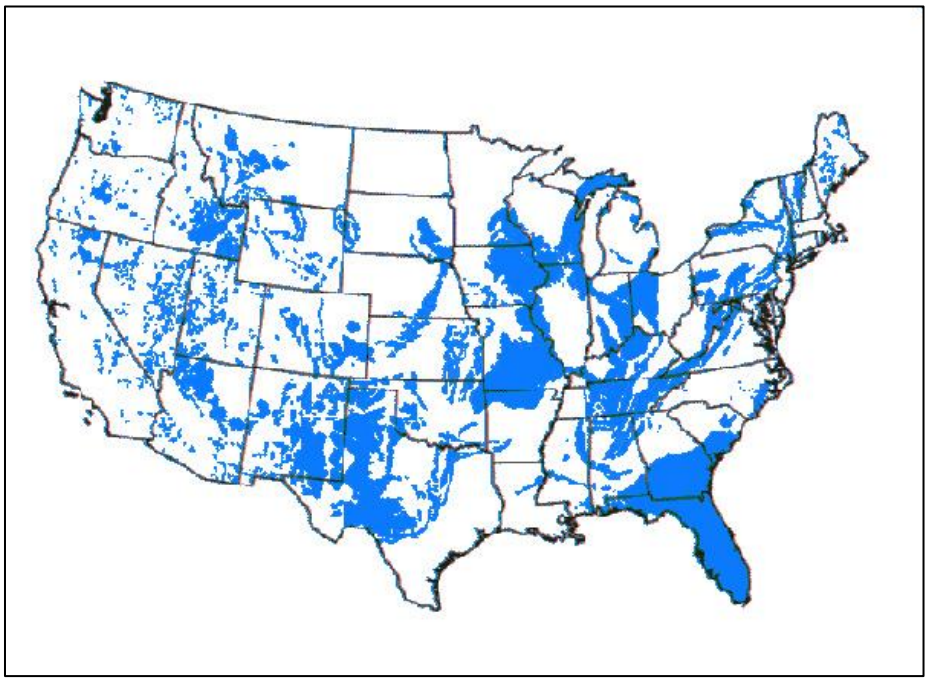

Figure 2.1: Major karst regions of the lower 48 United States (Epstein et al., 2002).

Chemical loads typically dominate karst waters during low to moderate flow conditions, but some research has shown that the particulate inorganic carbon (PIC) in suspended and bed loads can be a major component of carbon mass flux under higher flow conditions during moderate to extreme storm events (Newson 1971; Herman et al. 2008). To investigate carbon cycle dynamics related to carbonate PIC flux driven by hydraulics and sediment transport in karst, this research tested the following hypotheses:

1) The carbonate fraction of both bed load and suspended load can be a significant missing component of carbon sink calculations in some karst settings.
2) The mass flux of PIC material through karst systems is larger than currently estimated because of inadequately characterized bed and suspended sediment transport during storm runoff events.

PIC Conceptual Model

Carbonate material cycles through karst systems by a variety of processes. To assist in understanding potential sources, sinks and transport, a conceptual model of the PIC cycle was developed (Fig. 2.2). For PIC production, the dominant process will depend on the recharge type, water chemistry and conduit geometry/hydraulics. For example, autogenic recharge through sinkhole plains would provide little direct surface input of carbonate sediment, but the increased contact of water with limestone bedrock could increase the saturation to the point of precipitating suspended carbonate in the water column. PIC transport will depend primarily on system hydraulics and particle sizes and types. PIC reduction can occur by chemical and mechanical means, with dissolution of transported grains depending on carbonate saturation and particle mineralogy and morphology.

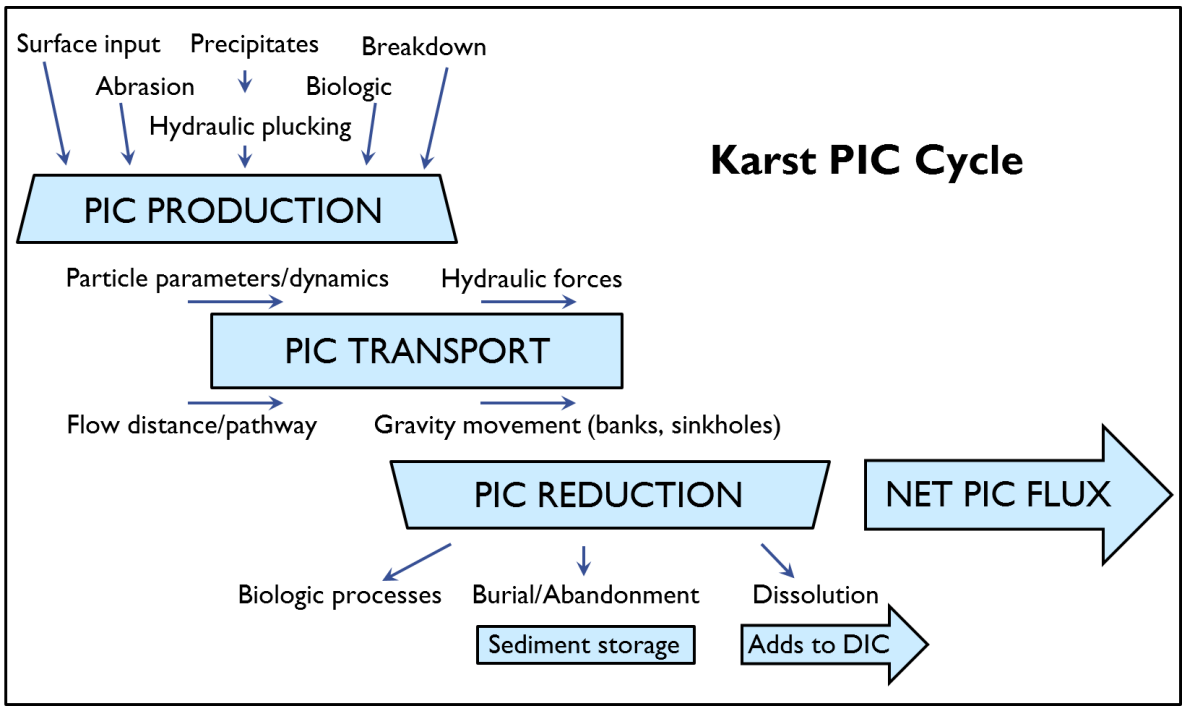

Figure 2.2: Conceptual model of the karst PIC cycle.

A positive net PIC flux ultimately depends on the production and transport rates overcoming the reduction rate in the system. Water chemistry in autogenic recharge systems such as Mammoth Cave, Kentucky and Cheddar Cave, England indicate that reduction in PIC concentration may be minimal in waters highly saturated with carbonate and that mobile precipitates with long lifetimes may form (Newson 1971; Groves & Meiman 2001). However, the largest net PIC fluxes likely occur during storm events where material is produced and transported much faster than it is dissolved or deposited.

Carbon dynamics in karst

Studies of carbonate dissolution in karst settings have clearly demonstrated the significance of the dissolution sequestration process as a sink in the global carbon cycle from the uptake of CO_2 and creation of bicarbonate:

$CaCO_3 + CO_2 + H_2O \rightarrow Ca^{2+} + 2HCO_3^-$ (Limestone dissolution) (eq. 1)
$CaMg(CO_3)_2 + 2CO_2 + 2H_2O \rightarrow Ca^{2+} + Mg^{2+} + 4HCO_3^-$ (Dolomite dissolution) (eq. 2)
(Groves & Meiman 2001; Cheng & Daoxian 2002).

However, studying karst landscape dynamics by looking only at dissolved components does not account for carbonate loss by removal of both small (suspended load) and large (bed load) particulates. Actual carbon removal and sequestration of CO_2 may be underestimated in many settings.

Some evidence shows carbonate clastics (suspended and bed loads) can be a major component of mass flux under typical storm flow conditions, accounting for a large percentage of the annual removal of carbonate. Studies of sediment dynamics in karst systems have shown that the karst landscape (caves, sinkholes, blind valleys, and epikarst) can store significant amounts of sediment over a large temporal range (days to millennia), but can also transport vast quantities of sediment during punctuated events such as storm flow or cover collapse (Bosch & White 2007; van Gundy & White 2009). Newson (1971) tracked both dissolved inorganic carbon load and particulate inorganic carbon load in a karst system of Great Britain and found that mechanical removal of carbonate was greater than removal by dissolution above a certain discharge threshold (Fig. 2.3). Similarly, Herman et al. (2008) found that runoff events

that exceed certain thresholds can produce a significant flux of particulate carbonate at karst springs. In certain rare flood events, some karst systems have been observed to move massive amounts of sediment as bedload or subsurface debris flows (Crawford 1996; van Gundy & White 2009).

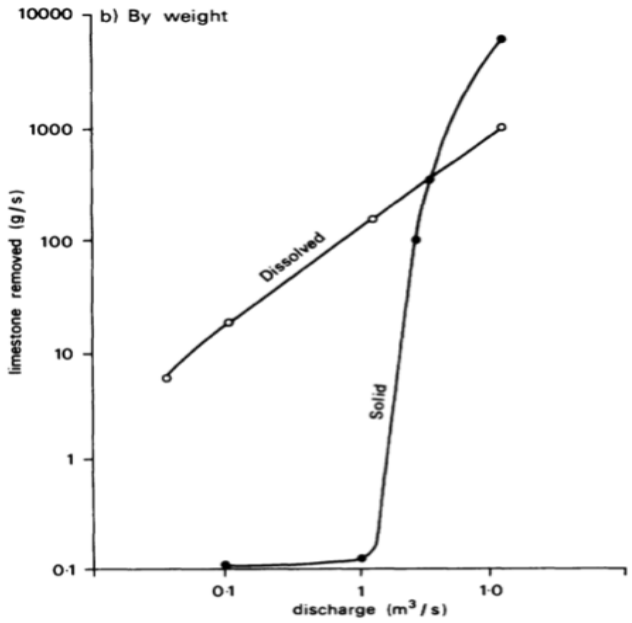

Figure 2.3: The relationship between conduit discharge and type of limestone removal at the Cheddar Gorge spring, England (Newson 1971).

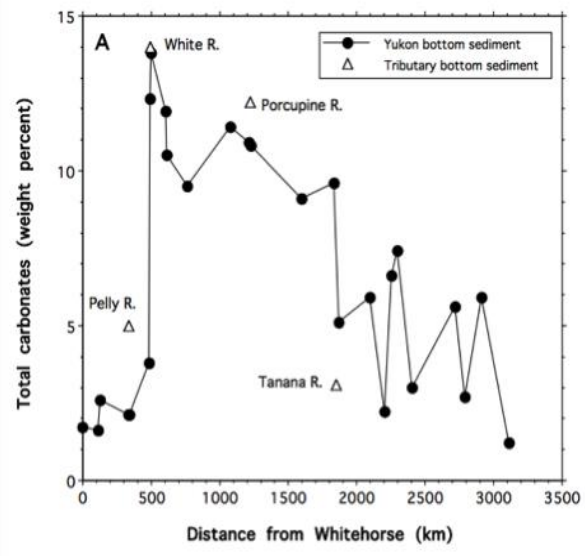

Figure 2.4: Total sedimentary carbonate flux along the Yukon River, indicating dissolution of material downstream from the White River tributary source (Eberl 2004).

The clastic mass exiting a karst system is important to carbon sink calculations because the carbonate fraction can continue to dissolve in undersaturated surface water downstream of sampling points, adding to carbon sinks. Studies on the PIC load of transported sediment in major rivers have shown that PIC decreases significantly along the flow path in most cases (Aucour et al. 1999; Dornblaser & Striegl 2009). For example, a study of the Yukon River in Alaska (Eberl 2004) showed that approximately 1.2×10^6 metric tons of carbonate bed load dissolves along a typical section each year (Fig. 2.4). This total included about 30% of the calcite and 15% of the dolomite loads. The carbonate fraction of bed and suspended load material in the Mississippi River and tributaries decreases steadily downstream from source areas until it is nearly absent at its mouth (Piper et al. 2006). Inversely, carbonate alkalinity of the Mississippi generally increases downstream, indicating that dissolution of transported carbonate loads is a likely

contributor (Raymond & Cole 2003). Once bicarbonate in river water reaches the ocean, it can be stored for long periods of time until carbonate is precipitated again through inorganic and organic processes. An assumption in the long-term global carbon cycle has been that carbon sequestered in bicarbonate from land masses is in net balance with ocean release of carbon by precipitation of carbonate over time, but recent studies have suggested that the balance is shifted in the short term because of enhanced weathering from rising atmospheric CO_2 levels (Berner et al., 1983; Sundquist, 1991, Raymond and Cole, 2003).

The objectives of this study were to determine if the carbonate fraction of both bed load and suspended load is a significant missing component of carbon sink calculations, and whether mass flux of PIC has been inadequately characterized during storm events by: 1) Quantifying bed load transport and flux of PIC at the study sites, 2) Quantifying suspended load transport and flux of PIC at the study sites, 3) Quantifying dissolved inorganic carbon (DIC) load at the study sites, and 4) Comparing total inorganic carbon (TIC) to PIC and evaluate significance of PIC to inorganic carbon removal.

Sediment transport in karst

Numerous studies have addressed sediment dynamics and sediment deposits in karst systems (e.g., Mahler & Lynch 1999; Massei et al. 2003; Peterson & Wicks 2003; Dogwiler & Wicks 2004; Sasowsky & Mylroie 2007; Hajna & Mihevc 2008; Pronk et al. 2009). Caves, sinkholes, and epikarst features act as both avenues of transport and repositories for many types of deposits. Particulate materials transported and stored in karst can be derived locally (autogenic), such as breakdown of cavern walls, or transported from other locations (allogenic), such as suspended and bed sediment in underground streams (Bosch & White 2007). Because caves both trap and transport sediments from the surface, cave deposits and their sources are intimately linked to conduit development and dynamics (Farrant & Smart 2011). Sediment storage and transport processes in the subsurface can change rapidly during storm events, but few existing studies have focused on these dynamics (White 2002).

To better understand sediment transport dynamics in karst, knowledge of subsurface storm response is needed. Karst is considered a triple-porosity regime, with original rock porosity, secondary fracture/bedding plane porosity, and conduit porosity. Karst groundwater movement is often dominated by turbulent and rapid conduit flow, typically recharged by sinking surface streams and runoff into sinkholes (Ford & Williams 2007). During storm events, sediments from karst land surfaces are eroded and transported underground, particularly in fluviokarst basins with developed surface streams, or in locations where streams from non-karst areas flow onto karst areas and sink.

Sediment can also be moved into the subsurface by sinkhole inflow and collapse, and infiltration through enlarged epikarst fractures. Some fine-grained sediment may get transported through the karst system without settling out of suspension, but if sediments get deposited in the subsurface, they can remain in storage from days to millenia depending on local hydraulic conditions, conduit morphology and magnitude of storm events (Bosch & White 2007). Additionally, some sediments are produced directly in the subsurface as the insoluble fraction of weathered rock is left behind from dissolution, carbonate is precipitated in supersaturated conditions, or cave walls are mechanically eroded.

METHODS AND MATERIALS

Site locations

Three karst research locations were initially chosen to represent a range of sediment types, sediment loads and recharge conditions (Fig. 2.5). The most extensively studied location was Kentucky's Sunnybrook Blowing Cave basin, a sediment-rich system with allogenic recharge. The bed load consists of silt to large boulder material, derived from the surrounding high relief sandstone and limestone plateau that feeds sinking streams. Missouri's Tumbling Creek Cave and basin was investigated as a sediment-limited system with allogenic recharge and a major overland flow component. Filtered but rapid recharge dominates Tumbling Creek Cave, and bed load in the system consists primarily of autochthonous weathering residuum. Kentucky's Mammoth Cave was investigated as a possible moderate bed load system with primarily autogenic recharge from a sinkhole plain. In the literature, Mammoth Cave bed

loads have generally been reported as silt to small cobble material of chert and limestone (Bosch & White 2007). Knowledge gained from these sites can be extended to many other regions with similar settings and climate. The typical wet season for the region occurs from January through May, although precipitation from summer thunderstorms can cause intense recharge events.

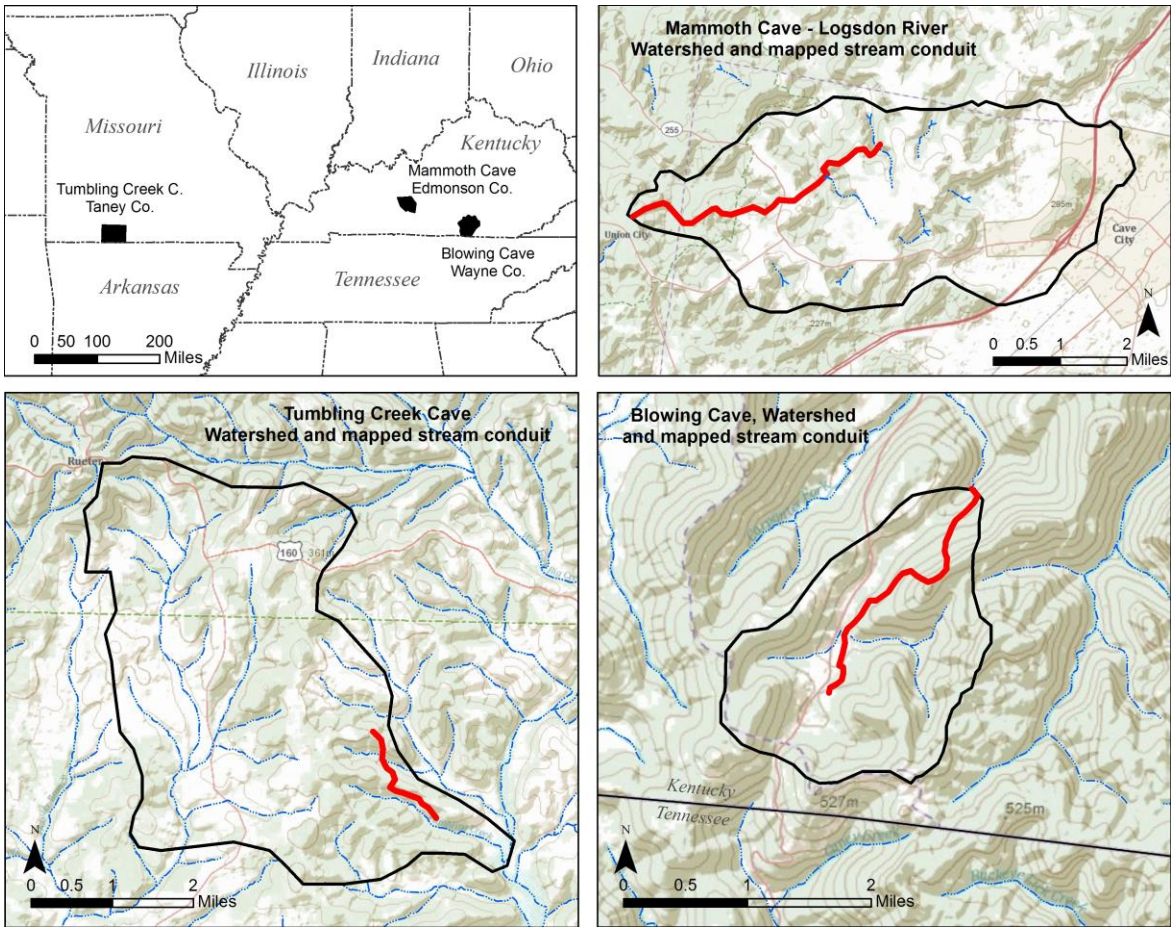

Figure 2.5: Locations and hydrologic settings of research sites. The extent of the three underground stream reaches are delineated within the recharge basins of each study area (Elliott et al. 2007; Schenk-Brown 2008).

Sunnybrook Blowing Cave has a drainage area of approximately 5.8 km^2, which is primarily forested and drains the high-relief, rugged escarpment of the Cumberland Plateau in Kentucky. The basin is underlain by Pennsylvanian conglomerates, sandstones and shales and Mississippian limestones and dolostones. The cave system and subsurface stream are formed in the Monteagle and St. Louis limestones (Lewis 1977). Tumbling Creek Cave and its 23 km^2 recharge area are located in a grassland and forest region of

the gently rolling topography of the Salem Plateau, Missouri. The area is underlain by Cambrian and Ordovician age limestones and dolomites (Noltie & Wicks 2001). The cave and drainage basin are formed within the Cotter Formation, a massive to thinly bedded dolomite interbedded with chert (Aley et al. 2007). Mammoth Cave is formed in Mississippian age rocks beneath the gently-dipping Dripping Springs escarpment and drains an extensive agricultural sinkhole plain and upland areas capped with sandstone. The 25 km^2 Logsdon River sub-basin has the most accessible subsurface river system in Kentucky, and is formed primarily in the Girkin, St. Genevieve and St. Louis limestones, with some ridges capped with Hardinsburg Sandstone (Haynes 1964).

Measurement of suspended and dissolved material

Both suspended load and dissolved load sampling relied on similar field methods. Sampling for dissolved load involved collection of water grab samples across the course of a storm event, as well as during low-flow conditions. When necessary, ISCO automatic water samplers were deployed at the study reaches to sample during high-flow events. Discreet samples and ISCO automatic samples were collected according to standard U.S. Geological Survey protocols (Edwards & Glysson 1999), cation samples were treated with trace-metal grade nitric acid after collection, and all samples were placed on ice for transport and lab analysis. Major anions were analyzed on a Dionex ICS-900 (ion chromatography) instrument, and cations on a Perkin-Elmer ICP (inductively coupled plasma) instrument. Alkalinity was measured by titration in the field using a Hach digital titrator and standard acid cartridges. Although dissolved carbonate loads can be calculated exclusively from HCO_3^- concentrations, pH, temperature and carbonate equilibrium constants, a more accurate method was used that calculates contributions from limestone and dolostone dissolution in karst systems using both HCO_3^- and the Ca^{2+}/Mg^{2+} ions. Calculated HCO_3^- concentrations derived from field titrations resulted from an advanced speciation model (Rounds, 2012) that incorporated initial pH and the temperature-dependent Debye–Hückle equilibrium relationships in a U.S. Geological Survey online calculator.

Field parameters were measured both manually and automatically, and included field-calibrated pH, specific conductance (SpC), temperature (T), and turbidity (NTU). A YSI-6910 multi-parameter hydrologic data recorder was deployed at the primary research site at Blowing Cave and was programmed for a fifteen minute sampling interval. Data from the water quality recorder were downloaded every six to eight weeks, and the probes were recalibrated and cleaned as needed. Manual measurements with handheld YSI field probes were also taken on each trip to verify and calibrate the data logger.

To characterize overall suspended load flux, direct sampling of suspended sediment concentration was coupled with time-series turbidity measurements from the deployed YSI-6910 logger. The optical turbidity probe was calibrated with formazin standards on a regular basis. Because water depths were generally less than 3 feet, grab samples for suspended sediment concentration (TSS) and PIC were taken by moving the sample bottle from the surface to near the streambed and back, and the YSI-6910 was installed so that the turbidity probe was at 0.5 depth under most conditions. Water samples for TSS analysis were filtered in the lab, dried and weighed for TSS mass, and the measured mass used to calibrate turbidity measurements. PIC fraction of suspended sediment was determined using two different methods. The initial method conducted on site was dual Gran F1 alkalinity titrations on a pair of filtered (0.45 or 0.22 μm) and unfiltered samples. Any suspended carbonate material in the unfiltered sample rapidly dissolves by acidification to pH 2 in the Gran method, and the difference in alkalinity between the filtered and unfiltered samples was used to indicated the carbonate sediment fraction. The Gran F1 titration method was used instead of inflection point titration to minimize possible interference from organic acids (Rounds 2012). The second method of suspended PIC measurement used a pair of filtered/unfiltered grab samples acidified to pH 2 with trace-metal grade nitric acid to dissolve particulate carbonate. The samples were then analyzed for differences in cations. Since Ca^{2+} and Mg^{2+} in typical karst waters are derived almost exclusively from carbonate (Ford & Williams 2007), the difference between the filtered and unfiltered samples can be used to calculate the amount of PIC in the suspended load.

To calculate the continuous flux of both particulate and dissolved loads, accurate flow and velocity measurements were necessary for each study reach. A Sontek-IQ acoustic Doppler velocity/stage logger was installed at carefully measured channel locations. The Doppler logger automatically calculated flow volume at 10-minute intervals from stage, velocity and surveyed cross section. In addition, staff gauges were installed at key locations to calculate stage-discharge relationships. At Blowing Cave, data gaps in discharge due to instrument malfunction were filled with correlated discharge records ($r^2 = 0.98$) from a nearby USGS gauging station downstream of the site (Beaver Creek, USGS 03413200). For the YSI sonde, instrument drift between calibrations was adjusted with regression corrections.

Determining bed load movement

Flux and dynamics of bed load transport at the research sites were determined using direct tracing methods and sediment transport calculations calibrated to tracing results. Hydraulic parameters of each study reach were carefully measured and a stream power equation was used to determine the stability and movement of streambed sediment. A cobble tracer method utilizing RFID tracking was used to quantify actual movement of bed load material along the flow path. The predicted bed movement from the calculated methods were compared and correlated to observations of tracer movement.

Tracing bed sediment

Cobble tracer experiments have been used extensively by stream geomorphologists to determine conditions of entrainment (Reid & Frostick 1984), travel distances (Ferguson & Wathen 1998), and vertical mixing and burial (Church & Hassan 1992). None of the cited cobble tracer experiments were specifically designed to investigate sediment transport in cave streams. However, the design of the short-term radio-tagged cobble tracer experiment of Nichols (2004) seemed most appropriate for this study. The characteristics of the open channel reaches at the research sites are similar to those of stream reaches in which tracer experiments have been successfully conducted (Laronne & Carson 1976; Reid & Frostick 1984; Church & Hassan 1992; Ferguson & Wathen 1998; Ferguson & Hoey 2002; Nichols 2004).

A statistically valid set of cobbles were selected from the stream bed inside of the caves or in surface channels to serve as the tracers. Along each tracer line, tracers were deployed following the design of Ferguson and Wathen (1998) and Ferguson and Hoey (2002), which involved laying out tagged cobbles in an imbricated pattern to match natural stream cobble patterns. In-situ cobbles were modified and utilized as tracers at each site. Tracer movement was tracked with passive radio frequency identification (RFID) tags. A small hole was drilled in each cobble using a diamond bit on a mounted Dremel tool or drill press, and chips were secured with a non-toxic waterproof epoxy that did not alter the overall density or other properties of the cobbles. Because of their reliability and detection distance, this study used waterproof, passive, half-duplex 12 mm and 23 mm 134.2 kHz RFID tags from Texas Instruments (nos. TRPGR30TGC, RI-TRP-REHP-30).

In addition to the RFID tags, most tracers were painted with various colors of road marking paint, and individual ID numbers written with indelible ink or etched into the rock for more rapid identification in the field. The RFID particle tracking system consisted of a custom-built reader and antenna and was implemented in a manner similar to that of a metal detector. Tagged material was found by walking the stream channel and sweeping the coil of the reader over the channel bed. Each chip's unique identification string was recorded and linked to the individually measured cobble parameters: mass, rock type, and the A, B and C axes of each particle. A key advantage of using a tracking system was detecting buried tracer particles for loss prevention and to get an estimate of thickness of the mobile bed material (Nichols 2004).

Tracer movement was measured along the central axis of each stream reach using a measuring tape from a fixed zero datum. For tracers that were lost due to malfunction or extreme burial depth, replacement tracers were added so there would always be at least 75 tracers available in low-energy reaches and at least 100 available in higher energy reaches.

Calculation of virtual bed load velocity, and measurement of bed rock type and grain size

From the tagged tracer method, the ratio of the measured distance that sediment traveled to the time that velocity exceeded the critical flow condition (i.e. movement time) yielded a virtual velocity for each individual particle (Hassan et al. 1992). Virtual velocity for the entire streambed was calculated from measured cobble movement to yield the volumetric and mass rate of sediment transport (e.g, Hassan et al. 1992; Wilcock 1997), and the amount of time bed sediment was in storage—also known as transit time or response time (Wathen et al. 1997). The flux relationship of Hassan and others (1992) was used to calculate total bed flux from tagged tracers:

$$q_b = v_b \, d_s \, w_s \, (1 - P) \, \rho_s \qquad \text{(eq. 3)}$$

Where $\boldsymbol{v_b}$ is the average virtual velocity for all measured particles during a specific runoff event, $\boldsymbol{d}$ is the active channel width, $\boldsymbol{w}$ is the depth of the active and mobile sediment bed, $\boldsymbol{P}$ is the bed porosity, and $\boldsymbol{\rho_s}$ is the particle density.

Once the virtual velocity was known, a ratio of PIC to total bed material was needed for each study area to convert total mass flux to PIC flux. Sediment size distributions and rock type for large material were measured using photographic methods (Graham et al. 2005) that utilized a non-invasive digitization and GIS scaling to extract the A and B axes of large areas with geometric analysis tools. Sediment size distribution of finer bed material were determined by standard sieve analysis of bed samples, and mineralogy was determined using a petrographic microscope.

Calculating bed transport dynamics

In order to apply measured bed load transport to the full time-series flow record, correlations with bed transport formula are necessary. Numerous empirical bed load entrainment and transport formula have been utilized for surface stream studies (e.g., van Rijn 1985; Buffington & Montgomery 1997; Ferguson & Wathen 1998; Almedeij 2002; Martin 2003; Barry et al. 2006; Holmes & Holmes 2010; Turowski et al.

2011), and some subsurface karst studies (Dogwiler & Wicks 2004; Rossman 2010; Wicks et al. 2010). In previous studies of bed load transport in karst, three different methods have generally been evaluated: the Einstein probability function, the Shields critical shear function and the Bagnold stream power function. The original critical shear method was first introduced by Shields (1936) who related the critical shear stress, τ_c to sediment density (ρ_s), density of water (ρ), particle diameter (d), and gravity (g). The parametric adaptation of Lorang and Hauer (2003) has proven useful in other subsurface studies, and was evaluated for datasets from this study:

$$\tau_{ci} = 0.045(\rho_s - \rho) g d_{50}^{0.6} d_i^{0.4} \quad \text{(eq. 4)}$$

where $\boldsymbol{\tau_{ci}}$ = the critical shear for particle size $\boldsymbol{i}$, $\boldsymbol{d_{50}}$ is the length of the intermediate axis of the particle that is larger than 50% of all the other particles at a particular location, and $\boldsymbol{d_i}$ is the length of the intermediate axes of the particle size of interest. However, the critical shear method was found to underestimate critical thresholds of movement in a cave environment with flashy flow, so an adaptation of the critical stream power function (Bagnold 1977; Martin & Church 2000; Ferguson 2005) was tested and yielded superior results. In this method, the energy available for particle entrainment (W/m^2) is calculated using unit stream power (ω):

$$\omega = \frac{\rho g Q S}{b} \quad \text{(eq. 5)}$$

where ρ is fluid density, g is gravity, S the energy slope, Q is stream discharge, and b is the width of the active channel. Within Blowing Cave, cross-sections and grain size were carefully measured at three locations that represented different flow dynamics in order to accurately estimate the flow conditions necessary to mobilize different sediment sizes. The water surface slope of each reach was estimated by using the measured stream bed slope, which is an accurate proxy if measured over an adequately long reach (tens of meters or more) in plane-bed and pool-riffle streams (Martin and Church, 2000). The initial test value for critical stream power was determined from the adaptation by Ferguson (2005):

$$\omega_0 = 0.104 \frac{D_b^{1.5}}{S^{0.17}} \left(\frac{D_i}{D_b}\right)^{0.67} \quad \text{(eq. 6)}$$

Where the overall bed material size (D_{50}) = D_b, the grain size of interest = D_i and slope = S. The empirical constant 0.104 incorporates gravity and is also related to the Manning-Strickler resistance law, and yields units of W/m^2 when using mm for grain size. The value is generally valid for Reynolds numbers > 400, slopes < 0.02, and d_{max}/d_{50} < 22, (Aguirre-Pe et al. 2003) but varies based on the bed structure and range of grain sizes on the bed. Grain sizes at the chosen field sites varied from silt to large cobble material but the d_{max}/d_{50} was generally less than 5. Calculated critical stream power was compared to thresholds of bed movement observed in the field in order to calibrate the empirical constant. To determine the critical threshold for bed load movement, the critical unit stream power was compared to the stream power measured from high-resolution time-series velocity and discharge. If the ratio $\omega_b : \omega_{ci} > 1$, sediment movement was predicted. Using calculated and critical stream power, the bed load transport rate q_b can then be determined from the transport function of Martin and Church (2000), which is a derivation of Bagnold's original formula that incorporates a gravity term:

$$q_b = [\omega - \omega_0]^{3/2} \left[D_{50}^{1/4}/d\right]\left[1/\rho_r^{1/2} g^{1/4}\right] \quad \text{(eq. 7)}$$

Where d = water depth, and ρ_r = the rock density in water. The results are in units of kg/m/s.

Determining total inorganic carbon flux

The total inorganic carbon flux is the sum of each of the three measured time-series components: bed flux, suspended flux and dissolved flux. To determine the total suspended PIC flux, the results of PIC concentration measurements were multiplied by the time-series discharge and summed. The flux of DIC was calculated based on the proven observation that the concentrations of dissolved Ca^{2+} and Mg^{2+} ions in natural waters of karst aquifers are derived almost exclusively from the dissolution of limestone and dolomite (Ford & Williams 2007). Continuous direct analysis of HCO_3^-, Ca^{2+} and Mg^{2+} was prohibitive because of the necessity for field titration or need for countless water samples, but the YSI data sonde

recorded continuous specific conductance (SpC), which was correlated to activities of dissolved species for a high-resolution record of dissolved carbon fluxes across storm events. In addition, the dissolved inorganic carbon derived from rock sources was determined by the ratio of Ca^{2+} +Mg^{2+}/ HCO_3^-. If all dissolved ions came from rock dissolution by CO_2 acidification, the ratio should be 0.50, however, in many karst settings the ratios are typically higher because of dissolution of rock by other compounds (e.g., organic acids, sulfuric acid)(Groves & Meiman 2001).

Determination of bed PIC movement from the tagged tracer tests, continuous flow measurements and sediment transport modeling yielded direct values of bed load carbon flux, $\boldsymbol{q_{bc}}$. Determination of PIC suspended and dissolved loads from direct sampling and discharge yielded carbon fluxes $\boldsymbol{q_{sc}}$ and $\boldsymbol{q_{dc}}$. The uncertainties in the components are derived from the measurement and analysis uncertainties of the individual methods. The TIC flux was then calculated by simply adding the terms:

$$q_{tic} = q_{bc} + q_{sc} + q_{dc} \qquad \text{(eq. 8)}$$

Evaluating significance of measured PIC flux

The significance of PIC to carbonate erosion from karst regions can be described directly, because the sum of particulate and dissolved carbonate mass will equal the total carbon removal from the system at the sampling locations. The significance of PIC flux to atmospheric CO_2 removal will depend almost entirely on the rate of continued dissolution of the PIC bed loads and suspended loads downstream of karst basins. Some recent studies have shown that PIC is virtually nonexistent at the outfall of the Mississippi River to the Gulf of Mexico (Piper et al. 2006), and nearby surface streams in the study areas are typically undersaturated with respect to calcite and dolomite (USGS 1995) so this study assumed that all PIC removed from karst systems will contribute to CO_2 uptake by dissolution in undersaturated waters downstream.

RESULTS

Evaluation of sites and activities at each

The three initial sites were investigated for bed load movement and bed and suspended load composition. At Mammoth Cave (MC), a permitted trip to the Logsdon River was undertaken to analyze bed and suspended loads. Except for small segments of the river where breakdown of limestone had occurred from the ceiling and walls (less than 2% of the investigated river length), the bed material consisted entirely of small chert cobbles, gravels and silica sand/silt. Where carbonate rock did occur in the bed, the blocks were generally much larger than the common bed load (>8x) and were essentially immobile as indicated by the strong development of directional solution scallops on all surfaces. Some chert bed material was cemented together with silty and sandy carbonate, but investigating the production and fate of the material was beyond the scope of this study. Samples taken at the Cedar Sink karst window for analysis of suspended load during a storm event did show a small (~3-5%) potential PIC component during storm flow, and may warrant further investigation. Dissolved loads were moderate to high at all sampling times, ranging from 63-164 mg/L HCO_3^-. The difficulty of access and issues with sampling marginally mobile PIC components at MC eliminated the site for this study, but it should be investigated more fully in the future.

At Tumbling Creek Cave (TCC), a prior bed load investigation (Rossman 2010) demonstrated that significant bed movement occurred during moderate to large storm events. However, the in-cave stream has a limited flow capacity because of restricted surface inflow, which results in activation of numerous well-developed surface channels within the basin during big rain events. The surface channel bed transport from the prior study was shown to greatly exceed the in-cave transport. In addition, like MC, the in-cave bed material consisted almost entirely of chert cobbles and gravel (>99%), so significant PIC flux from in-cave bed transport is not probable. Unlike MC, the suspended sediment load during storm events at TCC was small, and analyses of the PIC content of suspended sediment showed no measureable PIC above the analysis error. The surface channel bed loads within the TCC karst basin contain from about

6% (Bear Creek Hollow) to more than 15% (Rozell Road channel) carbonate, as both dolomite and limestone, so work at Tumbling Creek focused on tracking surface cobble movement during storm events.

Initial tests for both bed flux and suspended carbonate flux were promising at Blowing Cave, showing significant cobble movement (>10 meters) and suspended carbonate (~9% of total load) during a moderate storm event. Because of these results, the majority of dissertation field research occurred at Blowing Cave, and it was chosen as the site for full instrument deployment. The remaining results focus on Blowing Cave and the surface channels at Tumbling Creek Cave.

Collected logger data

The record of logger data at Blowing Cave spans a period from November 10, 2012 to October 27, 2013 (Fig. 2.6). Both the YSI sonde and the Sontek flow meter were deployed in a perennially wet and uniform reach of the main cave stream approximately 0.8 km upstream of the lower entrance. A data gap of about

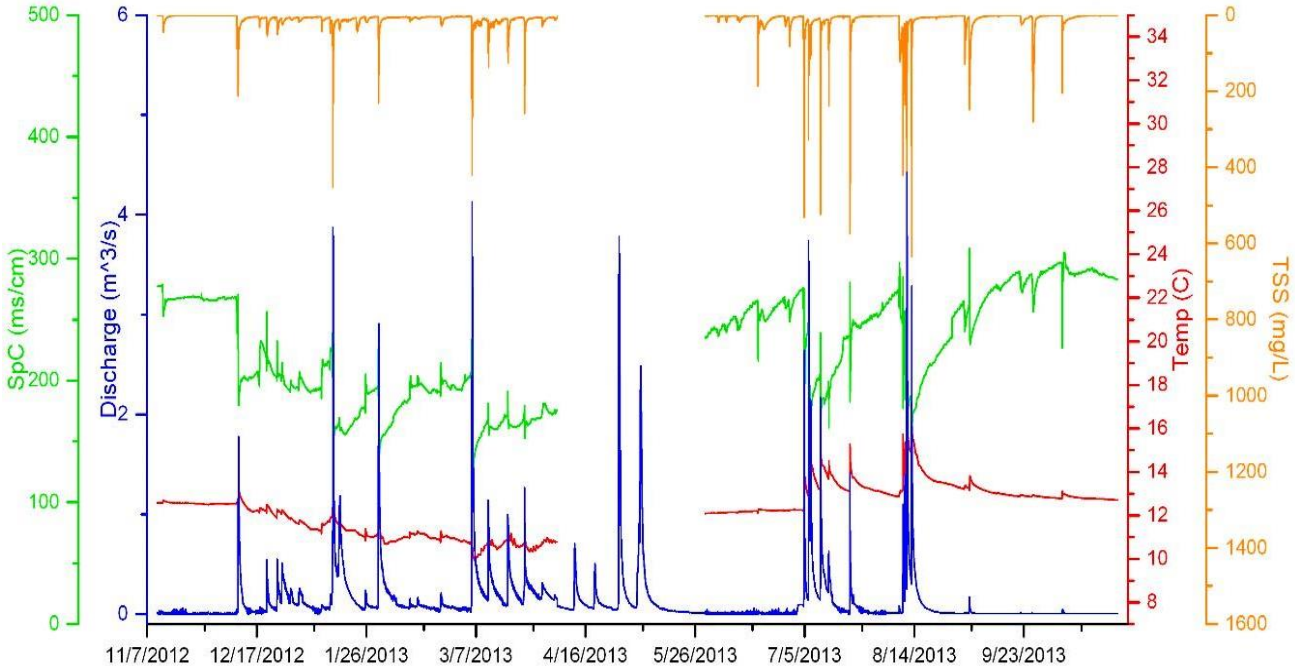

Figure 2.6: Time-series data for Blowing Cave. Discharge record is continuous from Nov. 2012 to Oct. 2013. Water quality data include two continuous runs with a 7-week gap (TSS data reversed for clarity).

seven weeks (YSI) to five weeks (Sontek) occurred during April and May, 2013 due to premature battery failure, but only two moderate storm events were missed. Figure 2.6 shows time-series data from the Sontek-IQ flow instrument and YSI-6910 quality sonde. Although no water quality data were recorded during the gap, the gap in flow data was filled by correlating to the nearest USGS surface gauge during a storm just before the instrument failure ($r^2 = 0.98$, Appendix 2.1), as well as measurements from a staff gauge at the cave spring for which a rating curve was developed (Appendix 2.2).The data demonstrate a strong, rapid response to rain events and a small seasonal component of increased base flow and lower SpC and T during winter. SpC values ranged from 113–305 μS/cm, T from 9.9–17.3 °C, and pH from 7.2–8.4. Flow was extremely variable and flashy, and ranged from a low of less than 0.004 m^3/s during Fall dry season to 4.42 m^3/s at the largest storm flow that occurred in early August, 2013, a difference over three orders of magnitude. TSS was calculated from instrument data by correlating turbidity to a set of automatic water samples taken over a 24-hour period spanning the July 6 storm event. TSS typically peaked just before or at peak discharge, reaching a maximum storm value of 635 mg/l during the August 2013 event. TSS was very low between both summer and winter storms, averaging less than 12 mg/l.

Results of bed load data collection

The records of tracer cobble and gravel sizes, mass, rock type and chip IDs (where used) are listed in Appendix 2.3. These tables include the measured movement after four storm events at BC that resulted in significant runoff in the cave stream, and one storm event at TCC at two surface channel sites. Grain size analysis was completed for the three BC and two TCC cross-sections using photographic and sieving methods. The results of the photographic analysis of surface bed load are shown in Figs. 2.7 and 2.8. The results of the sieve analysis for BC XS1 are shown in Fig. 2.9. Between 250 and 500 individual bed particles were digitized in GIS from scaled field photographs of each cross section bed surface. At BC, there is a clear progression in bed load grain size from larger particles at the upstream end (XS3) to smaller particles nearer the downstream cave outlet (XS1). At TCC, the particle size at the Rozell Road (RZR) channel is significantly larger than at the Bear Cave Hollow (BCH) channel, likely a function of

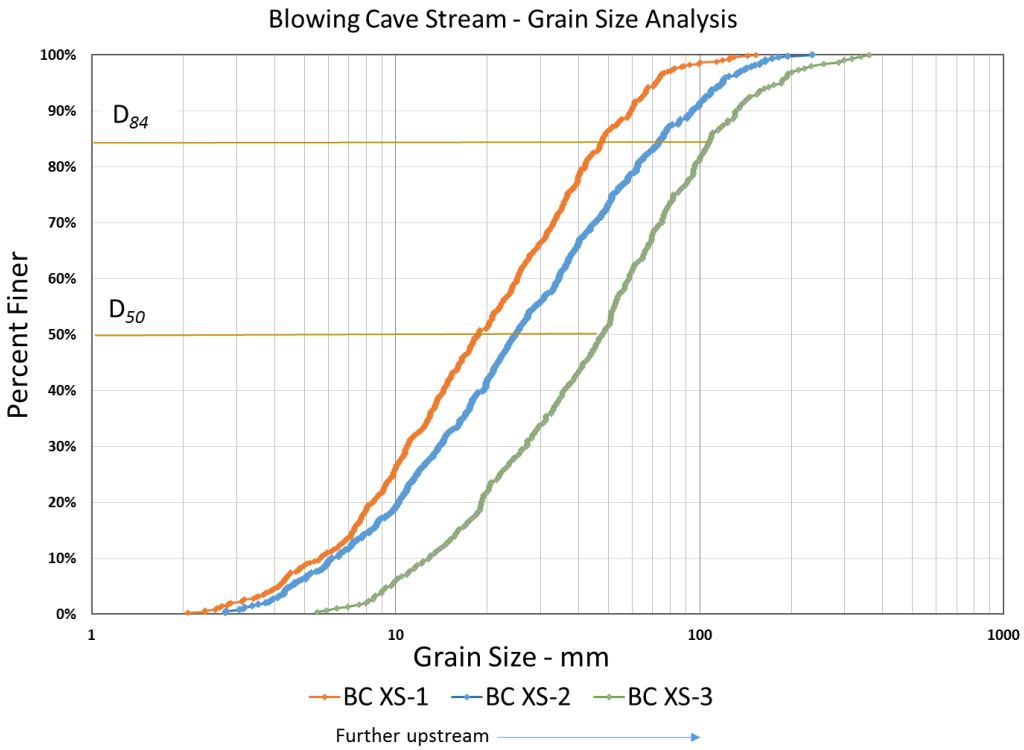

Figure 2.7: Photographic grain size analysis for the three in-cave cross-sections at Blowing Cave.

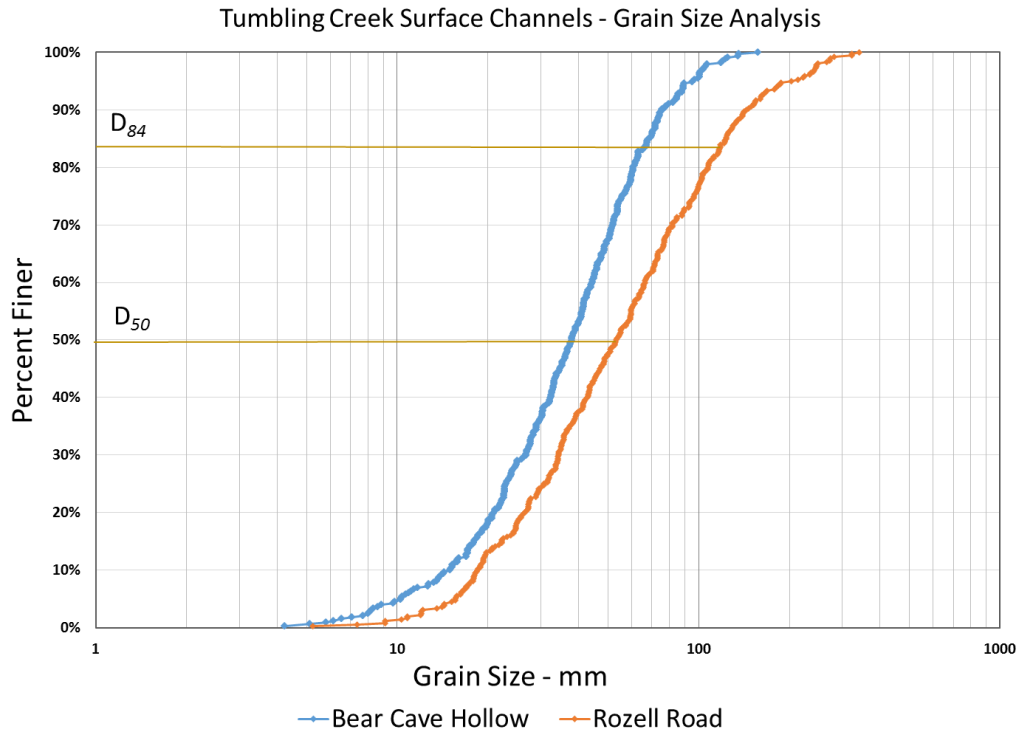

Figure 2.8: Photographic grain-size analysis for the two cross-sections in the Tumbling Creek karst basin.

the much larger basin area and larger stream power at RZR. Also at each site, the photographic analysis allowed measurement of the approximate carbonate content of the bed load, which was needed to determine bed load PIC flux. To test carbonate content of smaller sediment fractions, the mineralogy of the sieved BC XS1 material was analyzed and showed that below about 16 mm (-4 phi), over 98% the sediment was silicate. Similar fine bed material composition was noted by field inspection at the other BC and TCC cross sections, suggesting that dissolution of the finer carbonate fraction is relatively rapid and only the larger carbonate particles persist in bed load for any length of time at these sites. Because of this observation, D_{50} particle size was used for hydraulic modeling of overall bed movement, but the PIC flux was calculated based on the D_{84} grain size of bed load at each site. D_{84} is customarily used in streambed sediment studies because the size represents one standard deviation from the median grain size (Bunte & Abt 2001). Additional channel parameters needed for calculating hydraulics and running models were measured at each site. Table 1 lists channel morphologies, results of the grain size analysis and the results of measured carbonate percentages.

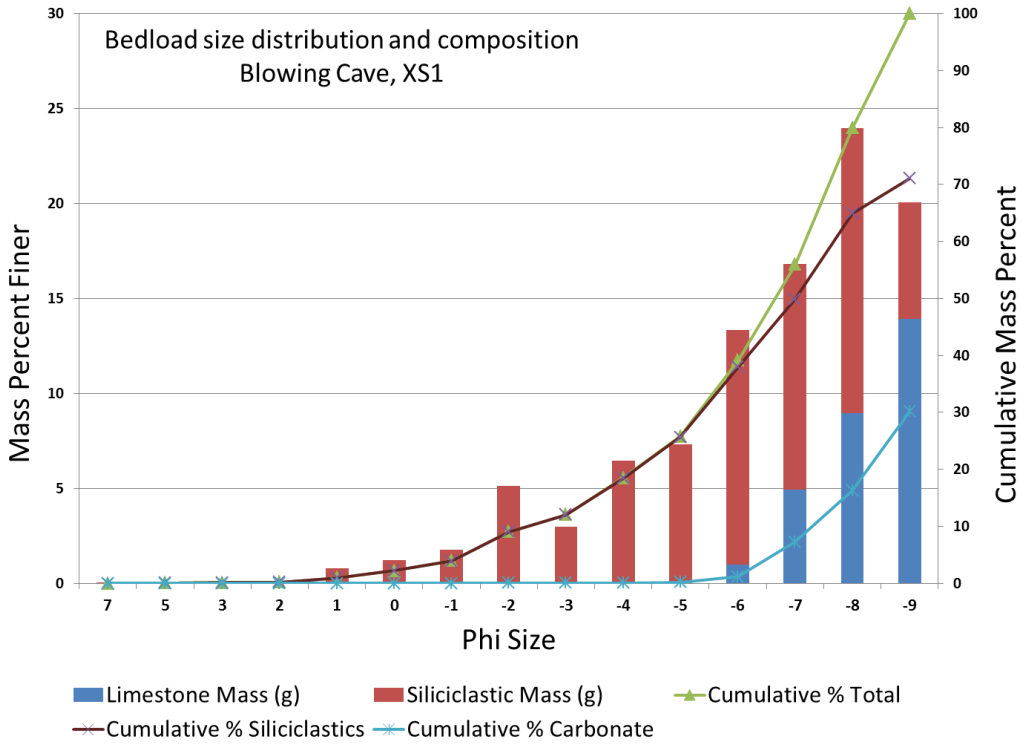

Figure 2.9: Seive analysis and carbonate composition for the bed load at XS1 in Blowing Cave.

The majority of bed load transport data for the Kentucky site were collected during 10 trips into BC to measure tagged cobble movement before and after each of four different storm events at cross-section 1: Dec. 10, 2012; Jan. 30, Apr. 28, and July 6, 2013, and the three latter storm events at cross-section 2. 158 tracing cobbles and pebbles were initially placed in BC at XS1 in November 2012, and 75 at XS2 in mid-December 2012. The initial set of tracers at XS1 included 42 small cobble and pebble single-use tracers that were painted but were too small to be chipped or numbered. An additional set of 109 larger tagged cobbles were added to XS1 on Dec. 14, 2012 to replace the single-use tracers and bring the total number

Table 2.1: Measured channel parameters for the five study reaches

Site ID	Active Channel Width (m)	Channel Slope (m/m)	D_{50} Grain Size (mm)	D_{84} Grain Size (mm)	% Carbonate in Bed Load	Channel Classification
BC XS1 (moderate gradient site)	4.31	0.008	18	43	7%	Plane bed
BC XS2 (low gradient site)	4.10	0.005	25	75	13%	Pool/Riffle
BC XS3 (high-gradient site for modeling)	3.80	0.012	50	105	16%	Plane bed
TCC RZR (main basin overflow)	6.78	0.009	54	118	15%	Pool/Riffle
TCC BCH (tributary hollow)	5.45	0.011	38	67	6%	Plane Bed

of long-term tracers to 170. At TCC, tagged cobbles were placed in surface channels in September 2013 and two trips measured cobble movement before and after a large surface runoff event in April 2014. Surface channel tracers were measured at two locations at TCC: approximately 100 meters upstream of the Rozell Road bridge at the primary karst basin overflow stream, and in the surface drainage upstream of the TCC entrance in Bear Cave Hollow. Increasingly larger storms were the targets of tagged bed transport measurement during the study period at BC. The December 10, 2012 storm was the first event after cobble deployment to move bed material. Because the mass, size, shape and rock types were known for all tracers (Appendix 2.3), effects of these parameters on particle movement were evaluated. At BC XS1, a mix of both carbonate (limestone and silty limestone) and non-carbonate (sandstone and chert) cobbles were tagged to determine if any significant differences existed in transport rates based on rock type.

After the initial storm measurement at XS1, no clear relationship was observed between rock type and transport distance (Figs. 2.10 – 2.13), so subsequent tagged cobble deployment at BC XS2 utilized only carbonate tracers for ease of chip installation. As other storms were measured, no significant correlation was observed between mass, shape, or particle size at any of the sites. At TCC, because of lack of storms and flow data at RZR and BCH, and the need for additional equipment deployment, bed load transport data were collected for a single storm event on April 28, 2014. Measuring this transport event allowed evaluation of the general magnitude of bed load PIC flux for the surface overflow component of the TCC basin. Figures 2.10 – 2.13 graph the full tagged particle transport vs particle size at BC XS1, and shows correlation between particle size vs distance traveled as regression lines. Figures 2.14 – 2.16 graph the data for BC XS2, and Figures 2.17 – 2.18 show TCC RZR and BCH. Table 2.2 lists the results of the bed transport at each of the BC and TCC sites, and the full tagged transport results are listed in Appendix 2.3.

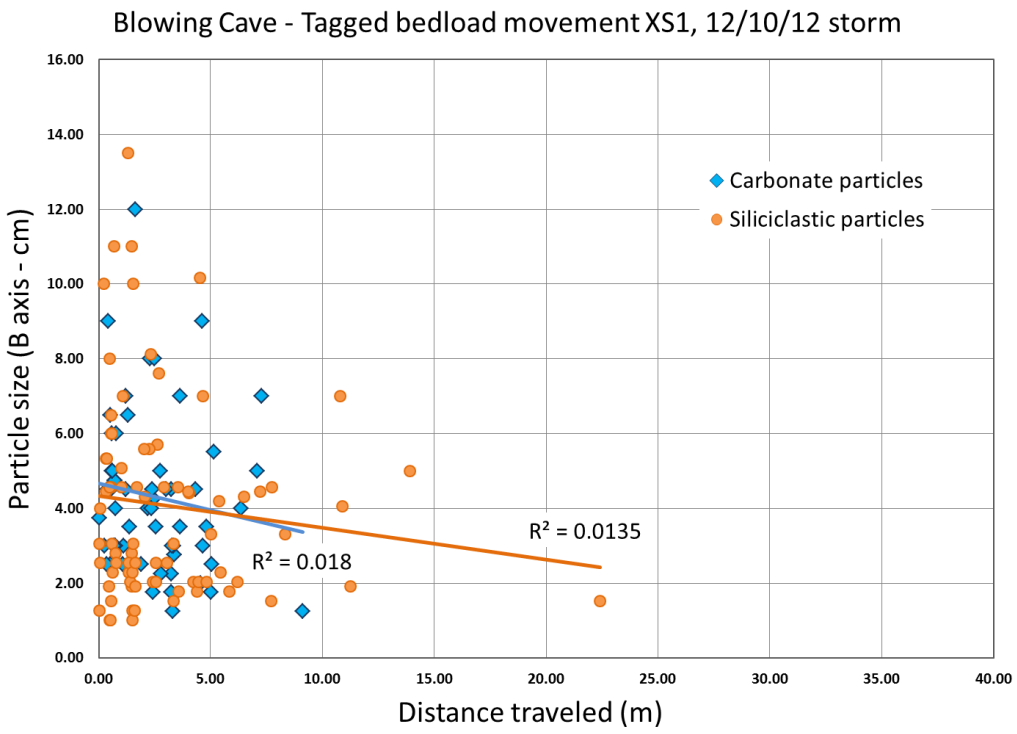

Figure 2.10: Measured movement vs. size of tagged bed particles for the 12/10/12 storm event at cross-section 1 in the Blowing Cave stream channel. The correlation between distance traveled and particle size for each component are shown as regression lines.

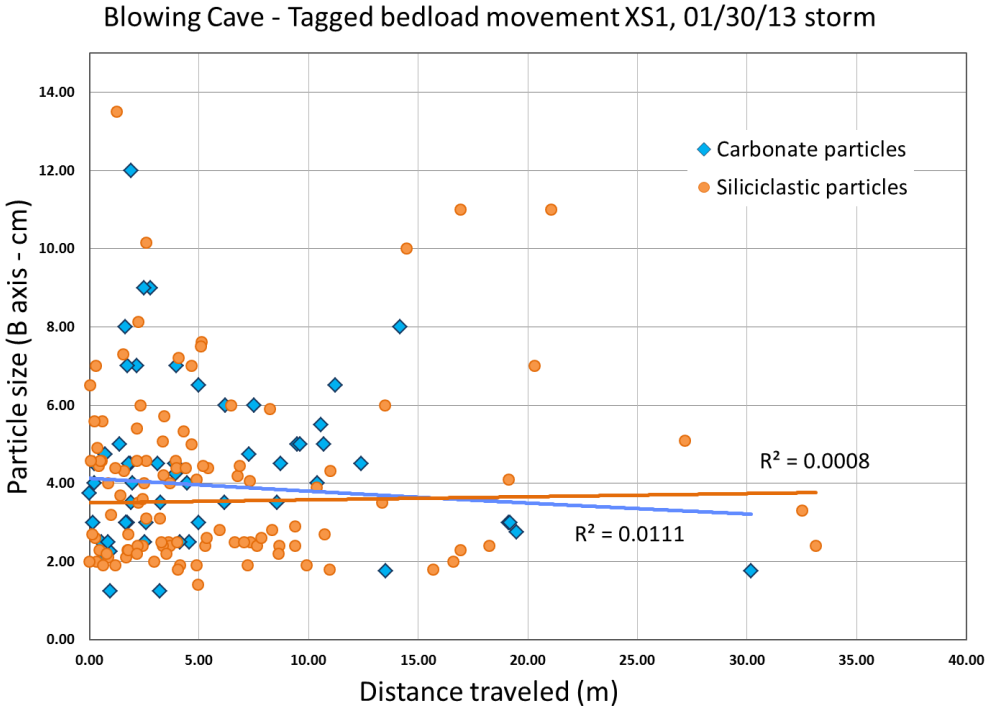

Figure 2.11: Measured movement vs. size of tagged bed particles for the 1/30/13 storm event at cross-section 1 in the Blowing Cave stream channel.

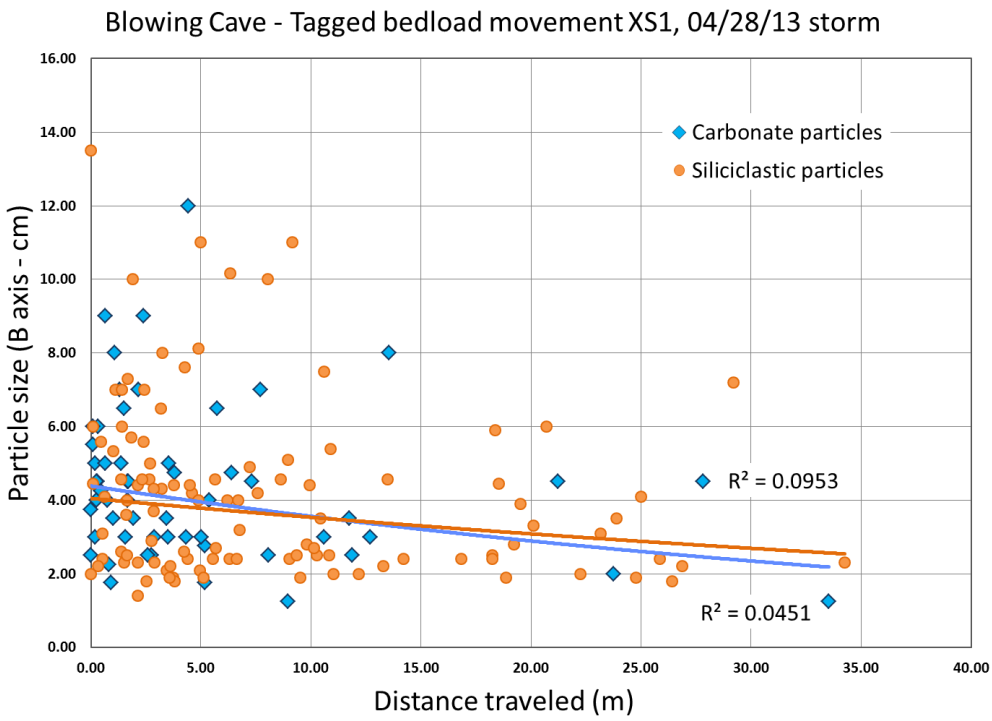

Figure 2.12: Measured movement vs. size of tagged bed particles for the 4/28/13 storm event at cross-section 1 in the Blowing Cave stream channel.

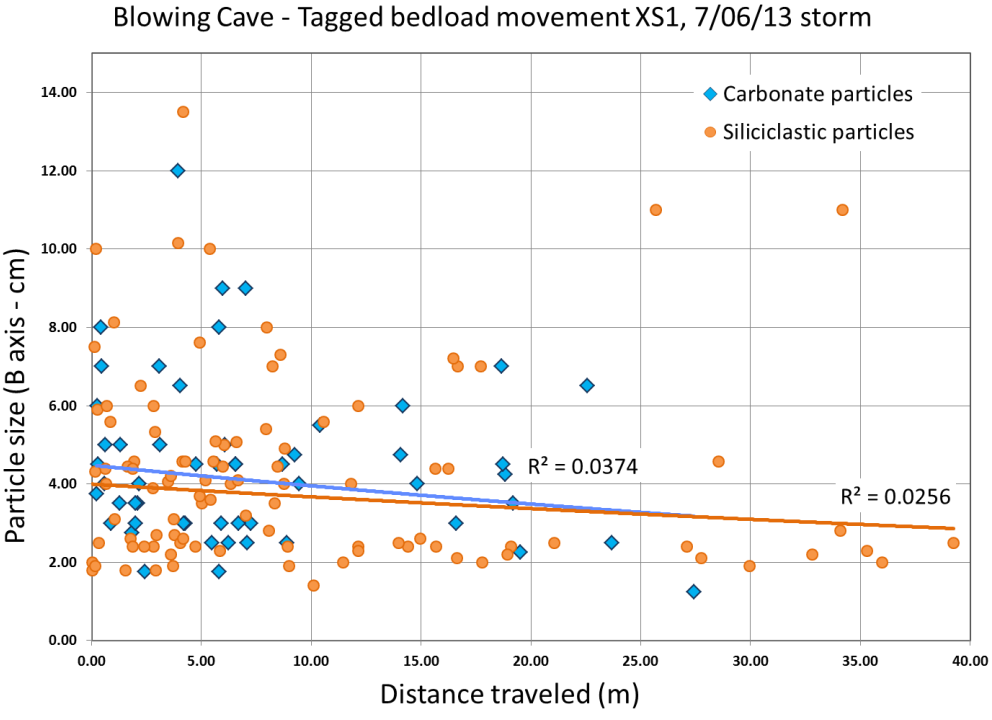

Figure 2.13: Measured movement vs. size of tagged bed particles for the 7/6/13 storm event at cross-section 1 in the Blowing Cave stream channel.

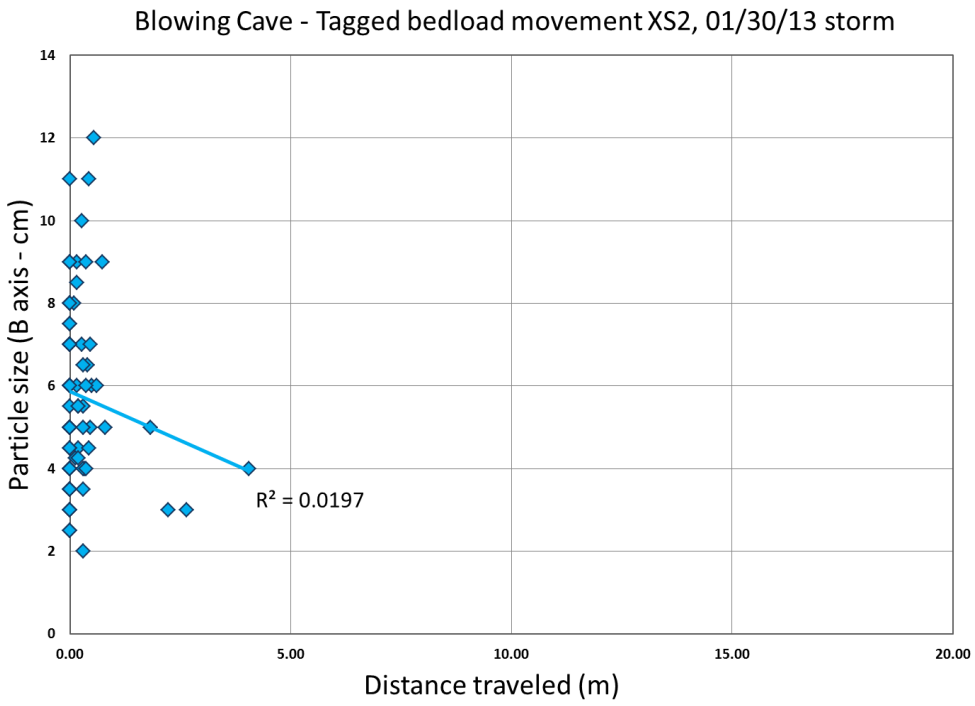

Figure 2.14: Measured movement vs. size of tagged bed particles for the 1/30/13 storm event at cross-section 2 in the Blowing Cave stream channel. All particles are carbonate tracers.

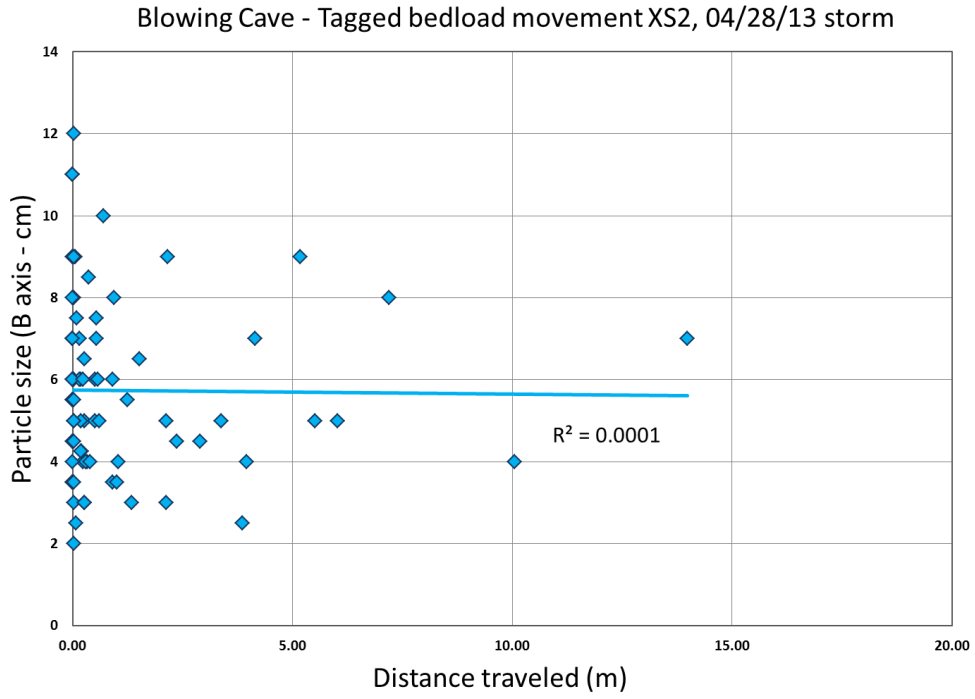

Figure 2.15: Measured movement vs. size of tagged bed particles for the 4/28/13 storm event at cross-section 2 in the Blowing Cave stream channel. All particles are carbonate tracers.

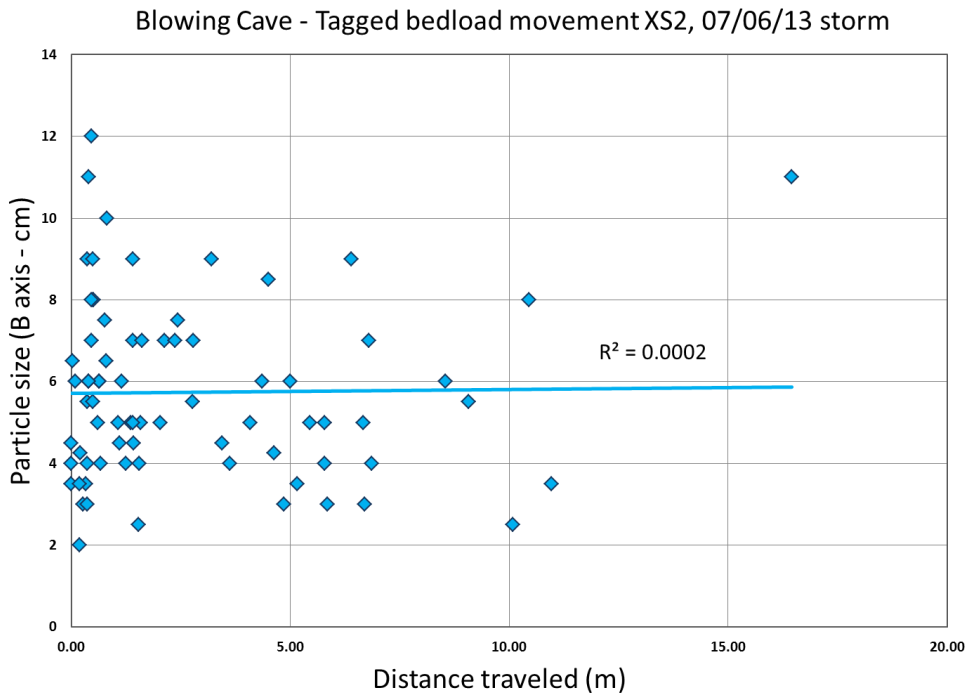

Figure 2.16: Measured movement vs. size of tagged bed particles for the 7/6/13 storm event at cross-section 2 in the Blowing Cave stream channel. All particles are carbonate tracers.

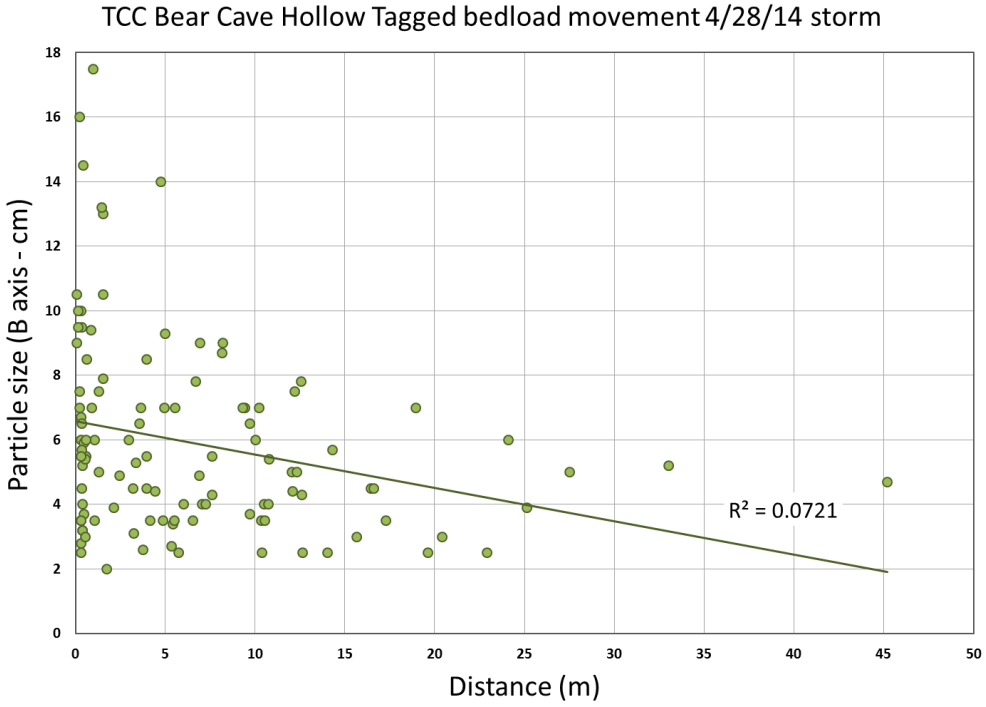

Figure 2.17: Measured movement vs size of tagged bed particles for the 4/28 storm event at TCC karst basin Bear Cave Hollow overflow channel.

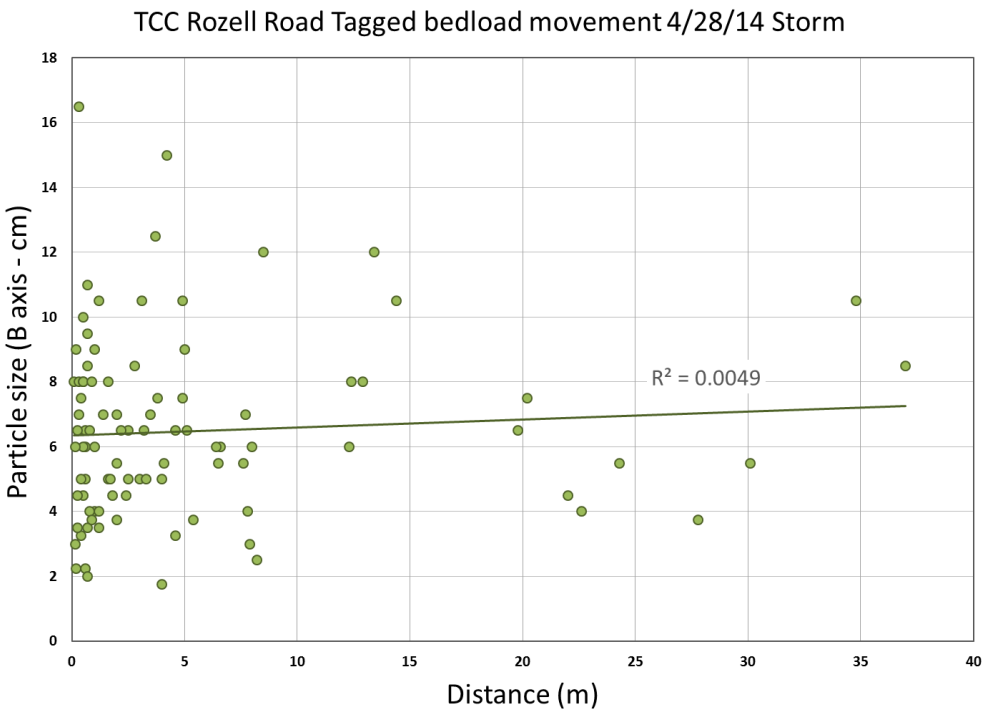

Figure 2.18: Measured movement vs size of tagged bed particles for the 4/28 storm event at TCC karst basin Rozell Road overflow channel.

Table 2.2: Tagged bed load transport results

Site	Storm event date	Mean transport distance (m)	Total measured PIC mass movement per storm (kg)	Peak storm discharge (m^3/s)	Peak Stream Power (W/m^2)	Duration above critical stream power (Hrs)
BC XS1 (moderate gradient site)	12/10/2012	2.86	635.2	1.77	32.3	4.75
	1/30/2013	5.85	1769.3	2.91	52.9	9.25
	4/28/2013	7.16	2165.2	3.78	68.8	14.0
	7/6/2013	8.82	2677.8	3.72	67.6	16.5
BC XS2 (low gradient site)	1/30/2013	0.28	90.8	2.91	34.8	5
	4/28/2013	1.23	454	3.78	45.2	8.25
	7/6/2013	2.79	1035.3	3.72	44.3	10.5
TCC RZR (main basin overflow)	4/28/2014	5.27	1672	4.16	54.6	5.25
TCC BCH (tributary hollow)	4/28/2014	6.67	1134.5	1.36 (from peak stage)	26.9	-

Calculating bed flux

The results for measured mass transport, continuous stream discharge, and stream channel and bed load parameters were combined to determine a total time-series PIC transport in bed material for BC and TCC. Using equation (5), unit stream power was calculated from discharge records at BC XS1,2 and 3, and TCC RZR (Figs. 2.19 – 2.22). At BC, unit stream power ranged from a low of about 0.1 W/m^2 during a drought in the Fall of 2013 to a high of 194 W/m^2 at BC XS3 during a large thunderstorm on August 11, 2013. At TCC, the karst basin's surface overflow channels only flow during large runoff events, and only one storm runoff dataset was obtained. The unit stream power at TCC RZR ranged from a low of zero before flow initiation to a high of 66.2 W/m^2 during the measured April 28, 2014 storm (Table 2.2).

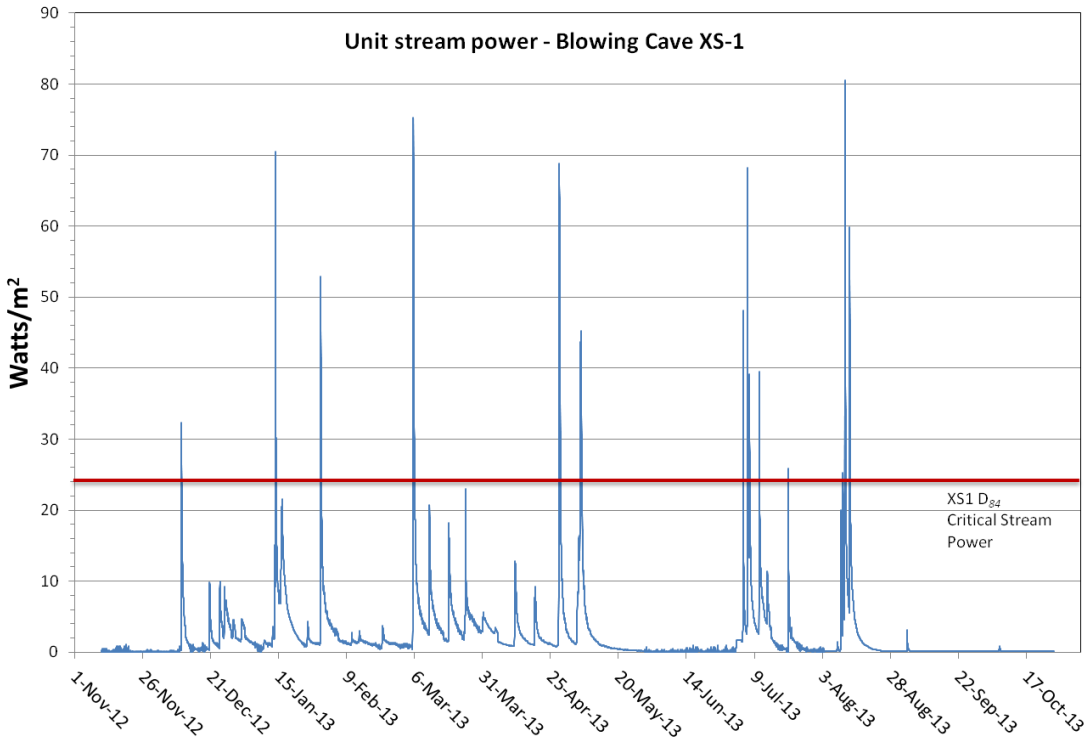

Figure 2.19: Time-series of unit stream power and the critical stream power threshold for BC XS1.

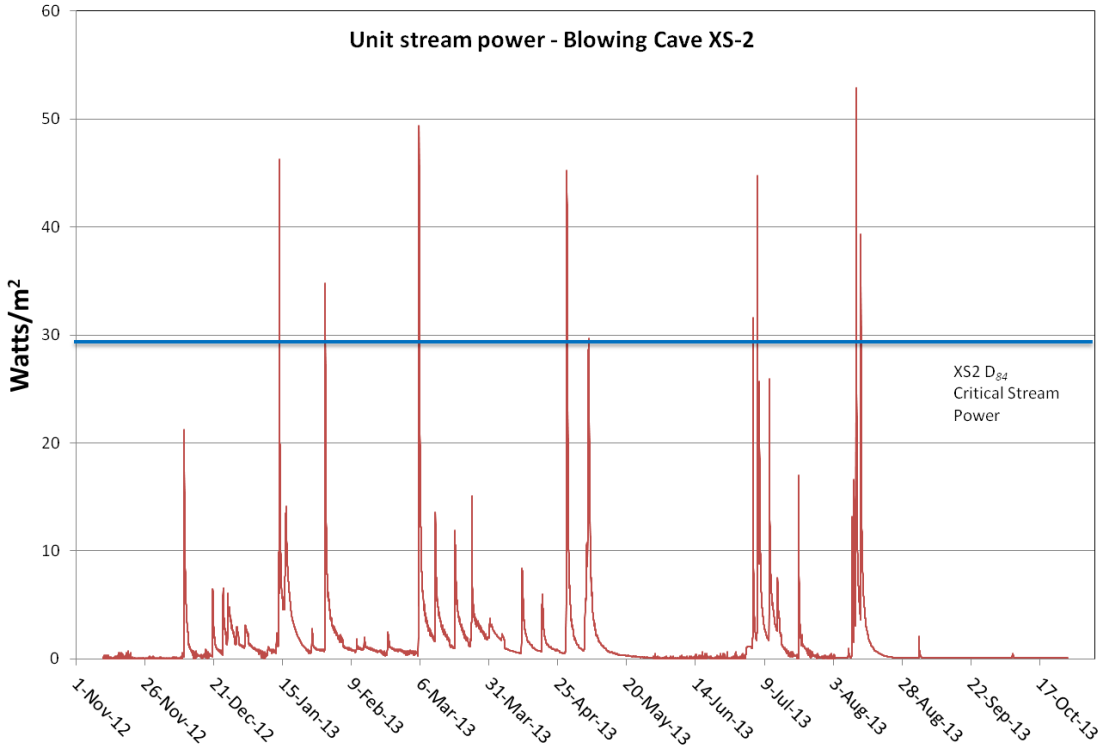

Figure 2.20: Time-series of unit stream power and the critical stream power threshold for BC XS2.

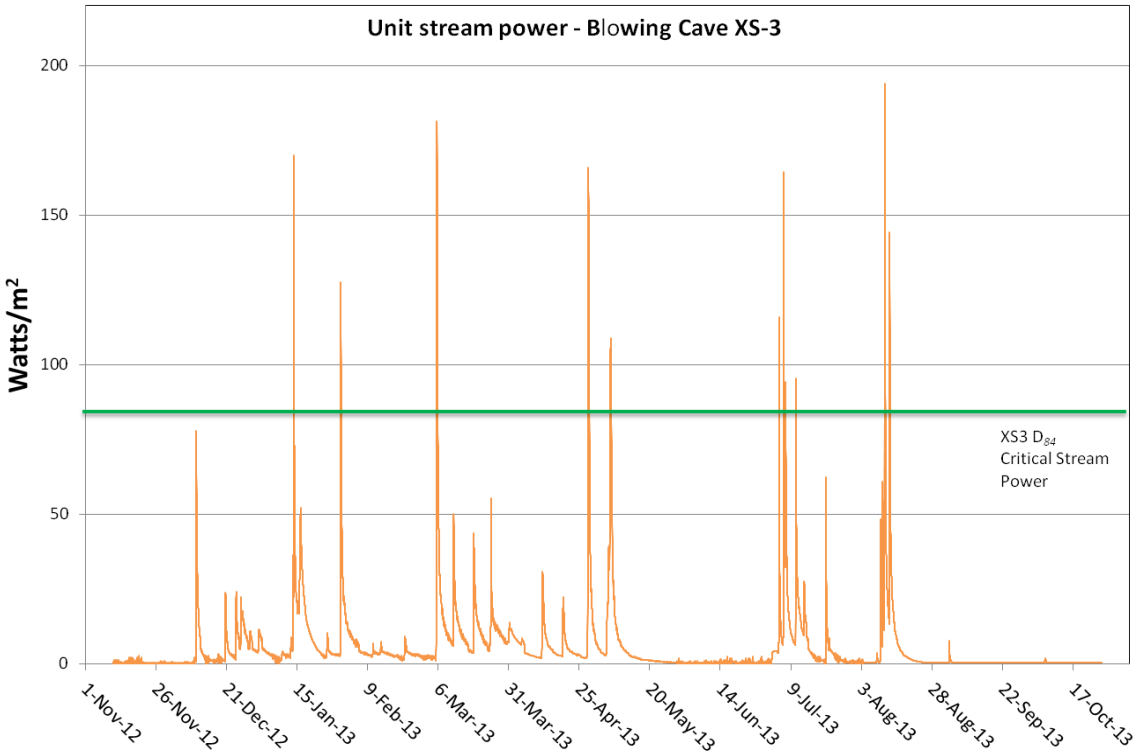

Figure 2.21: Time-series of unit stream power and the critical stream power threshold for BC XS3.

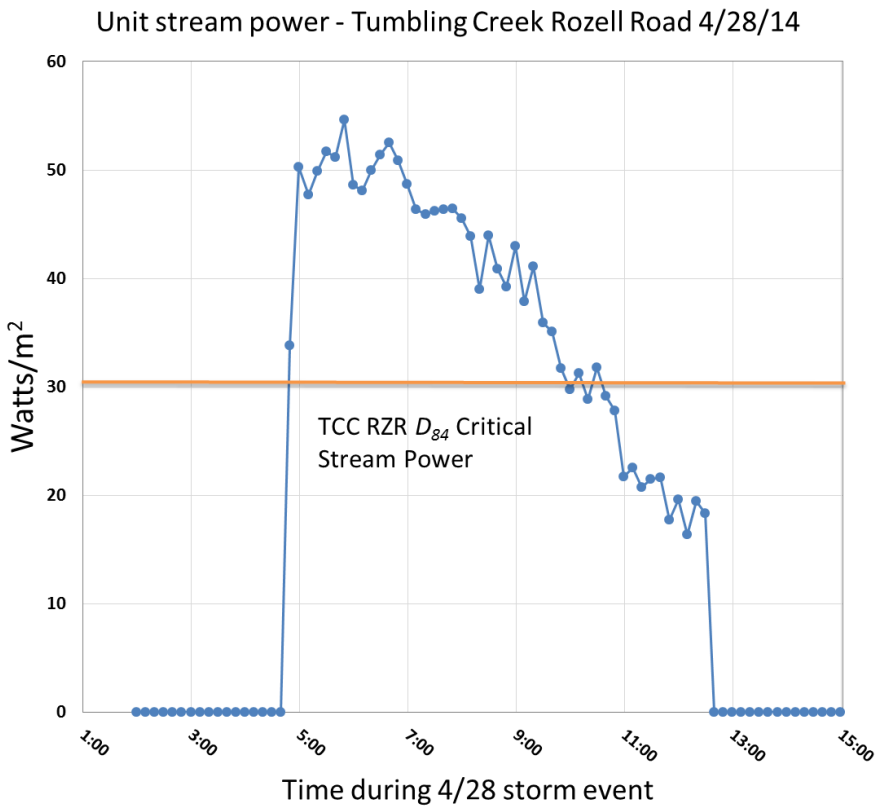

Figure 2.22: Time-series of unit stream power and critical threshold for TCC RZR 4/28/2014 storm.

Once unit stream power was calculated for the sites, critical stream power (ω_0) for initiation of bed movement was derived by a combination of methods. Equation (6) was used to derive a critical threshold based on channel and D_{84} bed load parameters. Although the transport distance of individual cobbles measured from tagged tracers was not very sensitive to grain size overall, the initiation of total bed movement was not observed to occur until critical stream power reached a value that could move the larger bed material. Therefore, the D_{84} grain size for each reach was adopted for modeling and calibration. The initial calculations for the three cross sections overestimated ω_0 by approximately 20% to 85%, but the variety of peak storm flows and number of measured storm events at BC allowed an accurate assessment of the critical threshold based on field observations. For instance, the December 10, 2012 storm event moved material a short distance at BC XS1, but not at XS2 or 3. Later events moved material at XS1 and 3 but not at XS2. Some smaller storm events moved no bed material at all, and only 8 storm

events transported bed load at all three of the BC sections during the study period (Figs 2.19, 2.20, 2.21). At TCC, time of initiation of movement at the beginning of the 4/28 storm event was observed and compared to time-series stream power results (Fig 2.22). Note that BC XS3 was used as a high-gradient site for modeling to incorporate the full range of channel types that occur in the BC system. Although no tagged cobbles were utilized at XS3 due to difficulty of access, all other parameters were measured, timing of bed movement observed, and calibrations from XS1 and XS2 used to make similar adjustments for XS3. From observations at all three sites, the empirical constant in equation (6) was adjusted and the calibrated results determined ω_0 for further computations (Table 2.2).

Using the time-series unit stream power and calibrated critical threshold, equation (7) derived a dimensioned mass transport at each site for each time-series interval (every 30 minutes during the study period). The model gave relatively accurate predictions of the start and end of bed transport, but initially overestimated total mass flux when compared to the results of total bed movement from the tagged tracer tests (Table 2.2) because the empirical constant in equation (6) needed fine tuning beyond the rough calibration from field observations. After fine tuning equation (6) in order to adjust the results of equation (7), modeled transport agreed closely with measured transport and a full calibrated mass flux time series was obtained (Fig 2.23). The highest calculated bed PIC transport at BC occurred during the August 11, 2013 storm, where 2132 kg of PIC material was moved over a 30-minute period at peak storm discharge. The movement of bed material in the BC system is highly punctuated, appearing as rapid short spikes on the time-series graph, even at log scales (Fig. 2.23). The rapid rise and fall of stream power during storm events in the system causes the critical transport threshold to be quickly passed for all grain sizes. That dynamic is is reflected in the insensitivity of bed load travel distance to mass for most storms. The short duration and intensity of these events shows the difficulty of accurately assessing sediment transport in flashy systems.

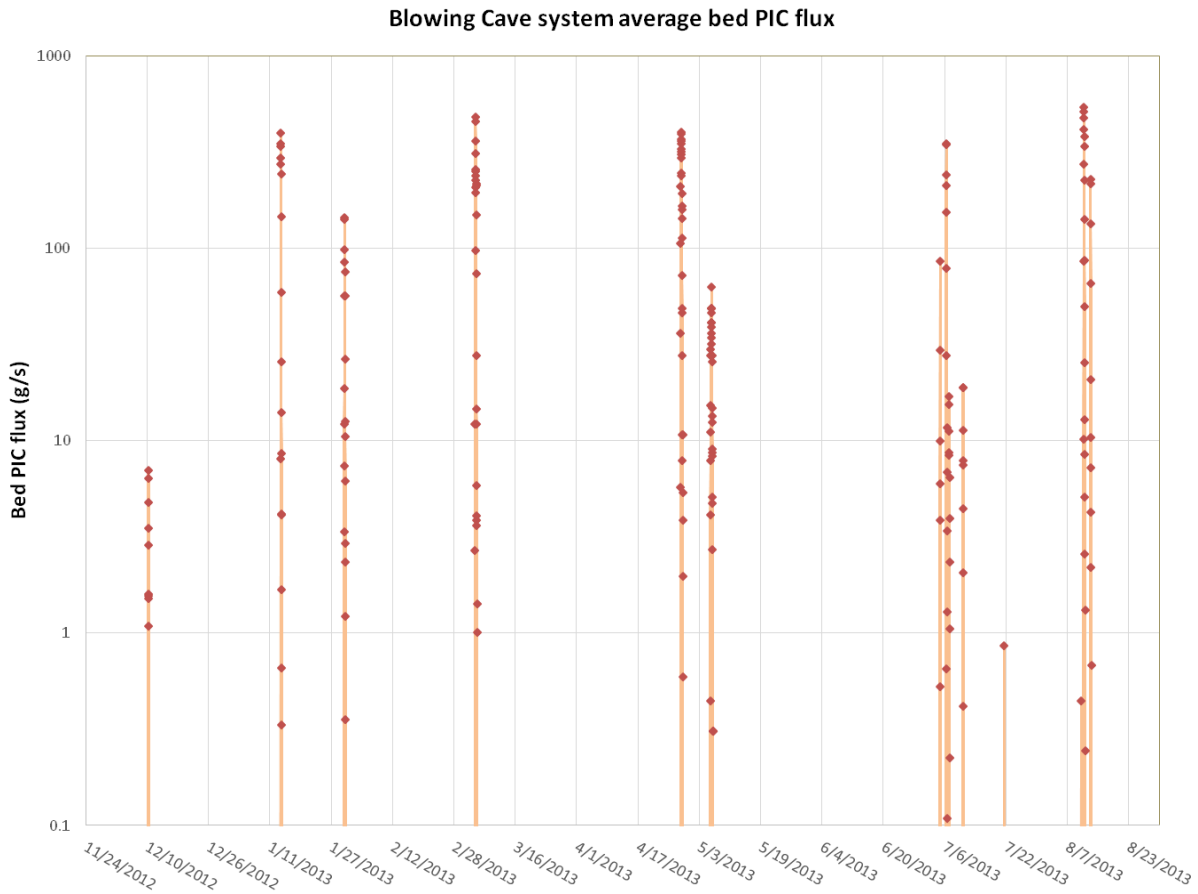

Figure 2.23: Bed PIC flux for the Blowing Cave system. Flux is the average of three modeled cross sections representing the main channel types in the system.

Results of suspended and dissolved load data collection

In order to determine PIC flux in suspended loads at BC, three separate types of data were collected and correlated. A continuous time series record of turbidity was collected as described above. Measurements of TSS were conducted in order to convert turbidity to a time-series TSS record. The amount of carbonate in suspended sediment loads was determined for two major storm events. To correlate turbidity to TSS, 500 ml grab samples were taken every 30 minutes with an ISCO automatic sampler for a span of 12 hours over the course of the January 30, 2013 storm event. Additional low turbidity grab samples were collected manually at other times. The turbidity to TSS correlation was a linear function correction and is included in Appendix 2.4.

The initial method used to determine PIC concentration within suspended loads was the Gran F1 alkalinity titration of filtered (0.45 or 0.22 µ) vs unfiltered grab samples. Numerous titrations were conducted for pairs of filtered and unfiltered samples over storm events on December 10th 2012, and July 4, 2013 (Appendix 2.5). Results from the paired titrations showed a small but observable difference in HCO_3^- that was attributed to suspended carbonate material (e.g., Fig. 2.24).

The alkalinity tests showed that there was a persistent but moderate amount of suspended PIC related to turbid storm flows in the BC system. The PIC breakthrough coincided with or immediately preceded turbidity spikes (Fig. 2.25). However, many of the paired samples during non-peak but turbid flows had differences in HCO_3^- that were difficult to resolve because they were near the inherent error of field titrations of ~ +/-2%. Because of this, the alternative method of analyzing calcium and magnesium cations between pairs of acidified filtered and unfiltered samples was adopted for the rest of the study period.

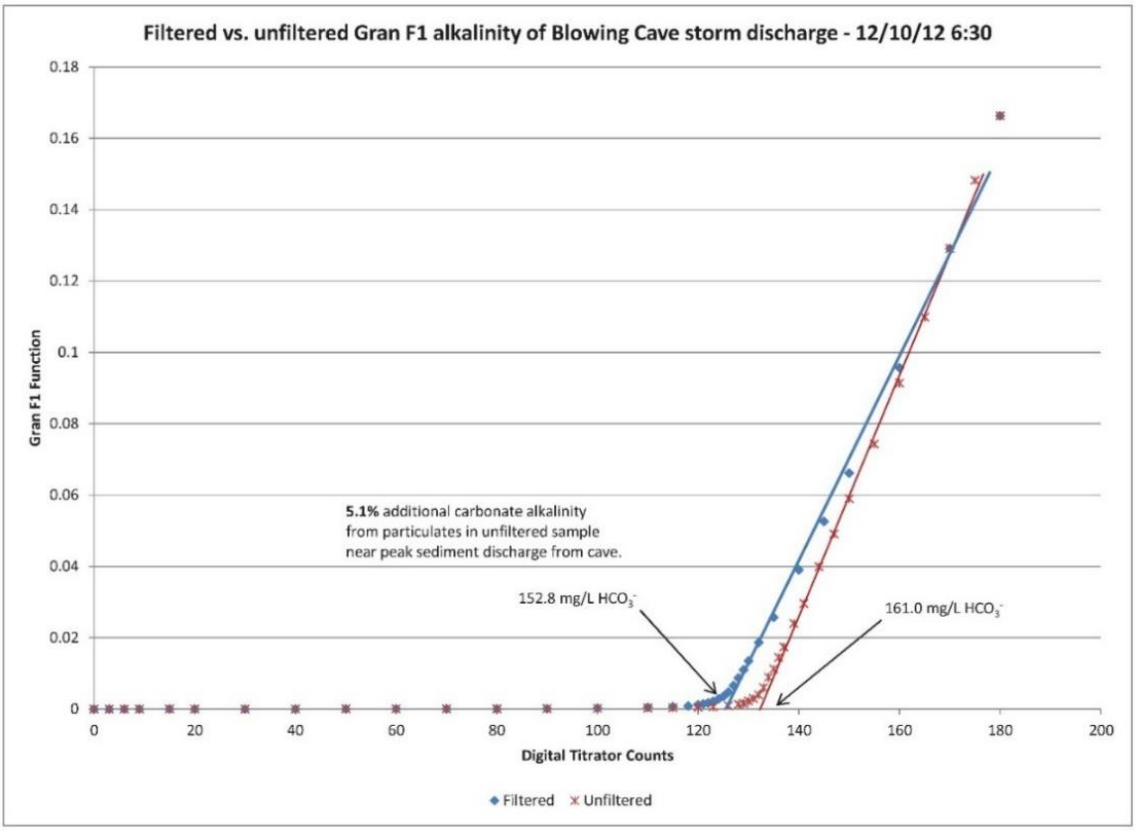

Figure 2.24: Difference in filtered vs. unfiltered titrated carbonate alkalinity for the peak of a moderate storm event at Blowing Cave.

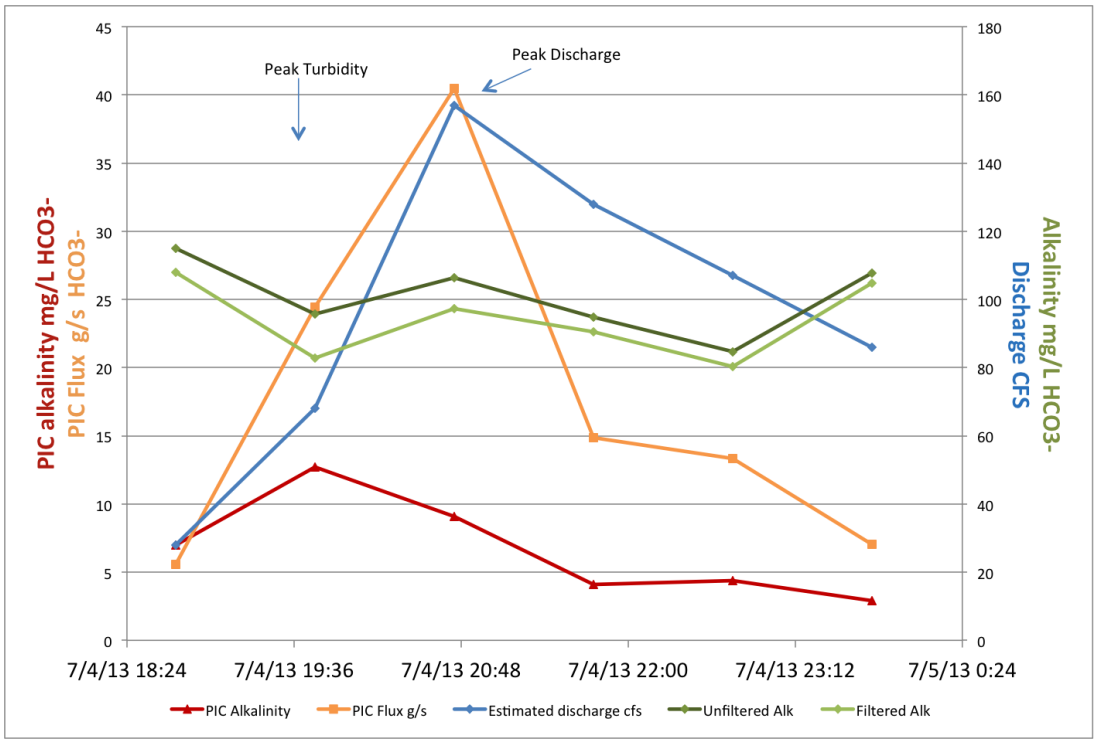

Figure 2.25: Time-series of filtered (light green) vs. unfiltered (dark green) titrated carbonate alkalinity across a moderate storm event in July at BC XS1. PIC difference between paired samples is shown in red.

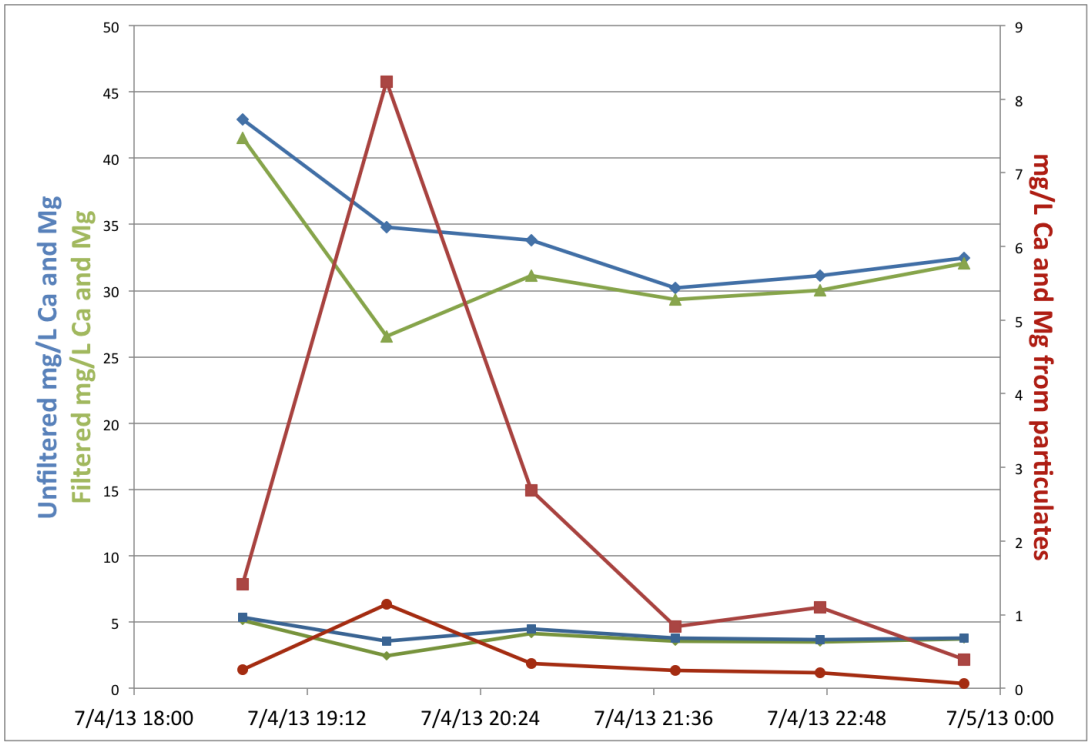

Figure 2.26: Difference in filtered vs. unfiltered carbonate alkalinity for the peak of a moderate storm event at Blowing Cave.

Paired cation analysis of filtered/unfiltered samples proved to be a more precise method for assessing excess PIC in suspended sediment. The precision of the ICP lab analysis allowed differences of less than +/-0.5% in Ca^{2+} and Mg^{2+} to be determined in most cases. For samples collected at BC for regression analysis, Ca^{2+} and Mg^{2+} concentrations ranged from 32.0 – 51.2 and 2.6 – 7.3 mg/l respectively, and HCO_3^- ranged from 75.5 to 147.0 mg/l (Appendix 2.5). The results of the paired cation tests showed a time-series flux pattern across turbid storm events similar to the pattern from the paired alkalinity tests (Fig. 2.26). The alkalinity titrations and cation analyses used for the paired PIC flux measurements during storm events were also used to determine overall dissolved carbonate loads. pCO2 is accounted for in the calculation, and of the remaining dissolved carbon species, HCO_3^- was >99.2% of the total in all tested samples.

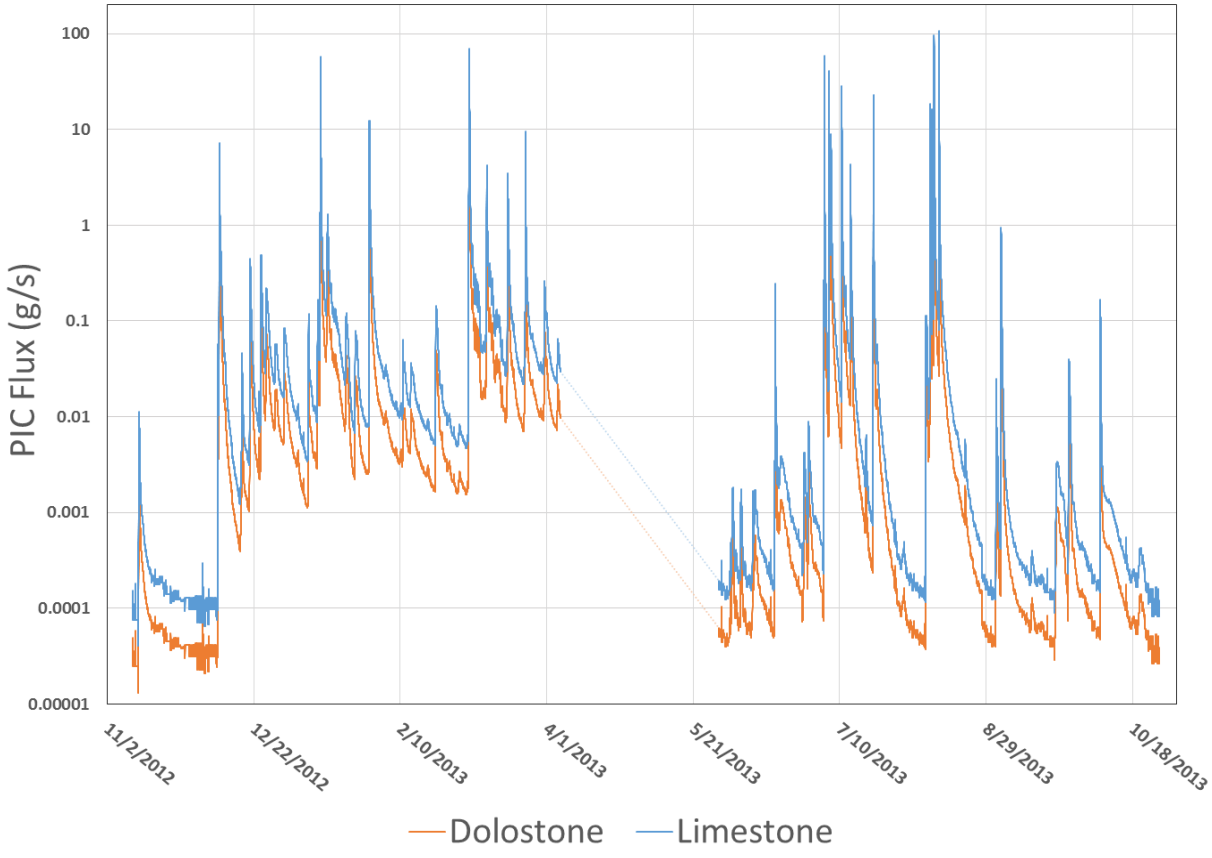

Figure 2.27: Modeled PIC flux in suspended load for the Blowing Cave system. Gap in modeled flux is from lack of turbidity logs from instrument downtime. Limestone PIC flux is shown in blue, dolostone PIC flux in orange.

Calculating suspended flux

After correlating TSS to turbidity and calculating a time series of suspended solids discharge, a regression analysis was applied to TSS and the individual suspended PIC measurements. The analysis produced a suspended PIC flux dataset for BC (Fig. 2.27). Some significant scatter occurred in the correlation of PIC to TSS and discharge because peak PIC concentrations did not always correspond to the peak TSS discharge, and more importantly, TSS typically reached a peak 15 to 45 minutes before peak storm discharge, but sometimes after. The resulting hysteresis between the collected data was too unpredictable to adjust easily, but did not greatly impact the overall PIC flux modeling.

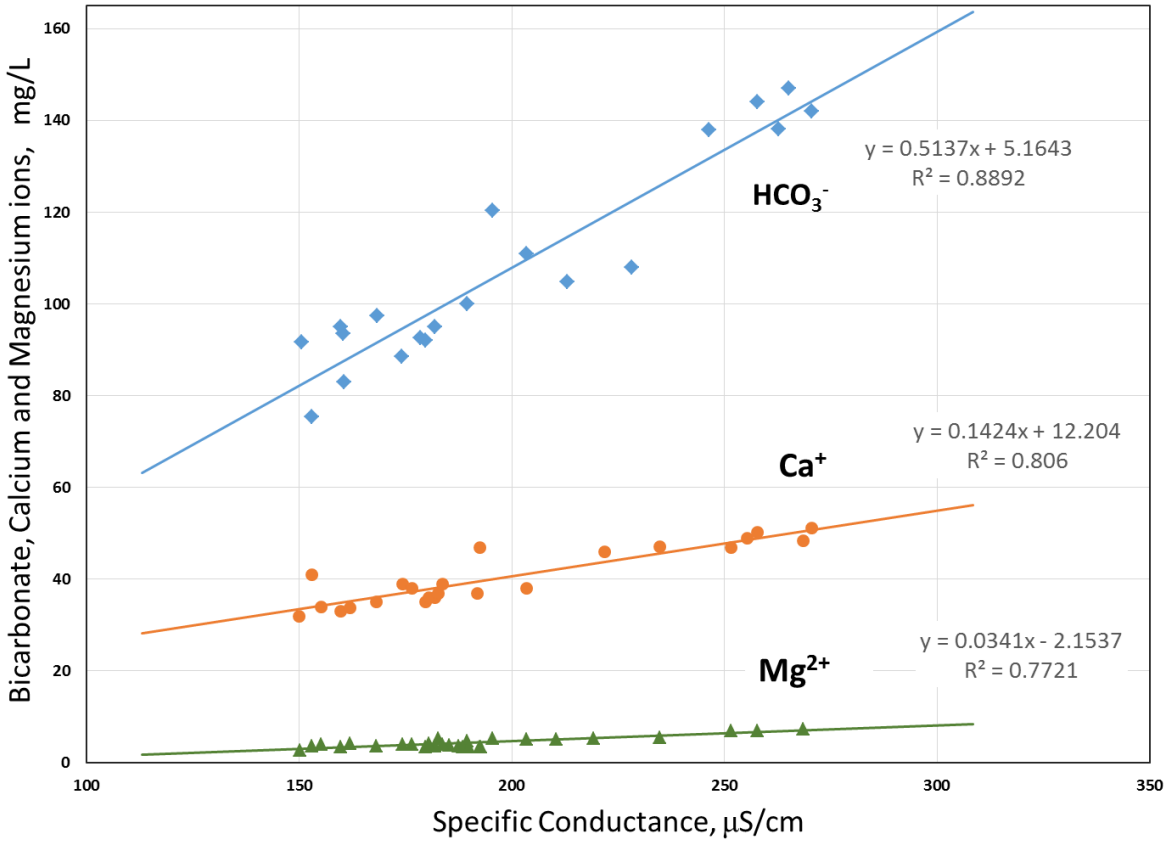

Figure 2.28: Regression analysis of Mg^{2+}, Ca^{2+}, and HCO_3^- with SpC measurements at BC, used to construct time-series of ion concentrations from data sonde SpC time-series.

Calculating dissolved flux

To construct the time-series dataset for dissolved carbonate in BC, regressions were calculated between SpC data and Mg^{2+}, Ca^{2+}, and HCO_3^- dissolved concentration results (Fig. 2.28; Appendix 2.6). Slopes of the regressions were all positive since higher concentrations of dissolved constituents result in higher SpC levels. The correlation coefficients for the regressions were moderately good: 0.89 for HCO_3^-, 0.81 for Ca^{2+} and 0.77 for Mg^{2+}. The regression equations were applied to the full SpC dataset and the resulting 15-minute concentrations converted to mmol for analysis of ion ratios and calculation of the amount and types of carbonate bedrock dissolved. The modeled molar concentrations for HCO_3^- ranged from 1.04 to 2.68 mmol/l, Ca^{2+} from 0.49 to 1.48 mmol/l and Mg^{2+} from 0.07 to 0.34 mmol/l, tracking temporal changes to SpC.

Carbonate bedrock in the BC basin consists of both limestone and dolostone, so Ca^{2+} and Mg^{2+} need to be compared in order to attribute the Mg^{2+} and an equal amount of Ca^{2+} to dolostone dissolution. The modeled chemistry indicates that 24.4% of the Mg^{2+} and Ca^{2+} in solution originates from dolomite dissolution. The molar results of the Ca^{2+}, Mg^{2+} and HCO_3^- can be compared to determine the ratio of bicarbonate to dissolved carbonate bedrock. If all the dissolution of the bedrock is attributable to reaction with CO_2 (equations 1 and 2), then the $Ca^{2+} + Mg^{2+}$ to HCO_3^- ratio will be 1:2 (0.5). In many karst settings, however, the ratio is typically >0.5. A ratio of 0.57 has been measured at Mammoth Cave, and a ratio of 0.64 at Redmond Creek, a site just a few miles from Blowing Cave. (Groves & Meiman 2003; Florea 2015). For this study, the modeled ratio ranged from 0.54 to 0.67 depending on conditions and flow. The additional bedrock corrosion may be attributable to dissolution by other compounds such as organic acids or sulfuric acid derived from oxidation of pyrite. Results for the different modeled dissolved components produced a time-series dataset for the DIC flux (Fig. 2.29).

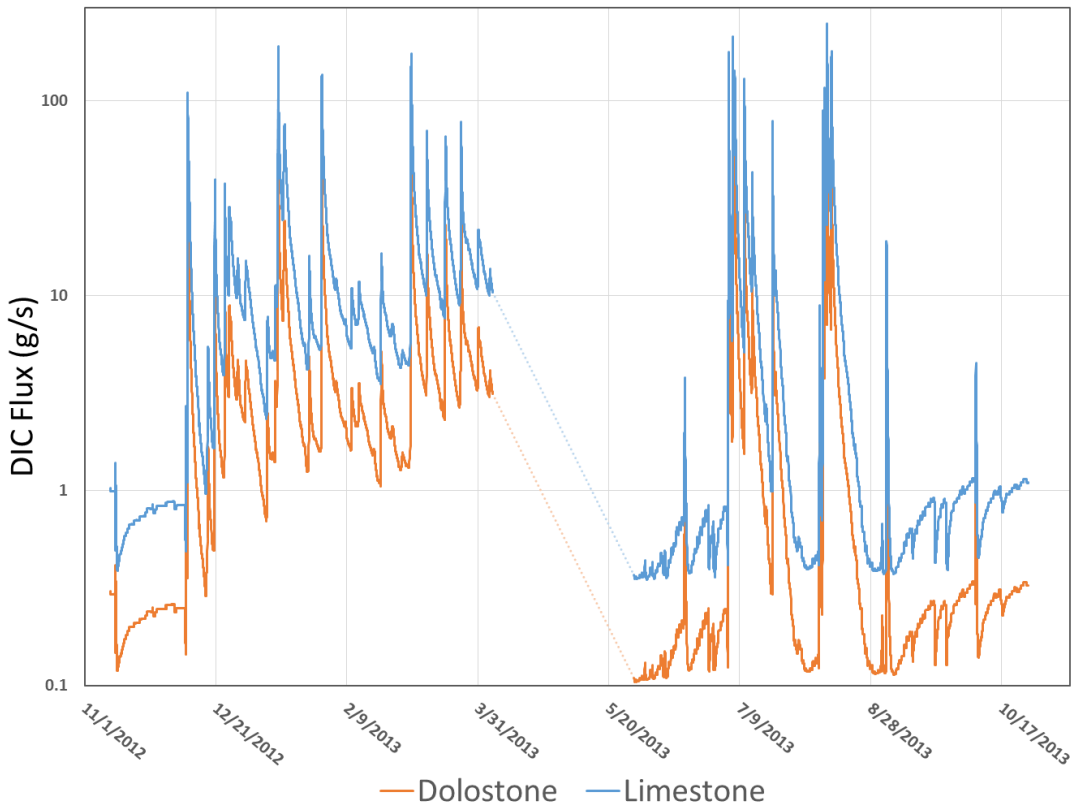

Figure 2.29: Modeled DIC flux as representative bedrock species for the Blowing Cave system. Gap in modeled flux is from lack of SpC logs from instrument downtime. Limestone DIC flux is shown in blue, dolostone DIC flux in orange.

DISCUSSION

Comparison of inorganic carbon fluxes

With the three IC flux components completed at BC, annual totals of removed mass were calculated and tabulated (Table 2.3). Errors were calculated from the maximum measurement or analysis error for each method, resulting in a 3.4% error for dissolved load components, a 5.0% for suspended load components and an 11.0% for bed load components. The dissolution of carbonate resulted in a total of over 330 metric tons (t) of bedrock removed, with about 250 t from limestone and about 80 t from dolostone. Carbonate in suspended loads added a small but somewhat significant 8 t, and carbonate removal in bed loads totaled over 30 t. Overall, 376 t of TIC was removed for the annual period. Suspended PIC was 2.3% of the total flux, and bed load PIC was 8% of the total flux. In all, mechanical erosion of PIC made up 10.3% of the total carbon removal, with DIC making up 89.7%. The removal of PIC material is highly dependent on

storm events, and the study confirmed that DIC dominates carbon flux at low to moderate flow conditions. During regular storm flow, bed and suspended PIC become more significant, and at discharges of 3 m^3/s and larger, they become the dominant IC mass removal components. At the largest recorded storm event during this study, the combined bed and suspended PIC flux was 50% larger than the DIC flux. Figure 2.30 shows the relationship between PIC/DIC and discharge demonstrated by the research results. The pattern is similar to the PIC relationship revealed by Newson (1971) shown in Figure 2.3.

Initial observations of mechanical erosion evidence in the BC system indicated that significant removal of carbonate bedrock may be occurring from scouring of cave walls by smaller sediment (sand and pebbles) and bashing by larger sediment (cobbles and boulders) during storm events. It was thought that the PIC produced in this process could add considerable carbonate material to the suspended loads exiting the system during storms, but while some suspended carbonate was observed, it was not the primary mechanical removal process. As shown in the conceptual model, even if large amounts of suspended carbonate are produced by mechanical processes during storm events, aggressive storm water could be dissolving the smaller fraction in the water column before it is transported far in the stream. The lack of fine carbonate material in bed load (Fig. 2.9) supports that interpretation, and suggests that determining the actual magnitude of mechanical enlargement of bedrock conduits by sediment scouring and bashing may be challenging because of the rapid conversion of material to dissolved load.

The removal of carbonate bedrock by bed load transport turned out to be the most significant mechanical process in the BC system. Eleven different storm events transported bed load during the study year. Carbonate bed material is large enough to persist for long periods of time as it is continually produced by breakdown of cave walls and moved downstream, ultimately exiting the system to continue being dissolved in surface waters. In the TCC system, observed and previously studied processes showed little significant PIC transport in the subsurface, but the overflow components of the karst basin were shown to be significant contributors to carbonate transport during moderate storm events that initiate surface flow.

Table 2.3: Annual inorganic carbon removal from the Blowing Cave basin for the 2012/2013 water year			
Material removed	Metric tons IC	% of total	Equivalent CO_2 removal, metric tons/year
Mass of carbonate from dissolution of limestone	255.1 +/- 8.7	67.8 +/- 2.3	112.2 +/- 3.8
Mass of carbonate from dissolution of dolostone	82.2 +/- 2.8	21.9 +/- 0.7	39.3 +/- 1.3
Mass of carbonate in suspended load from mechanical erosion	8.6 +/- 0.4	2.3 +/- 0.1	3.5 +/- 0.2
Mass of carbonate in bed load from mechanical erosion	30.2 +/- 3.3	8.0 +/- 0.9	12.1 +/- 1.3
Total DIC removal	337.3 +/- 11.5	89.7 +/- 3.0	151.4 +/- 5.1
Total PIC removal	38.7 +/- 3.7	10.3 +/- 1.0	15.6 +/- 1.5
Total inorganic carbon mass removal	376.0 +/- 15.2	100.0	166.9 +/- 6.6

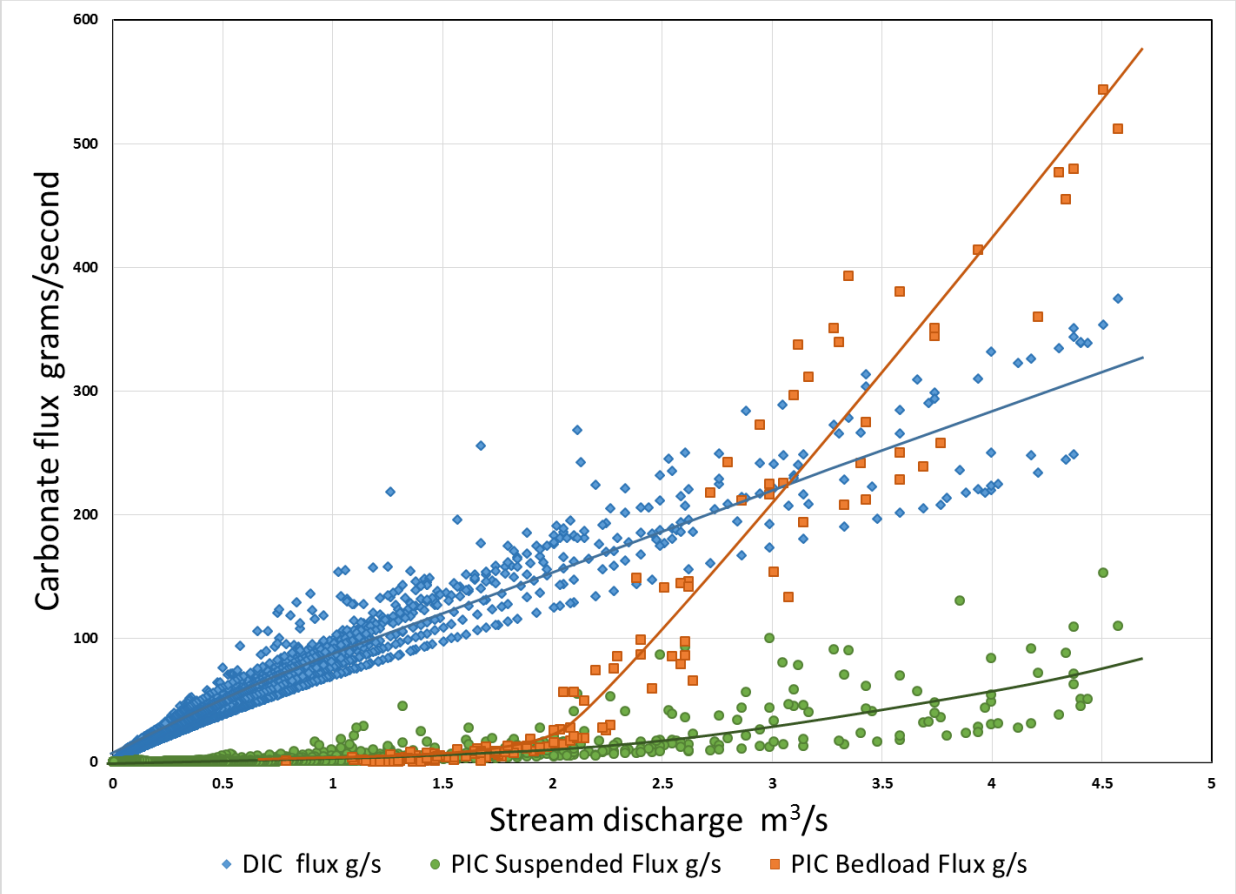

Figure 2.30: Comparison of measured and modeled IC fluxes for the Blowing Cave system, 2012/2013 water year.

Significance of measured fluxes to the carbon budget

Inorganic carbon flux from bedrock weathering has been estimated at vastly different scales in past studies, from the entire Mississippi River basin (Stets & Striegl 2012) to regional and local karst basins such as Mammoth Cave (Groves & Meiman 2001) and Redmond Creek, Kentucky (Florea 2015). Normalized by area, highly developed karst terrains can produce IC fluxes nearly two orders of magnitude greater than regional or continental watersheds as a whole, e.g., 2.7 metric tons/km^2 CO_2 annual removal (averaged across the Mississippi basin) vs. 195 metric tons/km^2 CO_2 annual removal at Mammoth Cave, indicating the importance of karst processes in carbon sequestration. This study determined that the dissolution of limestone and dolostone at BC removed about 64 metric tons/km^2 of CO_2 annually for the carbonate outcrop area, and an additional 6.6 metric tons/km^2 from mechanical removal of carbonate and dissolution downstream. The TCC and MC field sites may have similar levels of PIC transport on a basin-wide scale, although the initial tests at TCC indicated overland channels may be the primary route of carbonate bed load, while suspended load transport at MC may be the primary process of PIC removal.

The significance of karst weathering to the global carbon cycle has been dismissed in many climate models because of the assumption of steady-state feedback where the sink of carbon (as bicarbonate) delivered to the oceans from rivers will be released again during precipitation of carbonate minerals by inorganic and organic processes. However, the current rapid rise in atmospheric CO_2 is contributing to non-steady-state enhanced weathering of landmasses in the short term (Raymond & Cole 2003). In addition, ocean acidification and the long time scales involved in remineralization of dissolved ocean carbonate (thousands to hundreds of thousands of years) indicate that carbon fluxes in karst likely play an important role in atmospheric CO_2, at least on century scales (Berner et al. 1983; Sundquist 1991; Raymond & Cole 2003). Changing climate from increased greenhouse gasses may also contribute to changes in intensity of storms in fluviokarst regions. If regional storms become more severe, as climate

models suggest, storms that surpass the critical threshold of bed movement will be more frequent and enhance mechanical removal of carbonate in the future.

Limitations and further work

The most significant limitation in the data collected is related to the rarity of large storm events. Although 11 events moved bed load and many smaller storm events increased TSS, there is evidence that larger infrequent storms (<2 events/decade return period) radically increase removal of sediment from the system. Before field data collection began at BC, the aftermath of a storm in 2009 was observed that left high water marks at XS1 5.2 meters above the streambed, over 6 times higher than any recorded storm for the study period. At that level, the change from open-channel hydraulics to pipe-full conditions in much of the stream can create velocities that move massive amounts of material. After the event, over 1.5 meters of bed material had been completely removed near XS1 and transported downstream. A more comprehensive and longer study would be necessary to capture this type of flow event. The initial results from analysis of bed load material at MC indicated larger cobble to boulder material is rarely mobile in the low-gradient conduits, but that PIC in suspended loads may be significant. More work would be needed to fully evaluate the significance of suspended PIC flux at the site. The results of surface bed transport at TCC is informative, but because no good record of chemical parameters were available at surface sites, a comparison of PIC to DIC transport was not completed there. Additional work would be beneficial at TCC surface overflow streams because of the different setting and bedrock type. Research at both TCC and BC focused on well-defined but small basins, so extrapolation of results to a regional scale should be done with caution.

CONCLUSIONS

Particulate inorganic carbon flux was demonstrated to be a significant component of total carbon removal in the basins studied. Because the areas studied are typical of most mixed-bedrock fluviokarst settings in humid climates, knowledge gained from these sites can be extended to many other regions. PIC fluxes are highly dependent on storm flow and stream power, so careful evaluation of stream dynamics was

necessary to adequately characterize the full mass transport, and this type of study is applicable to other areas of mixed carbonate/non-carbonate fluviokarst. Some flood events with approximately 8-month return periods have been shown to produce PIC fluxes that exceed the DIC flux by over 50%. The flux of carbonate bed load was the most prominent process in PIC movement through the studied systems. The contribution of PIC to the total inorganic carbon removal and carbon sequestration for the annual study period at BC was 10.3%, of which 2.3% came from suspended PIC and 8.0% came from bed load PIC. The total amount CO_2 captured by karst dissolution and erosion in the basin for the 2012/2013 season was 167 metric tons. Much larger storms and more significant bed load fluxes have been observed at the study site in the past, but further monitoring would be needed to capture that data.

REFERENCES

Aguirre-Pe, J., Olivero, M.L. & Moncada, A.T., 2003. Particle densimetric Froude number for estimating sediment transport. *Journal of Hydraulic Engineering-Asce*, 129(6), pp.428–437.

Aley, T.J. Aley, C., Moss, P., Hertzler, E., 2008. Hydrogeological characteristics of delineated recharge areas for 40 biologically significant cave and spring systems in Missouri, Arkansas, Oklahoma, and Illinois. In *Proceedings of the National Cave and Karst Management Symposium*. St. Louis, pp. 154–167.

Almedeij, J.H., 2002. *Bedload transport in gravel-bed streams under a wide range of Shields stresses*, PhD Dissertation, Virginia Polytechnic Institute.

Aucour, A.M., Sheppard, S., Guyomar, O., Wattelet, J., 1999. Use of 13C to trace origin and cycling of inorganic carbon in the Rhone river system. *Chemical Geology*, 159, pp.87-105.

Bagnold, R.A., 1977. Bed load transport by natural rivers. *Water Resources Research*, 13(2), p.303.

Barry, J.J., Buffington, J.M., King, John G., Goodwin, P., 2006. Performance of bed load transport equations in mountain gravel-bed rivers: a re-analysis. In *Proceedings of the Eighth Federal Interagency Sedimentation Conference (8thFISC), April2-6, 2006, Reno, NV, USA*. pp. 90–97.

Berner, R.A., Lasaga, A.C. & Garrels, R.M., 1983. The carbonate-silicate geochemical cycle and its effect on atmospheric carbon dioxide over the past 100 million years. *American Journal of Science*, 238, pp.640–683.

Bosch, R.F. & White, W.B., 2007. Lithofacies and transport of clastic sediments in karstic aquifers. In I. D. Sasowsky & J. Mylroie, eds. *Studies of Cave Sediments: Physical and Chemical Records of Paleoclimate*, pp.1-22.

Buffington, J.M. & Montgomery, D.R., 1997. A systematic analysis of eight decades of incipient motion studies, with special reference to gravel-bedded rivers. *Water Resources Research*, 33(8), pp.1993–2029.

Bunte, K. & Abt, S.R., 2001. Sampling Surface and Subsurface Particle-Size Distributions in Wadable Gravel- and Cobble-Bed Streams for Analyses in Sediment Transport , Hydraulics , and Streambed Monitoring, U.S. Forest Service, Technical Report RMRS-GTR-74, 428 p.

Cheng, Z. & Daoxian, Y., 2002. *Karst Processes and the Carbon Cycle: Final Report of ICGP379*, Beijing, China: Geological Publishing House.

Church, M. & Hassan, M.A., 1992. Size and distance of travel of unconstrained clasts on a streambed. *Water Resources Research*, 28(1), pp.299–303.

Crawford, N.C., 1996. *The Karst Hydrogeology of the Cumberland Plateau Escarpment of Tennessee* Pt. 4, Report of Investiagations no. 44, Tennessee Division of Geology.

Dogwiler, T. & Wicks, C.M., 2004. Sediment entrainment and transport in fluviokarst systems. *Journal of Hydrology*, 295(1–4), pp.163–172.

Dornblaser, M.M. & Striegl, R.G., 2009. Suspended sediment and carbonate transport in the Yukon River Basin, Alaska: Fluxes and potential future responses to climate change. *Water Resources Research*, 45(6), 12 p.

Dreybrodt, W. & Eisenlohr, L., 2000. Limestone dissolution rates in karst environments. In A. Klimchouk et al., eds. *Speleogenesis and Evolution of Karst Aquifers*. Huntsville, AL: National Speleological Society, pp. 136–148.

Eberl, D.D., 2004. Quantitative Mineralogy of the Yukon River System : Variations with Reach and Season , and Sediment Source Unmixing, American Mineralogist, 89(11-12), pp.1784-1794.

Edwards, T.K. & Glysson, G.D., 1999. Field methods for measurement of fluvial sediment-Review. In *U.S. Geological Survey Techniques of Water-Resources Investigations, book 3, chapter C2*, p.89.

Elliott, W.R., Aley, T.J. & Aley, C.L., 2007. Conserving and Ozark Cave. *Missouri Conservationist*, pp.17–21.

Farrant, A.R. & Smart, P.L., 2011. Role of sediment in speleogenesis; sedimentation and paragenesis. *Geomorphology*, 134, pp.79–93.

Ferguson, R.I., 2005. Estimating critical stream power for bedload transport calculations in gravel-bed rivers. *Geomorphology*, 70(1–2), pp.33–41.

Ferguson, R.I. & Hoey, T.B., 2002. Long-term slowdown of river tracer pebbles: Generic models and implications for interpreting short-term tracer studies. *Water Resources Research*, 38(8), pp.11–17.

Ferguson, R.I. & Wathen, S.J., 1998. Tracer-pebble movement along a concave river profile : Virtual velocity in relation to grain size and shear stress transport and deposition. *Water Resources Research*, 34(8), pp.2031–2038.

Florea, L.J., 2015. Carbon flux and landscape evolution in epigenic karst aquifers modeled from geochemical mass balance. *Earth Surface Processes and Landforms*, 1072-1087.

Ford, D. & Williams, P.D., 2007. *Karst Geomorphology and Hydrology*, London: Unwin Hyman, 576 p.

Gombert, P., 2002. Role of karstic dissolution in global carbon cycle. *Global and Planetary Change*, 33(1–2), pp.177–184.

Graham, D.J., Rice, S.P. & Reid, I., 2005. A transferable method for the automated grain sizing of river gravels. *Water Resources Research*, 41(7), pp.1–12.

Groves, C. & Meiman, J., 2001. Inorganic Carbon Flux and Aquifer Evolution in the South Central Kentucky Karst., U.S. Geological Survey Karst Interest Group Proceedings, St. Petersburg, Florida, pp.99–105.

Groves, C.G. & Meiman, J., 2003. Could Mammoth Cave be reduced to a single equation? ,*Speleogenesis and Evolution of Karst Aquifers*, 1(4), pp.1–5.

van Gundy, J.J. & White, W.B., 2009. Sediment flushing in Mystic Cave, West Virginia, USA, in response to the 1985 Potomac Valley flood. *International Journal of Speleology*, 38(2), pp.103–109.

Hajna, N.Z. & Mihevc, A., 2008. Karst Sediments. In N. Z. Hajna & A. Mihevc, eds. *16th International Karstological School*.

Hassan, M. A., Church, M. & Ashworth, P.J., 1992. Virtual rate and mean distance of travel of individual clasts in gravel-bed channels. *Earth Surface Processes and Landforms*, 17(6), pp.617–627.

Haynes, D.D., 1964. Geology of the Mammoth Cave quadrangle, Kentucky, U.S. Geological Survey 7.5-minute geologic map, p.1.

Herman, E.K., Toran, L. & White, W.B., 2008. Threshold events in spring discharge: Evidence from sediment and continuous water level measurement. *Journal of Hydrology*, 351(1–2), pp.98–106.

Holmes, R.R. & Holmes, R.R.J., 2010. Measurement of bedload transport in sand-bed rivers: A look at two indirect sampling methods. *US Geological Survey Scientific Investigations Report*, (1914), pp.236–252.

Laronne, J.B. & Carson, M.A., 1976. Interrelationships between bed morphology and bed-material transport for a small, gravel-bed channel. *Sedimentology*, 23(1), pp.67–85.

Lewis, R.Q., 1977. Geologic map of the Powersburg quadrangle and part of the Pall Mall quadrangle, Wayne and Clinton Counties, Kentucky, U.S. Geological Survey 7.5-minute geologic map, p.1.

Liu, Z., Zhao, J., 1997. Contribution of Carbonate Rock Weathering to the Atmospheric CO_2 Sink. *Environmental Geology*, 39(9), pp.1053–1058.

Lorang, M.S. & Hauer, F.R., 2003. Flow competence and streambed stability: an evaluation of technique and application. *Journal of the North American Benthological Society*, 22(4), pp.475–491.

Mahler, B.J. & Lynch, F.L.L., 1999. Muddy waters: temporal variation in sediment discharging from a karst spring. *Journal of Hydrology*, 214(1–4), pp.165–178.

Martin, J.B. & White, W.B., 2008. *Frontiers in Karst Research* J. B. Martin & W. B. White, eds., Special Publication 13, Karst Waters Institute, p.128.

Martin, Y., 2003. Evaluation of bed load transport formulae using field evidence from the Vedder River, British Columbia. *Geomorphology*, 53(1–2), pp.75–95.

Martin, Y. & Church, M., 2000. Re-examination of Bagnold's empirical bedload formulae. *Earth Surface Processes and Landforms*, 25(9), pp.1011–1024.

Massei, N., Wang, H.Q., Dupont, J.P., Rodet, J., Laignel, B., 2003. Assessment of direct transfer and

resuspension of particles during turbid floods at a karstic spring. *Journal of Hydrology*, 275, pp.109–121.

Newson, M.D., 1971. A Model of subterranean limestone erosion in the British Isles based on hydrology. *Transactions of the Institute of British Geographers*, 54, pp.55–70.

Nichols, M.H., 2004. A radio frequency identification system for monitoring coarse sediment particle displacement. *Applied Engineering in Agriculture*, 20(6), pp.783–787.

Noltie, D.B. & Wicks, C.M., 2001. How hydrogeology has shaped the ecology of Missouri's Ozark cavefish, Amblyopsis rosea, and southern cavefish, Typhlichthys subterraneus. *Journal of the Environmental Biology of Fishes*, 62, pp.171–192.

Palmer, A.N., 2007. *Cave Geology*, Dayton, Ohio: Cave Books, p.454.

Peterson, E.W. & Wicks, C.M., 2003. Characterization of the physical and hydraulic properties of the sediment in karst aquifers of the Springfield Plateau, Central Missouri, USA. *Hydrogeology Journal*, 11(3), pp.357–367.

Piper, D.Z., Ludington, S., Duval, J.S., Tayloer, H.E., 2006. Geochemistry of bed and suspended sediment in the Mississippi river system: provenance versus weathering and winnowing. *The Science of the total environment*, 362(1–3), pp.179–204.

Pronk, M., Goldscheider, N., Zopfi, J., Francois, Z., 2009. Percolation and particle transport in the unsaturated zone of a karst aquifer. *Ground Water*, 47(3), pp.361–369.

Raymond, P.A. & Cole, J.J., 2003. Increase in the export of alkalinity from North America's largest river. *Science (New York, N.Y.)*, 301(July), pp.88–91.

Reid, I.A. & Frostick, L.E., 1984. Particle interaction and its effect on the thresholds of initial and final bedload motion in coarse alluvial channels. In E. H. Koster & R. J. Steel, eds. *Sedimentology of Gravels and Conglomerates*. Canadian Society of Petroleum Geologists, pp. 61–68.

van Rijn, L.C., 1985. Sediment transport, part 1: bed load transport. *Journal of Hydraulic Engineering*, 110(10), pp.1431–1456.

Rossman, N.R., 2010. *Entrainment and transport of coarse stream bed material in a fluviokarst watershed, south-central Missouri: a tracer particle study*. Master's Thesis, University of Missouri.

Rounds, S. a, 2012. Alkalinity and Acid Neutralizing Capacity. In F. D. Wilde, ed. *U.S. Geological Survey Techniques of Water-Resources Investigations Book 9*. U.S. Geological Survey, pp. 1–45.

Sasowsky, I.D. & Mylroie, J., 2007. *Studies of Cave Sediments: Physical and Chemical Records of Paleoclimate* 2nd ed., p.329.

Schenk-Brown, J., 2008. *Atrazine Contamination and Suspended Sediment Transport within Logsdon River, Mammoth Cave, Kentucky*. Master's Thesis, Western Kentucky University.

Shields, A., 1936. Anwendung der Aehnlichkeitsmechanik und der Turbulenzforschung auf die Geschiebebewegung. *Technology*, p.26.

Stets, E. & Striegl, R., 2012. Carbon export by rivers draining the conterminous United States. *Inland Waters*, 2(4), pp.177–184.

Sundquist, E.T., 1991. Steady- and non-steady-state carbonate-silicate controls on atmospheric CO2. *Quaternary Science Review*, 10, pp.283–296.

Turowski, J.M., Badoux, A. & Rickenmann, D., 2011. Start and end of bedload transport in gravel-bed streams. *Geophysical Research Letters*, 38(4), p.5.

USGS, 1995. USGS Water Quality Samples: Beaver Creek at Monticello, KY. *Historic NWIS Data*. Available at: http://nwis.waterdata.usgs.gov/usa/nwis/qwdata/?site_no=03413200 [Accessed January 1, 2016].

Wathen, S.J., Hoey, T.B. & Werritty, A., 1997. Quantitative Determination of the Activity of Within-Reach Sediment Storage in a Small Gravel-Bed River Using Transit Time and Response Time. *Geomorphology*, 20(1–2), pp.113–134.

White, W.B., 2000. Dissolution of limestone from field observations. In A. B. Klimchouk et al., eds. *Speleogenesis and Evolution of Karst Aquifers*. Huntsville, AL: National Speleological Society, pp. 149–155.

White, W.B., 2002. Karst hydrology : recent developments and open questions. *Engineering Geology*, 65(13), pp.85–105.

White, W.B., 1984. Rate processes: chemical kinetics and karst landform development. *Zeitschrift fur Geomorphologie, Groundwater as a Geomorphic Agent*, pp.227–248.

Wicks, C., Noltie, D.B., Peterson, E.W., Dogwiler, T., 2010. Disturbances in the habitat of Macrocotyla glandulosa (Kenk). *Ecohydrology* 3(1), pp.116–125.

Wilcock, P.R., 1997. Entrainment, displacement and transport of tracer gravels. *Earth Surface Processes and Landforms*, 22(12), pp.1125–1138.

CHAPTER 3: ESTIMATING SURFACE/SUBSURFACE SEDIMENT MIXING IN KARST SETTINGS USING ^{7}Be AND ^{137}Cs ISOTOPES

ABSTRACT

This study sought to develop a better understanding of rapid changes in sediment flux and transport through karst aquifers to inform a variety of related processes such as organic and inorganic carbon transport, soil loss and erosion, sediment-associated pollutant loading, subsurface sediment storage, and ecological impacts. The purpose of this study was to use cosmogenic and fallout radioactive isotopes to determine the ratios of surface sediment to remobilized subsurface sediment in suspended loads during runoff events in karst regions. The activities of beryllium-7 and cesium-137 were measured in two different karst settings at both surface and subsurface sites before and after storm runoff events.

At the initial test site (Blowing Cave, KY), subsurface sampling indicated ^{7}Be-enriched sediment could be detected up to 1.5 km along a stream conduit after a moderate storm event, but that activity of ^{137}Cs was too variable to show a meaningful pattern. Subsequent ^{7}Be testing of suspended sediment samples during an intense storm event in a larger karst basin and cave system (Hidden River Cave, KY) allowed calculation of a time-series of the contribution of surface-derived sediment to total subsurface sediment flux. As much as 62% of the initial flush of sediment was estimated to come from fresh surface material, and approximately 34% of the total sediment flux during the 4-day runoff event was estimated to originate from surface erosion.

INTRODUCTION

Purpose and significance

Surface water and groundwater are intimately linked in karst terrains. Soluble bedrock underlies about one-fifth of the United States and world landmasses (Martin & White 2008), and rapid turbulent flow into and through well-developed conduits in these regions can transport sediment and pollutants in dynamic and unpredictable ways (Vesper 2013). A better understanding of rapid changes in sediment flux and transport through karst aquifers is needed to sort out a variety of related processes such as organic and inorganic carbon transport, soil loss and erosion, sediment-associated pollutant loading, subsurface sediment storage, and ecological impacts.

An important and poorly studied processes in karst ground- and surface water interaction is the mixing of freshly-eroded surface material with reworked and remobilized sediment stored in subsurface stream conduits, and how the provenance of suspended load evolves during storm runoff events (Herman et al. 2006). Determining residence times of sediments within conduits, and investigating the surface/subsurface sediment mixing ratios in storm runoff has been difficult in karst regions (Herman et al. 2008). The purpose of this study was to deconstruct storm sediment spikes in karst aquifers using naturally-occurring radioactive isotopes to determine the ratios of surface sediment and remobilized subsurface sediment in suspended loads during runoff events.

Sediment dynamics in karst basins

Numerous studies have addressed sediment dynamics and sediment deposits in karst systems (e.g., Mahler & Lynch, 1999; Massei et al., 2003; Peterson & Wicks, 2003; Dogwiler & Wicks, 2004; Sasowsky & Mylroie, 2007; Hajna & Mihevc, 2008; Pronk et al., 2009). Caves, sinkholes, and epikarst features act as both avenues of transport and repositories for many types of deposits. Particulate materials transported and stored in karst can be derived locally (autogenic), such as breakdown of cavern walls, or transported from other locations (allogenic), such as suspended and bed sediment in underground streams (Fig. 1). Because caves both trap and transport sediments from the surface, cave deposits and their

sources are intimately linked to conduit development and dynamics (Farrant & Smart 2011). Sediment storage and transport processes in the subsurface can change rapidly during storm events, but few existing studies have focused on these dynamics (White 2002).

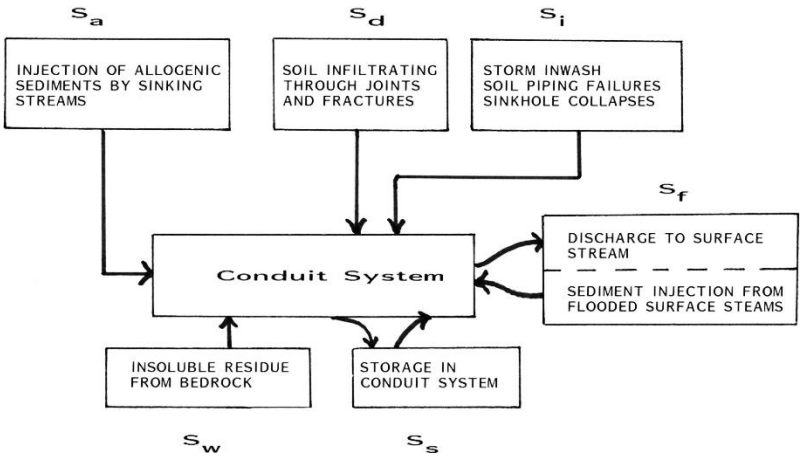

Figure 3.1: Flow diagram for sediment transport in karst (Bosch & White 2007)

To better understand sediment transport dynamics in karst, knowledge of subsurface storm response is needed. Karst is considered a triple-porosity regime, with original rock porosity, secondary fracture/bedding plane porosity, and conduit porosity. Karst groundwater movement is often dominated by turbulent and rapid conduit flow, typically recharged by sinking surface streams and runoff into sinkholes (Ford & Williams 2007). During storm events, sediments from karst land surfaces are eroded and transported underground, particularly in fluviokarst basins with developed surface streams, or in locations where streams from non-karst areas flow onto karst areas and sink. Sediment can also be moved into the subsurface by sinkhole inflow and collapse, and infiltration through enlarged epikarst fractures. Some fine-grained sediment may get transported through the karst system without settling out of suspension, but if sediments get deposited in the subsurface, they can remain in storage from days to millenia depending on local hydraulic conditions, conduit morphology and magnitude of storm events (Bosch & White 2007). Additionally, some sediments are produced directly in the subsurface as the insoluble fraction of weathered rock is left behind from dissolution, carbonate is precipitated in supersaturated conditions, or cave walls are mechanically eroded.

Sediment tracking

Tracing sediment transport using introduced materials or naturally occurring compounds can be effective tools for analyzing karst sediment dynamics. A lanthanide-tagged method to directly trace clay transport and storage times in karst was developed by Mahler et al. (1998). However, the large amount of lanthanide-tagged clay needed for injection becomes prohibitive if high sediment loads are expected during storm events in large karst basins. Other recent methods of for tracing fine-grained sediment includes application of materials such as microspheres, macrophages, and introduced radioactive compounds (e.g., Auckenthaler et al., 2002; Harvey et al., 2008; Hess, 2008; Goldscheider et al., 2008) all of which can be difficult and expensive to implement on a large scale.

As an alternative to introduced tracers, sediment fingerprinting techniques can yield significant information on the origin and movement of transported material. Geochemical, biochemical, and physical properties can be used in many different ways to determine provenance and transformations of sediment (Koiter et al. 2013; Walling 2013). Choosing an appropriate fingerprinting or tracking technique depends on what type of questions are of interest, and what temporal and spatial scales are investigated. For tracking sediment over short to medium time scales within subsurface deposits and loads, reviews show one of the best options is analysis of short half-life cosmogenic/fallout radionuclides (D'Haen et al. 2012). Sediments stored in karst conduits are cut off from direct atmospheric fallout of radionuclides, so investigating natural radionuclide activities may provide a stark contrast between surface and subsurface sediments that can be exploited.

Cosmogenic/fallout isotopes in sediment studies

Isotopic methods that have been used successfully in many soil and sediment erosion studies could be highly effective for determining sediment mixing in karst conduits. Cosmogenic and fallout radioactive isotopes have been used extensively in surface erosion studies for decades (Guzmán et al. 2013; Mabit et al. 2013). The most common isotopes utilized for quantifying moderate to long-term soil erosion and redistribution in the past have been cesium-137 (^{137}Cs, $T_{1/2}$ = 30.2 years) and excess lead-210 ($^{210}Pb_{ex}$, $T_{1/2}$

= 22.2 years). Because these isotopes are strongly adsorbed to soil and sediment particles that are then redistributed in the landscape by physical processes, they are a very effective means of tracing sediment movement (Mabit et al. 2008). More recently, beryllium-7 (^{7}Be, $T_{1/2}$ = 53.4 days) has gained attention and research because it can be utilized to study sediment transport events at its relatively short half-life scale. Like ^{137}Cs and $^{210}Pb_{ex}$, ^{7}Be becomes strongly attached to sediment particles and makes an effective conservative physical tracer (Walling 2013).

Beryllium-7 is a naturally-occurring isotope that is produced in the stratosphere and troposphere of the Earth by cosmic ray bombardment and spallation of oxygen and nitrogen. Production of ^{7}Be varies by latitude and with solar activity cycles, and is scavenged from the upper atmosphere by aerosol particles that become nuclei for cloud formation and precipitation (Kaste et al. 2002). It is estimated that over 90% of ^{7}Be fallout to the Earth's surface occurs as wet fallout (Walling 2013), so there is usually a seasonal component to the deposition of ^{7}Be related to regional wet periods. Beryllium-7 decays by electron capture to lithium-7, and while about 90% decays to ground-state ^{7}Li, about 10% decays to an excited ^{7}Li state that drops to ground state by emission of gamma rays at 477.6 keV (Kaste et al. 2002). The sediment/water partitioning coefficient (K_d) for ^{7}Be is very high because of the isotope's great affinity for sediment particles, averaging around 10^5 for typical silts and clays in fresh surface waters of normal pH and ionic strength. The adsorption process is very rapid, rising exponentially and normally reaching >90% total K_d within hours (You et al. 1989). Because of a 53.4-day half-life and its rapid fixation to sediment, ^{7}Be is normally only found within the first centimeter of soil and rarely at depths greater than about 3 cm in undisturbed soil, although tillage can alter the distribution (Walling 2013) (Fig. 3.2).

Cesium-137 has been the most widely used soil tracer in a large variety of settings and scales (Mabit et al., 2008; Walling & He, 1993). Unlike ^{7}Be, it does not occur naturally in the environment but is a product of thermonuclear testing before the early 1970s, and in more limited areas from nuclear disasters such as Chernobyl or Fukushima (Yasunari et al. 2011; Matisoff & Whiting 2012). Cesium-137 decays to metastable barium-137 ($T_{1/2}$=153 seconds) by beta emission which then releases gamma rays at 662 keV

to reach the stable ^{137}Ba ground state (Ritchie & McHenry 1990). Vertical distribution of ^{137}Cs in surface soils is significantly different than ^{7}Be because of its 30.2-year half-life and cessation of most production in the 1970s. Maximum activities of ^{137}Cs in undisturbed soil can occur a few centimeters below the surface, but tillage can homogenize the isotope in the upper 10 cm or so of soil (Mabit et al. 2008) (Fig. 3.2). A broad array of literature discusses the use of excess ^{210}Pb for soil erosion studies that are related to ^{7}Be and ^{137}Cs research, and in many cases all three isotopes are used to determine sediment redistribution rates at different time scales. Excess ^{210}Pb was not a target of investigation for this study, but it is likely useful for determining sediment storage times in the subsurface and may warrant further research.

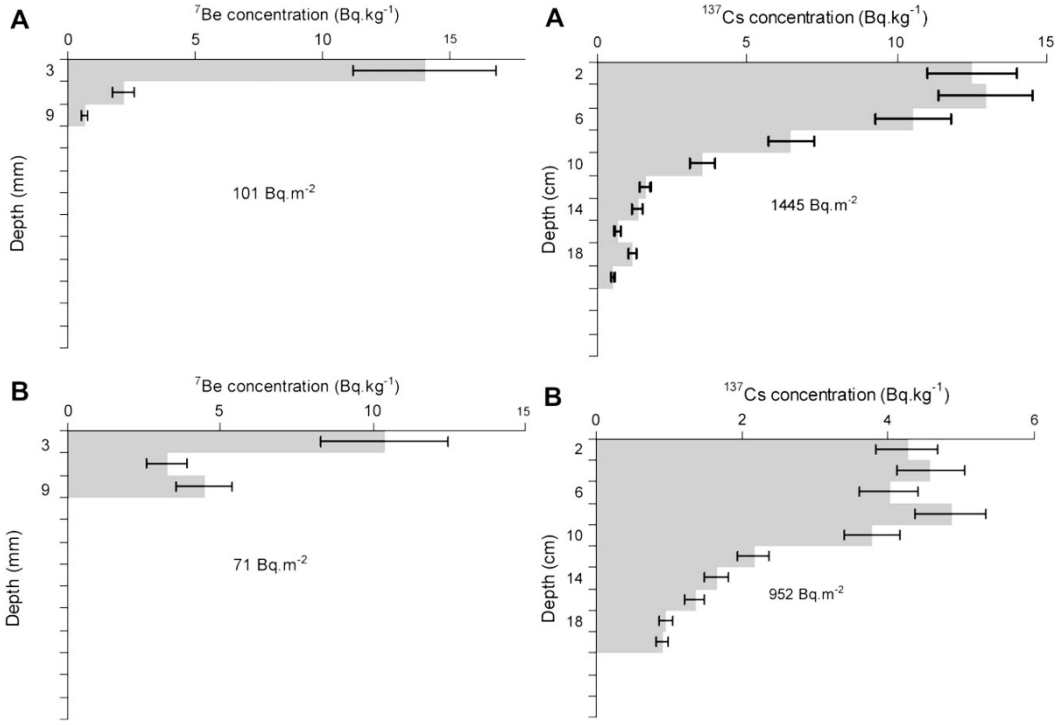

Figure 3.2: Typical distribution of ^{7}Be and ^{137}Cs in undisturbed vs. tilled surface soils (Mabit et al. 2008).

METHODS

In order to determine mixing of surface and stored sediment and sediment residence times for this study, well-researched surficial streambed methods (e.g., Neal et al. 1992; Bonniwell et al. 1999; Le Cloarec et al. 2007; Porto & Walling 2012) were adapted for subsurface study sites. Measuring the activities of ^{7}Be

and ^{137}Cs at each study site gave insight into fine sediment residence times. Beryllium-7 in particular has a short enough half-life that once surface sediments enriched in ^{7}Be flow underground and are stored, they rapidly become depleted in ^{7}Be. Likewise, if freshly eroded sediment from the surface is transported quickly through a conduit to a spring outlet, it will be enriched in ^{7}Be. By monitoring the ^{7}Be activity at surface input points of the karst system, short-term mixing of sediment in the subsurface can be estimated by the level of depletion from input concentrations, as a simple ratio of corrected isotope activities. Cesium-137 can potentially be useful in a similar way to investigate longer-term mixing. These methods can work for sampling of active suspended sediment as well as fresh sediment that is deposited along the length of karst stream conduits.

Site Locations

Two different karst settings were investigated in this study. Initial tests for the presence and magnitude of pre- and post-storm sediment isotopes were carried out within the Sunnybrook Blowing Cave (BC) karst valley in Wayne County, Kentucky. The 5.8 km^2 basin lies at the edge of the Cumberland Escarpment, with high-gradient, allogenic surface drainage that mainly sinks at one discreet swallow hole. The sediment load consists primarily of silt to cobble size siliciclastic material derived from the surrounding high relief sandstone plateau. All the drainage for the basin flows through the stream conduit of BC for over 3 km to the main valley spring. Land use/land cover in the basin consists of approximately 88 percent forest, 9 percent agricultural, and 3 percent other (Fry et al. 2011). Most of the stream conduit from the central swallow hole to the spring is traversable for sampling at low to moderate flow. Sampling locations included three control sites within the surface drainage for the swallow hole and six in-cave sites along the length of the BC stream conduit (Figs. 3.5, 3.6).

More detailed research was conducted on surface/subsurface sediment mixing at Hidden River Cave (HRC) in Hart County, Kentucky. The 182 km^2 HRC basin drains both an extensive sinkhole plain and numerous sinking streams. Short-term isotopic variations during storm event sediment spikes were investigated at HRC. Land use/land cover in the HRC basin consists of approximately 85 percent pasture

and cropland, 8 percent developed land, and 7 percent forest (Fry et al. 2011). The sediment load in the stream of HRC is almost entirely composed of silt to clay siliciclastic material derived from the insoluble fraction of Mississippian limestone and dolostone that underlies the surrounding sinkhole plain. The site was chosen because of easy access to the underground river, and because HRC exhibits much higher suspended sediment concentrations than BC. The cave has a history of sediment-related contaminant transport that sediment mixing studies may help address because some of the contaminants have been deposited over time within the conduits. The karst drainage system of HRC lies beneath the town of Horse Cave that has had significant problems with waste disposal in the past including sewage discharge and hexavalent chromium spills from a plating plant (Lewis 1995). The surrounding agricultural land has also impacted the groundwater with pesticide, primarily atrazine, which attaches to and is mobilized with the sediment load (Schenk-Brown 2008). Filtration of suspended load samples in the HRC basin was conducted at two control sites where surface streams feed into the karst flow system, and within the main cave stream at the base of the stairs in the commercial HRC entrance (Figs 3.3, 3.4).

Karst groundwater basin boundaries can be difficult to determine, but knowing them is essential to understand sediment source areas. In many karst systems, flow to springs may be poorly or completely unrelated to surface topography. Numerous water tracing methods can be used to identify direct connections between surface water sink points and springs for construction of karst groundwater basin maps. For both field sites, standard fluorescent dye tracing methods (e.g., Göppert & Goldscheider, 2008) have been used to constrain basin recharge boundaries. At HRC, extensive dye tracing was conducted by many different researchers (Fig. 3.3) from the 1970s to 1989 and used to produce a regional groundwater flow and basin map (Quinlan & Ray 1989) that was later revised with additional tracing data. Because tracing data were unavailable at BC, new dye tracing was conducted for this study around the valley to delineate the basin boundaries and confirm flow paths.

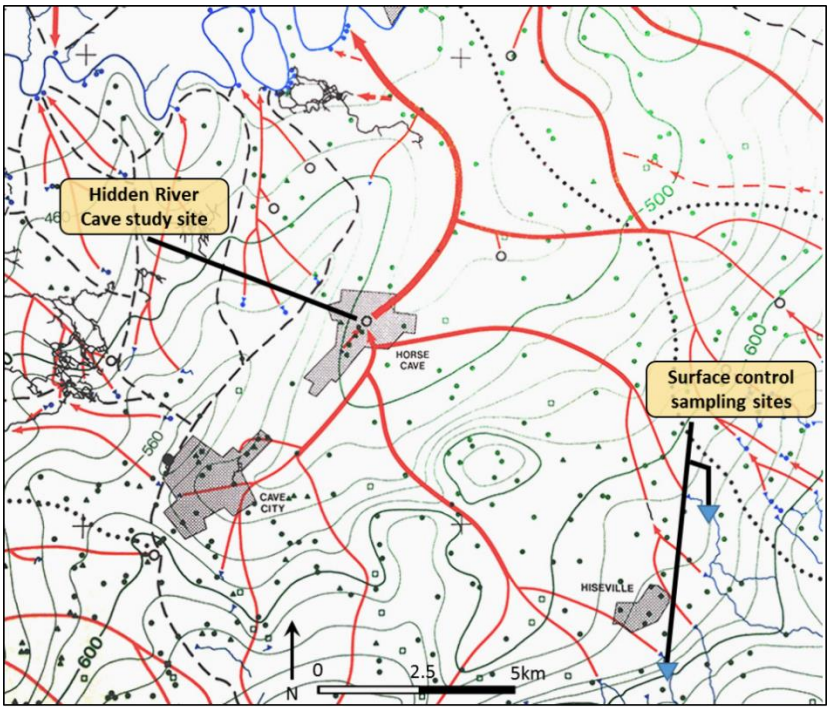

Figure 3.3: Study area, sampling sites and groundwater flow in the Hidden River Cave basin (Quinlan & Ray 1989). Red lines are dye-traced flow paths, positioned by analysis of the aquifer potentiometric surface (green contours). Surface sampling sites are near the terminus of surface flow at sinking streams that feed into HRC.

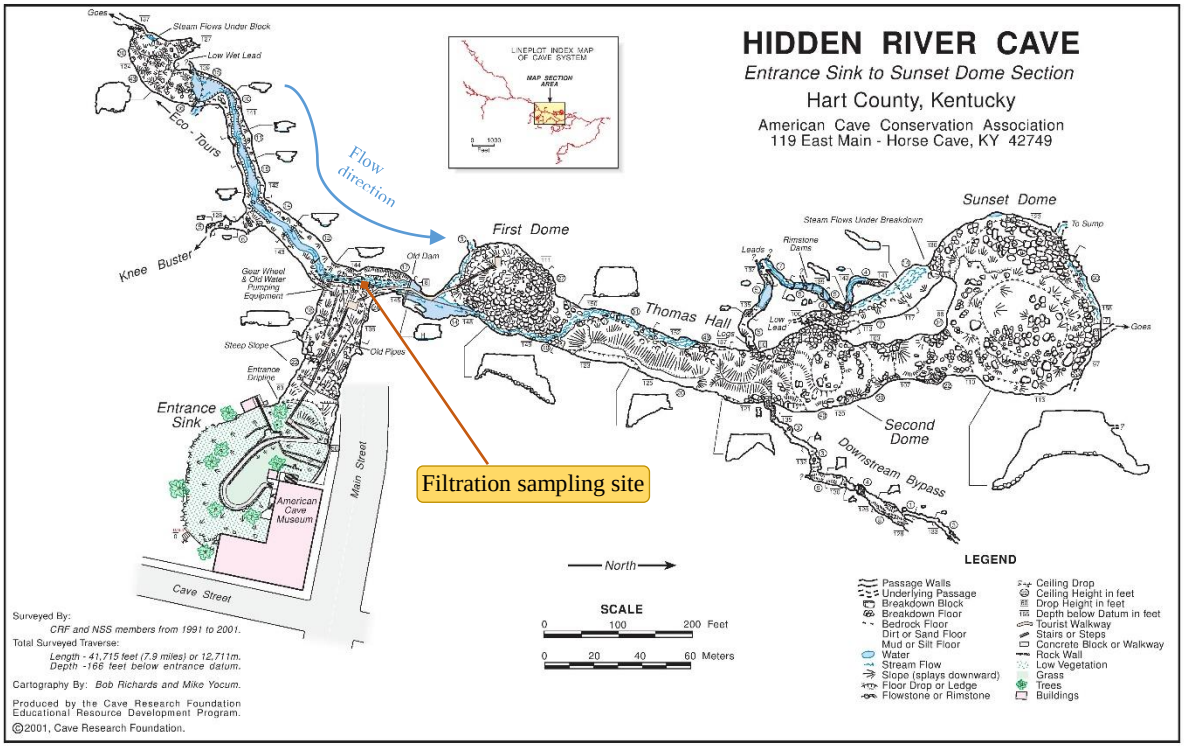

Figure 3.4: Detail map of the commercial section of Hidden River Cave, showing the subsurface stream channel and location of suspended sediment sampling.

Field methods

Field methods used in surficial erosion studies (e.g., Bonniwell et al., 1999; Blake et al., 2002; Ciffroy et al., 2003; Walling et al., 2005; Yin & Li, 2008; Bentley et al., 2012) were adapted to account for dual surface/subsurface transport, to more effectively target suspended loads, and to address rapid changes in sediment loads that are common in karst stream conduits during storm events. To investigate storm flow deposits in cave streams and short-term variations in isotope activity that occur during subsurface storm runoff, samples were needed from designated reference sites at the surface. In most surficial erosion studies that utilize isotopes, redistribution dynamics are typically assessed by comparison to a stable landscape reference site within the basin (Walling et al. 2005). For the BC basin investigation, an average isotope surface activity was determined from three reference soil sample locations within the immediate drainage area (Figs. 3.5, 3.6). Because the target of the study at HRC involved only suspended loads during storm runoff events, and because isotopes in surface soil samples in the HRC basin were highly variable (Broderick 2015), a more effective surface reference was filtered suspended sediment from sinking streams that drain into HRC (Fig 3.3).

Surficial reference samples at BC were gathered one to two weeks before the primary storm event, after a small rain event. Filtered surface reference samples for HRC were gathered both during low-flow conditions when turbidity was minimal and during the rising limb of a flow peak from a moderate storm event that significantly increased surface stream turbidity. Once surface control samples were obtained, storm event isotope variations in both suspended loads (HRC) and in-cave sediment deposits (BC) were investigated by targeted sampling during runoff peaks or immediately after fresh sediment deposition in the subsurface. Storm event sediments along the cave stream in BC were collected from freshly deposited fine material (clay and silt) within a few days of the depositional event, and then sealed and stored for lab processing and analysis.

Sampling suspended load for isotope analysis required large volumes of water to obtain sufficient amounts of material for analysis. Leader Ecodiver-750 and -1200 high-volume submersible pumps were

operated off of field generators or available power supplies and their discharge directed through canister filtration systems. The pumps were capable of pushing up to 45 l/min through the filter line, and the total pumped volume was monitored with an in-line Badger flow meter. Standard 5 micron and 1 micron 10-inch polyethylene canister filters were connected in series when turbidity was low in order to maximize suspended load capture, and reduce sampling times. At the highest turbidities during peak flow, only 5 micron filters were used. Use of these different filter sizes should produce minimal bias in different samples because a parallel study that investigated ^{7}Be activity of different grain sizes in this cave system showed no statistically significant correlation between grain size and activity (Broderick, 2015). The minimum target sample size was 5 grams or more dried mass, and initial field tests determined the reduction in filter outflow rates that yielded the minimum target mass. For each sample, water was filtered continuously until the flow rate from the filters dropped below 3 l/min. Both background and storm event filtration were conducted at sinking surface streams and in the main stream channel of HRC (Figs 3.3, 3.4). Completed filter sets were sealed and labeled with location, initial dry weight, time, and total pumped volume before transport and lab processing.

While sampling suspended sediment, concurrent water chemistry and physical hydrologic measurements were needed to analyze storm flow dynamics. A YSI-6910 multi-parameter data sonde was installed in the HRC cave stream for time-series measurements of specific conductance (SpC), temperature, turbidity, stage, and pH. SpC was used to identify the initial arrival of the rainwater pulse in the cave stream because precipitation has a much lower SpC than karst groundwater (Ford & Williams 2013). Rainfall data for storm events at both study sites were obtained from the nearest available MET stations: the Glasgow Airport NOAA station for HRC (13 km southwest of study site, along spring storm tracks) and the Beaver Creek USGS station for BC (11 km north).

Laboratory and data analysis methods

Sample treatment and analysis were similar for both filtered suspended sediment and grab samples. Grab samples were weighed and dried to determine mass, disaggregated if necessary and sealed in airtight

analysis containers. Sealing the sample containers is not necessary for ^{7}Be and ^{137}Cs analysis, but to allow for future analysis of ^{210}Pb if needed. Lead-210 must be allowed to reach equilibrium with radon-222 decay products for a minimum of two weeks in order to accurately determine excess ^{210}Pb associated with atmospheric deposition (Walling et al., 2005). The sediment gathered from suspended loads was trapped in polyethylene canister filters. The filters were processed by drying to determine overall filtered mass, then combusted to ash in a large muffle furnace at 500°C for 5-7 hours to remove all filter material and any organic mass. The final ashed mass was recorded and the resulting material sealed for analysis using the same method for grab samples. Samples for ^{7}Be measurement were analyzed within less than one half-life from the date of collection.

The specific gamma ray energy emissions from each isotope were analyzed on LSU's Coastal Studies Institute Canberra LEGe 3825 or BEGe 3825 detectors calibrated for energy and efficiency using standard reference materials (US National Institute of Standards and Technology, and International Atomic Energy Agency). Detector efficiency for the 477 KeV peak of ^{7}Be (not present in the LSU CSI lab standards) was determined by interpolation from adjacent peaks in NIST and IAEA samples. Samples were counted for 12-24 hours to decrease counting error arising from small sample mass and low radionuclide activities. Results are reported in decays per minute per dry gram of sediment (dpm/g), where 1 dpm= 60 Bq. The resulting number of counts beneath the gamma energy peaks (477.6 keV for ^{7}Be, 662 keV for ^{137}Cs) were then normalized by sample mass, and corrected for decay from time of sampling using standard decay curves.

Corrections were not made for sediment size because the filtering process at HRC resulted in relatively uniform clay to fine silt material. Grab samples from BC were carefully gathered to maximize fine clay and silt content and a parallel study (Broderick 2015) found no statistically significant relationship between grain size and isotope activity for in-cave grab samples that are mostly silt/clay. At HRC, the hydrologic data gathered with the YSI-6920 logger were utilized for partitioning the storm hydrograph in

order to estimate input water sources and timing. TSS grab samples gathered at the same time as filtration at HRC were used to create a calibration curve for the turbidity (NTU) time-series from the YSI data. (Appendix 3.1). All of the resulting time-series, rainfall and isotope activity data were graphed together for storm event analysis.

RESULTS

Blowing Cave

The initial test to determine the viability of using fallout isotopes to track short-term movement and mixing of surface and subsurface sediments in karst resulted in varied data. The BC site was chosen for the initial test because it is a relatively simple system with discreet inputs. All of the sampling conducted at BC occurred in the fall season of 2011at the end of a long dry period with little runoff (Table 3.1). The last storm to create runoff in the system before this period was on 6/21/2011. Surface reference samples were collected on 9/4/2011 and 9/10/2011. Two of the surface samples were uncultivated soils adjacent to the stream feeding the cave system and were taken both before and after a small storm event. The third surface sample was from in-stream clay deposited during a runoff event on 9/6/2011. Initial in-cave samples were gathered at two locations on 9/4/2011: C1 and C6 (Figs 3.5, 3.6). Location C1 is a few

Table 3.1: BC isotope sampling, Fall 2011

Sampling time period	*Sample location*	*^{7}Be dpm/g*	*Percent of control reference*	*^{137}Cs dpm/g*	*Percent of control*
After small storm 9/4-9/11	Surface Control	1.783 ±0.167	100	0.893 ±0.064	100
Pre-storm dry period 9/4	C1 UEP	nd	nd	nd	nd
	C6 MS	nd	nd	0.159 ±0.028	17.8
After small storm 9/10	C1 UEP	0.539 ±0.158	30.2	0.129 ±0.027	14.4
	C6 MS	nd	nd	0.107 ±0.028	12.0
After moderate storm 11/20-11/21	C1 UEP	0.941 ±0.314	52.8	0.076 ±0.027	8.5
	C2 INTPOOL	0.724 ±0.201	40.6	0.102 ±0.020	11.4
	C3 CANSPL	0.594 ±0.185	33.3	0.266 ±0.057	29.7
	C4 FOGPSG	nd	nd	0.109 ±0.026	12.2
	C5 PENDCR	nd	nd	0.190 ±0.035	21.3
	C6 MS	nd	nd	0.074 ±0.022	8.2

hundred feet inside the upper entrance, which is also the primary surface stream input. Location C6 is approximately 0.2 km upstream from the lower spring entrance of the system, at a low area that always has fine clay deposited after runoff events.A small storm event dropped approximately 9.5 mm of rain on 9/6, initiating flow into and through the cave system. Additional samples were gathered at C1 and C6 on 9/10 once flow had subsided, and the sampling results are shown in Table 3.1. No detectable ^{7}Be was found at either cave site before the 9/6/11 rain event, and no ^{137}Cs was found at the C1 upstream site on that date. However ^{137}Cs was detected at C6 before any significant seasonal precipitation event, and the activity there was approximately 18% of the measured surface reference. After the flow event, ^{7}Be was detected at C1 at about 30% of the surface activity, but no detectable ^{7}Be was found at C6. At both C1 and C6, ^{137}Cs was found at about 14% and 12% of surface activity, respectively.

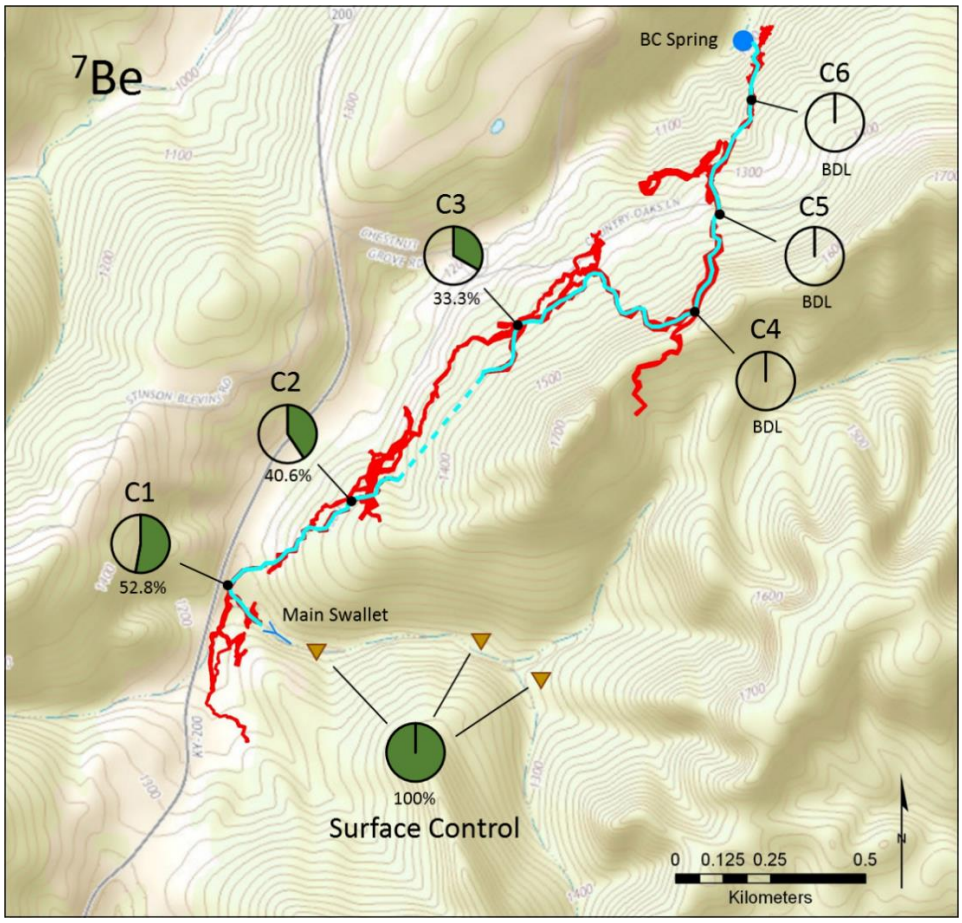

Figure 3.5: Map of sample locations and results of ^{7}Be analysis along the flow path of Blowing Cave. Red indicates mapped cave passages and light blue indicates the primary subsurface stream channel.

The next significant storm event did not occur until 11/16-17/2011, when 37 mm of rain fell over 2 days. Once storm flow subsided, freshly-deposited sediment was sampled on 11/20 and 11/21 at 6 different sites along the length of the cave stream. Sites C1 and C6 were the same locations as before, and an additional four sites, C2-C5 were added (Figs. 3.5 and 3.6). Cesium-137 was detected at all in-cave sampling sites, and ranged from approximately 8% to 30% of the surface reference activity. Beryllium-7 was detected at sites C1-C3 at about 33% to 53% of surface activity, but was undetectable in the remaining downstream locations (Table 3.1).

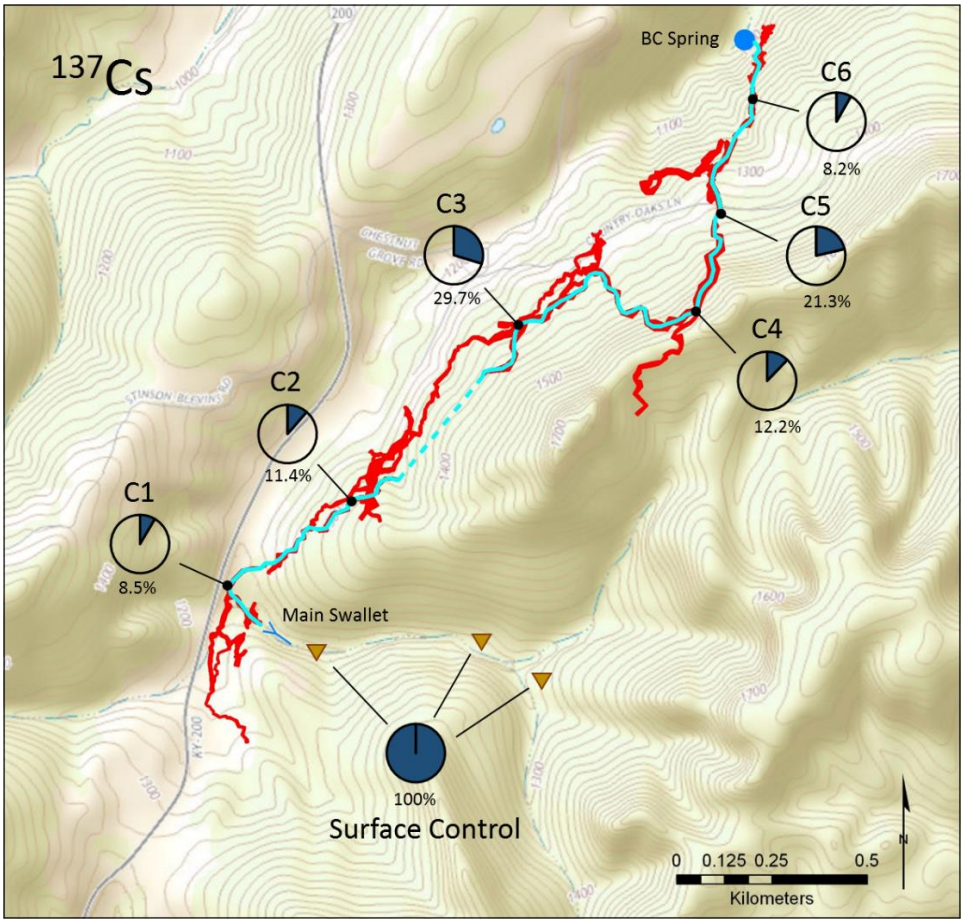

Figure 3.6: Map of sample locations and results of ^{137}Cs analysis along the flow path of Blowing Cave. Red indicates mapped cave passages and light blue indicates the primary subsurface stream channel.

Hidden River Cave

With results from the BC site showing that tracking surface sediment pulses through subsurface streams using isotopes could be an effective method, further investigation at Hidden River Cave was undertaken in the spring of 2014. The initial results for filtered suspended sediment samples for low-flow background activity and at surface reference sites is shown in Table 3.2. On 4/14, with antecedent dry conditions for at least two weeks prior to sampling, filtered suspended sediment was obtained at the HRC stream channel (Fig. 3.4) and at the surface channel of Blue Spring Creek (BSC) at Hiseville-Center Road (Fig 3.3). The activity of both ^{137}Cs and ^{7}Be in HRC suspended sediment was low but detectable at 0.12 and 1.8 dpm/g respectively (detection limits were around 0.06 and 0.3 dpm/g respectively depending on delay until analysis). The activity of ^{137}Cs and ^{7}Be at the BSC surface channel was relatively higher (0.34 and 11.8 dpm/g respectively) than at the HRC stream despite lack of recent runoff. Because of the low suspended sediment concentration at both sites, water was pumped through the 5μ filters for over 3 hours at HRC and 2 hours at BSC.

A moderate rain event occurred during the day on 4/15, with approximately 18 mm of precipitation falling within the drainage basin of HRC. That morning, an additional suspended sediment sample was obtained at HRC before runoff reached the system, with the pumps running for 4.7 hours to obtain sufficient material because of the very low turbidity. Isotope activities were nearly identical to the previous day. In the afternoon, surface sampling at another contributing stream was conducted in the channel of Strader Branch (STB) at the Hiseville-Center Bridge (Fig 3.3). The sampling was conducted for 1 hour as the storm flow was peaking in the channel and turbidities were high. The ^{137}Cs and ^{7}Be isotope activities at this location for the storm peak were the highest of any measured at the surface (0.4 and 18.5 dpm/g respectively), and these data served as the surface reference control value for estimating ratios of surface/subsurface mixing because they represented activities of infeeding streams at the peak of an average storm runoff event.

Two weeks after the background and reference sampling, an intense spring storm brought heavy rain and flooding to the HRC basin that caused a 3-day runoff event in the subsurface. A total of 97 mm fell in the 13 hours between 8 AM and 9 PM, at times up to 16 mm/hr, causing rapid surface runoff, erosion of surface soils and movement of large quantities of sediment into the subsurface. Suspended sediment sampling began at the HRC stream at 6PM as discharge and turbidity began rising, and results are shown in Table 3.2. The flood in the cave forced abandonment of filtered sampling near midnight on 4/28 because water rose nearly 10 meters and inundated the electrical supply box. Sampling was resumed the next day using electrical supply from the cave's visitor center, and a grab sample of newly-deposited fine silt and clay was obtained from the stairway at the high-water point (4/29 09:30 sample, Table 3.2). Filtered sampling was continued for an additional 2 days as the turbid flood water receded back to normal levels.

Table 3.2: Filtered sample isotope results for HRC

Date/Time start of sampling	Sample location	Filter sizes	Filtered volume (L)	Ashed filter mass (g)	Filtered SSC mg/L	^{7}Be activity dpm/g	^{137}Cs activity dpm/g	Product of normalized ^{7}Be and ^{137}Cs ratios	% of ^{7}Be surface control
4/14 10:20	BSC	5µ	4698	11.17	2.38	11.82 ±0.59	0.342 ±0.044	3.46±0.29	-
4/14 14:41	HRC	5µ	4952	19.98	4.03	1.83 ±0.26	0.119 ±0.031	1.03±0.16	19.8
4/15 9:50	HRC	5µ	11648	36.51	3.13	1.73 ±0.28	0.139 ±0.034	0.96±0.13	19.2
4/15 15:45	STB	5µ	204.4	13.25	64.82	18.48 ±0.89	0.403 ±0.053	5.01±0.24	100.0ǂ
4/28 18:00	HRC	5µ	499.6	10.09	20.17	5.45 ±0.55	0.099 ±0.019	1.35±0.14	26.9
4/28 18:43	HRC	5µ	2086	35.78	17.15	11.58 ±1.07	0.121 ±0.023	2.18±0.20	43.4
4/28 19:40	HRC	5µ	480.7	22.32	46.43	9.63 ±0.95	0.251 ±0.050	2.86±0.28	56.9
4/28 20:06	HRC	5µ	779.8	23.01	29.51	17.80 ±1.58	0.163 ±0.032	3.13±0.27	62.3
4/28 21:00	HRC	5µ	283.9	24.61	86.68	11.45 ±1.04	0.210 ±0.041	2.85±0.26	56.8
4/28 22:07	HRC	5µ	147.6	19.83	134.3	7.37 ±0.73	0.237 ±0.047	2.43±0.24	48.4
4/28 22:30	HRC	5µ	302.8	30.62	101.1	6.86 ±0.60	0.187 ±0.038	2.08±0.18	41.6
4/28 23:04	HRC	5µ	393.7	33.38	84.79	10.75 ±0.73	0.170 ±0.036	2.49±0.17	49.6
4/29 09:30	HRC	*	-	-	-	3.99 ±0.97	0.260 ±0.064	1.87±0.46	37.4
4/29 14:35	HRC	5µ	88.9	13.69	153.9	3.04 ±0.41	0.212 ± 0.037	1.47±0.19	29.4
4/30 15:40	HRC	5µ	545.1	14.90	27.34	2.58 ±0.45	0.243 ±0.048	1.45±0.26	28.9
5/01 9:10	HRC	5µ	1340	20.02	14.94	1.71 ±0.37	0.193 ±0.034	1.06±0.23	21.0

*Grab sample of fine silt and clay deposited from storm at high water mark, adjusted for measured difference between grab and suspended sample activities. ǂ Surface storm event control reference at Strader Branch. BSC=Blue Spring Creek, STB = Strader Branch, HRC=Hidden River Cave stream

DISCUSSION

BC storm event response

The initial testing done at Blowing Cave revealed that no detectable levels of ^{7}Be were found in the subsurface after a protracted dry period because in-cave ^{7}Be had time to decay for at least 2.5 half-lives. In the relatively simple BC system, a moderate influx of storm sediment enriched in ^{7}Be was traced about half way through the main stream conduit, to a point where it was no longer detectable because of mixing, deposition or limited transport distance. The levels of ^{137}Cs found in cave sediments both before and after storm flow were variable and no pattern of mixing or deposition was apparent. Because testing indicated there was still ^{137}Cs activity in some cave sediments after long dry periods – a result of its 30.2-year half-life – the random nature of the results are interpreted to be a function of reworked cave sediment deposited in the system over a number of years, as well as differences in local surface source types.

HRC storm event response

Beryllium-7 activity reached its maximum value during the initial rise in storm-related TSS and when SpC indicated contribution to runoff from surface water was increasing (Fig. 3.7). Activities of ^{7}Be ranged from about 1.7 to 17.8 dpm/g, with an initial spike in material enriched in ^{7}Be, then reduction of activity at peak turbidity and beyond. For graphing and further analysis, a background pre-storm filtered sample was used as the initial $^{7}Be_0$, and subsequent ^{7}Be measurements were normalized to this initial value. The $^{7}Be_t/^{7}Be_0$ results are graphed in Figure 3.7, along with error envelopes and a reference line that represents decay of the initial sample over the length of the storm event. Cesium-137 activity showed less variability during storm runoff, ranging from about 0.1 to 0.35 dpm/g. As with ^{7}Be, ^{137}Cs values were normalized to an intial $^{137}Cs_0$ value and the resulting $^{137}Cs_t/^{137}Cs_0$ ratio was graphed with an error envelope and reference line that represents decay of the initial ^{137}Cs sample (Fig. 3.8). Virtually no ^{137}Cs decayed in these short time frames because of its 30-year half-life.

In many past studies, the goal of measuring changes in fallout isotopes was to determine sediment travel distance or age as it mixed with other active isotope sources at the surface (e.g., Bonniwell et. al. 1999;

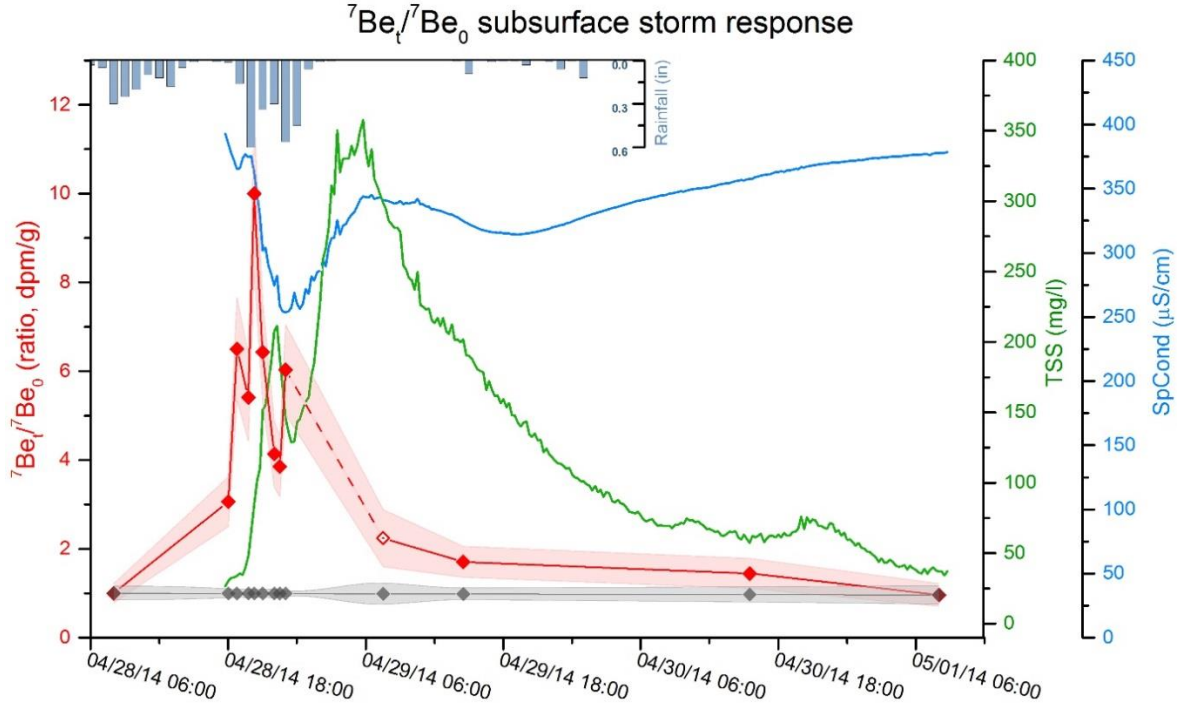

Figure 3.7: Results of normalized $^{7}Be_t/^{7}Be_0$ analysis for filtered samples, plotted with time series of rainfall, SpC and TSS during the 4/28/14 flood event at Hidden River Cave. The decay curve for initial background sample ($^{7}Be_0$) is shown in gray, with error envelope. Dashed line indicates gap in sampling where isotope activity may be changing rapidly. Open isotope symbol is a high-water grab sample.

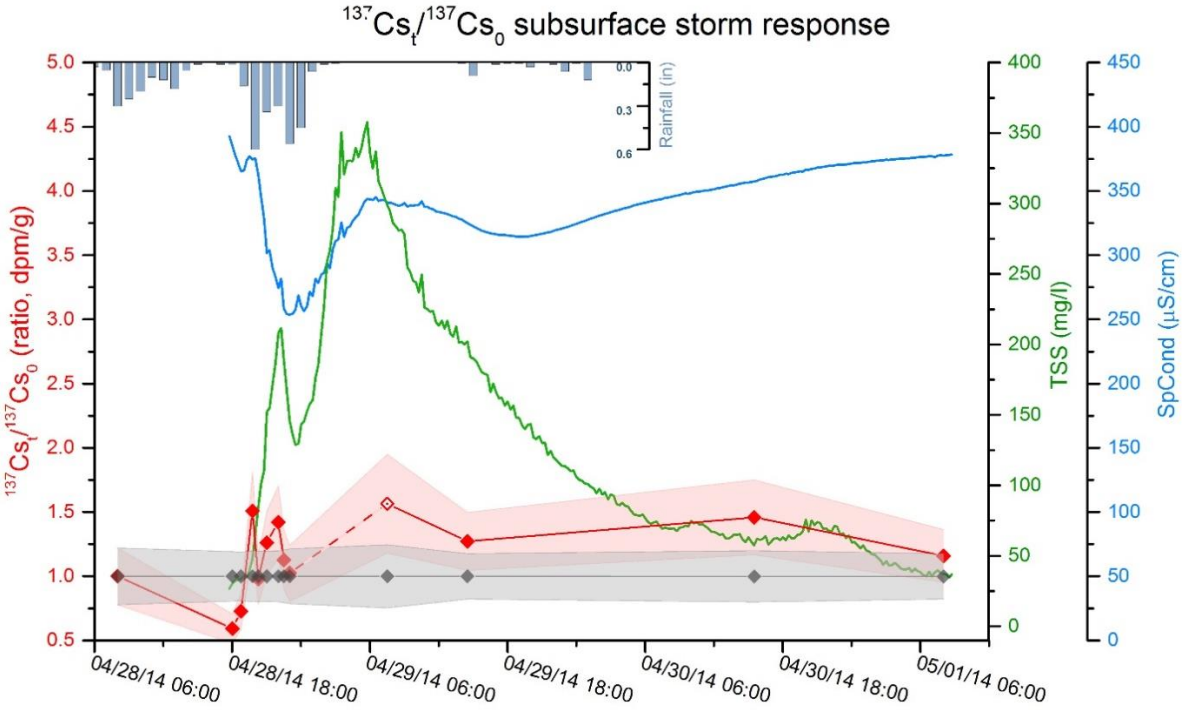

Figure 3.8: Results of normalized $^{137}Cs_t/^{137}Cs_0$ analysis for filtered samples, plotted with time series of rainfall, SpC and TSS during the 4/28/14 flood event at Hidden River Cave. The decay curve for initial background sample ($^{137}Cs_0$) is shown in gray, with error envelope. Dashed line indicates gap in sampling where isotope activity may be changing rapidly. Open isotope symbol is a high-water grab sample.

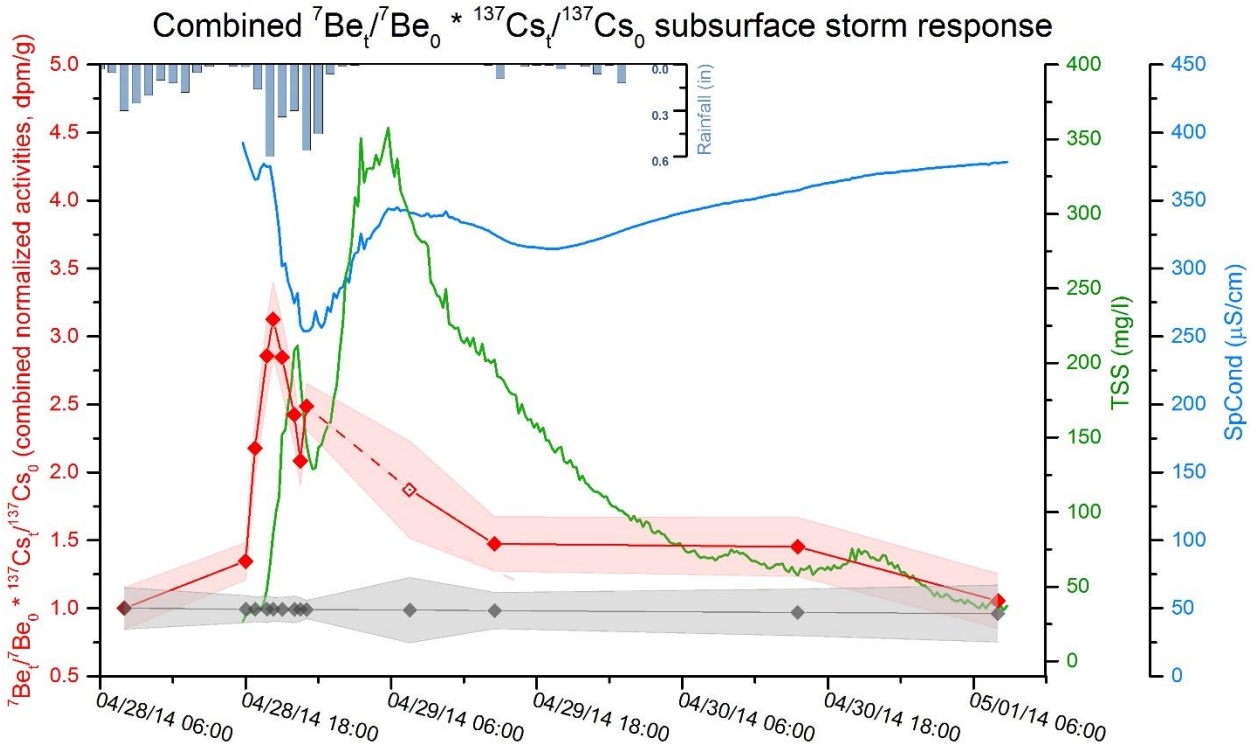

Figure 3.9: Results of combined normalized $^{137}Cs/^{137}Cs_0$ and $^{7}Be/^{7}Be_0$ for filtered samples, plotted with rainfall, SpC and TSS during the 4/28/14 flood event at Hidden River Cave. The decay curve for initial background sample is shown in gray, with error envelope. Dashed line indicates gap in sampling where isotope activity may be changing rapidly. Open isotope symbol is a high-water grab sample.

Matisoff et. al. 2005). Many of those studies utilized excess lead-210 ($^{210}Pb_{ex}$) to normalize ^{7}Be and ^{137}Cs for grain size and source variations in the landscape. Filtering suspended sediment to obtain samples within a karst stream controlled for grain size variations for this project. The land surface within the Hidden River basin is a mix of actively tilled farmland, forests, old overgrown fields and commercial development, so a lot of variation in Be and Cs depth profiles in soil is common. Both ^{137}Cs and ^{7}Be should be eroded from surface zones (depending on erosion depth and soil disturbance) and delivered into the subsurface where it will mix with depleted material. Because the dynamics of karst flow and agricultural surface runoff produce erosion from both shallow and deep sources, as well as disturbed and undisturbed sources, combining the two normalized isotope ratios as a product helped reduce surface signal variability. The measure $(^{7}Be/^{7}Be_0)*(^{137}Cs/^{137}Cs_0)$ was found to be the more effective measure of surface/subsurface sediment mixing in this setting (Fig. 3.9).

Sediment fluxes by source

An important observation in the HRC system is a division flow sources upstream of the sampling point. The majority of water flowing into the entrance chamber and continuing downstream originates from a source beneath the base of the entrance breakdown (talus) slope. Around 70% or more of the water flow in this part of the cave system comes from the discharge beneath the talus, and this water was dye traced (Quinlan and Ray, 1989) from the sinking streams where reference isotope sampling occurred. The rest of the flow through the entrance area comes from a related branch called the South River (Figs. 3.3, 3.4), which has been dye traced from the Cave City area, about 7 km to the southwest (Quinlan and Ray, 1989). Because of its shorter flow route, the South River should have a quicker time of concentration than the flow route from the Blue Spring Creek area. The TSS and SpC data appear to support this, showing a rapid but brief spike in TSS followed by a significant dip in conductivity from dilution of aquifer water by rainwater (Figs. 3.7 – 3.9).

A much larger TSS spike arrived 6 to 7 hours later, followed by a more subtle but broader dip in SpC (Figs. 3.7 – 3.9) likely due to arrival of surface runoff from Blue Spring Creek and related sinking streams in the far southeastern part of the basin. This dynamic suggests that the observed spike in ^{7}Be (and to a lesser extent ^{137}Cs) may be sourced mainly from initial sheet erosion and runoff through South River. Unfortunately, the flood event was large enough that it interrupted planned continuous sampling for part of the period. The last filtered sample before the data gap showed ^{7}Be rising again (Fig. 3.7), and a second spike of ^{7}Be in advance of the larger turbidity spike is possible.

The product of the mass activity ratios, $(^{7}Be/^{7}Be_{0})*(^{137}Cs/^{137}Cs_{0})$, was used to develop an estimated time-series of surficially-derived suspended sediment load (Fig. 3.10, Table 3.2) by comparing normalized isotope data to the surface reference storm site at Strader Branch (normalized cave isotopes/surface isotopes in storm runoff). A data gap exists between when the cave flooded and when it was accessible again the following day. The data gap was treated conservatively, even though surface sediment load may have been higher than indicated from midnight on 4/28 to 8AM on 4/29. Using the indicated

surface/subsurface contribution percentages, it is estimated that 34.2% of the total suspended flux for this storm event can be attributed to flux of eroded surface material, and that about 65.8% of the total suspended flux was derived from depleted materials in the subsurface or deep soil profile.

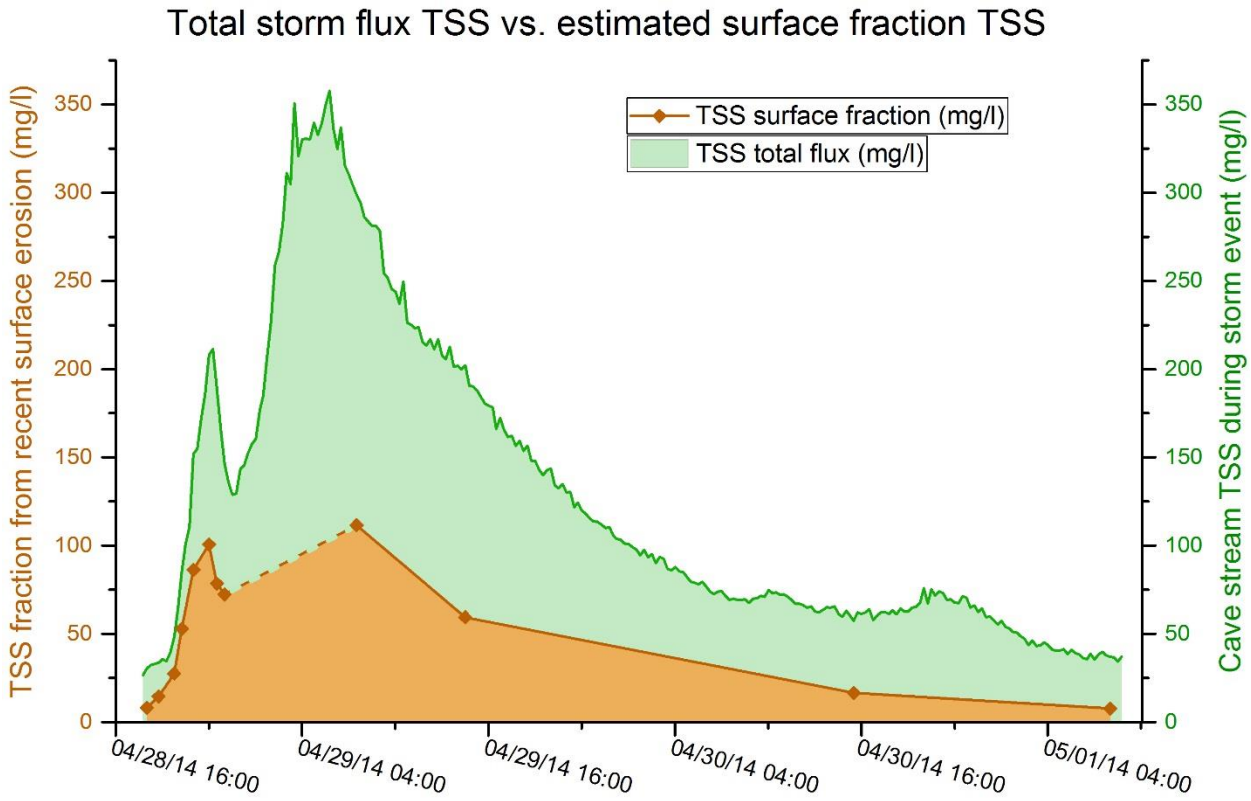

Figure 3.10: Approximate contribution of surficially-eroded material to the total suspended sediment flux for the 4/28/2014 storm event at Hidden River Cave. The percentage of surficial suspended material in the total load was estimated from the combined $^{137}Cs/^{137}Cs_0$ and $^{7}Be/^{7}Be_0$ measurements compared to the surface storm control site at the Strader Branch sinking stream.

Significance to carbon flux

A long-term study at BC that paralleled this work looked into inorganic carbon dynamics in sediment loads of karst systems. While significant data on inorganic carbon fluxes in the HRC system was not a priority, some relevant data were obtained. Work done in conjunction with Broderick (2015) tested the mineralogy of both grab and suspended sediment samples by XRD analysis. The results are plotted in Figure 3.11, showing the percentages of quartz, carbonate and clay minerals in samples. Surface grab

samples had the highest percentage of inorganic carbon (as carbonate), up to about 6% of the total sample. Filtered sediment samples from the storm event had very low amounts of carbonate for the size fraction that was obtained, averaging less than 2%. Interestingly, suspended sediment obtained at lower flow had a slightly higher average of around 4% carbonate, possibly because low flow conditions are commonly periods of high carbonate saturation, which may keep suspended carbonate particles from dissolving in the water column. However, storm TSS can be orders of magnitude higher than base-flow TSS, and even at 2%, the total mass flux of carbonate will be significantly higher during storms.

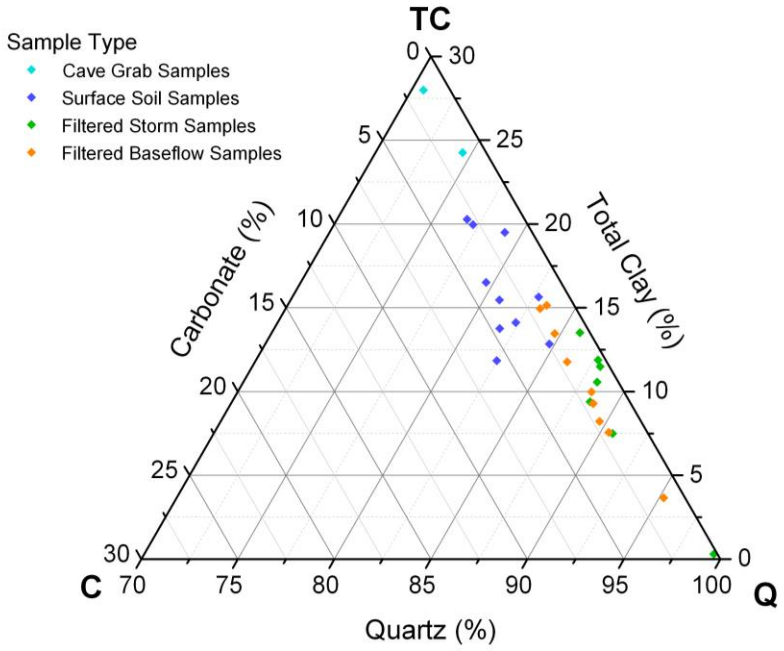

Figure 3.11: XRD mineralogy for surface, subsurface and filtered sediment samples in the Hidden River karst basin.

Limitations and further work

Ideally, isotope activity at primary input points would be monitored immediately prior to and concurrently with subsurface sampling. Because the targeted brief storm events created time and equipment deployment constraints, the difficulties prevented such additional monitoring in this study. Additionally, large karst basins can have complex input geometry, and the HRC basin is a combination of both allogenic (streams) and autogenic (sinkholes) flow to the subsurface. A possible alternative to concurrent surface monitoring is to use additional isotopes and calculate other isotope ratios beyond what

was done for this study. Recent work by Matisoff et al. (2005) used the $^{7}Be/^{210}Pb_{ex}$ ratio to determine fractions of new sediment in suspension, and obtained excellent results. Future work at HRC may benefit from expanding work to include analysis of $^{210}Pb_{ex}$. The total mass of material transported during the HRC storm event were not calculated because total flow volume for the entire storm could not be readily obtained. While the cave stream was flowing as an open channel in the beginning of the 4/28 storm event, velocities and channel cross-section area could be measured or estimated to calculate discharge. Once intense flooding and pipe-full conditions occurred in the middle of the storm event, accurate measurements of flow in the system were prevented. Future work would benefit from installation of Doppler velocity meters to track changes in discharge across the open channel/pipe full conversion and derive a total sediment mass flux for the basin.

CONCLUSIONS

Monitoring ^{7}Be in karst sediment deposits and fluxes appears to be an effective tool for investigating the transport and mixing of surface and subsurface sediments at short time scales in karst. ^{137}Cs by itself may be a good tool for estimating long-term flux and transport of surface sediment into karst conduits, but further work is needed to account for existing ^{137}Cs activity in the subsurface. Filtering the suspended sediment for analysis, along with utilization of the product of normalized ^{7}Be and ^{137}Cs activity ratios appear to be effective methods that help control for variation in sediment sources and grain size and allow estimates of surface soil erosion and transport. An initial field test showed that a moderate storm event moved and deposited fine surface sediment up to 1.5 km along the Blowing Cave, KY stream conduit. A very large storm event studied at Hidden River Cave, KY produced a spike in the breakthrough curves of ^{7}Be and ^{137}Cs in the main cave stream that preceded the maximum turbidity spike and dip in SpC from rainwater dilution. Surface sediment accounted for up to about 62% of total suspended sediment during first flush, and an overall estimated 34.2% of the total sediment flux over the 4 days of the flow event that were studied, with the rest of the sediment likely derived from older stored deposits in the subsurface that were remobilized.

REFERENCES

Auckenthaler, A., Raso, G. & Huggenberger, P., 2002. Particle transport in a karst aquifer: Natural and artificial tracer experiments with bacteria, bacteriophages and microspheres. In *Water Science and Technology*. pp. 131–138.

Bentley, S.J., Fabre, J., Li, C., Smith, E., Walker, N., White, J., Rouse, L., Bargu, S., 2012. Fluvial Sediment Flux during High Discharge Events: Harnessing Mississippi River Sediment to Build New Land on an Endangered Coast. In *Proceedings of the Ocean Sciences Meeting*. Salt Lake City.

Blake, W.H., Walling, D.E. & He, Q., 2002. Using cosmogenic beryllium-7 as a tracer in sediment budget investigations. *Geografiska Annaler, Series A: Physical Geography*, 84(2), pp.89–102.

Bonniwell, E.C., Matisoff, G. & Whiting, P.J., 1999. Determining the times and distances of particle transit in a mountain stream using fallout radionuclides. *Geomorphology*, 27(1–2), pp.75–92.

Bosch, R.F. & White, W.B., 2007. Lithofacies and transport of clastic sediments in karstic aquifers. In I. D. Sasowsky & J. Mylroie, eds. *Studies of Cave Sediments: Physical and Chemical Records of Paleoclimate*, pp.1-22.

Broderick, C.A., 2015. *Tracing Sediment in the Subsurface Using Beryllium-7: Green River Basin, KY*. Master's thesis, Louisiana State University.

Ciffroy, P., Reyss, J.-L. & Siclet, F., 2003. Determination of the residence time of suspended particles in the turbidity maximum of the Loire estuary by 7Be analysis. *Estuarine, Coastal and Shelf Science*, 57(4), pp.553–568.

Le Cloarec, M.F., Bonte, P., Lefevre, I., Mouchel, J.M., Colbert, S., 2007. Distribution of ^{7}Be, ^{210}Pb and ^{137}Cs in watersheds of different scales in the Seine River basin: inventories and residence times. *The Science of the total environment*, 375(1–3), pp.125–39.

D'Haen, K., Verstraeten, G. & Degryse, P., 2012. Fingerprinting historical fluvial sediment fluxes. *Progress in Physical Geography*, 36, pp.154–186.

Dogwiler, T. & Wicks, C.M., 2004. Sediment entrainment and transport in fluviokarst systems. *Journal of Hydrology*, 295(1–4), pp.163–172.

Farrant, A.R. & Smart, P.L., 2011. Role of sediment in speleogenesis; sedimentation and paragenesis. *Geomorphology*, 134, pp.79–93.

Ford, D. & Williams, P., 2007. *Karst Hydrogeology and Geomorphology*, Wiley Online Library, p.576.

Fry, J., Xian, G., Jin, S., Dewitz, J.A., Homver, C.G., Yang, L., Barnes, C.A., Herold, N.D., Wickham, J.D., 2011. Completion of the 2006 National Land Cover Database for the Conterminous United States. *PE&RS*, 77(9), pp.858–864.

Goldscheider, N., Meiman, J., Pronk, M., Smart, C., 2008. Tracer tests in karst hydrogeology and speleology. *International Journal of Speleology*, 37(January), pp.27–40.

Göppert, N. & Goldscheider, N., 2008. Solute and colloid transport in karst conduits under low- and high-flow conditions. *Ground water*, 46(1), pp.61–8.

Guzmán, G., Quinton, J.N., Nearing, M.A, Mabit, L., Gomez, J.A., 2013. Sediment tracers in water erosion studies: Current approaches and challenges. *Journal of Soils and Sediments*, 13, pp.816–833.

Hajna, N.Z. & Mihevc, A., 2008. Karst Sediments. In N. Z. Hajna & A. Mihevc, eds. *16th International Karstological School*.

Harvey, R.W., Metge, D.W., Shapiro, A.M., Renken, R.A., Osborn, C.L, Ryan, J.N., Cunningham, K.J., Landkamer, L., 2008. Pathogen and chemical transport in the karst limestone of the Biscayne aquifer: 3. Use of microspheres to estimate the transport potential of Cryptosporidium parvum oocysts. *Water Resources Research*, 44(8).

Herman, E.K., Tancredi, J.H., Toran, L., White, W.B., 2006. Mineralogy of suspended sediment in three karst springs. *Hydrogeology Journal*, 15(2), pp.255–266.

Herman, E.K., Toran, L. & White, W.B., 2008. Threshold events in spring discharge: Evidence from sediment and continuous water level measurement. *Journal of Hydrology*, 351(1–2), pp.98–106.

Hess, J.W., 2008. Methods in Karst Hydrogeology. *Ground Water*, 46, pp.172–172.

Kaste, J.M., Norton, S. a. & Hess, C.T., 2002. Environmental Chemistry of Beryllium-7. *Reviews in Mineralogy and Geochemistry*, 50(1), pp.271–289.

Koiter, A. J., Owens, P.N., Petticrew, E.L., Lobb, D.A., 2013. The behavioural characteristics of sediment properties and their implications for sediment fingerprinting as an approach for identifying sediment sources in river basins. *Earth-Science Reviews*, 125, pp.24–42.

Lewis, J.J., 1995. The Devastation and Recovery of Caves and Karst Affected by Industrialization. In *National Cave Management Symposium*. p. 14.

Mabit, L., Benmansour, M., Abril, J.M., Alewell, C., 2013. Fallout ^{210}Pb as a soil and sediment tracer in catchment sediment budget investigations: A review. *Earth-Science Reviews*, 138, pp.335–351.

Mabit, L., Benmansour, M. & Walling, D.E., 2008. Comparative advantages and limitations of the fallout radionuclides (137)Cs, (210)Pb(ex) and (7)Be for assessing soil erosion and sedimentation. *Journal of environmental radioactivity*, 99(12), pp.1799–807.

Mahler, B.J., Bennett, P.C. & Zimmerman, M., 1998. Lanthanide-labeled clay: A new method for tracing sediment transport in karst. *Ground water*, 36(5), pp.835–843.

Mahler, B.J. & Lynch, F.L.L., 1999. Muddy waters: temporal variation in sediment discharging from a karst spring. *Journal of Hydrology*, 214(1–4), pp.165–178.

Martin, J.B. & White, W.B., 2008. *Frontiers in Karst Research* J. B. Martin & W. B. White, eds.,

Massei, N., Wang, H.Q., Dupont, J.P., Rodet, J., Laignel, B., 2003. Assessment of direct transfer and resuspension of particles during turbid floods at a karstic spring. *Journal of Hydrology*, 275, pp.109–121.

Matisoff, G. & Whiting, P.J., 2012. *Handbook of Environmental Isotope Geochemistry* M. Baskaran, ed., Berlin, Heidelberg: Springer Berlin Heidelberg.

Matisoff, G., Wilson, C.G. & Whiting, P.J., 2005. The7Be/210Pbxs ratio as an indicator of suspended sediment age or fraction new sediment in suspension. *Earth Surface Processes and Landforms*, 30(9), pp.1191–1201.

Neal, C., Jeffery, H.A., Conway, T., Ryland, G.P., Smith, C.J., Neal, M., Norton, S.A., 1992. Beryllium concentrations in rainfall, stemflow, throughfall, mist and stream waters for an upland acidified area

of mid-Wales. *Journal of Hydrology*, 136, pp.33–49.

Peterson, E.W. & Wicks, C.M., 2003. Characterization of the physical and hydraulic properties of the sediment in karst aquifers of the Springfield Plateau, Central Missouri, USA. *Hydrogeology Journal*, 11(3), pp.357–367.

Porto, P. & Walling, D.E., 2012. Validating the use of 137Cs and 210Pb ex measurements to estimate rates of soil loss from cultivated land in southern Italy. *Journal of Environmental Radioactivity*, 106, pp.47–57.

Pronk, M., Goldscheider, N., Zopfi, J., Zwahlen, F., 2009. Percolation and particle transport in the unsaturated zone of a karst aquifer. *Ground Water*, 47(3), pp.361–369.

Quinlan, J.F. & Ray, J.A., 1989. Groundwater basins in the Mammoth Cave region, Kentucky. Friends of Karst Occasional Publication 3, p.1.

Ritchie, J.C. & McHenry, J.R., 1990. Application of radioactive fallout cesium-137 for measuring soil erosion and sediment accumulation rates and patterns: A review. *Journal of Environmental Quality*, 19, pp.215–233.

Sasowsky, I.D. & Mylroie, J., 2007. *Studies of Cave Sediments: Physical and Chemical Records of Paleoclimate* 2nd ed.,

Schenk-Brown, J., 2008. *Atrazine Contamination and Suspended Sediment Transport within Logsdon River, Mammoth Cave, Kentucky*. Master's thesis, Western Kentucky University.

Vesper, D.J., 2013. Water in Karst: Management, Vulnerability, and Restoration. *Groundwater*, 51(5), p.656.

Walling, D.E., 2013. Beryllium-7: The Cinderella of fallout radionuclide sediment tracers? *Hydrological Processes*, 27(6), pp.830–844.

Walling, D.E. & He, Q., 1993. Use of Cesium-137 as a tracer in the study of rates and patterns of floodplain sedimentation. IAHS Publication, pp.319-319.

Walling, D.E., Zhang, Y. & He, Q., 2005. Models for Converting Radionuclide (^{137}Cs, Excess ^{210}Pb , and ^{7}Be) Measurements to Estimates of Soil Erosion and Deposition Rates (Including Software for Model Implementation), p.31.

White, W.B., 2002. Karst hydrology: recent developments and open questions. *Engineering Geology*, 65(13), pp.85–105.

Yasunari, T.J., Stohl, A., Hayano, R.S., Burkhart, J.F., Eckhardt, S., Yasunari, T., 2011. Cesium-137 deposition and contamination of Japanese soils due to the Fukushima nuclear accident. *Proceedings of the National Academy of Sciences*, 108(49), pp.19530–19534.

Yin, C. & Li, L., 2008. An investigation on suspended solids sources in urban stormwater runoff using 7Be and 210 Pb as tracers. *Water science and technology : a journal of the International Association on Water Pollution Research*, 57(12), pp.1945–50.

You, C., Lee, T. & Li, Y.-H., 1989. The partition of Be between soil and water. *Chemical Geology*, 77, pp.105–118.

CHAPTER 4: COMPARISON OF KARST LANDSCAPE DENUDATION RATES USING DISSOLVED LOAD VS. TOTAL LOAD CALCULATIONS

ABSTRACT

Landscape denudation rates in karst settings have been calculated using a number of different methods by past researchers. The most widely applied method involves measurement of dissolved carbonate load at base-level springs, calculating denudation using the area of exposed carbonate outcrop, and assuming other outcrop types are in equilibrium. In mixed carbonate/non-carbonate lithologies (which includes most fluviokarst settings), much of the landscape is also eroded by transport of sediments through conduits. For this study, rates were derived from both the carbonate dissolved load method and total sediment load/dissolved load method at Blowing Cave basin.

A denudation rate of 60.3 mm/ka was calculated for the 2.31 km^2 carbonate outcrop surface of the basin, and a rate of 41.7 mm/ka was calculated for the 3.95 km^2 surface of non-carbonate outcrop area. The basin average rate of landscape denudation (aggregating both carbonate and non-carbonate areas) was 48.5 mm/ka. At Blowing Cave basin, denudation rates for carbonate and non-carbonate outcrop areas are not in equilibrium. These rate differences are reflected in the evolution of the basin, which has developed by steep-walled escarpment retreat along with piracy of allogenic runoff into well-developed karst conduits. Landscape evolution in fluviokarst settings is more complex than can be measured by solute load analysis alone, and complete mass flux measurement of all erosion components will help improve future studies.

INTRODUCTION

Purpose and significance

Carbonate bedrock underlies about one-fifth of the United States (Fig. 4.1) and world landmasses. (Martin & White 2008). Landscape denudation in karst terrain has been studied extensively in many different settings and regions (e.g., Kaufmann & Braun 2001; Kaufmann 2003; Groves & Meiman 2005; Anthony & Granger 2007; De Waele et al. 2009; Gabrovšek 2009; Shopov et al. 2009; Florea 2015). Methods of measuring bedrock removal rates in karst have ranged from tracking mass change in buried limestone tablets, running GIS watershed evolution models, to tracking total geochemical fluxes exiting karst basins (Gabrovšek 2009; Florea 2015). Rates can be roughly estimated from precipitation using equilibrium constants. For instance, Gombert (2002) calculated the maximum denudation rate of carbonate terrain as a function of dissolution at the surface using the expression:

$$D_{max} = 100/(\rho 4^{1/3})(K_S K_1 K_0/K_2)^{1/3} p\mathrm{CO}_2^{1/3}(P-E) \qquad \text{(eq. 1)}$$

Where D_{max} is the denudation rate (mm/ka), ρ is the limestone density, P is precipitation (mm/yr), E is evapotranspiration (mm/yr), and the K terms are carbonate equilibrium constants. The equation assumes calcite saturation at the base of the epikarst zone, but such methods are poorly suited to calculating total denudation in mixed karst/non-karst regions. Many karst terrains are underlain by a mix of carbonate and non-carbonate lithologies, and even relatively pure carbonates have some percentage of insoluble material in the form of chert, sand, silt and clay. The general assumption that has dominated karst denudation research is that mixed lithology landscapes appear to be in equilibrium, so must have similar rates of carbonate and non-carbonate removal (White 2002). Using that assumption, studying landscape denudation rates becomes simpler, because only dissolution of carbonate needs to be measured as the key removal processes in the system. Once chemical carbonate removal is calculated, the result is typically averaged over the exposed carbonate outcrop area of a basin to yield landscape lowering rates, and the non-carbonate lithologies are assumed to lower at the same rate (White 1984; Palmer 2007). The assumption has not been rigorously tested. Some past results of karst basin denudation based strictly on

solute load are shown in Table 4.1, and give an idea of the ranges and magnitudes of karst surface removal in varied settings. These settings, climates and sampling methods vary greatly, with precipitation, sampling frequency and storm flow characterization the key factors that drive rate differences.

Table 4.1: Example of values for karst landscape denudation rates based on solute flux

Location	Denudation rate (mm/ka)	Reference
Baget (Ariège, Pyrenees, various locations and years)	48 83 88 56 89	(Bakalowicz 1979)
Slovenia, Ljubljanica	60	(Gams 2004)
Austrian Alps	95	(Plan 2005)
Waitomo, New Zealand	69	(Gunn 1981)
Slovenian Alps	94	(Kunaver 1979)
Caves Branch, Belize	90	(Miller 1982)
Cooleman Plain, Australia	24	(Jennings 1972)
Derbyshire, UK	83	(Pitty 1968)
Fergus River, Ireland	55	Williams (1963)
Jura Mtns, Switzerland	98	(Aubert 1969)
Yorkshire, UK	83	(Sweeting 1966)
Riwaka, New Zealand	100	(Williams & Dowling 1979)
Somerset Island, Canada	2	(Smith 1972)
Svartisen, Norway	32.5	(Lauritzen 1990)
Monroe County, WV	22	(Ogden 1982)
Redmond Creek, KY	17.9	(Florea 2015)

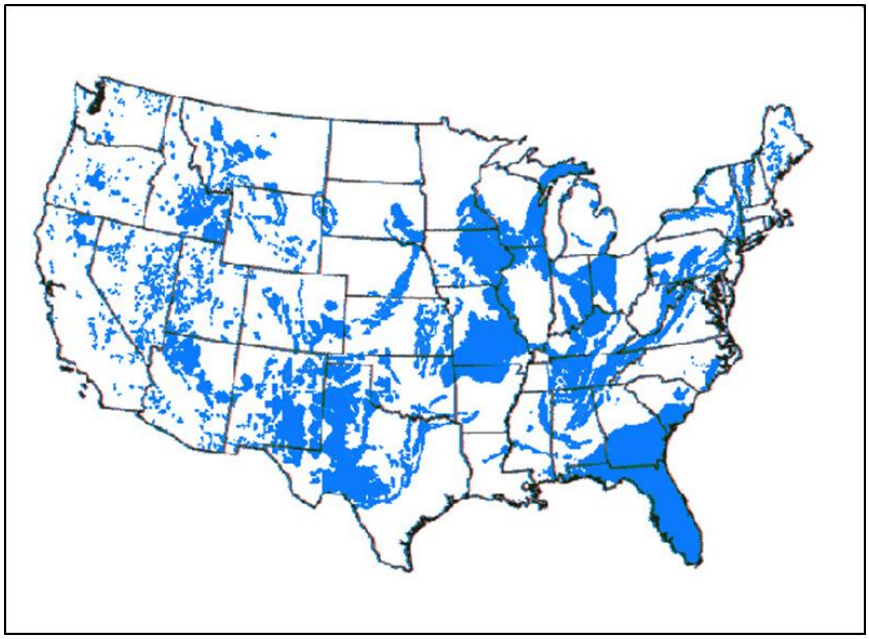

Figure 4.1: Major karst regions of the lower 48 United States (Epstein et al., 2002).

Most past research on fluxes of material through karst systems has focused on dissolved carbonate (e.g., Liu et al. 1997; Dreybrodt & Eisenlohr 2000; White 2000; Groves & Meiman 2001; Gombert 2002), and chemical loads do typically dominate karst waters during low to moderate flow conditions, but for calculating total mixed-bedrock removal rates, both carbonate and non-carbonate particulates in suspended and bed loads are a major component of mass flux under higher flow conditions during moderate to extreme storm events (Newson, 1971; Herman et al., 2008). To investigate denudation assumptions in mixed bedrock settings, this research built on previous calculations of particulate inorganic carbon (PIC) flux in karst (Chapter 2) and tracked total carbonate/noncarbonated sediment loads to compare total load methods to carbonate load methods for calculating landscape evolution.

Sediment and chemical loads cycle through karst systems by a variety of processes. To assist in understanding potential sediment sources, sinks and transport, a conceptual model of the karst sediment cycle was developed by Bosch & White (2007) (Fig. 4.2). For sediment production, the dominant process will depend on the recharge type and conduit geometry/hydraulics. Sediment transport will depend primarily on system hydraulics and particle sizes and types.

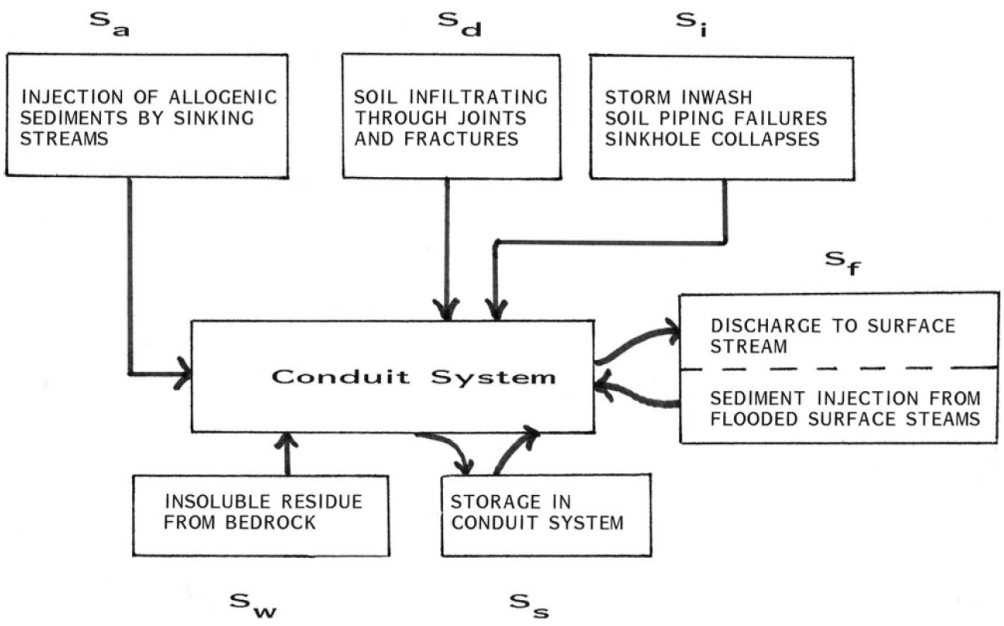

Figure 4.2: Conceptual model of the fluviokarst sediment budget (Bosch & White 2007)

When considering removal of carbonate from karst basins, particulate carbonate (PIC) removed by mechanical erosion becomes part of the total sediment load and should be considered when calculating denudation based on carbonate outcrop area. Overall flux for both carbonate and non-carbonate mass ultimately depends on production and transport rates of both dissolved and sediment loads. The largest net carbonate sediment fluxes likely occur during storm events where mobile carbonate material is produced and transported much faster than it is dissolved or deposited, and the material is transported along with non-carbonate loads.

Carbon dynamics in karst

In order to compare landscape denudation rates on different lithologies, standard methods to calculate dissolved carbonate removal are needed. Studies of carbonate dissolution in karst settings have clearly demonstrated the significance of the dissolution process to bedrock removal:

$CaCO_3 + CO_2 + H_2O \rightarrow Ca^{2+} + 2HCO_3^-$ (Limestone dissolution) (eq. 2)
$CaMg(CO_3)_2 + 2CO_2 + 2H_2O \rightarrow Ca^{2+} + Mg^{2+} + 4HCO_3^-$ (Dolomite dissolution) (eq. 3)
(Groves & Meiman 2001; Cheng & Daoxian 2002).

Some evidence shows carbonate clastics (suspended and bed loads) can be a major component of mass flux under typical storm flow conditions, accounting for an important percentage of the annual removal of carbonate. Studies of sediment dynamics in karst systems have shown that the karst landscape (caves, sinkholes, blind valleys, and epikarst) can store significant amounts of sediment over a large temporal range (days to millennia), but can also transport vast quantities of sediment during punctuated events such as storm flow or cover collapse (Bosch & White 2007; van Gundy & White 2009). Newson (1971) tracked both dissolved carbonate load and particulate carbonate load in a karst system of Great Britain and found that mechanical removal of carbonate was greater than removal by dissolution above a certain discharge threshold (Fig. 4.3). Similarly, Herman et al. (2008) found that runoff events that exceed certain thresholds can produce a significant flux of particulate carbonate at karst springs. In certain rare flood events, some karst systems have been observed to move massive amounts of sediment as bed load or subsurface debris flows (Crawford 1996; van Gundy & White 2009). These components of mass flux need to be addressed to properly quantify denudation rates in fluviokarst basins.

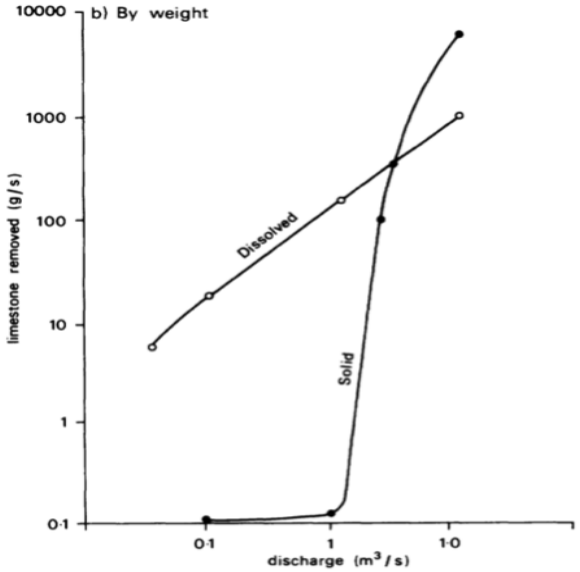

Figure 4.3: The relationship between conduit discharge and type of limestone removal at the Cheddar Gorge spring, England (Newson 1971).Sediment transport in karst

Numerous studies have addressed sediment dynamics and sediment deposits in karst systems (e.g., Mahler & Lynch 1999; Massei et al. 2003; Peterson & Wicks 2003; Dogwiler & Wicks 2004; Sasowsky & Mylroie 2007; Hajna & Mihevc 2008; Pronk et al. 2009). Caves, sinkholes, and epikarst features act as both avenues of transport and repositories for many types of deposits. Particulate materials transported and stored in karst can be derived locally (autogenic), such as breakdown of cavern walls, or transported from other locations (allogenic), such as suspended and bed sediment in underground streams (Bosch & White 2007). Because caves both trap and transport sediments from the surface, cave deposits and their sources are intimately linked to conduit development and dynamics (Farrant & Smart 2011). Sediment storage and transport processes in the subsurface can change rapidly during storm events, but few existing studies have focused on these dynamics (White 2002).

To better understand sediment transport dynamics in karst, knowledge of subsurface storm response is needed. Karst is considered a triple-porosity regime, with original rock porosity, secondary fracture/bedding plane porosity, and conduit porosity. Karst groundwater movement is often dominated by turbulent and rapid conduit flow, typically recharged by sinking surface streams and runoff into sinkholes (Ford & Williams 2007). During storm events, sediments from karst land surfaces are eroded and transported underground, particularly in fluviokarst basins with developed surface streams, or in locations where streams from non-karst areas flow onto karst areas and sink. Sediment can also be moved into the subsurface by sinkhole inflow and collapse, and infiltration through enlarged epikarst fractures. Some fine-grained sediment may get transported through the karst system without settling out of suspension, but if sediments get deposited in the subsurface, they can remain in storage from days to millenia depending on local hydraulic conditions, conduit morphology and magnitude of storm events (Bosch & White 2007). Additionally, some sediments are produced directly in the subsurface as the insoluble fraction of weathered rock is left behind from dissolution, carbonate is precipitated in supersaturated conditions, or cave walls are mechanically eroded.

The objectives of this study were: 1) Quantify the major bedrock removal processes within a well-defined mixed-bedrock fluviokarst basin; 2) Calculate time-series fluxes of all the various bedrock removal components; and 3) Compare landscape denudation rates based only on carbonate removal to rates based on total carbonate/non-carbonate mechanical and chemical removal.

METHODS AND MATERIALS

Site location

Kentucky's Sunnybrook Blowing Cave basin was chosen as the field site for investigating mixed-bedrock fluviokarst landscape denudation. The Blowing Cave karst basin is sediment rich with allogenic recharge from siliciclastic caprock running onto massive carbonate lithologies with a well-developed subsurface stream conduit (Fig 4.4). The bed load in the subsurface consists of silt to large boulder material, derived from the surrounding high relief sandstone and limestone plateau escarpment. Knowledge gained from this site can be extended to many other regions with similar settings and climate. The typical wet season for the region occurs from January through May, although precipitation from summer thunderstorms can cause intense recharge events.

Sunnybrook Blowing Cave has a drainage area of approximately 6.3 km^2, which is primarily forested and drains the high-relief, rugged escarpment of the Cumberland Plateau in Kentucky. The basin is underlain by Pennsylvanian conglomerates, sandstones and shales and Mississippian limestones and dolostones. The cave system and subsurface stream are formed in the Kidder and St. Genevieve members of the Monteagle limestone, as well as the St. Louis limestone, and allogenic runoff that drains into the karst system is produced from lithologies including the Breathitt shales and sandstone, the Rockcastle conglomerate, and the marine Pennington shale and Hartselle sandstone (Lewis 1977).

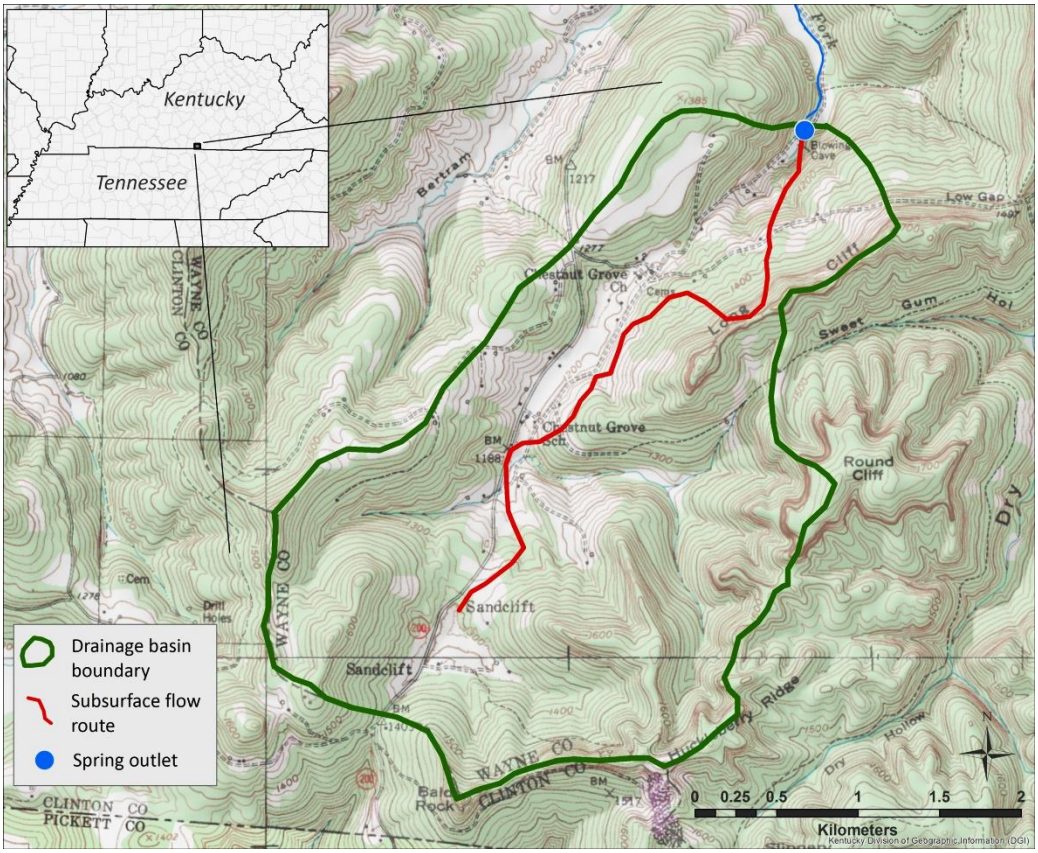

Figure 4.4: Location and hydrologic setting of the Blowing Cave Basin research site. The extent of the main underground stream conduit is shown within the recharge basin of the study area.

Measurement of suspended and dissolved material

Both suspended load and dissolved load sampling relied on similar field methods. Sampling for dissolved load involved collection of water grab samples across the course of a storm event, as well as during low-flow conditions. When necessary, ISCO automatic water samplers were deployed at the study reaches to sample during high-flow events. Discreet samples and ISCO automatic samples were collected according to standard U.S. Geological Survey protocols (Edwards & Glysson 1999), cation samples were treated with trace-metal grade nitric acid after collection, and all samples were placed on ice for transport and lab analysis. Major anions were analyzed on a Dionex ICS-900 (ion chromatography) instrument, and cations on a Perkin-Elmer ICP (inductively coupled plasma) instrument. Alkalinity was measured by titration in the field using a Hach digital titrator and standard acid cartridges. Although dissolved carbonate loads can be calculated exclusively from HCO_3^- concentrations, pH, temperature and carbonate equilibrium

constants, a more accurate method was used that calculates contributions from limestone and dolostone dissolution in karst systems using both HCO_3^- and the Ca^{2+}/Mg^{2+} ions. Calculated HCO_3^- concentrations derived from field titrations resulted from an advanced speciation model (Rounds, 2012) that incorporated initial pH and the temperature-dependent Debye–Hückle equilibrium relationships in a U.S. Geological Survey online calculator.

Field parameters were measured both manually and automatically, and included field-calibrated pH, specific conductance (SpC), temperature (T), and turbidity (NTU). A YSI-6910 multi-parameter hydrologic data recorder was deployed at the primary research site at Blowing Cave and was programmed for a fifteen minute sampling interval. Data from the water quality recorder were downloaded every six to eight weeks, and the probes were recalibrated and cleaned as needed. Manual measurements with handheld YSI field probes were also taken on each trip to verify and calibrate the data logger.

To characterize overall suspended load flux, direct sampling of suspended sediment concentration was coupled with time-series turbidity measurements from the deployed YSI-6910 logger. The optical turbidity probe was calibrated with formazin standards on a regular basis. Because water depths were generally less than 3 feet, grab samples for suspended sediment concentration (TSS) and particulate carbonate were taken by moving the sample bottle from the surface to near the streambed and back, and the YSI-6910 was installed so that the turbidity probe was at 0.5 depth under most conditions. Water samples for TSS analysis were filtered in the lab, dried and weighed for TSS mass, and the measured mass used to calibrate turbidity measurements. Carbonate fraction of suspended sediment was determined using a pair of filtered/unfiltered grab samples acidified to pH 2 with trace-metal grade nitric acid to dissolve particulate carbonate. The samples were then analyzed for differences in cations. Since Ca^{2+} and Mg^{2+} in typical karst waters are derived almost exclusively from carbonate (Ford & Williams 2007), the difference between the filtered and unfiltered samples can be used to calculate the amount and types of carbonate in the suspended load.

To calculate the continuous flux of both particulate and dissolved loads, accurate flow and velocity measurements were necessary for each study reach. A Sontek-IQ acoustic Doppler velocity/stage logger was installed at carefully measured channel locations. The Doppler logger automatically calculated flow volume at 10-minute intervals from stage, velocity and surveyed cross section. In addition, staff gauges were installed at key locations to calculate stage-discharge relationships. At Blowing Cave, data gaps in discharge due to instrument malfunction were filled with correlated discharge records ($r^2 = 0.98$) from a nearby USGS gauging station downstream of the site (Beaver Creek, USGS 03413200). For the YSI sonde, instrument drift between calibrations was adjusted with regression corrections.

Determining bed load movement

Flux and dynamics of bed load transport at the research sites were determined using direct tracing methods and sediment transport calculations calibrated to tracing results. Hydraulic parameters of each study reach were carefully measured and a stream power equation was used to determine the stability and movement of streambed sediment. A cobble tracer method utilizing RFID tracking was used to quantify actual movement of bed load material along the flow path. The predicted bed movement from the calculated methods were compared and correlated to observations of tracer movement.

Tracing bed sediment

Cobble tracer experiments have been used extensively by stream geomorphologists to determine conditions of entrainment (Reid & Frostick 1984), travel distances (Ferguson & Wathen 1998), and vertical mixing and burial (Church & Hassan 1992). None of the cited cobble tracer experiments were specifically designed to investigate sediment transport in cave streams. However, the design of the short-term radio-tagged cobble tracer experiment of Nichols (2004) was adopted for this study. The characteristics of the open channel reaches at the research sites are similar to those of stream reaches in which tracer experiments have been successfully conducted (Laronne & Carson 1976; Reid & Frostick 1984; Church & Hassan 1992; Ferguson & Wathen 1998; Ferguson & Hoey 2002; Nichols 2004).

A statistically valid set of cobbles were selected from the stream bed inside of the caves or in surface channels to serve as the tracers. Along each tracer line, tracers were deployed following the design of Ferguson and Wathen (1998) and Ferguson and Hoey (2002), which involved laying out tagged cobbles in an imbricated pattern to match natural stream cobble patterns. In-situ cobbles were modified and utilized as tracers at each site. Tracer movement was tracked with passive radio frequency identification (RFID) tags. A small hole was drilled in each cobble using a diamond bit on a mounted Dremel tool or drill press, and chips were secured with a non-toxic waterproof epoxy that did not alter the overall density or other properties of the cobbles. Because of their reliability and detection distance, this study used waterproof, passive, half-duplex 12 mm and 23 mm 134.2 kHz RFID tags from Texas Instruments (nos. TRPGR30TGC, RI-TRP-REHP-30).

In addition to the RFID tags, most tracers were painted with various colors of road marking paint, and individual ID numbers written with indelible ink or etched into the rock for more rapid identification in the field. The RFID particle tracking system consisted of a custom-built reader and antenna and was implemented in a manner similar to that of a metal detector. Tagged material was found by walking the stream channel and sweeping the coil of the reader over the channel bed. Each chip's unique identification string was recorded and linked to the individually measured cobble parameters: mass, rock type, and the A, B and C axes of each particle. A key advantage of using a tracking system was detecting buried tracer particles for loss prevention and to get an estimate of thickness of the mobile bed material (Nichols 2004).

Tracer movement was measured along the central axis of each stream reach using a measuring tape from a fixed zero datum. For tracers that were lost due to malfunction or extreme burial depth, replacement tracers were added so there would always be at least 75 tracers available in low-energy reaches and at least 100 available in higher energy reaches.

Calculation of virtual bed load velocity, and measurement of bed rock type and grain size

From the tagged tracer method, the ratio of the measured distance that sediment traveled to the time that velocity exceeded the critical flow condition (i.e. movement time) yielded a virtual velocity for each individual particle (Hassan et al. 1992). Virtual velocity for the entire streambed was calculated from measured cobble movement to yield the volumetric and mass rate of sediment transport (e.g, Hassan et al. 1992; Wilcock 1997), and the amount of time bed sediment was in storage—also known as transit time or response time (Wathen et al. 1997). The flux relationship of Hassan and others (1992) was used to calculate total bed flux from tagged tracers:

$$q_b = v_b \, d_s \, w_s \, (1 - P) \, \rho_s \qquad \text{(eq. 4)}$$

Where $\boldsymbol{v_b}$ is the average virtual velocity for all measured particles during a specific runoff event, $\boldsymbol{d}$ is the active channel width$_s$ $\boldsymbol{w}$ is the depth of the active and mobile sediment bed, $\boldsymbol{P}$ is the bed porosity, and $\boldsymbol{\rho_s}$ is the particle density.

Once the virtual velocity was known, a ratio of carbonate to non-carbonate bed material was needed for each study area to compare mass fluxes of the different bedrock types. Sediment size distributions and rock type for large material were measured using photographic methods (Graham et al. 2005) that utilized a non-invasive digitization and GIS scaling to extract the A and B axes of large areas with geometric analysis tools. Sediment size distribution of finer bed material were determined by standard sieve analysis of bed samples, and mineralogy was determined using a petrographic microscope.

Calculating bed transport dynamics

In order to apply measured bed load transport to the full time-series flow record, correlations with bed transport formula are necessary. Numerous empirical bed load entrainment and transport formula have been utilized for surface stream studies (e.g., van Rijn 1985; Buffington & Montgomery 1997; Ferguson & Wathen 1998; Almedeij 2002; Martin 2003; Barry et al. 2006; Holmes & Holmes 2010; Turowski et al.

2011), and some subsurface karst studies (Dogwiler & Wicks 2004; Rossman 2010; Wicks et al. 2010). In previous studies of bed load transport in karst, three different methods have generally been evaluated: the Einstein probability function, the Shields critical shear function and the Bagnold stream power function. The original critical shear method was first introduced by Shields (1936) who related the critical shear stress, τ_c to sediment density (ρ_s), density of water (ρ), particle diameter (d), and gravity (g). The parametric adaptation of Lorang and Hauer (2003) has proven useful in other subsurface studies, and was evaluated for datasets from this study:

$$\tau_{ci} = 0.045(\rho_s - \rho) g d_{50}^{0.6} d_i^{0.4} \quad \text{(eq. 5)}$$

where $\boldsymbol{\tau_{ci}}$ = the critical shear for particle size $\boldsymbol{i}$, $\boldsymbol{d_{50}}$ is the length of the intermediate axis of the particle that is larger than 50% of all the other particles at a particular location, and $\boldsymbol{d_i}$ is the length of the intermediate axes of the particle size of interest. However, the critical shear method was found to underestimate critical thresholds of movement in a cave environment with flashy flow, so an adaptation of the critical stream power function (Bagnold 1977; Martin & Church 2000; Ferguson 2005) was tested and yielded superior results. In this method, the energy available for particle entrainment (W/m^2) is calculated using unit stream power (ω):

$$\omega = \frac{\rho g Q S}{b} \quad \text{(eq. 6)}$$

where ρ is fluid density, g is gravity, S the energy slope, Q is stream discharge, and b is the width of the active channel. Within Blowing Cave, cross-sections and grain size were carefully measured at three locations that represented different flow dynamics in order to accurately estimate the flow conditions necessary to mobilize different sediment sizes. The water surface slope of each reach was estimated by using the measured stream bed slope, which is an accurate proxy if measured over an adequately long reach (tens of meters or more) in plane-bed and pool-riffle streams (Martin and Church, 2000). The initial test value for critical stream power was determined from the adaptation by Ferguson (2005):

$$\omega_0 = 0.104 \frac{D_b^{1.5}}{S^{0.17}} \left(\frac{D_i}{D_b}\right)^{0.67} \quad \text{(eq. 7)}$$

Where the overall bed material size (D_{50}) = D_b, the grain size of interest = D_i and slope = S. The empirical constant 0.104 incorporates gravity and is also related to the Manning-Strickler resistance law, and yields units of W/m^2 when using mm for grain size. The value is generally valid for Reynolds numbers > 400, slopes < 0.02, and d_{max}/d_{50} < 22, (Aguirre-Pe et al. 2003) but varies based on the bed structure and range of grain sizes on the bed. Grain sizes at the chosen field sites varied from silt to large cobble material but the d_{max}/d_{50} was generally less than 5. Calculated critical stream power was compared to thresholds of bed movement observed in the field in order to calibrate the empirical constant. To determine the critical threshold for bed load movement, the critical unit stream power was compared to the stream power measured from high-resolution time-series velocity and discharge. If the ratio $\omega_b : \omega_{ci} > 1$, sediment movement was predicted. Using calculated and critical stream power, the bed load transport rate q_b can then be determined from the transport function of Martin and Church (2000), which is a derivation of Bagnold's original formula that incorporates a gravity term:

$$q_b = [\omega - \omega_0]^{3/2} \left[D_{50}^{1/4}/d\right]\left[1/\rho_r^{1/2} g^{1/4}\right] \quad \text{(eq. 8)}$$

Where d = water depth, and ρ_r = the rock density in water. The results are in units of kg/m/s.

Determining total system flux

The total mass flux of both carbonate and non-carbonate material through the karst system is the sum of each of the three measured time-series components for each rock type: carbonate bed, suspended and dissolved flux, as well as non-carbonate bed, suspended and dissolved flux. To determine the total suspended fluxes, the concentration of carbonate and non-carbonate suspended sediment was multiplied by the time-series discharge and summed. The flux of dissolved carbonate and non-carbonate species was calculated based on the proven observation that the concentrations of dissolved Ca^{2+} and Mg^{2+} ions in natural waters of karst aquifers are derived almost exclusively from the dissolution of limestone and dolomite (Ford & Williams 2007). Continuous direct analysis of HCO_3^-, Ca^{2+} and Mg^{2+} was prohibitive

because of the necessity for field titration or need for countless water samples, but the YSI data sonde recorded continuous specific conductance (SpC), which was correlated to activities of dissolved carbonate species for a high-resolution record of carbon fluxes across storm events. Other dissolved ions in the aquifer system rarely exceeded 2% of the dissolved carbonate ions by mass, so the difference between the total dissolved solids (TDS) calculation from the YSI data sonde and the calculated dissolved carbonate was used as the dissolved non-carbonate component for mass removal.

Determination of bed movement from the tagged tracer tests, continuous flow measurements and sediment transport modeling yielded direct values of bed load flux for carbonate and non-carbonate, $\boldsymbol{q_{bc}}$ and $\boldsymbol{q_{bn}}$. Determination of suspended and dissolved loads from direct sampling and discharge yielded the carbonate and non-carbonate fluxes $\boldsymbol{q_{sc}}$, $\boldsymbol{q_{sn}}$ and $\boldsymbol{q_{dc}}$, $\boldsymbol{q_{dc}}$. The uncertainties in the components are derived from the measurement and analysis uncertainties of the individual methods. The total flux was then calculated by simply adding the terms:

$$q_t = \underbrace{(q_{bc} + q_{sc} + q_{dc})}_{carbonate} + \underbrace{(q_{bn} + q_{sn} + q_{dn})}_{non\text{-}carbonate} \qquad \text{(eq. 9)}$$

Evaluating significance of measured fluxes

The significance of differences in denudation calculated by total mass removal compared to dissolved carbonate mass removal can be described directly, because all six major mass-removal components are described. The calculated differences in denudation rates will help determine the validity of assumptions that fluviokarst basin evolution can be described by just the dissolved carbonate geochemistry. If differences in rate calculations are found between bedrock types, the geomorphology of the karst basin should be in disequilibrium, especially the slopes of individual lithologic outcrops.

RESULTS

Collected logger data

The record of logger data at Blowing Cave spans a period from November 10, 2012 to October 27, 2013. Both the YSI sonde and the Sontek flow meter were deployed in a perennially wet and uniform reach of the main cave stream approximately 0.8 km upstream of the lower entrance. A data gap of about seven weeks (YSI) to five weeks (Sontek) occurred during April and May, 2013 due to premature battery failure, but only two moderate storm events were missed. A graph of time-series data from the Sontek-IQ flow instrument and YSI-6910 quality sonde are shown in Figure 4.5. Although no water quality data were recorded during the gap, the gap in flow data was filled by correlating to the nearest USGS surface gauge during a storm just before the instrument failure ($r^2 = 0.98$, Appendix 2.1), as well as measurements from a staff gauge at the cave spring for which a rating curve was developed (Appendix 2.2).

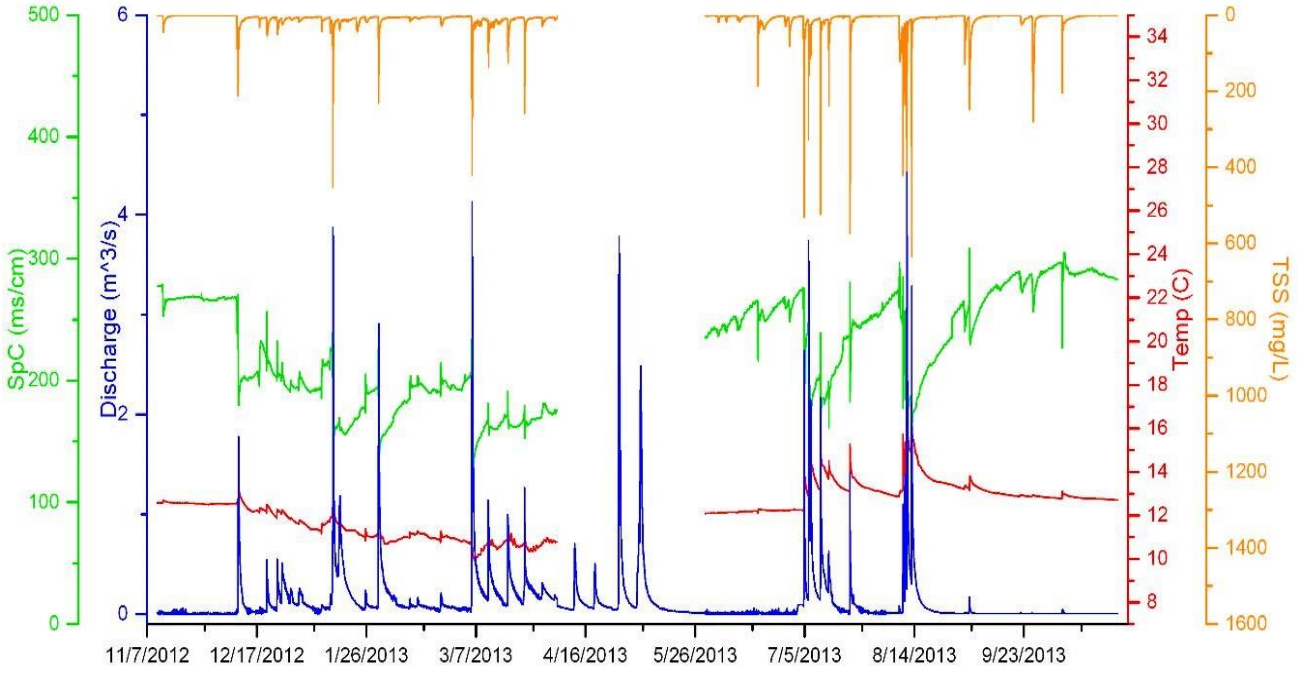

Figure 4.5: Time-series data for Blowing Cave. Discharge record is continuous from Nov. 2012 to Oct. 2013. Water quality data include two continuous runs with a 7-week gap (TSS data is reversed for clarity).

The data demonstrate a strong, rapid response to rain events and a small seasonal component of increased base flow and lower SpC and T during winter. SpC values ranged from 113–305 μS/cm, T from 9.9–17.3 °C, and pH from 7.2–8.4. Flow was extremely variable and flashy, and ranged from a low of less than 0.004 m^3/s during Fall dry season to 4.42 m^3/s at the largest storm flow that occurred in early August, 2013, a difference over three orders of magnitude. TSS was calculated from instrument data by correlating turbidity to a set of automatic water samples taken over a 24-hour period spanning the July 6 storm event. TSS typically peaked just before or at peak discharge, reaching a maximum storm value of 635 mg/l during the August 2013 event. TSS was very low between both summer and winter storms, averaging less than 12 mg/l.

Results of bed load data collection

The records of tracer cobble and gravel sizes, mass, rock type and chip IDs (where used) are listed in Appendix 2.3. These tables include the measured movement after four storm events at Blowing Cave that resulted in significant runoff in the cave stream. Grain size analysis was completed for the three Blowing Cave cross-sections using photographic and sieving methods. The results of the photographic analysis of surface bed material are shown in Figs. 4.6. The results of the sieve analysis for Blowing Cave cross-section 1 (BC XS1) are shown in Fig. 4.7. Between 250 and 500 individual bed particles were digitized in GIS from scaled field photographs of each cross section bed surface. At Blowing Cave, there is a clear progression in bed load grain size from larger particles at the upstream end (XS3) to smaller particles nearer the downstream cave outlet (XS1). The photographic analysis also allowed measurement of the approximate carbonate content of the bed load, which was needed to determine bed load carbonate flux to separate total carbonate vs. non-carbonate removal from the basin. To test carbonate content of smaller sediment fractions, the mineralogy of the sieved BC XS1 material was analyzed and showed that below

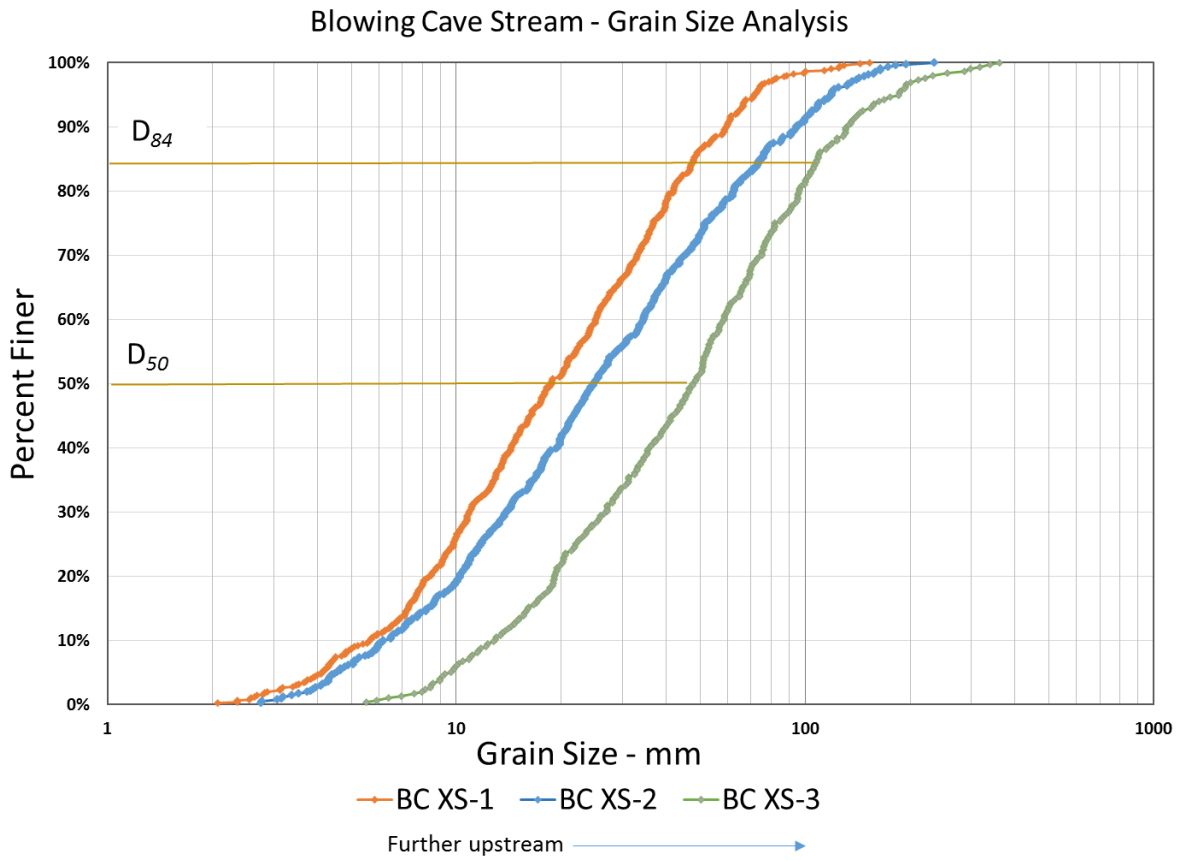

Figure 4.6: Photographic grain size analysis for the three in-cave cross-sections at Blowing Cave.

about 16 mm (-4 phi), over 98% the sediment was silicate. Similar fine bed material composition was noted by field inspection at the other BC cross sections, suggesting that dissolution of the finer carbonate fraction is relatively rapid and only the larger carbonate particles persist in bed load for any length of time at these sites. The overall bed flux was calculated based on the D_{84} grain size of bed load at each site. D_{84} is customarily used in streambed sediment studies because the size represents one standard deviation from the median grain size (Bunte & Abt 2001). Additional channel parameters needed for calculating hydraulics and running models were measured at each site. Table 4.2 lists channel morphologies, results of the grain size analysis and the results of measured carbonate percentages.

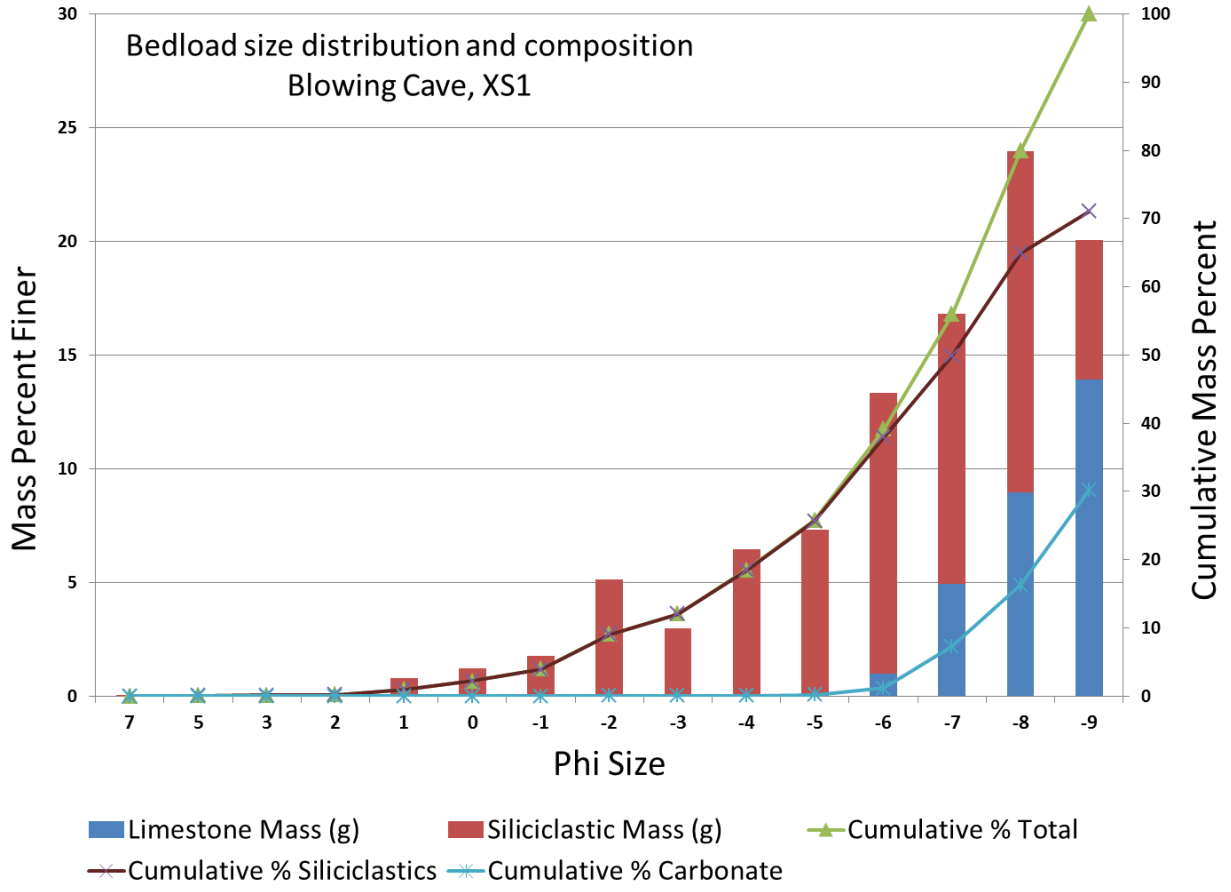

Figure 4.7: Seive analysis and carbonate composition measurement for the bed load at cross-section one in Blowing Cave.

The majority of bed load transport data were collected during 10 trips into BC to measure tagged cobble movement before and after each of four different storm events at cross-section 1: Dec. 10, 2012; Jan. 30, Apr. 28, and July 6, 2013, and the three later storm events at cross-section 2. 158 tracing cobbles and pebbles were initially placed in BC at XS1 in November 2012, and 75 at XS2 in mid-December 2012. The initial set of tracers at XS1 included 42 small cobble and pebble single-use tracers that were painted but were too small to be chipped or numbered. An additional set of 109 larger tagged cobbles were added to XS1 on Dec. 14, 2012 to replace the single-use tracers and bring the total number of long-term tracers to 170.

Table 4.2: Measured channel parameters for the three study reaches

Site ID	Active Channel Width (m)	Channel Slope (m/m)	D_{50} Grain Size (mm)	D_{84} Grain Size (mm)	% Carbonate in Bed Load	% Non-carbonate in Bed Load	Channel Classification
BC XS1 (moderate gradient site)	4.31	0.008	18	43	7%	93%	Plane bed
BC XS2 (low gradient site)	4.10	0.005	25	75	13%	87%	Pool/Riffle
BC XS3 (high-gradient site for modeling)	3.80	0.012	50	105	16%	84%	Plane bed

Increasingly larger storms were the targets of tagged bed transport measurement during the study period at BC. The December 10, 2012 storm was the first event after cobble deployment to move bed material. Because the mass, size, shape and rock types were known for all tracers (Appendix 2.3), effects of these parameters on particle movement were evaluated. At BC XS1, a mix of both carbonate (limestone and silty limestone) and non-carbonate (sandstone and chert) cobbles were tagged to determine if any significant differences existed in transport rates based on rock type. After the initial storm measurement at XS1, no clear relationship was observed between rock type and transport distance (Figs. 4.8 – 4.11), so subsequent tagged cobble deployment at BC XS2 utilized only carbonate tracers for ease of chip installation. As other storms were measured, no significant correlation was observed between mass, shape, or particle size at any of the sites. Figures 4.8 – 4.11 graph the full tagged particle transport vs particle size at BC XS1, and shows correlation between particle size vs distance traveled as regression lines. Figures 4.12 – 4.14 graph the data for BC XS2. Table 4.2 lists the results of the bed transport at each of the BC cross sections, and the full tagged transport results are listed in Appendix 2.3.

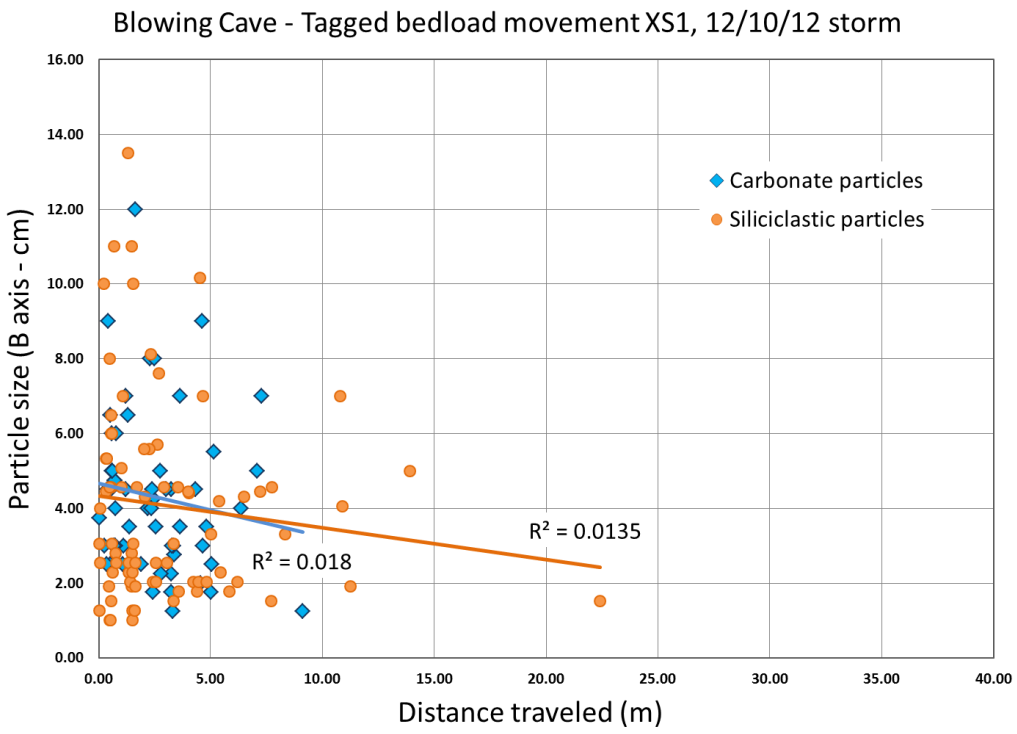

Figure 4.8: Measured movement vs size of tagged bed particles for the 12/10/12 storm event at cross-section 1 in the Blowing Cave stream channel. The correlation between distance traveled and particle size for each component are shown as regression lines.

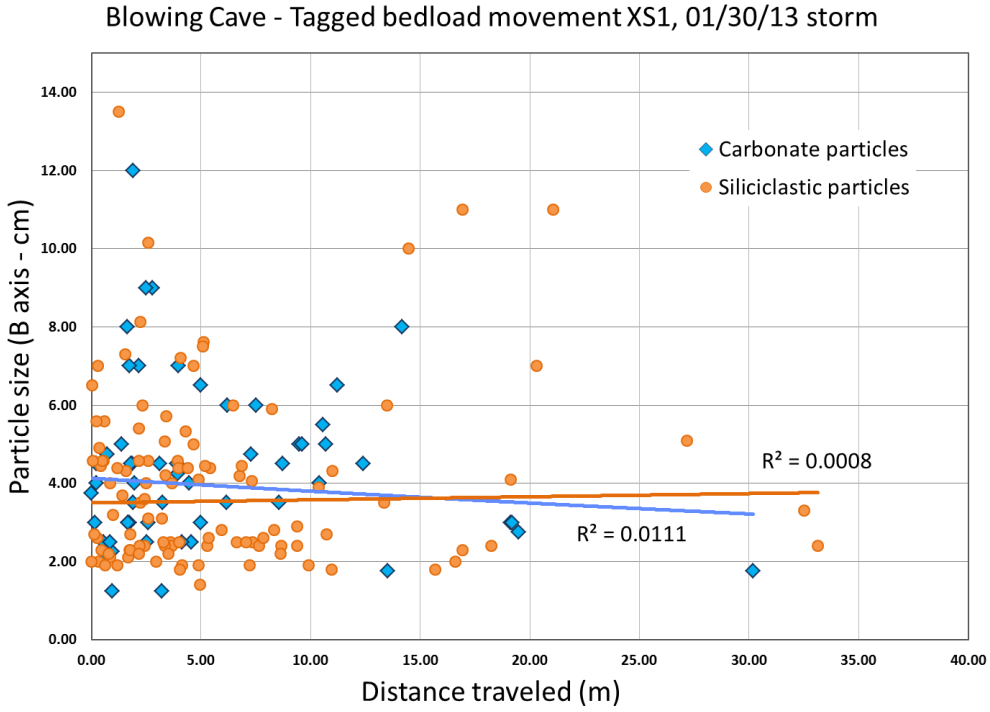

Figure 4.9: Measured movement vs size of tagged bed particles for the 1/30/13 storm event at cross-section 1 in the Blowing Cave stream channel.

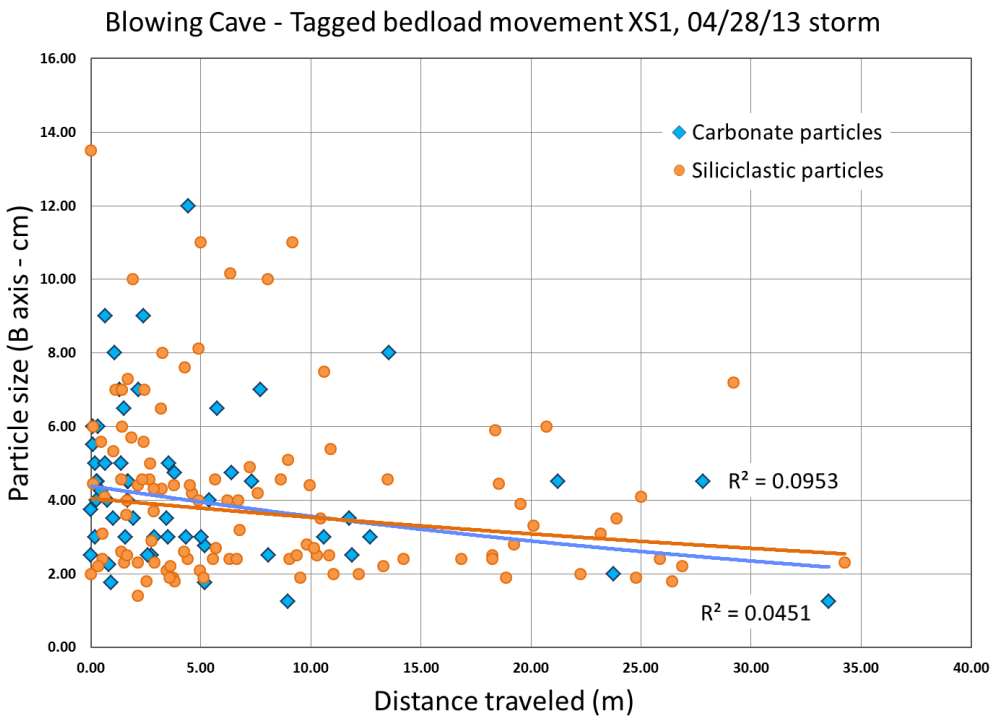

Figure 4.10: Measured movement vs size of tagged bed particles for the 4/28/13 storm event at cross-section 1 in the Blowing Cave stream channel.

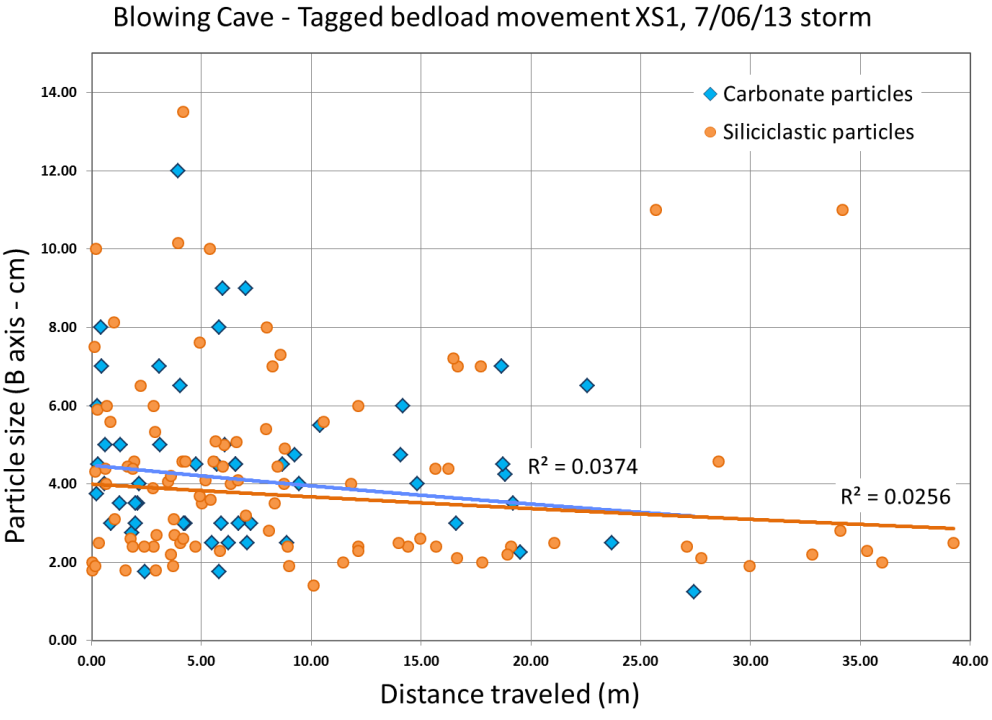

Figure 4.11: Measured movement vs size of tagged bed particles for the 7/6/13 storm event at cross-section 1 in the Blowing Cave stream channel.

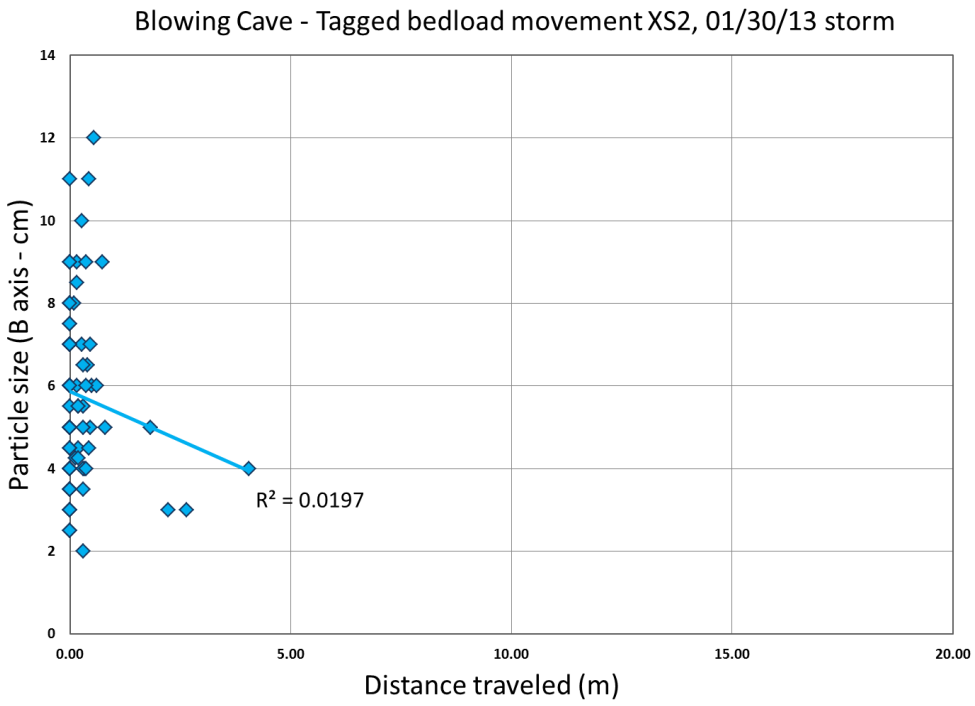

Figure 4.12: Measured movement vs size of tagged bed particles for the 1/30/13 storm event at cross-section 2 in the Blowing Cave stream channel. All particles are carbonate tracers.

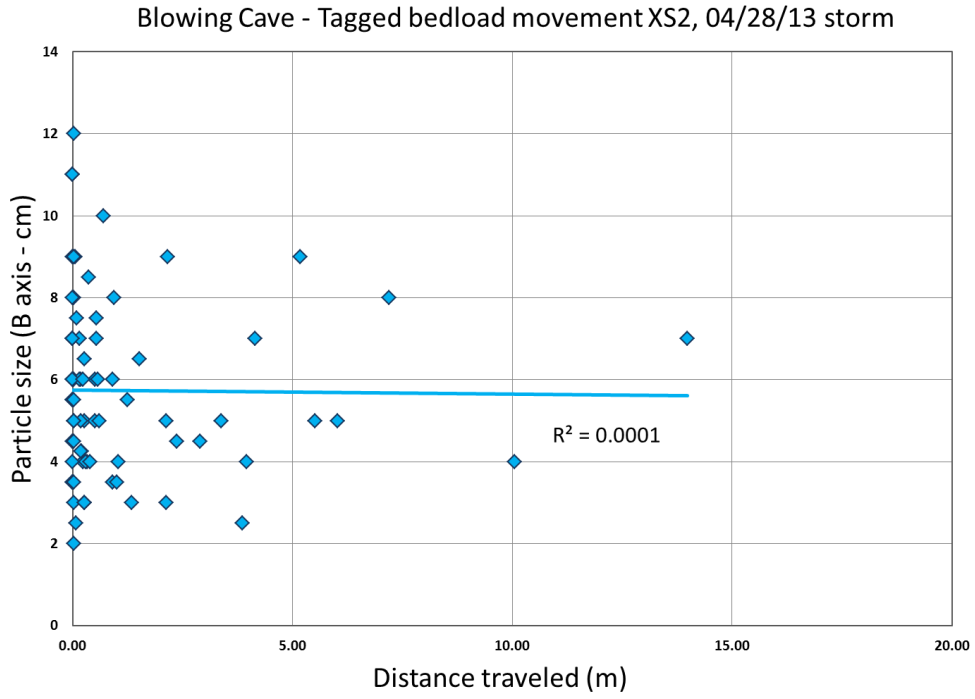

Figure 4.13: Measured movement vs size of tagged bed particles for the 1/30/13 storm event at cross-section 2 in the Blowing Cave stream channel. All particles are carbonate tracers.

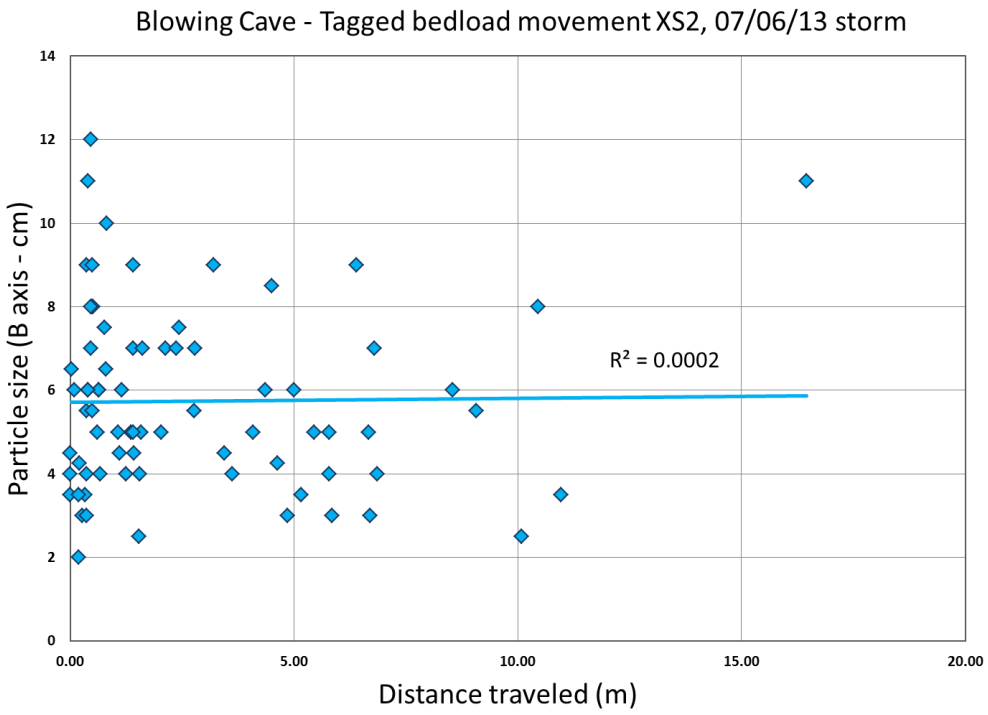

Figure 4.14: Measured movement vs size of tagged bed particles for three storm events at cross-section 2 in the Blowing Cave stream channel. All particles are carbonate tracers.

Calculating bed flux

The results for measured mass transport, continuous stream discharge, and stream channel and bed load parameters were combined to determine a total time-series PIC transport in bed material for BC and TCC. Using equation (5), unit stream power was calculated from discharge records at BC XS1,2 and 3, and TCC RZR (Figs. 2.19 – 2.22). At BC, unit stream power ranged from a low of about 0.1 W/m^2 during a drought in the Fall of 2013 to a high of 194 W/m^2 at BC XS3 during a large thunderstorm on August 11, 2013. At TCC, the karst basin's surface overflow channels only flow during large runoff events, and only one storm runoff dataset was obtained. The unit stream power at TCC RZR ranged from a low of zero before flow initiation to a high of 66.2 W/m^2 during the measured April 28, 2014 storm (Table 4.3).

Table 4.3: Tagged bed load transport results							
Site	Storm event date	Mean transport distance (m)	Carbonate mass movement per storm (kg)	Non-carbonate mass movement per storm (kg)	Peak storm discharge (m^3/s)	Peak Stream Power (W/m^2)	Duration above critical stream power (Hrs)
BC XS1 (moderate gradient site)	12/10/2012	2.86	635.2	5139.3	1.77	32.3	4.75
	1/30/2013	5.85	1769.3	10025.9	2.91	52.9	9.25
	4/28/2013	7.16	2165.2	12269.7	3.78	68.8	14.0
	7/6/2013	8.82	2677.8	15117.8	3.72	67.6	16.5
BC XS2 (low gradient site)	1/30/2013	0.28	90.8	558.8	2.91	34.8	5
	4/28/2013	1.23	454	2368.9	3.78	45.2	8.25
	7/6/2013	2.79	1035.3	5358.3	3.72	44.3	10.5

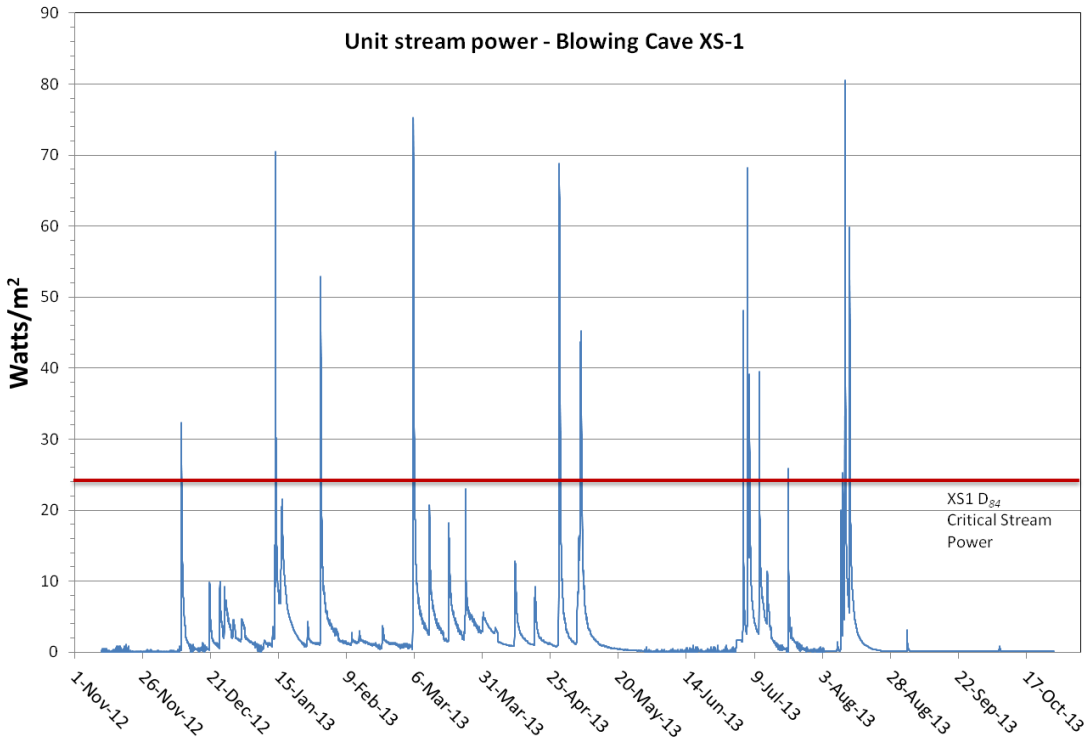

Figure 4.15: Time-series of unit stream power and the critical stream power threshold for BC XS1.

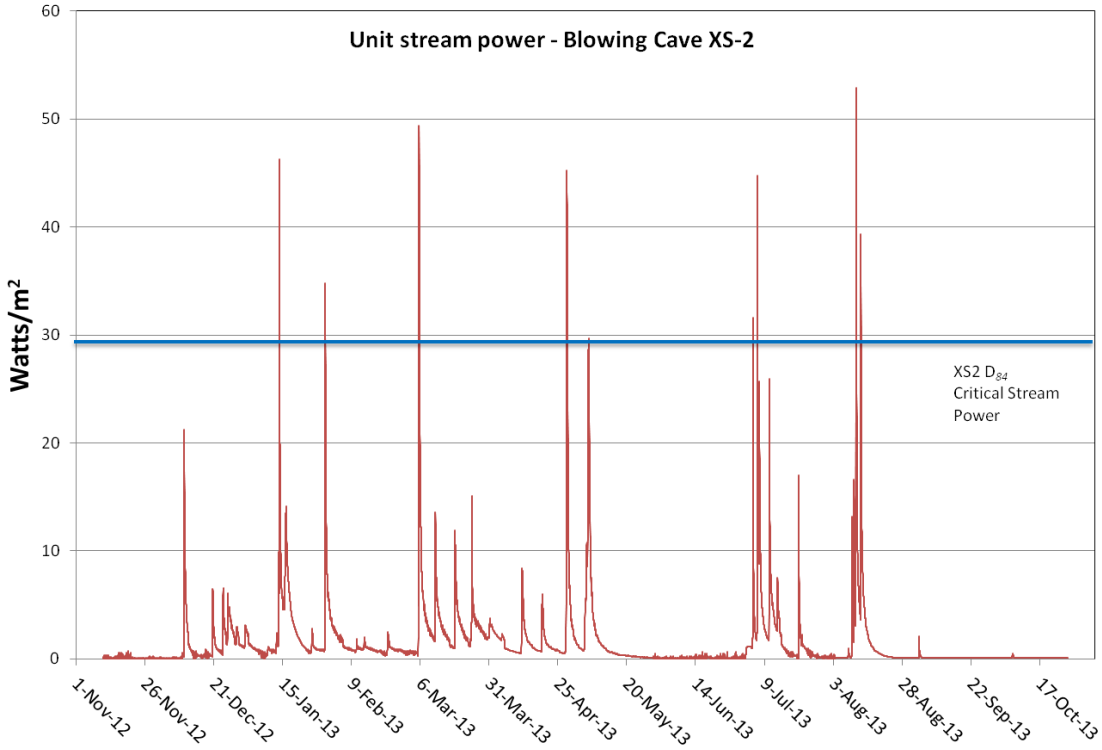

Figure 4.16: Time-series of unit stream power and the critical stream power threshold for BC XS2.

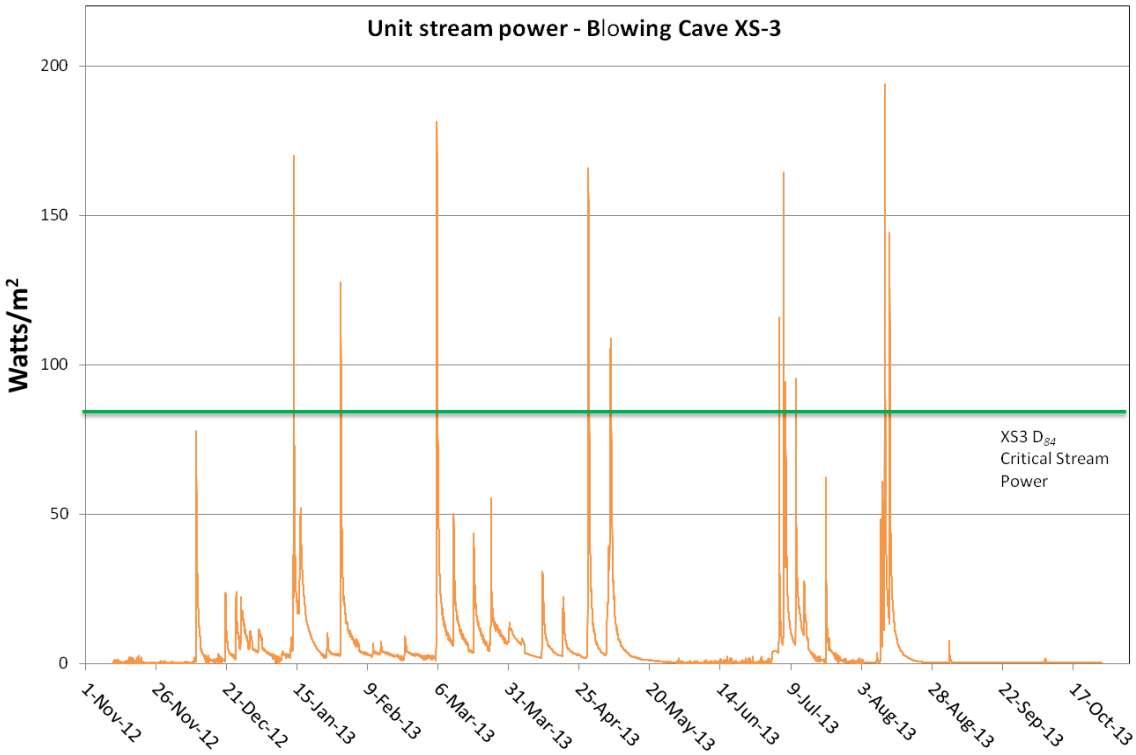

Figure 4.17: Time-series of unit stream power and the critical stream power threshold for BC XS3.

Once unit stream power was calculated for the sites, critical stream power (ω_0) for initiation of bed movement was derived by a combination of methods. Equation (7) was used to derive a critical threshold based on channel and D_{84} bed load parameters. Although the transport distance of individual cobbles measured from tagged tracers was not very sensitive to grain size overall, the initiation of total bed movement was not observed to occur until critical stream power reached a value that could move the larger bed material. Therefore, the D_{84} grain size for each reach was adopted for modeling and calibration. The initial calculations for the three cross sections overestimated ω_0 by approximately 20% to 85%, but the variety of peak storm flows and number of measured storm events allowed an accurate assessment of the critical threshold based on field observations. For instance, the December 10, 2012 storm event moved material a short distance at BC XS1, but not at XS2 or 3. Later events moved material at XS1 and 3 but not at XS2. Some smaller storm events moved no bed material at all, and only 8 storm events transported bed load at all three of the BC sections during the study period (Figs 4.15, 4.16, 4.17). Note that BC XS3 was used as a high-gradient site for modeling to incorporate the full range of channel types that occur in the BC system. Although no tagged cobbles were utilized at XS3 due to difficulty of access, all other parameters were measured, timing of bed movement observed, and calibrations from XS1 and XS2 used to make similar adjustments for XS3. From observations at all three sites, the empirical constant in equation (6) was adjusted and the calibrated results determined ω_0 for further computations (Table 4.2).

Using the time-series unit stream power and calibrated critical threshold, equation (8) derived a dimensioned mass transport at each site for each time-series interval (every 30 minutes during the study period). The model gave relatively accurate predictions of the start and end of bed transport, but initially overestimated total mass flux when compared to the results of total bed movement from the tagged tracer tests (Table 4.2) because the empirical constant in equation (7) needed fine tuning beyond the rough calibration from field observations. After fine tuning equation (7) in order to adjust the results of equation (8), modeled transport agreed closely with measured transport and a full calibrated mass flux time series was obtained (Fig 4.18). The highest bed load transport rate at BC occurred during the August 11, 2013

storm at XS3, where 1184 g/s of carbonate material and 6247 g/s of non-carbonate material was calculated at the storm peak. The movement of bed material in the BC system is highly punctuated, appearing as rapid short spikes on the time-series graph, even at log scales (Fig. 4.18). The rapid rise and fall of stream power during storm events in the system causes the critical transport threshold to be quickly passed for all grain sizes. That dynamic is reflected in the insensitivity of bed load travel distance to particle size for most storms. The short duration and intensity of these events shows the difficulty of accurately assessing sediment transport in flashy systems.

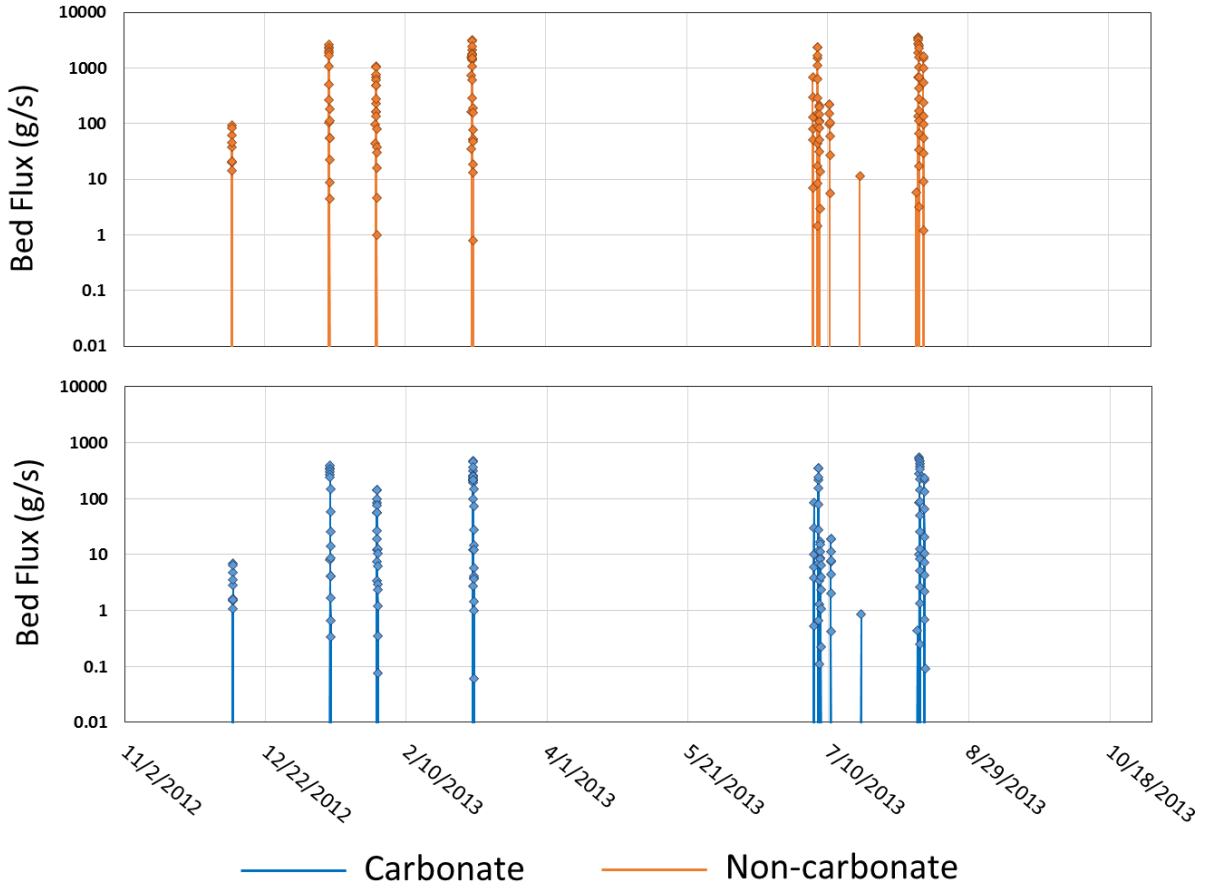

Figure 4.18: Carbonate and non-carbonate bed load flux for the Blowing Cave system. Flux is the average of three modeled cross sections representing the main channel types in the system.

Results of suspended and dissolved load data collection

In order to determine sediment flux in suspended loads at BC, three separate types of data were collected and correlated. A continuous time series record of turbidity was collected as described above. Measurements of TSS were conducted in order to convert turbidity to a time-series TSS record. The amount of carbonate in suspended sediment loads was determined for two major storm events. To correlate turbidity to TSS, 500 ml grab samples were taken every 30 minutes with an ISCO automatic sampler for a span of 12 hours over the course of the January 30, 2013 storm event. Additional low turbidity grab samples were collected manually at other times. The turbidity to TSS correlation was a linear function correction and is included in Appendix 2.4.

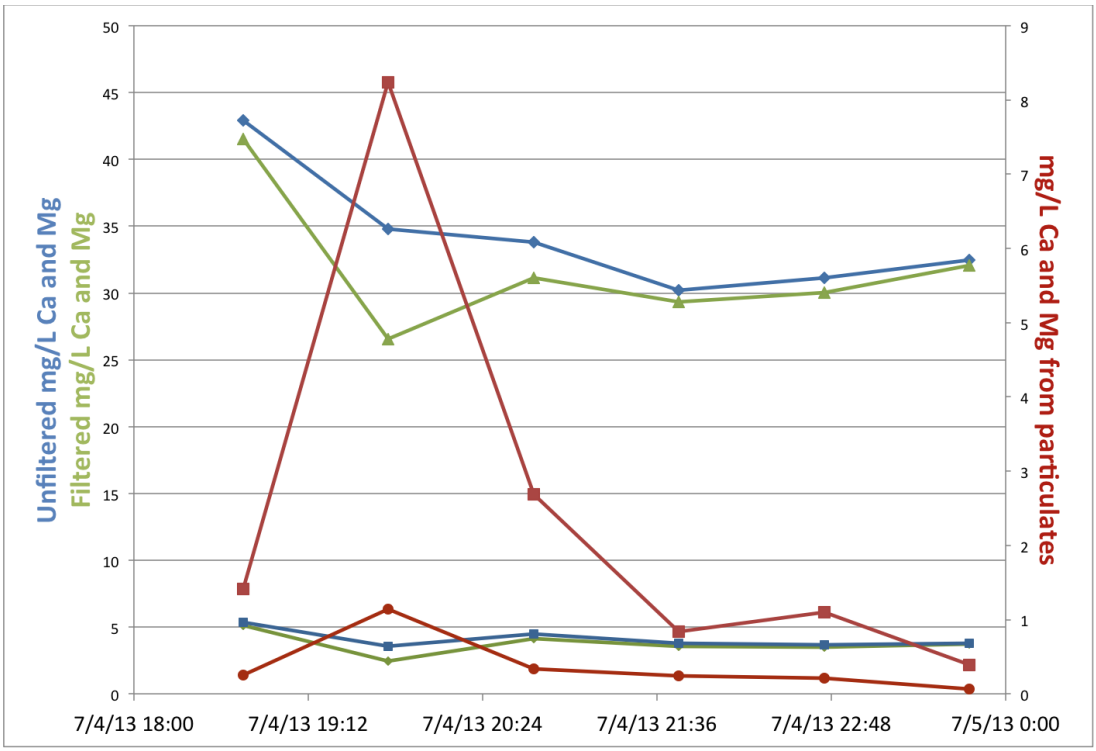

Figure 4.19: Difference in filtered vs unfiltered carbonate alkalinity for the peak of a moderate storm event at Blowing Cave.

Paired analysis of filtered/unfiltered cation samples were used to assess carbonate content in suspended sediment in order to separate bedrock sources of sediment. The precision of ICP lab analyses allowed differences of less than +/-0.5% in Ca^{2+} and Mg^{2+} to be determined in most cases. For samples collected

for regression analysis, Ca^{2+} and Mg^{2+} concentrations ranged from 32.0 – 51.2 and 2.6 – 7.3 mg/l respectively, and HCO_3^- ranged from 75.5 to 147.0 mg/l (Appendix 2.5). The results of the paired cation tests showed a spike in the carbonate time-series flux that corresponded to or immediately preceded TSS spikes (Fig. 4.19). Alkalinity titrations and cation analyses used for the paired carbonate flux measurements during storm events were also used to determine overall dissolved carbonate loads. pCO2 is accounted for in the calculation, and of the remaining dissolved carbon species, HCO_3^- was >99.2% of the total in all tested samples.

Calculating suspended flux

After correlating TSS to turbidity and calculating a time series of suspended solids discharge, a regression analysis was applied to TSS and individual suspended carbonate measurements. The analysis produced both suspended carbonate and suspended non-carbonate flux datasets (Fig. 4.20). Some significant scatter occurred in the correlation of suspended carbonate and non-carbonate sediment to discharge because peak concentrations did not always correspond to peak stream discharge. TSS typically reached a peak 15 to 45 minutes before peak storm discharge, but sometimes during and after. The resulting hysteresis between the collected data was too unpredictable to adjust easily, but did not greatly impact the overall suspended sediment flux modeling, because sampling was averaged to 30-minute intervals.

Calculating dissolved flux

Carbonate accounts for up to 98% of the dissolved mineral load at Blowing Cave. A time-series dataset was constructed for calculating regressions between SpC data and Mg^{2+}, Ca^{2+}, and HCO_3^- (Fig. 4.21; Appendix 2.6). Slopes of the regressions were all positive since higher concentrations of dissolved constituents result in higher SpC levels. The correlation coefficients for the regressions were moderately good: 0.89 for HCO_3^-, 0.81 for Ca^{2+} and 0.77 for Mg^{2+}. The regression equations were applied to the full

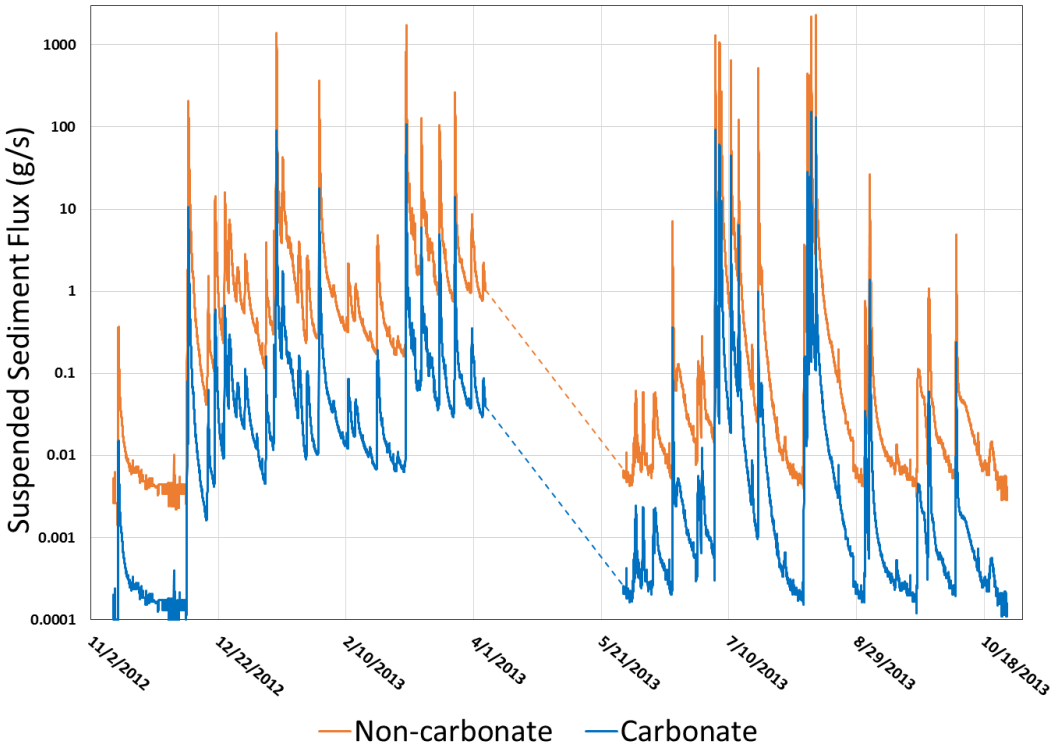

Figure 4.20: Modeled suspended sediment flux for the Blowing Cave system. Gap in modeled flux is from instrument downtime. Carbonate flux is shown in blue, non-carbonate flux in orange.

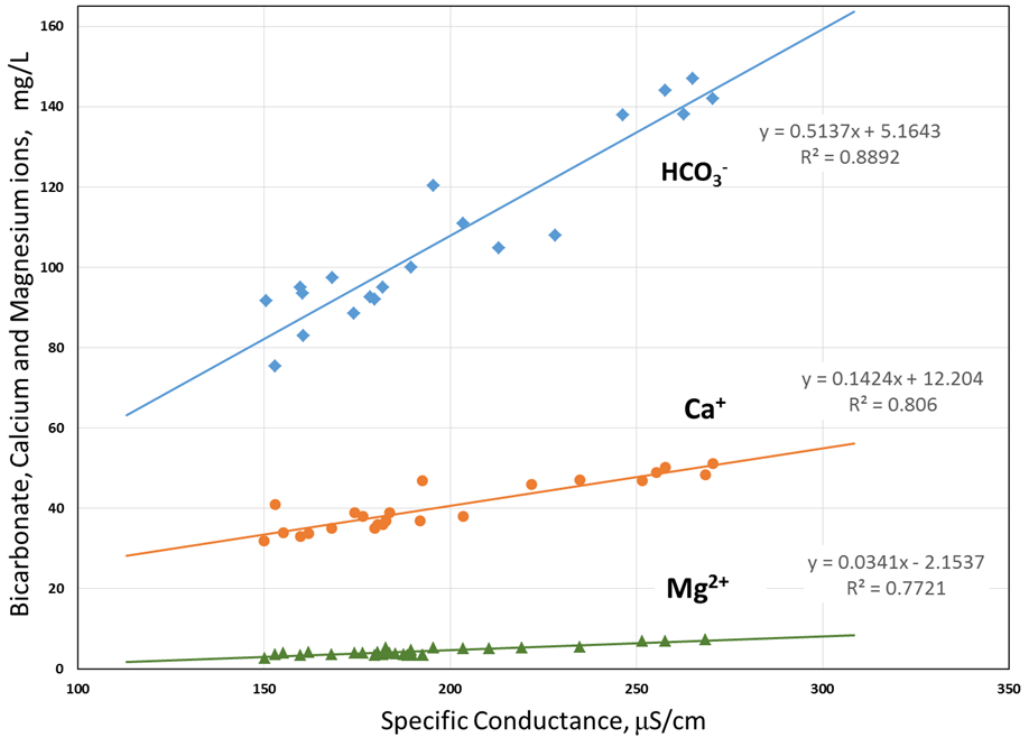

Figure 4.21: Regression analysis of Mg^{2+}, Ca^{2+}, and HCO_3^- with SpC measurements at Blowing Cave, used to construct time-series of ion concentrations from data sonde SpC time-series.

SpC dataset and the resulting 15-minute concentrations converted to mmol for analysis of ion ratios and calculation of the amount and types of carbonate bedrock dissolved. The modeled molar concentrations for HCO_3^- ranged from 1.04 to 2.68 mmol/l, Ca^{2+} from 0.49 to 1.48 mmol/l and Mg^{2+} from 0.07 to 0.34 mmol/l, tracking temporal changes to SpC. Carbonate bedrock in the BC basin consists of both limestone and dolostone, so Ca^{2+} and Mg^{2+} were compared in order to attribute the Mg^{2+} and an equal amount of Ca^{2+} to dolostone dissolution. The modeled chemistry indicates that 24.4% of the Mg^{2+} and Ca^{2+} in solution originates from dolomite dissolution. Other dissolved ions in the aquifer system rarely exceeded 2% of the dissolved carbonate ions by mass, so the calculated dissolved carbonate was subtracted from the total dissolved solids (TDS) calculation of the YSI data sonde and used as the dissolved non-carbonate component for mass removal. Results for the different modeled dissolved components produced time-series datasets for the dissolved carbonate and non-carbonate fluxes (Fig. 4.22).

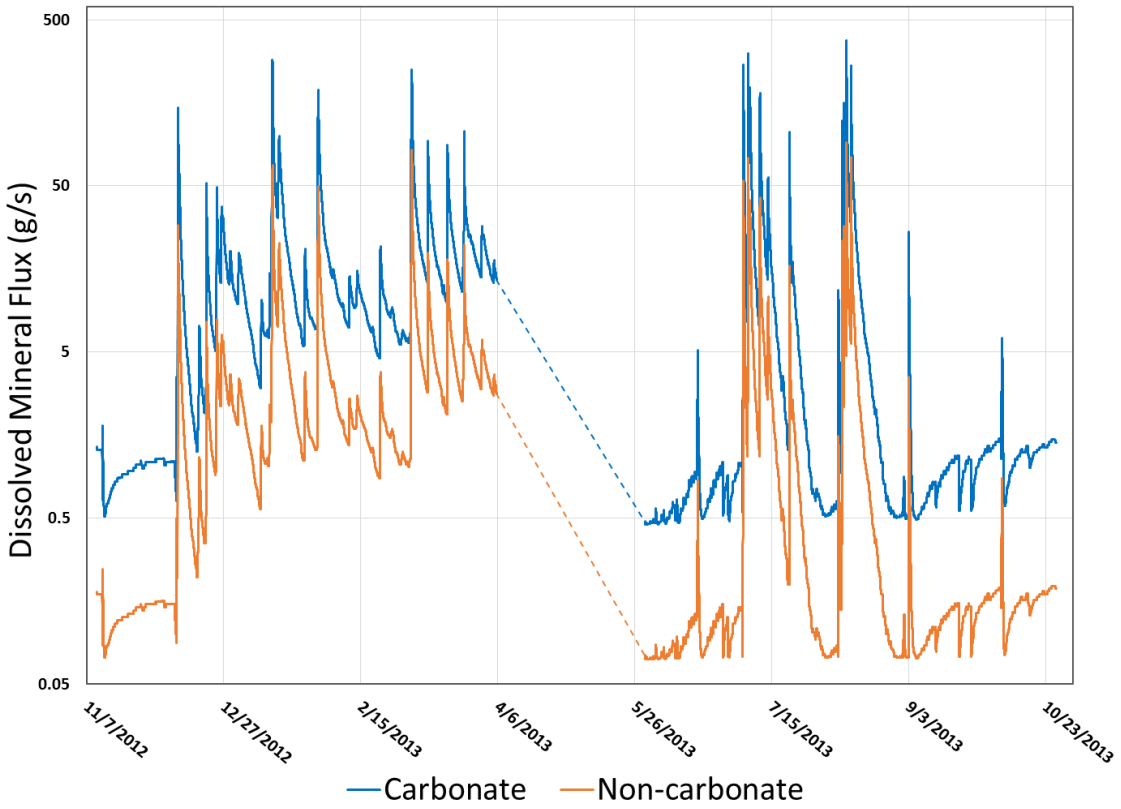

Figure 4.22: Modeled dissolved carbonate and non-carbonate fluxes for the Blowing Cave system. Gap in modeled flux is from lack of SpC logs from instrument downtime. Dissolved carbonate flux is shown in blue, dissolved non-carbonate flux in orange.

DISCUSSION

Comparing landscape denudation rates from carbonate and non-carbonate fluxes

With the separate carbonate and non-carbonate flux components completed for the basin, annual totals of removed mass were calculated and tabulated (Table 4.4). Uncertainties were calculated from the

Table 4.4: Comparison of annual carbonate and non-carbonate mass fluxes for Blowing Cave basin

Material removed	Metric tons	% of total basin load
Mass of carbonate from dissolution of limestone	255.1 +/- 8.7	31.1
Mass of carbonate from dissolution of dolostone	82.2 +/- 2.8	10.0
Mass of carbonate from suspended load	8.6 +/- 0.4	1.1
Mass of carbonate from bed load	30.2 +/- 3.3	3.7
Mass of non-carbonate from dissolution of silicates and detrital lithologies	70.1+/- 2.4	8.5
Mass of non-carbonate from suspended load	172.3 +/- 8.6	21.0
Mass of non-carbonate from bed load	202.1 +/- 15.0	24.6
Total annual carbonate mass removal	376.0 +/- 21.1	45.8
Total annual non-carbonate mass removal	444.5+/- 22.3	54.2
Annual basin mass removal	820.5 +/- 43.4	100

maximum measurement errors or analysis errors for each method, resulting in a 3.4% error for dissolved load components, a 5.0% for suspended load components, 7.4% for non-carbonate bed load and 11.0% for carbonate bed load components. The dissolution of carbonate resulted in a total of over 330 metric tons (t) of bedrock removed, with about 250 t from limestone and about 80 t from dolostone. Carbonate in suspended loads added a small but important 9 t, and carbonate removal in bed loads totaled over 30 t. Overall, 376 t of carbonate was removed for the annual period. Non-carbonate bed load added over 200 t to the total basin flux, with suspended non-carbonate load adding about 170 t. Dissolved non-carbonate consisted mostly of silica, and sulfate and iron from pyrite weathering. The dissolved non-carbonate species added about 70 t to the total basin flux. The removal of mass from the basin is highly dependent on storm events, and the study confirmed that dissolved carbonate dominates overall flux at low to moderate flow conditions. However, during storm flow, bed and suspended fluxes become more

significant, becoming the dominant mass removal components when flow rapidly increases in channels and subsurface conduits. The comprehensive set of sediment transport and carbonate geochemical data produced by this study was used to calculate comparisons of both carbonate and non-carbonate denudation rates for the Blowing Cave drainage basin and address the question of whether denudation rates differ in mixed lithologies (Table 4.5).

Table 4.5: Comparison of carbonate and non-carbonate denudation rates for Blowing Cave basin

Material removed	metric tons	% of overall basin total	Area underlain by bedrock type (km^2)	Calculated denudation rate for outcrop area (mm/ka)
Total annual carbonate removal (from Table 4.4)	376.0 +/- 21.1	45.8	2.31	60.1 +/- 3.3
Total annual non-carbonate removal (from Table 4.4)	444.5+/- 22.3	54.2	3.95	41.7 +/- 2.1
All material	820.5 +/- 43.4	100	6.26	48.5 +/- 2.5 (area averaged rate)

The landscape denudation rate at BC based only on the carbonate removal and area of carbonate bedrock in the basin was over 60 mm/ka, which is somewhat faster than related studies for similar areas (e.g., Sasowsky et al. 1995; Granger et al. 2001). The BC basin lies in a high-relief region with average annual rainfall of 1423 mm/yr (National Weather Service 2016), so the high rate is reasonable. A similar recent mass-balance study conducted a few miles from the BC basin (Florea 2015) yielded much slower rates for carbonate denudation, reporting a maximum of 17.9 mm/ka. However, those results may be low because of a combination of underestimated storm flow, a relatively dry water year, and lack of data for mechanical carbonate removal. The denudation rate based on removal of non-carbonate material in the BC basin was 41.7 mm/ka, over 30% slower than the carbonate rate, suggesting that assumption of equilibrium between bedrock types is not valid in mixed-lithology fluviokarst.

Lithologic control on denudation and geomorphology

With a disparity of over 30% in denudation rates from different lithologic units in the study area, the geomorphology of the basin was investigated to determine if there is geomorphic evidence of

disequilibrium. A GIS analysis of lithologic outcrop area, average slopes, corrected surface areas and unit composition and thicknesses was completed for the basin. The results of the analysis are shown in Table 4.6. The study area is underlain by 2.31 km^2 carbonate and 3.95 km^2 non-carbonate lithologies, when map outcrop areas are adjusted to account for sloping surfaces. Average slope for the various lithologies ranged from a low of about 5 degrees for Quaternary valley fill deposits to over 60 degrees for the cliff-

Table 4.6: Area and slopes of Blowing Cave Basin lithologic units

Unit:	Map Area (m^2)	Avg Slope angle (°)	Surface area adjusted for slope (m^2)	Average unit thickness (m)	Expected mode of erosion
Quaternary alluvium	115416	4.88	115835	59	Mechanical/Runoff
St. Louis and St. Genevieve Limestone	180486	18.26	190056	38	Dissolution and block creep
Kidder Limestone	1423100	11.4	1451741	6	Dissolution
Hartselle Sandstone	540369	6.81	544208	15	Mechanical/Runoff and Block Creep
Bangor Limestone	655854	10.16	666302	22	Dissolution
Pennington Shale	1012094	12.42	1036347	63	Mechanical/Runoff
Breathitt Fm (Sandstone and siltstone)	1723708	32.15	1889042	34	Mechanical/Runoff and Block fall and creep
Rockcastle Conglomerate	210741	64.96	367050	59	Mechanical/Block fall and creep
	5.16 km^2 Total Area	14.8° = Average carbonate slope 30.5° = Average non-carbonate slope	6.26 km^2 Total Adjusted Area	237 m Total Section Thickness	

forming Rockcastle Conglomerate at the top of the stratigraphic section. Figure 4.23 shows a plan view of the Blowing Cave basin with geology and slopes. The steepest parts of the surface are generally at the edges of the eroded valley, where resistant siliciclastic caprock of the Cumberland Plateau is retreating by headward erosion processes. The gentlest slopes occur in both the easily eroded shales such as the Pennington shale, as well as on thin resistant units like the Hartselle sandstone that are contained within

carbonates and forms flat, resistant benches as a result. Lithologic controls on landscape from bedrock variations have been a focus of increased study recently. Forte et al. (2016) looked specifically at how varying rocks strengths (and erodibility) strongly controlled complex denudation scenarios depending on order of the units and their orientation (dipping vs. flat-lying). Specifically, they found that steady-state denudation conditions are unlikely to develop in landscapes with significant contrasts in rock strength. Similarly, it is unlikely that steady-state denudation will develop across a basin with significant contrasts in erosion process such as dissolution of carbonate vs. mechanical erosion of non-carbonate.

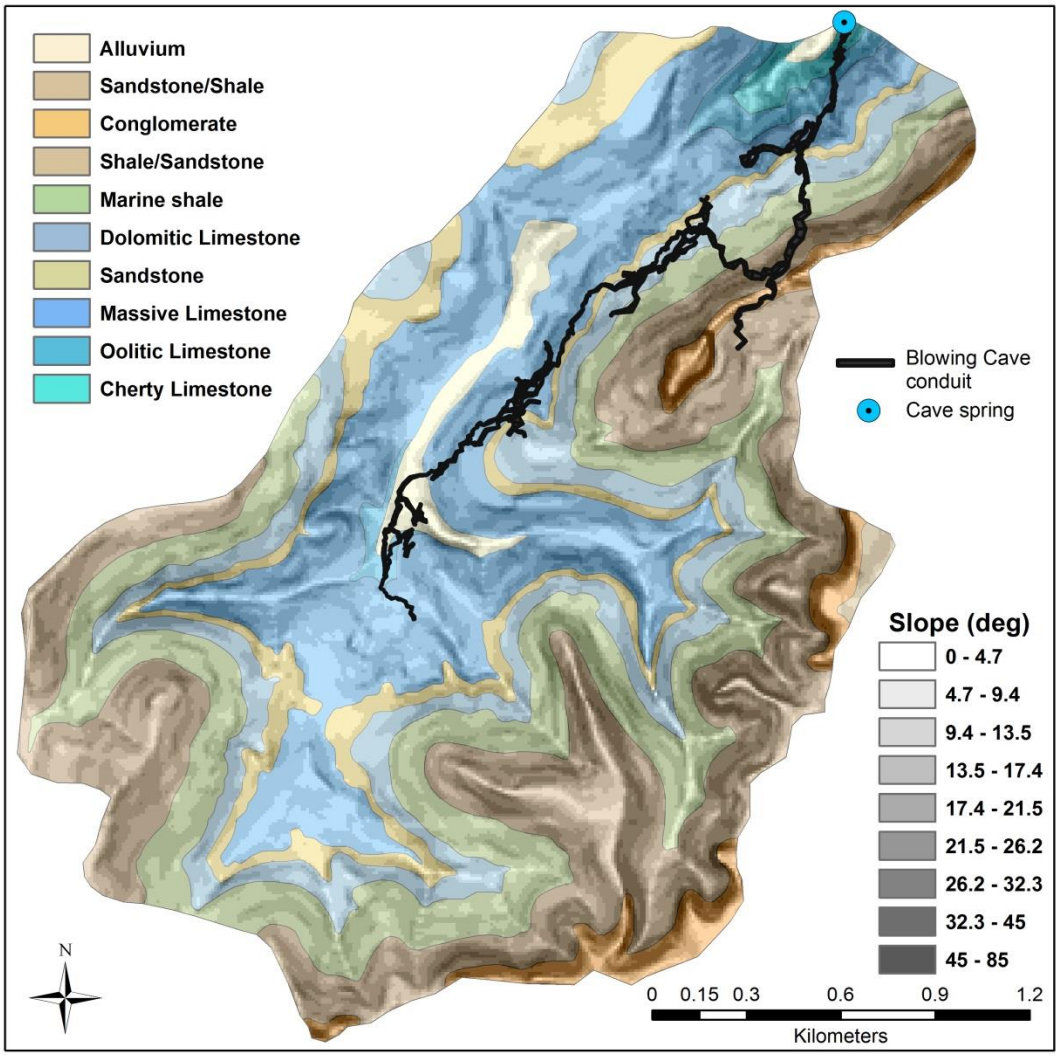

Figure 4.23: Plan view of the Blowing Cave basin showing surface slopes, lithologies, and the location of mapped cave passages and the base-level spring draining the catchment (adapted from Lewis 1977).

The average slope for all carbonate units in the Blowing Cave basin is 14.8°, normalized by outcrop area, and the average slope for all non-carbonate units is 30.5°. Figure 4.24 shows an idealized stratigraphic section of the geology underlying the basin, and graphically represents the average slope of each lithology within the basin, with a 2X exaggeration. Denudation rates on the different stratigraphic units are in disequilibrium, and that can clearly be seen by the large variations in slopes. Likewise, when looking at the carbonate outcrops vs. the non-carbonate outcrops as a whole, the carbonate bedrock is in disequilibrium with the non-carbonate units, mirroring the difference in mass removal from each bedrock type.

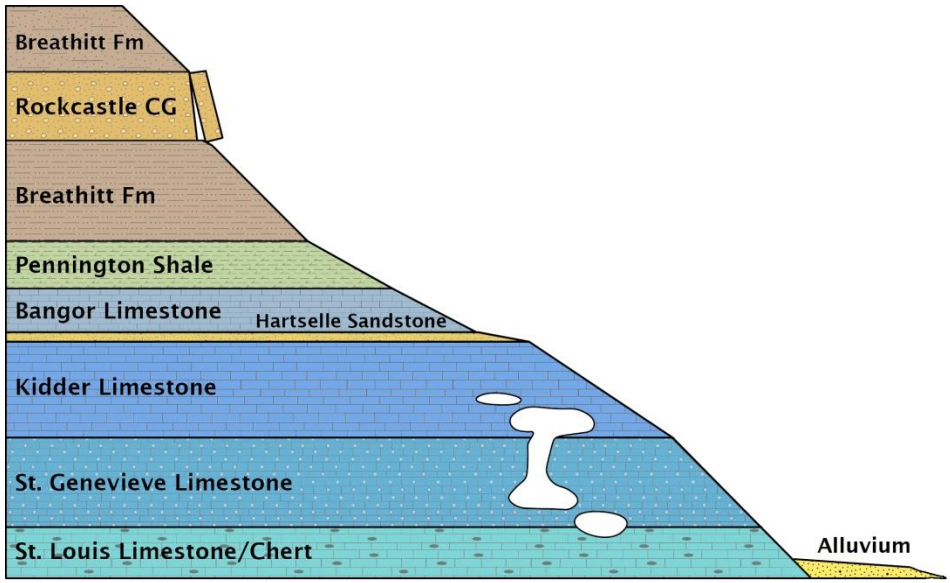

Figure 4.24: Idealized stratigraphic section of the Blowing Cave Basin lithology, representing the average slope of each unit within the karst drainage basin. The total section thickness is 237 meters, and the slopes in the figure are exaggerated 2 times. An idealized representation of the main Blowing Cave conduit levels is also shown.

Implications for age of cave passages

As landscape denudation progresses and valleys are incised over time, subsurface stream conduits that route water to base-level springs can be abandoned as the water finds lower routes to spring outlets. Abandoned subsurface stream passages can be recognized by infillings of imbricated and rounded cobbles and pebbles, and such passages occur at high levels in the Blowing Cave system (schematically shown in

Fig. 4.24). The vertical difference between the highest abandoned stream passage and the active subsurface stream gives a measure of the amount of landscape lowering for the basin while the cave was developing. The total vertical extent between the highest dry stream tube and the active stream in Blowing Cave is approximately 47 meters. Using the calculated average denudation rate for the basin of 48.5 +/-2.5 mm/ka, the approximate age of the highest cave level ranges between 920,000 and 1,020,000 years. This age represents the approximate time in the past that the main limestone unit in the valley captured allogenic runoff as the escarpment was retreating and lowering. The time generally corresponds to the most recent regional terrace level abandoned by the nearby Cumberland River incision and dated by cosmogenic isotopes from neighboring Cumberland Plateau cave passages (Anthony & Granger 2007).

Limitations and further work

One of the most significant limitations in the data collected is related to the rarity of large storm events. Although 11 events moved bed load and many smaller storm events increased TSS, there is evidence that larger infrequent storms (<2 events/decade return period) radically increase removal of sediment from the system. The denudation rate, especially for non-carbonate components, may be different if large, rare flood events were better characterized. A more comprehensive and longer study would be necessary to capture this type of flow event. Past differences in climate may also have driven important differences in denudation rates, affecting the calculations for age of cave passages. For future studies, incorporating past climate and estimated precipitation changes would yield more robust landscape ages based on denudation. Direct age dating of stream sediments in abandoned cave passages using cosmogenic isotope ratios would be extremely valuable as a test of the accuracy of denudation calculations and estimated landscape age.

CONCLUSIONS

Captured data gave denudation rates for both the carbonate and non-carbonate components of the basin, and the rates are somewhat higher than similar studies for the local area. For this study, rates were derived from both the carbonate dissolved load method and total sediment load/dissolved load method at Blowing

Cave basin. A denudation rate of 60.3 mm/ka was calculated for the 2.31 km2 carbonate outcrop surface of the basin, and a rate of 41.7 mm/ka was calculated for the 3.95 km2 surface of non-carbonate outcrop area. The basin average rate of landscape denudation (aggregating both carbonate and non-carbonate areas) was 48.5 mm/ka. At Blowing Cave basin, denudation rates for carbonate and non-carbonate outcrop areas are not in equilibrium. These rate differences are reflected in the evolution of the basin, which has developed by steep-walled escarpment retreat along with piracy of allogenic runoff into well-developed karst conduits. Landscape evolution in fluviokarst settings is more complex than can be measured by solute load analysis alone, and complete mass flux measurement of all erosion components will help improve future studies.

REFERENCES

Aguirre-Pe, J., Olivero, M.L. & Moncada, A.T., 2003. Particle densimetric Froude number for estimating sediment transport. *Journal of Hydraulic Engineering-Asce*, 129(6), pp.428–437.

Almedeij, J.H., 2002. *Bedload transport in gravel-bed streams under a wide range of Shields stresses*. PhD Dissertation, Virginia Polytechnical Institute.

Anthony, D.M. & Granger, D.E., 2007. An empirical stream power formulation for knickpoint retreat in Appalachian Plateau fluviokarst. *Journal of Hydrology*, 343(3–4), pp.117–126.

Aubert, D., 1969. Phenomenes et formes du karst jurassien. *Eclogae Geologicae Helvetiae*, 62(2), pp.325–399.

Bagnold, R.A., 1977. Bed load transport by natural rivers. *Water Resources Research*, 13(2), p.303.

Bakalowicz, M., 1979. *Contribution de la géochimie des eaux à la connaissance de l'aquifère karstique et de la karstification*. Univ. P. etM. Curie, Paris.

Barry, J.J. et al., 2006. Performance of bed load transport equations in mountain gravel-bed rivers: a re-analysis. In *PROCEEDINGS of the Eighth Federal Interagency Sedimentation Conference (8thFISC), April2-6, 2006, Reno, NV, USA*. pp. 90–97.

Bosch, R.F. & White, W.B., 2007. Lithofacies and transport of clastic sediments in karstic aquifers. In I. D. Sasowsky & J. Mylroie, eds. *Studies of Cave Sediments: Physical and Chemical Records of Paleoclimate*.

Buffington, J.M. & Montgomery, D.R., 1997. A systematic analysis of eight decades of incipient motion studies, with special reference to gravel-bedded rivers. *Water Resources Research*, 33(8), pp.1993–2029.

Bunte, K. & Abt, S.R., 2001. Sampling Surface and Subsurface Particle-Size Distributions in Wadable Gravel- and Cobble-Bed Streams for Analyses in Sediment Transport, Hydraulics, and Streambed Monitoring, U.S. Forest Service, Technical Report RMRS-GTR-74, 428 p.

Cheng, Z. & Daoxian, Y., 2002. *Karst Processes and the Carbon Cycle: Final Report of ICGP379*, Beijing, China: Geological Publishing House.

Church, M. & Hassan, M.A., 1992. Size and distance of travel of unconstrained clasts on a streambed. *Water Resources Research*, 28(1), pp.299–303.

Crawford, N.C., 1996. *The Karst Hydrogeology of the Cumberland Plateau Escarpment of Tennessee* Pt. 4, Report of Investiagations no. 44, Tennessee Division of Geology.

Dogwiler, T. & Wicks, C.M., 2004. Sediment entrainment and transport in fluviokarst systems. *Journal of Hydrology*, 295(1–4), pp.163–172.

Dreybrodt, W. & Eisenlohr, L., 2000. Limestone dissolution rates in karst environments. In A. Klimchouk et al., eds. *Speleogenesis and Evolution of Karst Aquifers*. Huntsville, AL: National Speleological Socieity, pp. 136–148.

Edwards, T.K. & Glysson, G.D., 1999. Field methods for measurement of fluvial sediment-Review. In *U.S. Geological Survey Techniques of Water-Resources Investigations, book 3, chapter C2*.

Farrant, A.R. & Smart, P.L., 2011. Role of sediment in speleogenesis; sedimentation and paragenesis. *Geomorphology*, 134, pp.79–93.

Ferguson, R.I., 2005. Estimating critical stream power for bedload transport calculations in gravel-bed rivers. *Geomorphology*, 70(1–2), pp.33–41.

Ferguson, R.I. & Hoey, T.B., 2002. Long-term slowdown of river tracer pebbles: Generic models and implications for interpreting short-term tracer studies. *Water Resources Research*, 38(8), pp.11–17.

Ferguson, R.I. & Wathen, S.J., 1998. Tracer-pebble movement along a concave river profile : Virtual velocity in relation to grain size and shear stress transport and deposition. *Water Resources Research*, 34(8), pp.2031–2038.

Florea, L.J., 2015. Carbon flux and landscape evolution in epigenic karst aquifers modeled from geochemical mass balance. *Earth Surface Processes and Landforms, 1072-1087*.

Ford, D. & Williams, P.D., 2007. *Karst Geomorphology and Hydrology*, London: Unwin Hyman, 576 p.

Forte, A.M., Yanites, B.J. & Whipple, K.X., 2016. Complexities of landscape evolution during incision through layered stratigraphy with contrasts in rock strength. *Earth Surface Processes and Landforms*, 41, pp.1736–1757.

Gabrovšek, F., 2009. On concepts and methods for the estimation of dissolutional denudation rates in karst areas. *Geomorphology*, 106(1–2), pp.9–14.

Gams, I., 2004. *Kras v Sloveniji v prostoru in času*, Ljubljana: ZRC Publishing.

Gombert, P., 2002. Role of karstic dissolution in global carbon cycle. *Global and Planetary Change*, 33(1–2), pp.177–184.

Graham, D.J., Rice, S.P. & Reid, I., 2005. A transferable method for the automated grain sizing of river gravels. *Water Resources Research*, 41(7), pp.1–12.

Granger, D.E., Fabel, D. & Palmer, A.N., 2001. Pliocene - Pleistocene incision of the Green River, Kentucky, determined from radioactive decay of cosmogenic ^{26}Al and ^{10}Be in Mammoth Cave sediments. *Bulletin of the Geological Society of America*, 113(7), pp.825–836.

Groves, C. & Meiman, J., 2001. Inorganic Carbon Flux and Aquifer Evolution in the South Central Kentucky Karst. U.S. Geological Survey Karst Interest Group Proceedings, St. Petersburg, Florida, pp.99–105.

Groves, C. & Meiman, J., 2005. Weathering, geomorphic work, and karst landscape evolution in the Cave City groundwater basin, Mammoth Cave, Kentucky. *Geomorphology*, 67(1–2 SPEC. ISS.), pp.115–126.

van Gundy, J.J. & White, W.B., 2009. Sediment flushing in Mystic Cave, West Virginia, USA, in response to the 1985 Potomac Valley flood. *International Journal of Speleology*, 38(2), pp.103–109.

Gunn, J., 1981. Limestone solution rates and processes in the Waitomo district, New- Zealand. *Earth Surface Processes and Landforms*, 6, pp.427–445.

Hajna, N.Z. & Mihevc, A., 2008. Karst Sediments. In N. Z. Hajna & A. Mihevc, eds. *16th International Karstological School*.

Hassan, M. A., Church, M. & Ashworth, P.J., 1992. Virtual rate and mean distance of travel of individual clasts in gravel-bed channels. *Earth Surface Processes and Landforms*, 17(6), pp.617–627.

Herman, E.K., Toran, L. & White, W.B., 2008. Threshold events in spring discharge: Evidence from sediment and continuous water level measurement. *Journal of Hydrology*, 351(1–2), pp.98–106.

Holmes, R.R. & Holmes, R.R.J., 2010. Measurement of bedload transport in sand-bed rivers: A look at two indirect sampling methods. *US Geological Survey Scientific Investigations Report*, (1914), pp.236–252.

Jennings, J.N., 1972. The Blue Waterholes, Cooleman Plain, NSW: the problem of karst denudation rate determination. *Transactions of the Cave Research Group of Great Britain*, 14, pp.109–117.

Kaufmann, G., 2003. Karst landscape evolution. In *Evolution of Karst: From Prekarst to Cessation*, Grabovsek, F. (ed.). Postojna-Ljubljana Zalozba ZRC, pp.243–258.

Kaufmann, G. & Braun, J., 2001. Modelling karst denudation on a synthetic landscape. *Terra Nova*, 13(1984), pp.313–320.

Kunaver, J., 1979. Some experiences in measuring the surface karst denudation in high Alpine environments. In *Actes du symposium international sur l'erosion karstique*. Aix-en-Provence-Marseille-Nimes: UIS, Commision de erosion du karst, pp. 75–85.

Laronne, J.B. & Carson, M.A., 1976. Interrelationships between bed morphology and bed-material transport for a small, gravel-bed channel. *Sedimentology*, 23(1), pp.67–85.

Lauritzen, S.-E., 1990. Autogenic and allogenic denudation in carbonate karst by the multiple basin method: an example from Svartisen, north Norway. *Earth Surface Processes and Landforms*, 15, pp.157–161.

Lewis, R.Q., 1977. Geologic map of the Powersburg quadrangle and part of the Pall Mall quadrangle, Wayne and Clinton Counties, Kentucky. U.S. Geological Survey 7.5-minute geologic map, p.1.

Liu, Z. et al., 1997. Contribution of Carbonate Rock Weathering to the Atmospheric CO2 Sink. *Environmental Geology*, 39(9), pp.1053–1058.

Lorang, M.S. & Hauer, F.R., 2003. Flow competence and streambed stability: an evaluation of technique and application. *Journal of the North American Benthological Society*, 22(4), pp.475–491.

Mahler, B.J. & Lynch, F.L.L., 1999. Muddy waters: temporal variation in sediment discharging from a karst spring. *Journal of Hydrology*, 214(1–4), pp.165–178.

Martin, J.B. & White, W.B., 2008. *Frontiers in Karst Research* J. B. Martin & W. B. White, eds.,

Martin, Y., 2003. Evaluation of bed load transport formulae using field evidence from the Vedder River, British Columbia. *Geomorphology*, 53(1–2), pp.75–95.

Martin, Y. & Church, M., 2000. Re-examination of Bagnold's empirical bedload formulae. *Earth Surface Processes and Landforms*, 25(9), pp.1011–1024.

Massei, N., Wang, H.Q., Dupont, J.P., Rodet, J., Laignel, B., 2003. Assessment of direct transfer and resuspension of particles during turbid floods at a karstic spring. *Journal of Hydrology*, 275,

pp.109–121.

Miller, T.E., 1982. *Hydrochemistry, hydrology and morphology of the Caves Branch karst, Belize*. PhD Dissertation, McMaster University.

National Weather Service, 2016. National Weather Service Climate Summaries. *NOWData - NOAA Online Weather Data*. Available at: http://w2.weather.gov/climate/xmacis.php?wfo=ohx [Accessed August 2, 2016].

Newson, M.D., 1971. A Model of subterranean limestone erosion in the British Isles based on hydrology. *Transactions of the Institute of British Geographers*, 54, pp.55–70.

Nichols, M.H., 2004. A radio frequency identification system for monitoring coarse sediment particle displacement. *Applied Engineering in Agriculture*, 20(6), pp.783–787.

Ogden, A.E., 1982. Karst denudation rates for selected spring basins in West Virginia. *NSS Bulletin*, 44, pp.6–10.

Palmer, A.N., 2007. *Cave Geology*, Dayton, Ohio: Cave Books, p.454.

Peterson, E.W. & Wicks, C.M., 2003. Characterization of the physical and hydraulic properties of the sediment in karst aquifers of the Springfield Plateau, Central Missouri, USA. *Hydrogeology Journal*, 11(3), pp.357–367.

Pitty, A.F., 1968. The scale and significance of solutional loss from the limestone tract of the southern Pennines. *Proceedings of the Geologist's Association*, 79(2), pp.153–177.

Plan, L., 2005. Factors controlling carbonate dissolution rates quantified in a field test in the Austrian alps. *Geomorphology*, 68, pp.201–212.

Pronk, M. et al., 2009. Percolation and particle transport in the unsaturated zone of a karst aquifer. *Ground Water*, 47(3), pp.361–369.

Reid, I.A. & Frostick, L.E., 1984. Particle interaction and its effect on the thresholds of initial and final bedload motion in coarse alluvial channels. In E. H. Koster & R. J. Steel, eds. *Sedimentology of Gravels and Conglomerates*. Canadian Society of Petroleum Geologists, pp. 61–68.

van Rijn, L.C., 1985. Sediment transport, part 1: bed load transport. *Journal of Hydraulic Engineering*, 110(10), pp.1431–1456.

Rossman, N.R., 2010. *Entrainment and transport of coarse stream bed material in a fluviokarst watershed, south-central Missouri: a tracer particle study*. Master's thesis, University of Missouri.

Sasowsky, I.D. & Mylroie, J., 2007. *Studies of Cave Sediments: Physical and Chemical Records of Paleoclimate* 2nd ed. p.329.

Sasowsky, I.D., White, W.B. & Schmidt, V.A., 1995. Determination of stream-incision rate in the Appalachian plateaus by using cave-sediment magnetostratigraphy. *Geology*, 23(5), pp.415–418.

Shields, a, 1936. Anwendung der Aehnlichkeitsmechanik und der Turbulenzforschung auf die Geschiebebewegung. *Technology*, p.26.

Shopov, Y. et al., 2009. Past Annual Variations of the Karst Denudation Rates. *Karst, Climate Change and Groundwater*, (1), pp.487–492.

Smith, D.I., 1972. The solution of limestone in an Arctic environment. In D. E. Sugden, ed. *Polar Geomorphology*. Institute of British Geographers, pp. 187–200.

Sweeting, M.M., 1966. The weathering of limestones. In G. H. Dury, ed. *Essays in Geomorphology*. London: Heinemann, pp. 177–210.

Turowski, J.M., Badoux, A. & Rickenmann, D., 2011. Start and end of bedload transport in gravel-bed streams. *Geophysical Research Letters*, 38(4), p.5.

De Waele, J., Plan, L. & Audra, P., 2009. Recent developments in surface and subsurface karst geomorphology: An introduction. *Geomorphology*, 106(1–2), pp.1–8. Available at: http://dx.doi.org/10.1016/j.geomorph.2008.09.023.

Wathen, S.J., Hoey, T.B. & Werritty, A., 1997. Quantitative Determination of the Activity of Within-Reach Sediment Storage in a Small Gravel-Bed River Using Transit Time and Response Time. *Geomorphology*, 20(1–2), pp.113–134.

White, W.B., 2000. Dissolution of limestone from field observations. In A. B. Klimchouk et al., eds. *Speleogenesis and Evolution of Karst Aquifers*. Huntsville, AL: National Speleological Society, pp. 149–155.

White, W.B., 2002. Karst hydrology : recent developments and open questions. , 65(13), pp.85–105.

White, W.B., 1984. Rate processes: chemical kinetics and karst landform development. *Zeitschrift fur Geomorphologie, Groundwater as a Geomorphic Agent*, pp.227–248.

Wicks, C., Noltie, D.B., Peterson, E.W., Dogwiler, T., 2010. Disturbances in the habitat of Macrocotyla glandulosa (Kenk). , 125(February), pp.116–125.

Wilcock, P.R., 1997. Entrainment, displacement and transport of tracer gravels. *Earth Surface Processes and Landforms*, 22(12), pp.1125–1138.

Williams, P.W. & Dowling, R.K., 1979. Solution of marble in the karst of the Pikikiruna Range, northwest Nelson, New Zealand. *Earth Surface Processes*, 4, pp.15–36.

APPENDIX A. CHAPTER 2

2.1 Correlation of Beaver Creek USGS Gauge discharge to Blowing Cave discharge

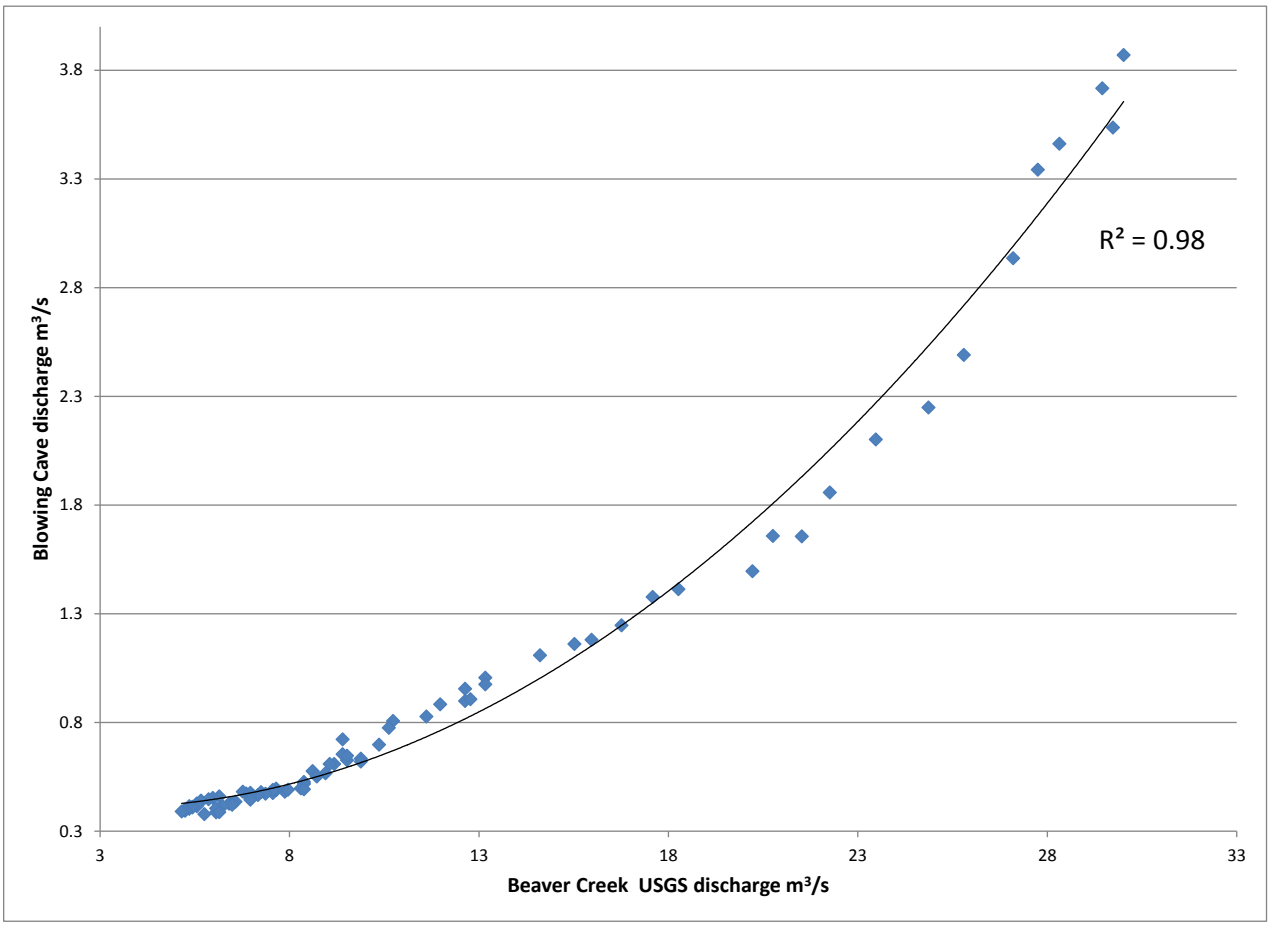

2.2 Stage-discharge at Blowing Cave spring

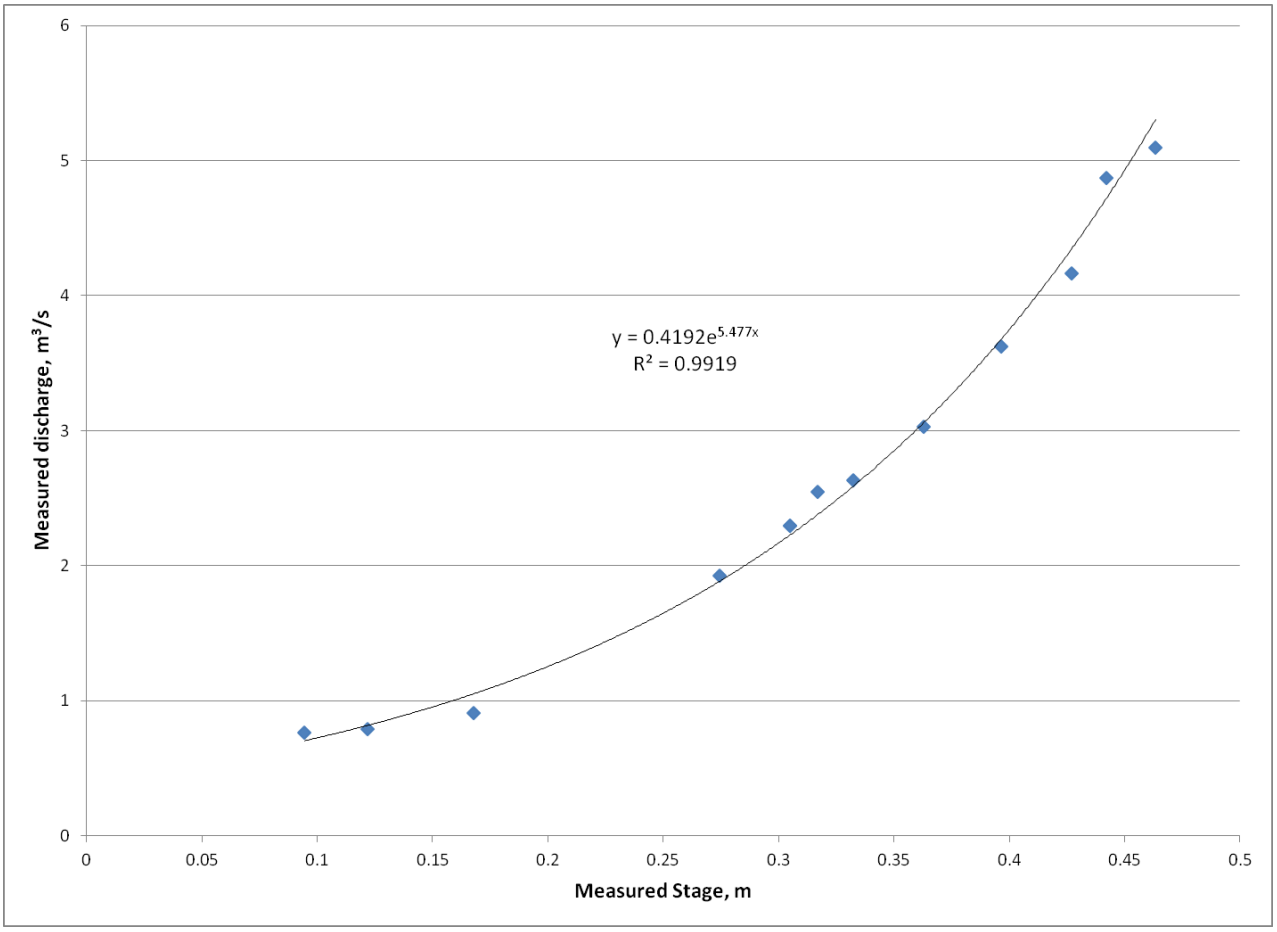

2.3 Tagged bed load tracer results from BC and TCC

Appendix 2.3.1: Tagged Tracer Data, Blowing Cave XS-1										
RFID Tag #	Rock label	Movement 12/10/12 XS1	Movement 1/30/13 XS1	Movement 4/28/13 XS1	Movement 7/6/13 XS1	A-axis	B-axis	C-axis	Mass	Rock Type
		meters	meters	meters	meters	cm	cm	cm	grams	
010107610706	076	0.59	6.20	0.34	14.17	6.50	6.00	1.00	45	Silty LS/DS
010107710505	077	0.38	0.23	1.68	0.30	5.00	4.50	1.75	70	Sparite
010107810403	078	4.65	1.75	10.61	5.91	4.00	3.00	2.25	39	Silty LS/DS
010107910703	079	3.37	19.49	5.18	1.83	6.50	2.75	2.50	54	Micrite
010108010605	080	0.73	0.73	6.40	14.08	6.00	4.75	1.75	41	Sparite
010108110604	081	4.83	8.55	1.92	1.28	6.00	3.50	1.00	27	Sparite
010108211404	082	6.35	4.47	1.68	9.45	13.50	4.00	3.00	107	Micrite
010108310403	083	0.27	1.68	4.33	7.25	4.00	3.00	1.50	17	Micrite
010108410503	084	1.12	0.16	0.18	0.88	4.50	3.00	1.00	17	Sparite
010108510504	085	2.19	0.22	0.76	0.58	4.75	4.00	1.50	40	Micrite
010108610604	086	0.76	1.95	0.27	2.16	6.00	4.00	1.50	37	Micrite
010108710604	087	2.46	3.93	0.46	18.84	6.00	4.25	2.50	59	Micrite
010108810504	088	0.03	0.00	0.00	0.21	5.00	3.75	1.00	28	Micrite
010108910603	089	5.05	4.55	8.08	23.68	5.50	2.50	1.00	25	Silty LS/DS
010109010904	090	2.55	3.24	11.73	2.10	9.00	3.50	2.00	68	Silty LS
010109110503	091	3.34	4.98	12.71	4.27	5.00	3.00	2.50	51	Micrite
010109210505	092	0.73	7.28	3.81	9.27	5.00	4.75	2.00	46	Micrite
010109310503	093	0.73	2.59	1.58	6.68	4.50	3.00	1.50	19	Silty LS
010109410502	094	3.25	lost	-	-	5.00	2.25	2.00	32	Micrite
010109510504	095	1.37	6.16	3.44	19.20	4.50	3.50	1.00	21	Micrite
010109610403	096	0.76	1.68	5.03	4.21	4.00	3.00	0.75	18	Sparite
010109710403	097	0.67	19.14	2.90	16.61	3.50	3.00	0.75	11	Silty LS
010109810605	098	0.58	9.48	1.37	1.31	5.50	5.00	1.00	29	Silty LS/DS
010109910402	099	4.56	0.48	23.76	lost	3.50	2.00	0.75	10	Micrite
010110010303	100	1.88	0.55	0.00	8.90	3.00	2.50	2.00	16	Micrite
010110110403	101	0.52	2.53	2.74	7.07	3.50	2.50	1.50	18	Micrite
010110210302	102	3.25	13.51	5.18	5.79	3.00	1.75	0.75	8	Sparite
010110310402	103	2.80	0.95	0.82	19.51	3.50	2.25	0.50	6	Sparite
010110410302	104	5.02	lost	-	-	3.00	1.75	1.50	14	Sparite
010110510302	105	2.43	30.18	0.91	2.44	2.75	1.75	1.25	6	Micrite
010110610301	106	3.31	0.95	33.53	27.43	2.75	1.25	0.75	4	Micrite
010110710201	107	9.12	3.21	8.95	lost	2.00	1.25	1.00	5	Micrite
010100110403	001	1.06	4.12	2.59	6.22	3.50	2.50	1.00	12	Micrite

010100210403	002	0.36	0.85	11.89	5.49	4.00	2.50	0.75	11	Sparite
010110810901	108	0.79	7.50	0.09	0.24	9.00	6.00	2.50	139	Sparite
010110910605	109	4.32	1.87	7.32	6.55	5.50	4.50	3.00	82	Sparite
010111011207	110	1.20	3.98	2.16	0.46	12.00	7.00	1.50	288	Micrite
010111110704	111	2.36	10.38	5.36	14.81	6.50	4.00	1.50	73	Micrite
010111210807	112	1.31	11.22	5.73	22.59	8.00	6.50	1.50	101	Sparite
010111410605	114	3.25	3.12	21.21	18.75	6.00	4.50	4.00	143	Micrite
010111510807	115	0.52	4.97	1.49	4.02	8.00	6.50	2.00	151	Micrite
010111611409	116	0.43	2.77	2.38	5.97	13.50	9.00	3.00	686	Sparite
010111710905	117	7.08	9.62	0.18	6.07	8.50	5.00	4.50	151	Micrite
215105425229	118	3.65	1.90	1.01	1.98	9.50	3.50	1.50	85	Silty LS
010111910605	119	3.01	12.41	27.83	8.69	6.00	4.50	3.00	85	Micrite
010112010906	120	5.14	10.56	0.09	10.39	8.50	5.50	3.50	172	Micrite
010112111912	121	1.64	1.89	4.42	3.93	19.00	12.00	2.50	840	Sparite
010112211508	122	2.28	14.18	1.07	0.43	15.00	8.00	2.50	404	Micrite
010112311107	123	7.30	2.15	1.31	3.08	11.00	7.00	2.00	198	Sparite
010112411109	124	4.62	2.48	0.64	7.01	11.00	9.00	2.50	278	Micrite
010112511008	125	2.49	1.62	13.56	5.79	10.00	8.00	2.50	237	Micrite
010112611005	126	2.74	10.71	0.64	0.61	10.00	5.00	2.00	129	Sparite
010112710705	127	0.55	3.89	0.30	5.70	6.50	4.50	3.00	87	Sparite
010112810605	128	1.22	1.80	0.27	4.75	5.50	4.50	2.50	77	Sparite
010112910805	129	0.62	1.36	3.54	3.11	7.50	5.00	1.50	93	Silty LS/DS
010113010807	130	3.65	1.75	7.71	18.68	8.00	7.00	2.00	110	Sparite
010113110605	131	2.39	8.73	1.71	6.55	5.50	4.50	2.50	39	Micrite
215105422708	132	3.28	19.20	3.51	2.01	6.00	3.00	1.50	41	Silty LS
010100121210	001ss	0.21	3.87	8.03	19.23	11.50	10.00	5.50	768	SS
010100221108	002cg	0.49	9.42	3.26	1.65	11.00	8.00	4.50	631	CG
010100320804	003ss	0.05	6.34	6.20	9.88	8.00	4.00	3.00	393	SS
215105424448	133	1.31	1.25	0.00	0.18	20.00	13.50	4.00	1528	SS
215105422900	134	10.79	20.30	1.13	7.99	8.00	7.00	6.50	690	SS
215105421071	135	1.06	0.28	1.40	0.64	10.50	7.00	2.00	224	Chert
215105422698	136	1.46	21.07	4.97	4.18	15.00	11.00	4.00	724	SS
215105424452	137	0.55	6.46	20.70	17.71	8.50	6.00	4.00	259	SS
215105420071	138	0.70	16.93	9.14	8.22	11.50	11.00	6.00	913	SS
091625968981	139	13.92	4.64	2.68	25.69	6.50	5.00	4.00	164	SS
215105420078	140	0.55	0.03	3.18	2.80	11.50	6.50	3.50	397	SS
215105419833	141	4.65	4.65	2.44	34.20	9.50	7.00	3.50	367	CG
215105424648	142	1.55	14.47	1.89	6.02	15.00	10.00	2.50	620	SS
215105421342	143	0.58	2.32	0.09	2.23	8.00	6.00	2.50	173	SS
010100120905	1001	0.55	2.59	2.65	16.67	8.64	4.57	3.56	184	SS
010100221108	1002	2.34	2.23	4.88	5.37	10.92	8.13	5.08	580	SS

010100321210	1003	4.53	2.59	6.32	12.14	12.19	10.16	7.62	742	SS
215105423982	1004	2.68	5.13	4.27	5.55	12.19	7.62	2.54	162	SS
215105423846	1005	0.33	0.43	0.09	1.01	6.86	4.45	2.54	70	SS
215105423559	1006	3.53	3.94	8.63	3.93	5.84	4.57	2.41	74	Chert
215105424122	1007	5.38	6.75	4.60	4.91	4.32	4.19	2.54	52	SS
215105420885	1008	2.61	3.42	1.83	5.97	6.60	5.72	5.33	118	SS
215105420535	1009	2.92	0.56	13.49	4.15	5.08	4.57	2.29	76	SS
215105424310	1010	0.33	lost	-	-	9.40	5.33	2.79	156	SS
215105423594	1011	1.02	0.50	1.37		5.84	4.57	1.91	56	SS
215105422639	1012	4.04	5.41	2.13	4.27	5.10	4.40	1.80	63	SS
215105420020	1013	7.75	2.15	5.64	2.90	5.33	4.57	3.30	78	SS
215105422854	1014	10.88	7.32			7.11	4.06	2.54	108	SS
215105419920	1015	8.33	32.51	20.12	0.61	4.57	3.30	3.05	57	SS
215105423146	1016	0.36	4.30	1.01	1.92	8.13	5.33	2.03	120	SS
215105423475	1017	2.07	10.98	3.20	3.47	9.65	4.32	2.54	94	SS
215105421915	1018	1.00	3.34	lost	-	9.14	5.08	2.79	144	Chert
215105421418	1019	7.20	5.17	18.53	lost	5.84	4.45	2.03	68	SS
215105422614	1020	4.01	6.87	lost	-	6.35	4.45	3.05	82	SS
215105421928	1021	2.25	0.59	2.38	6.58	6.99	5.59	3.05	115	SS
215105424509	1022	6.51	1.57	2.87	8.47	7.11	4.32	3.18	106	SS
215105423568	1023	0.49	0.06	2.34	1.65	5.33	4.57	2.03	64	SS
215105421922	1024	2.04	0.22	0.46	0.85	8.38	5.59	2.79	154	SS
215105424460	144*	n/a*	1.52	1.68	0.15	10.10	7.30	2.40	247	CG
215105420331	145	n/a	4.05	29.20	28.56	8.80	7.20	2.70	262	SS
215105423174	146	n/a	5.07	10.61	10.55	9.30	7.50	2.60	287	SS
215105419839	147	n/a	8.23	18.38	8.60	7.70	5.90	2.70	208	SS
215105420110	148	n/a	27.18	8.96	16.46	8.00	5.10	3.30	194	SS
215105423113	149	n/a	3.37	7.59	0.12	6.90	4.20	2.60	88	SS
215105422880	150	n/a	2.50	4.88	0.24	7.40	4.00	2.10	73	SS
215105422673	151	n/a	0.37	7.22	5.64	5.90	4.90	1.20	55	SS
215105419939	152	n/a	13.47	1.40	3.60	6.60	6.00	1.10	57	SS
215105423135	153	n/a	2.16	10.88	6.34	6.00	5.40	1.00	41	Chert
215105421825	154	n/a	1.19	3.78	8.78	6.40	4.40	1.50	51	SS
215105420634	155	n/a	4.88	0.61	0.70	5.00	4.10	1.80	37	SS
215105424045	156	n/a	10.36	19.51	7.92	5.00	3.90	2.00	46	SS
215105424131	157	n/a	3.96	4.48	16.25	4.90	4.40	1.40	30	SS
215105422424	158	n/a	0.85	6.68	6.64	5.10	4.00	2.10	34	SS
215105423302	159	n/a	2.59	23.16	2.77	6.50	3.10	1.50	32	SS
215105422677	160	n/a	0.98	6.77	1.86	4.60	3.20	1.60	29	SS
215105422922	161	n/a	4.39	9.94	11.80	4.50	4.40	0.80	16	SS
215105424804	162	n/a	3.66	1.65	1.04	5.10	4.00	1.30	35	SS

215105424865	163	n/a	2.23	10.42	7.01	4.00	3.50	1.00	21	SS
215105421573	164	n/a	19.14	24.99	15.64	4.30	4.10	0.80	19	Chert
215105423876	165	n/a	7.35	10.82	8.75	3.60	2.50	1.60	24	Chert
215105423611	166	n/a	13.35	23.90	5.03	4.00	3.50	0.90	17	SS
215105423579	167	n/a	1.40	2.87	5.18	4.60	3.70	0.90	19	SS
215105424136	168	n/a	5.93	9.81	21.06	3.00	2.80	1.20	12	SS
215105424808	169	n/a	2.44	1.62	8.32	5.40	3.60	2.00	41	CG
215105422129	170	n/a	0.34	22.26	4.91	4.00	2.00	1.60	18	SS
215105420611	171	n/a	0.27	1.37	8.08	5.00	2.60	0.50	14	SS
215105423548	172	n/a	9.40	2.74	5.39	4.30	2.90	1.10	17	SS
215105421166	173	n/a	3.20	0.52	0.03	3.60	3.10	0.60	7	Chert
215105420655	174	n/a	0.85	4.94	1.77	4.00	2.10	1.10	13	SS
215105420239	175	n/a	4.96	2.13	lost	4.50	1.40	0.80	12	SS
215105424546	176	n/a	15.70	2.53	3.75	3.30	1.80	1.50	13	SS
215105420363	177	n/a	3.62	18.25	16.64	2.90	2.50	2.00	17	SS
215105422500	178	n/a	8.32	19.23	10.09	3.00	2.80	1.30	12	SS
215105423070	179	n/a	0.12	5.67	1.52	4.00	2.70	0.50	9	SS
215105423960	180	n/a	33.13	0.52	0.34	3.10	2.40	0.90	8	Chert
215105423184	181	n/a	8.66	14.20	34.11	3.30	2.40	0.70	8	SS
215105420618	182	n/a	10.73	lost	-	3.10	2.70	0.60	7	SS
215105421114	183	n/a	5.27	6.31	4.72	3.20	2.40	0.60	7	SS
215105423557	184	n/a	9.37	25.85	2.80	3.60	2.40	0.50	6	SS
215105421474	185	n/a	3.66	9.02	3.78	3.00	2.40	1.10	9	SS
215105424369	186	n/a	4.14	9.52	8.93	3.50	1.90	0.40	4	SS
215105419851	187	n/a	1.74	2.88	14.39	2.70	2.30	0.60	5	SS
215105422506	188	n/a	1.68	3.44	1.86	3.00	2.10	1.20	7	SS
215105421553	189	n/a	6.63	lost	-	3.20	2.50	0.70	7	SS
215105420093	190	n/a	2.41	16.84	35.29	2.70	2.40	0.60	5	SS
215105424697	191	n/a	7.65	5.55	27.77	2.60	2.40	1.20	8	Chert
215105423724	192	n/a	3.35	6.61	39.26	3.20	2.40	0.80	7	SS
215105423091	193	n/a	4.04	26.43	27.10	3.40	1.80	1.00	8	Chert
215105423793	194	n/a	7.23	5.10	19.08	2.30	1.90	1.00	6	SS
215105422886	195	n/a	0.46	1.49	12.13	2.80	2.30	0.50	4	SS
215105424571	196	n/a	1.76	2.14	0.03	2.50	2.30	0.70	7	Chert
215105422918	197	n/a	1.19	3.75	8.99	2.60	1.90	0.50	5	SS
215105423976	198	n/a	4.89	18.87	5.85	2.00	1.90	1.00	6	SS
215105423203	199	n/a	2.96	11.03	12.13	2.90	2.00	0.50	4	SS
215105421105	200	n/a	3.51	26.88	29.96	2.90	2.20	0.40	5	SS
215105423404	201	n/a	0.00	0.00	0.15	2.90	2.00	0.60	4	SS
215105420752	202	n/a	2.19	18.23	11.46	2.60	2.40	0.40	4	SS
215105422953	204	n/a	8.62	13.29	3.60	3.10	2.20	1.00	7	SS

215105423525	206	n/a	10.94	3.81	36.00	3.10	1.80	0.50	4	SS
215105422615	207	n/a	3.99	1.65	2.38	2.60	2.50	0.60	5	Chert
215105423741	208	n/a	3.26	10.27	18.93	2.80	2.50	0.50	5	SS
215105423306	210	n/a	1.77	10.15	2.93	2.70	2.70	0.70	6	SS
215105420693	213	n/a	7.04	9.35	4.02	3.00	2.50	0.50	5	SS
215105424251	214	n/a	2.15	3.60	13.96	2.30	2.20	0.40	3	SS
215105421416	215	n/a	18.25	4.38	2.96	2.80	2.40	0.50	6	SS
215105420714	216	n/a	7.83	lost	-	2.60	2.60	0.40	4	SS
215105421896	217	n/a	5.33	4.23	32.80	2.70	2.60	0.50	5	SS
215105421475	218	n/a	9.90	24.77	15.67	2.10	1.90	0.40	2	Chert
215105424446	219	n/a	16.61	12.16	4.18	2.30	2.00	0.40	2	Chert
215105420412	220	n/a	16.92	34.26	14.97	2.40	2.30	0.50	4	SS
215105421725	222	n/a	0.79	0.34	3.72	2.20	2.20	0.60	4	SS
215105421756	228	n/a	0.61	3.57	17.77	2.20	1.90	0.50	3	SS
n/a	Y1[†]	0.04[†]	-	-	-	3.18	1.27	0.38	2	SS
n/a	Y2	0.04	-	-	-	3.56	3.05	1.27	16	SS
n/a	Y3	0.05	-	-	-	3.81	2.54	1.27	12	SS
n/a	Y4	0.46	-	-	-	1.91	1.91	0.51	1	SS
n/a	Y5	0.59	-	-	-	3.81	3.05	0.76	14	SS
n/a	Y6	0.50	-	-	-	1.27	1.02	0.33	1	Chert
n/a	Y7	0.52	-	-	-	1.78	1.02	0.38	1	SS
n/a	Y8	0.56	-	-	-	3.05	1.52	1.27	8	SS
n/a	Y9	0.61	-	-	-	2.54	2.29	0.51	6	SS
n/a	Y10	0.76	-	-	-	3.18	2.79	0.64	6	Chert
n/a	Y11	0.79	-	-	-	2.79	2.54	1.02	10	SS
n/a	Y12	1.70	-	-	-	4.83	4.57	0.76	30	SS
n/a	Y13	1.46	-	-	-	3.30	1.91	1.02	8	SS
n/a	Y14	1.46	-	-	-	3.81	2.79	1.02	12	SS
n/a	Y15	1.34	-	-	-	3.05	2.29	0.64	8	SS
n/a	Y16	1.40	-	-	-	2.54	2.03	0.51	2	SS
n/a	Y17	1.34	-	-	-	3.56	2.54	0.76	7	SS
n/a	Y18	1.52	-	-	-	3.30	2.29	0.76	6	Chert
n/a	Y18B	1.49	-	-	-	1.27	1.27	0.25	4	SS
n/a	Y19	1.64	-	-	-	3.56	2.54	1.02	10	SS
n/a	Y19B	1.52	-	-	-	1.27	1.02	0.38	2	SS
n/a	Y20	1.55	-	-	-	3.30	3.05	1.52	19	SS
n/a	Y21	1.61	-	-	-	1.52	1.27	0.51	4	SS
n/a	Y22	1.64	-	-	-	3.05	1.91	1.52	11	Sparite
n/a	Y23	2.42	-	-	-	3.56	2.03	0.89	9	SS
n/a	Y24	3.04	-	-	-	3.30	2.54	0.76	8	SS
n/a	Y25	2.55	-	-	-	3.30	2.54	0.64	8	SS

n/a	Y26	2.55	-	-	-	3.56	2.03	0.76	9	SS
n/a	Y27	3.56	-	-	-	2.03	1.78	0.38	3	SS
n/a	Y28	3.34	-	-	-	2.29	1.52	0.38	3	SS
n/a	Y29	3.34	-	-	-	3.81	3.05	1.27	14	SS
n/a	Y30	4.23	-	-	-	2.79	2.03	1.27	7	SS
n/a	Y31	4.38	-	-	-	2.54	1.78	1.02	17	SS
n/a	Y32	4.47	-	-	-	3.56	2.03	0.25	8	SS
n/a	Y33	4.80	-	-	-	2.29	2.03	0.76	7	Chert
n/a	Y34	5.02	-	-	-	4.57	3.30	0.89	20	SS
n/a	Y35	5.44	-	-	-	5.08	2.29	0.51	14	SS
n/a	Y36	5.85	-	-	-	2.54	1.78	0.38	6	SS
n/a	Y37	6.20	-	-	-	2.03	2.03	0.89	11	SS
n/a	Y38	7.69	-	-	-	2.03	1.52	1.27	7	SS
n/a	Y39	11.25	-	-	-	2.54	1.91	1.02	7	SS
n/a	Y40	22.40	-	-	-	2.54	1.52	0.51	6	SS

* Tracers 144-228 placed after first storm event

† Tracers Y1-Y40 were one-time painted gravel tracers with no radio chips

Appendix 2.3.2: Tagged Tracer Data, Blowing Cave XS-2									
RFID Tag #	Rock label	Movement 1/30/13 XS 1	Movement 4/28/13 XS1	Movement 7/6/13 XS1	A-axis	B-axis	C-axis	Mass	Rock Type
		meters	meters	meters	cm	cm	cm	grams	
010200112009	001	0.15	0.06	3.20	20	9	4.5	1693	Micrite
010200211709	002	0.00	5.18	6.40	17	9	4.5	1023	Micrite
010200311808	003	0.00	7.19	10.46	18	8	5.5	901	Oolite
010200411610	004	0.27	0.70	0.82	16	10	4	844	Oolite
010200511212	005	0.55	0.03	0.46	12	12	5.5	837	Micrite/oolite
010200611709	006	0.00	0.00	0.37	17	9	4	860	Sparry micrite
010200711808	007	0.00	0.94	0.49	18	8	3.5	521	Silty LS/DS
010200811211	008	0.43	0.00	0.40	12	11	3.5	526	Sparry micrite
010200911309	009	0.37	0.03	0.49	13	9	3	456	Micrite
010201011311	010	0.00	0.00	16.46	13	11	1.5	392	Micrite
010201111008	011	0.09	0.03	0.52	10	8	3.5	371	Sparry micrite
010201211107	012	0.27	4.15	2.13	11	7	3.5	319	Micrite
010201311206	013	0.49	0.03	8.55	12	6	4	314	Sparry micrite
010201411105	014	0.00	2.13	4.08	11	5	4.5	286	Silty LS/DS
010201510805	015	0.00	3.38	1.58	8	5	3.5	272	Micrite
010201610907	016	0.00	13.99	1.40	9	7	6.5	260	Silty LS/DS
010201710807	017	0.00	0.00	6.80	8	7	4	230	Sparry micrite
010201810806	018	0.00	0.52	0.40	8	6	3	196	Dolostone
010201910804	019	0.00	0.34	0.37	8	4	3	169	Micrite
010202010906	020	0.61	0.00	0.09	8.5	6	3	168	Silty LS/DS
010202111108	021	0.00	0.09	2.44	11	7.5	1.5	169	Silty LS/DS
010202210805	022	0.00	0.27	0.61	8	5	2	152	Micrite
010202311104	023	4.05	0.24	1.55	10.5	4	3.5	149	Micrite
010202410805	024	0.46	0.18	2.04	8	5	3	147	Micrite
010202511004	025	0.00	10.06	5.79	9.5	4	2.5	146	Sparite
010202610806	026	0.00	0.91	5.00	7.5	6	3.5	134	Micrite
010202710804	027	0.00	0.30	0.67	8	4	2.5	128	Sparite
010202810705	028	1.83	0.52	5.79	6.5	5	4	116	Silty LS/DS
010202910604	029	0.00	0.00	0.00	5.5	4	3.5	89	Sparite
010203011008	030	0.00	0.00	0.46	10	8	4.5	332	Micrite
010203110906	031	0.00	0.18	0.64	8.5	6	5	308	Dolostone
010203211105	032	0.30	0.03	1.37	11	5	2.5	280	Sparry micrite
010203311009	033	0.73	2.16	1.40	10	9	3	253	Micrite
010203411007	034	0.00	0.00	0.46	10	7	3	209	Silty LS/DS
010203510807	035	0.00	0.15	1.62	8	7	2.5	192	Silty LS

010203611006	036	0.00	0.15	0.64	10	6	2.5	140	Silty LS
010203710805	037	0.00	0.03	5.46	8	5	1.5	130	Silty LS/DS
010203810706	038	0.15	0.58	1.16	7	6	2.5	119	Micrite
010203910805	039	0.00	5.52	6.68	7.5	5	3	107	Silty LS
010204010704	040	0.34	1.04	3.63	7	4	2.5	77	Micrite
215105422665	041	0.00	0.00	4.37	8	6	2	94	Micrite
215105422303	042	0.18	0.00	9.08	6	5.5	1	43	Micrite
215105420765	043	0.00	0.00	0.37	8.5	5.5	1.25	80	Sparite
215105422402	044	0.18	2.90	3.44	6.5	4.5	1	37	Silty LS/Micrite
215105422510	045	0.46	0.00	2.79	8.5	7	1	107	Silty LS/DS
215105419968	046	0.30	0.03	0.49	7	5.5	1	85	Sparry micrite
215105420455	047	0.00	0.00	0.00	6.5	4.5	0.5	37	Sparite
215105421476	048	0.40	0.27	0.03	11	6.5	1	165	Micrite
215105421780	049	0.00	0.55	2.37	9	7	1.5	131	Silty LS
215105424085	050	0.15	0.37	4.51	12	8.5	1.5	218	Sparite
215105419902	051	0.00	0.55	0.76	10	7.5	1	128	Silty LS/DS
215105424144	052	0.00	0.61	1.07	11.5	5	1	60	Micrite
215105420296	053	0.37	0.24	0.40	8.5	6	1.5	84	Silty LS
215105420799	054	0.00	0.03	1.10	7	4.5	0.75	39	Silty LS/DS
215105420413	055	2.65	2.13	5.85	3.25	3	1.25	21	Silty LS/DS
215105420410	056	0.00	3.87	10.09	3.5	2.5	1	16	Micrite
215105422138	057	0.12	0.21	0.21	5.5	4.25	1.5	44	Micrite
215105420949	058	0.00	0.00	0.00	6	3.5	2.5	79	Sparite
215105421798	059	0.30	0.40	1.25	5	4	2	71	Sparite
215105420109	060	0.18	0.18	4.63	9	4.25	1	58	Silty LS/DS
215105420315	061	0.00	0.00	5.17	5	3.5	2	54	Sparite
215105424180	062	0.00	0.03	0.27	4.5	3	1.5	37	Sparite
215105422447	063	0.79	6.04	1.40	8	5	0.5	36	Sparite
215105424235	064	0.30	1.52	0.79	10.5	6.5	1.25	124	Silty LS/DS
215105420137	065	0.18	1.25	2.77	7	5.5	1	49	Sparite
215105423531	066	0.43	2.38	1.43	5.5	4.5	1.5	61	Micrite
215105422222	067	0.37	3.96	6.86	7.5	4	1.25	60	Micrite
215105422496	068	0.00	0.91	10.97	3.5	3.5	1.5	27	Micrite
215105423913	069	0.30	0.03	0.18	3	2	1.5	16	Silty LS/DS
215105420624	070	0.00	1.01	0.34	4	3.5	1.25	24	Micrite
215105421990	071	0.00	0.08	1.53	3.5	2.5	1.75	24	Micrite
215105420582	072	0.30	0.03	0.18	4.5	3.5	0.75	18	Sparite
215105419894	073	0.00	0.27	4.87	4.5	3	1.5	33	Silty LS/DS
215105423487	074	0.00	0.27	0.37	5.25	3	1.5	35	Micrite
215105421003	075	2.23	1.34	6.70	7	3	0.75	31	Sparite

Appendix 2.3.3: Tagged Tracer Data, Tumbling Creek Cave BCH section							
RFID Tag #	Rock label	Movement 4/28/2014 BCH	A-axis	B-axis	C-axis	Mass	Rock Type
		meters	cm	cm	cm	grams	
020100130905	1	12.0	8.5	5	4.5	279	Chert
020100230805	2	4.0	7.5	4.5	3	205	Chert
215105420828	3	lost	3	2.5	2	43	Chert
020100431609	4	4.0	15.5	8.5	7	1438	Chert
215105421650	5	1.5	11	10.5	4	625	Chert
215105421327	6	12.2	9	7.5	4	226	Chert
n/a*	7	5.5	8	7	3	158	Chert
n/a	8	9.5	8.5	7	2.5	244	Chert
215105423979	9	7.6	11	5.5	5	469	Chert
215105423192	10	0.3	15	10	3	1035	Chert
215105425945	11	19.0	8.5	7	2.5	134	Chert
215105420145	12	1.5	17	13	4	1408	Chert
215105421326	13	8.2	9	9	5	503	Chert
215105425705	14	0.9	16.5	7	5	593	Chert
n/a	15	10.0	6.5	6	3	164	Chert
215105424214	16	24.1	9.5	6	2.5	157	Chert
215105422430	17	1.1	8.5	6	4	326	Chert
215105422697	18	0.6	7	5.5	1.5	90	Chert
215105422434	19	3.6	9	6.5	4	309	Chert
215105424131	20	16.4	6	4.5	2	66	Chert
215105424210	21	9.7	8.5	6.5	4.5	279	Chert
215105419851	22	0.4	7	4.5	3	125	Chert
n/a	23	lost	6	3.8	1.9	46	Chert
n/a	24	2.4	5.3	4.9	1.9	55	Chert
215105422670	25	0.6	10.3	8.5	3.1	282	Chert
215105421844	26	5.0	12.6	9.3	4.6	483	Carbonate
215105423905	27	0.9	11.6	9.4	4.4	665	Carbonate
215105425743	28	3.4	17.7	5.3	2	254	Carbonate
215105424909	29	1.5	14.5	13.2	3	544	Carbonate
215105425252	30	0.4	3.7	3.2	2.4	358	Carbonate
215105424758	31	lost	12.4	7.6	2.7	23	Carbonate
215105422197	32	7.0	12.5	9	1.8	284	Carbonate
215105422922	33	9.3	7.3	7	2.5	78	Chert
215105419826	34	12.6	10.1	7.8	5.6	558	Chert
215105424225	35	8.2	12.1	8.7	5.3	541	Chert
215105424735	36	0.3	10.5	6	4.1	283	Chert

n/a	37	4.4	8.4	4.4	2.7	131	Chert
215105421576	38	0.4	9.4	5.2	3.3	212	Chert
215105421572	39	6.7	9.2	7.8	5.2	333	Chert
n/a	40	0.5	6.1	5.9	3.3	96	Chert
n/a	41	1.3	7.8	5	2.8	127	Chert
215105424983	42	0.3	7.3	6.7	5	285	Chert
n/a	43	15.7	7.4	3	2.3	83	Chert
n/a	44	lost	5.7	3.8	2.6	50	Chert
215105422686	45	lost	6.4	5	2.8	79	Chert
215105419786	46	1.5	13	7.9	4.4	573	Chert
n/a	47	45.2	5.9	4.7	1.8	72	Chert
n/a	48	lost	5.4	3.7	2.9	61	Chert
n/a	49	9.7	5.4	3.7	2.8	56	Chert
n/a	50	12.1	5.2	4.4	2.8	51	Chert
n/a	51	lost	4.5	3.2	2.1	34	Chert
n/a	52	0.4	6.4	3.2	2.6	70	Chert
n/a	53	lost	5.9	3.4	1.7	22	Chert
215105419599	54	14.3	7.2	5.7	2.8	108	Chert
215105424164	55	0.3	5.8	3.5	2.9	72	Chert
n/a	56	5.4	5	3.4	1.8	26	Chert
n/a	57	3.3	4.3	3.1	1.1	16	Chert
n/a	58	lost	4.4	3.1	1.2	16	Chert
n/a	59	7.6	6.3	4.3	2.5	62	Chert
215105424184	60	10.5	4.1	4	2.2	33	Chert
n/a	61	25.2	5.7	3.9	1.8	50	Chert
n/a	62	0.4	6	5.7	2.4	92	Chert
n/a	63	0.5	5.5	5.4	1.8	53	Chert
n/a	64	lost	8	5.7	1.6	89	Chert
n/a	65	33.0	6.4	5.2	3.2	112	Chert
215105424209	66	6.9	7.1	4.9	4	126	Chert
n/a	67	4.2	6.4	3.5	3.2	93	Chert
n/a	68	5.3	5.5	2.7	1.5	29	Chert
215105422154	69	lost	5.5	5.4	2.9	81	Chert
n/a	70	2.1	8.8	3.9	2.7	118	Chert
n/a	71	3.8	4.6	2.6	2.3	35	Chert
n/a	72	0.5	4.6	3.7	2.1	47	Chert
215105419849	73	10.8	6	5.4	4.8	249	Chert
n/a	74	12.6	6.5	4.3	4.2	176	Chert
215105424404	75	lost	5.9	4.5	2.6	104	Chert
n/a	76	17.3	4.2	3.5	2.3	40	Chert
n/a	77	10.3	4.9	3.5	2.4	32	Chert

n/a	78	0.3	7.9	2.8	2.6	77	Chert
n/a	79	lost	5	3.5	2.5	44	Chert
n/a	80	4.9	5	3.5	2.25	41	Chert
215105426039	81	1.7	5.5	2	1.5	23	Chert
n/a	82	20.4	3.5	3	1.5	26	Chert
n/a	83	0.3	4.5	3.5	2	46	Chert
215105420346	84	3.2	5.5	4.5	3	84	Chert
n/a	85	6.5	5	3.5	2	36	Chert
215105421336	86	10.7	6	4	2.5	48	Chert
n/a	87	lost	5	3	2	25	Chert
215105421367	88	lost	5	3	2.5	55	Chert
n/a	89	lost	4	2.5	2	22	Chert
215105421409	90	lost	4.5	3	2	29	Chert
n/a	91	lost	3	2.5	1.5	12	Chert
n/a	92	1.1	5	3.5	1.5	31	Chert
n/a	93	lost	4	3	2.5	27	Chert
n/a	94	lost	4	2.5	1	16	Chert
n/a	95	10.4	3.5	2.5	1.5	14	Chert
215105421347	96	27.5	6.5	5	3.5	107	Chert
215105420660	97	6.0	4.5	4	2	43	Chert
n/a	98	22.9	4	2.5	1.5	23	Chert
n/a	99	12.7	3.5	2.5	2.5	24	Chert
n/a	100	19.6	5.5	2.5	2	29	Chert
n/a	101	lost	4	2.5	1.5	17	Chert
n/a	102	lost	3	2.5	2	18	Chert
n/a	103	0.5	4.5	3	2.5	47	Chert
n/a	104	14.0	4	2.5	2	23	Chert
215105422427	105	0.3	6	2.5	2.5	33	Chert
215105419784	106	lost	4	3	2.5	37	Chert
215105425468	107	4.8	18	14	5.5	1324	Chert
n/a	108	7.0	6.5	4	3	107	Chert
215105423468	109	5.7	4	2.5	2	23	Chert
n/a	110	lost	5	3	1.75	31	Chert
n/a	111	5.5	4	3.5	2	21	Chert
215105420636	112	16.6	8.5	4.5	4.5	250	Chert
215105421338	113	0.1	27	9	8	3101	Carbonate
215105425199	114	0.2	20	16	5	2576	Carbonate
215105423362	115	1.0	17	17.5	5	1769	Carbonate
215105425975	116	0.1	17	10.5	6.5	1809	Carbonate
215105419303	117	0.4	16	14.5	4	1153	Carbonate
215105424150	118	1.3	11.5	7.5	7	999	Carbonate

215105425961	119	0.2	15.5	10	3.5	939	Carbonate
215105421934	120	0.2	15.5	7.5	5	806	Carbonate
215105422913	121	5.0	12.5	7	5	650	Carbonate
215105422428	122	0.4	13	9.5	4	572	Carbonate
215105423381	123	10.2	7.5	7	5	511	Carbonate
215105423107	124	0.6	11	6	4	442	Carbonate
215105420386	125	0.2	13	9.5	3	365	Carbonate
215105425751	126	0.4	7.5	6.5	5	326	Carbonate
215105420040	127	0.2	8	7	2	234	Carbonate
215105420851	128	lost	14	4	3	223	Carbonate
215105421344	129	3.7	7	7	2.5	173	Carbonate
215105425927	130	0.4	6.5	4	4	169	Carbonate
215105422126	131	3.0	6	6	2.5	112	Carbonate
215105424447	132	4.0	6	5.5	1.75	87	Carbonate
215105423966	133	0.3	6	5.5	1.5	73	Carbonate
215105423479	134	12.3	5.5	5	2.5	64	Carbonate
215105425495	135	10.5	4.5	3.5	2	50	Carbonate
215105425747	136	7.3	7.5	4	0.75	34	Carbonate
215105423675	137	lost	4	2.5	2.25	26	Carbonate
215105421362	138	lost	4	3	1.5	24	Carbonate
* Not all chert tracers were tagged with radio chips because of drilling difficulty in the field. Non-chipped tracers were engraved with the ID number instead.							

Appendix 2.3.4: Tagged Tracer Data, Tumbling Creek Cave RZR section							
RFID Tag #	Rock label	Movement 4/28/2014 RZR	A-axis	B-axis	C-axis	Mass	Rock Type
		meters	cm	cm	cm	grams	
030230112311	301	14.4	23	10.5	8	2329	Carbonate
030230211711	302	0.7	17	11	5.5	1564	Carbonate
030230311815	303	4.2	18	15	5	1934	Carbonate
030230411717	304	0.3	17	16.5	5.5	1900	Carbonate
030230512511	305	3.1	24.5	10.5	4.5	1318	Carbonate
030230611912	306	13.4	19	12	6.5	1857	Carbonate
030230711609	307	0.2	16	9	7	1146	Carbonate
030230911608	308	20.2	15.5	7.5	7	958	Carbonate
030231011413	309	3.7	13.5	12.5	3.5	630	Carbonate
030231212108	310	1.6	20.5	8	4	732	Carbonate
030231312311	311	lost	23	10.5	7	2374	Carbonate
030231511808	312	lost	17.5	7.5	5	960	Carbonate
030231611211	313	4.9	11.5	10.5	5	572	Carbonate
030231711311	314	34.8	13	10.5	3.5	572	Carbonate
030231811308	315	12.4	12.5	8	5	655	Carbonate
030231911308	316	0.1	13	8	5.5	791	Carbonate
030232011511	317	1.2	14.5	10.5	4	516	Carbonate
030232111109	318	1	10.5	9	6	660	Carbonate
030232411309	319	lost	12.5	9	4.5	729	Carbonate
030232511508	320	0.4	14.5	7.5	3.5	492	Carbonate
030232611605	321	1.6	15.5	5	4	572	Carbonate
030232911108	322	0.3	10.5	8	4	472	Carbonate
030233111108	323	12.9	10.5	8	4	468	Carbonate
030233311006	324	0.6	10	6	6	577	Carbonate
030233510806	325	6.6	8	6	5.5	282	Carbonate
215105419306	326	1.8	12	4.5	2.5	222	Carbonate
215105419345	327	2.5	10	6.5	2	228	Carbonate
215105419525	328	lost	5.5	3	1.75	34	Carbonate
215105419577	329	22	5	4.5	1.5	34	Carbonate
215105419608	330	lost	8.5	4.5	2	126	Carbonate
215105419809	331	5.1	8.5	6.5	3	241	Carbonate
215105419810	332	0.4	6.5	3.25	2	62	Carbonate
215105419854	333	lost	7.5	7.5	1.5	104	Carbonate
215105419861	334	0.5	12.5	8	2.5	343	Carbonate
215105420038	335	lost	6.5	5.5	1.5	90	Chart
215105420103	336	lost	6	3	2	51	Carbonate

215105420143	337	2.2	9.5	6.5	2	200	Carbonate
215105420299	338	2	5	3.75	1.5	37	Carbonate
215105420348	339	2.5	6.25	5	2.5	69	Carbonate
215105420358	340	37	13	8.5	1.5	188	Carbonate
215105420384	341	lost	3.5	1.25	1.25	11	Carbonate
215105420558	342	3.2	9.5	6.5	2.5	328	Carbonate
215105420603	343	3	7.5	5	2	178	Carbonate
215105420633	344	lost	3.5	2	1.25	14	Carbonate
215105420651	345	lost	6	3.25	1.5	44	Carbonate
215105420828	346	7.6	7	5.5	3.5	151	Carbonate
215105420836	347	7.9	3.75	3	1.5	26	Carbonate
215105420884	348	0.6	2.5	2.25	0.75	9	Carbonate
215105421067	349	3.3	7.5	5	1.5	69	Carbonate
215105421074	350	27.8	4	3.75	2	41	Carbonate
215105421092	351	lost	8	4.5	3.5	189	Carbonate
215105421129	352	1.2	5.5	3.5	1.75	35	Carbonate
215105421340	353	4	4	1.75	0.75	11	Carbonate
215105421356	354	0.7	13	8.5	2.5	573	Carbonate
215105421357	355	5	10	9	3	301	Carbonate
215105421368	356	lost	7	5	2.5	130	Carbonate
215105421413	357	0.2	4	2.25	1.75	27	Carbonate
215105421590	358	lost	7	4	2	86	Carbonate
215105421605	359	0.6	9	6.5	2.5	177	Carbonate
215105421637	360	5.4	6.5	3.75	1.75	80	Carbonate
215105421644	361	lost	4	2.5	1	15	Carbonate
215105421649	362	lost	5.25	4	1.5	48	Carbonate
215105421864	363	19.8	7.5	6.5	3.5	237	Carbonate
215105421871	364	6.5	11	5.5	2.5	193	Carbonate
215105421931	365	0.5	13.5	8	3	395	Carbonate
215105421940	366	lost	2.75	2	1.5	12	Carbonate
215105422088	367	0.7	4	2	1.75	21	Carbonate
215105422094	368	2.3	5.5	2.75	2	38	Carbonate
215105422095	369	lost	3.5	2	1.5	16	Carbonate
215105422110	370	4.1	8	5.5	3.5	237	Carbonate
215105422148	371	8.5	13.5	12	2	395	Carbonate
215105422156	372	4	6.25	5	1.5	71	Carbonate
215105422160	373	lost	4	2	1.25	21	Carbonate
215105422373	374	0.5	11.5	4.5	4	312	Carbonate
215105422389	375	lost	4.5	3.5	1	19	Carbonate
215105422396	376	12.3	8.5	6	3.5	310	Carbonate
215105422673	377	0.3	7	7	3	271	Carbonate

215105422699	378	lost	8	6.5	2	151	Carbonate
215105422855	379	lost	4.25	3	2	28	Chert
215105422862	380	0.9	10	8	2.5	290	Carbonate
215105423118	381	8	7.5	6	2.5	128	Carbonate
215105423119	382	1.7	8	5	2	113	Carbonate
215105423129	383	1	5.5	4	2.75	92	Carbonate
215105423217	384	0.6	7	5	2.5	120	Carbonate
215105423374	385	1.2	5.5	4	2.25	63	Carbonate
215105423406	386	lost	2.75	1.75	0.75	7	Carbonate
215105423411	387	4.9	8	7.5	2.5	199	Carbonate
215105423453	388	0.8	10.5	6.5	3	356	Carbonate
215105423472	389	0.7	10.5	9.5	2	214	Carbonate
215105423478	390	0.5	11	6	3.5	318	Carbonate
215105423643	391	2.4	9	4.5	1.75	99	Carbonate
215105423696	392	6.4	12.5	6	3	399	Carbonate
215105423881	393	7.8	6.5	4	2	61	Carbonate
215105423907	394	lost	8.5	3.5	1.75	57	Carbonate
215105423941	395	1	8.5	6	4	330	Carbonate
215105424147	396	lost	11.5	8	3	331	Carbonate
215105424156	397	0.25	5.5	4.5	2.75	106	Carbonate
215105424248	398	2.8	9.5	8.5	2	212	Carbonate
215105424426	399	0.5	12.5	10	3.5	513	Carbonate
215105424484	400	0.15	8.5	3	2.25	87	Carbonate
215105424500	401	2	8.5	7	2	151	Carbonate
215105424653	402	0.15	7	6	1.75	84	Carbonate
215105424666	403	2	7.5	5.5	3	204	Carbonate
215105424691	404	0.4	9	5	2	119	Carbonate
215105424899	405	lost	8	5.5	3.5	207	Carbonate
215105424920	406	24.3	8.5	5.5	1.5	75	Carbonate
215105424929	407	3.8	11.5	7.5	2.5	361	Carbonate
215105425187	408	1.4	11	7	2.5	285	Carbonate
215105425213	409	lost	13.5	6.5	2.5	309	Carbonate
215105425226	410	0.7	6	2	1.5	26	Carbonate
215105425232	411	0.25	6.5	3.5	3.5	123	Carbonate
215105425247	412	lost	6.5	5	2.5	113	Carbonate
215105425250	413	4.6	8	6.5	4	290	Carbonate
215105425263	414	4.6	4.5	3.25	1.5	36	Carbonate
215105425413	415	0.7	4.5	3.5	1.5	28	Carbonate
215105425416	416	30.1	7.5	5.5	5	383	Carbonate
215105425417	417	0.8	7	4	1.75	69	Carbonate
215105425420	418	7.7	10.5	7	2	230	Carbonate

215105425692	419	22.6	8	4	2.25	95	Carbonate
215105426022	420	lost	5	2.75	1.25	31	Carbonate
215105426040	421	8.2	4	2.5	1	12	Carbonate
215105426227	422	0.9	4	3.75	1.5	31	Carbonate
215105426252	423	0.25	7.5	6.5	3	152	Carbonate
215105426264	424	3.5	12.5	7	4.5	500	Carbonate
215105426281	425	lost	4.25	2.25	1.75	24	Carbonate
Note: Mostly carbonate tracers were utilized at RZR for ease of chip installation.							

2.4 Correlation of total suspended solids with turbidity at BC

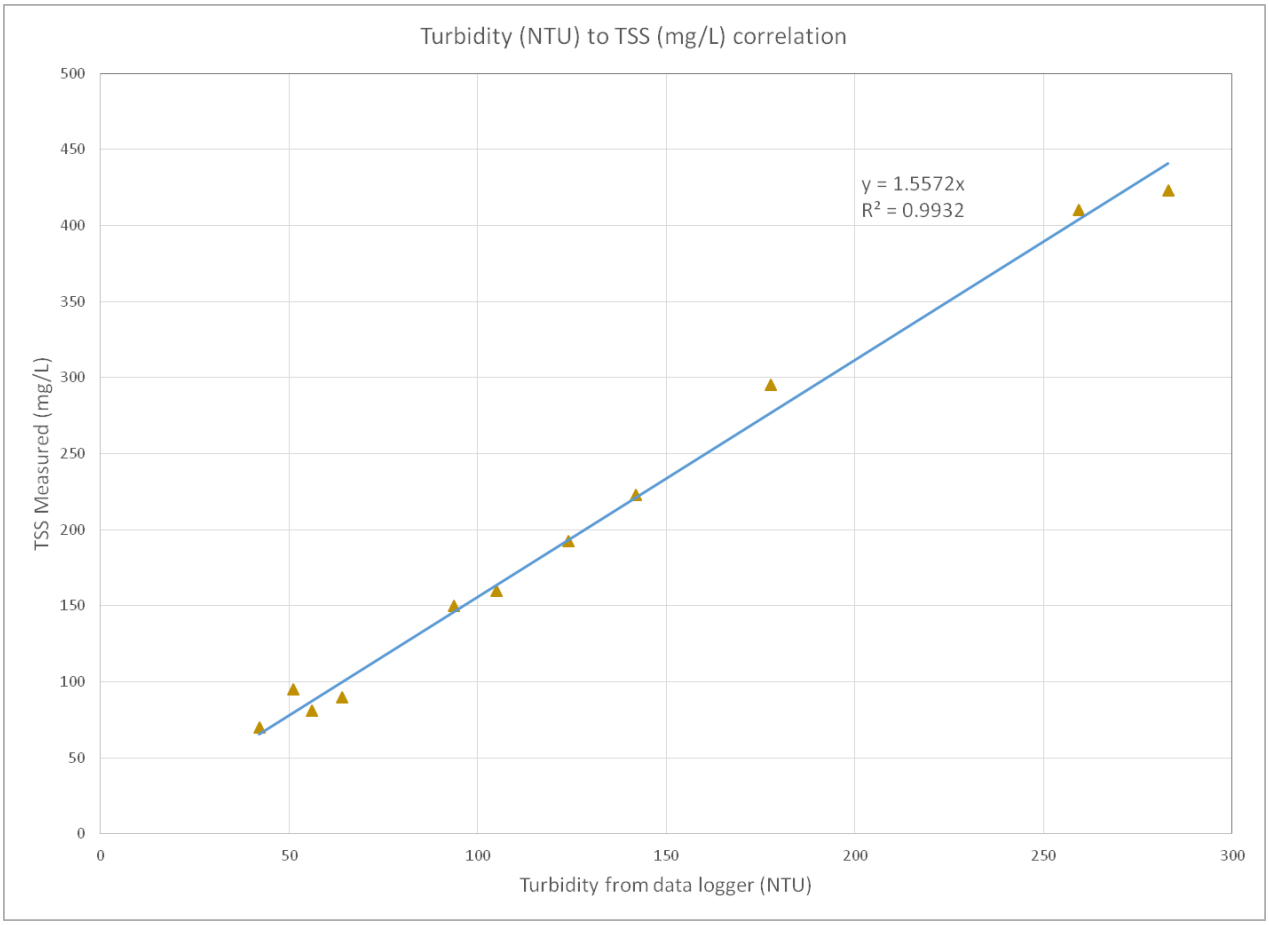

2.5 Correlation of differential cations and alkalinity with total suspended solids

Date/Time	Total Suspended Solids	Excess Ca^{2+} from PIC	Excess Mg^{2+} from PIC	Filtered/Unfiltered Alkalinity difference*
M/D/Y	mg/L	mg/L	mg/L	mg/L HCO_3^-
12/10/12 5:00	42.06	-	-	0.03
12/10/12 6:50	118.67	-	-	4.67
12/10/12 7:30	142.02	-	-	3.87
12/10/12 9:15	92.90	-	-	2.25
7/4/13 18:45	149.81	1.81	0.26	18.5
7/4/13 19:45	401.89	8.24	1.14	12.7
7/4/13 20:45	188.89	2.69	0.34	9.1
7/4/13 21:45	134.70	1.77	0.25	4.1
7/4/13 22:45	99.36	1.1	0.21	4.4
7/5/13 0:00	71.80	0.39	0.07	2.9
7/6/13 10:00	254.13	3.25	0.4	14.3
7/6/13 10:30	186.71	3.73	0.32	6.8
7/6/13 11:30	115.86	2.64	0.26	-
7/6/13 12:00	101.07	1.82	0.14	4.5
7/6/13 13:00	74.76	1.43	0.17	2.5
7/6/13 17:00	39.10	1	0.1	1.2
7/7/13 3:30	115.24	1.75	0.11	-
7/10/13 20:15	124.12	2.5	0.19	-

* Alkalinity difference between filtered/unfiltered samples shown for comparison. Data not used for modeling PIC flux in suspended loads. Note: Data used to correlate PIC to time-series TSS for modeling.

2.6 Correlation of specific conductance with dissolved Ca^{2+}, Mg^{2+} and HCO_3^- at BC

Date/Time of sample	Specific Conductance	Measured Ca^{2+}	Measured Mg^{2+}	Titrated Alkalinity, filtered
	µS/cm	mg/L	mg/L	mg/L HCO_3
12/9/2012 08:45	268.57	48.3	7.3	
12/9/2012 23:00	246.32			138
12/10/2012 4:15	251.46	46.9	6.9	
12/10/2012 5:00	255.25	49		
12/10/2012 5:30	257.71	50.3	7	144
12/10/2012 6:00	270.55	51.2		142
12/10/2012 6:15	265.07			147
12/10/2012 6:45	221.74	46		
12/10/2012 7:00	219.14		5.3	
12/10/2012 7:15	210.36		5	
12/10/2012 7:30	203.50	38	5	111
12/10/2012 8:00	195.48		5.2	120.3
12/10/2012 8:30	191.82	37		
12/10/2012 8:45	189.44		4.8	100
12/10/2012 9:45	181.91	35.9	3.6	95
12/10/2012 10:30	179.69	35	3.4	
12/10/2012 10:45	179.76			92
12/10/2012 11:30	180.59	36	4.2	
12/10/2012 12:30	182.70	37	5.2	
12/10/2012 13:30	185.32		3.9	
12/10/2012 14:30	187.42		3.7	
12/10/2012 15:30	188.57		3.5	
12/10/2012 17:00	189.80		3.4	
12/10/2012 19:30	192.58		3.5	
5/29/2013 18:00	234.75	47	5.5	
7/4/2013 19:00	228.25			108.0
7/4/2013 19:30	174.20			88.5
7/4/2013 20:30	160.48			83
7/4/2013 21:30	168.38			97.4
7/4/2013 22:30	178.53			92.6
7/5/2013 3:45	213.04			104.8
7/6/2013 8:45	262.68			138.1
7/6/2013 9:45	160.28			93.6
7/6/2013 10:00	152.90	41	3.6	75.5
7/6/2013 10:15	150.62			91.6
7/6/2013 10:30	150.05	32	2.6	
7/6/2013 11:30	155.13	34	4.1	

7/6/2013 12:00	159.74	33	3.5	95
7/6/2013 13:00	168.14	35	3.5	
7/6/2013 17:00	183.63	39	3.9	
7/7/2013 3:30	174.42	39	4	
7/10/2013 20:30	161.94	33.7	4.1	
7/11/2013 1:00	176.59	38	4	
7/13/2013 15:00	192.49	46.9	3.5	
Note: This data used to construct Figure 2.22 regression analysis. All samples collected at main BC spring outlet, alkalinity was titrated in the field and ion samples analyzed in ICP lab.				

APPENDIX B. CHAPTER 3

3.1 Correlation of total suspended solids to turbidity at HRC

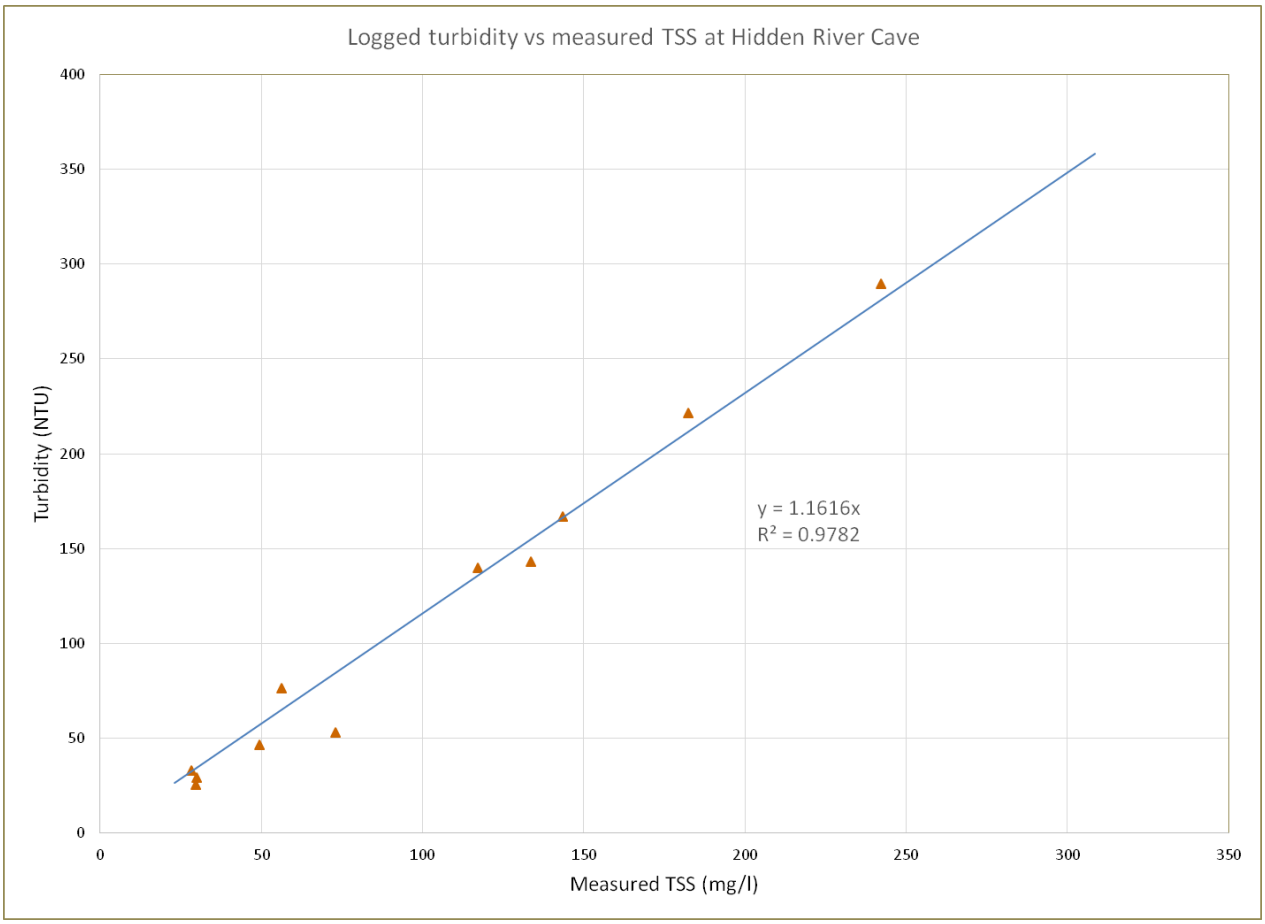

3.2 Isotope sample data and analysis

Appendix 3.2.1: Blowing Cave isotope sample data and analysis												
Sample #	Count Mass	Collection Date	Count Date	Count Time	^{7}Be Area counts	^{7}Be error counts	^{137}Cs Area Counts	^{137}Cs error counts	^{7}Be Activity at collection	^{7}Be error	^{137}Cs Activity at collection	^{137}Cs error
BCS1-C1	18.55	9/4/2011	10/1/2011	65525	0	0.0	0	0.0	nd		nd	
BCS1-C6	17.32	9/4/2011	10/2/2011	72283	0	0.0	85	15.2	nd		0.159	0.028
BCS1B-C1	20.05	9/11/2011	9/28/2011	48150	31	9.1	53	11.0	0.539	0.159	0.129	0.027
BCS1B-C6	18.62	9/10/2011	9/28/2011	34167	0	0.0	29	7.6	nd		0.107	0.028
BCS2-C1	17.38	11/21/2011	12/1/2011	31842	34	11.4	18	6.3	0.941	0.314	0.076	0.027
BCS2-C2	16.31	11/21/2011	12/1/2011	33727	26	7.2	24	4.7	0.724	0.201	0.102	0.020
BCS2-C3	16.74	11/20/2011	11/30/2011	46218	30	9.4	60	13.0	0.594	0.186	0.265	0.057
BCS2-C4	14.89	11/20/2011	11/30/2011	35550	0	0.0	36	9.3	nd		0.109	0.028
BCS2-C5	15.87	11/20/2011	11/29/2011	48053	0	0.0	62	11.3	nd		0.190	0.035
BCS2-C6	19.42	11/20/2011	11/28/2011	75428	0	0.0	46	13.6	nd		0.074	0.022
BCS1-S1	14.23	9/4/2011	9/30/2011	31245	0	0.0	304	21.9	nd		1.600	0.115
BCS1-S2	16.36	9/10/2011	9/29/2011	75687	60	13.6	534	31.5	0.835	0.189	1.010	0.060
BCS1-CK1	16.69	9/10/2011	9/30/2011	86400	373	25.7	42	9.7	4.513	0.311	0.069	0.016

Appendix 3.2.2: Hidden River Cave isotope sample data and analysis												
Sample #	Count Mass	Collection Date	Count Date	Count Time	^{7}Be Area counts	^{7}Be error counts	^{137}Cs Area Counts	^{137}Cs error counts	^{7}Be Activity at collection	^{7}Be error	^{137}Cs Activity at collection	^{137}Cs error
F1-BSC	8.01	4/14/2014	4/22/2014	86400	548	27.6	101	13.1	11.820	0.595	0.342	0.044
F3A-HRC	9.32	4/14/2014	4/25/2014	86400	95	13.7	41	10.8	1.831	0.264	0.119	0.031
F3B-HRC	8.00	4/14/2014	4/26/2014	86400	93	15.6	61	12.4	2.116	0.355	0.207	0.042
F4A-HRC	9.72	4/15/2014	4/29/2014	86367	90	14.6	50	12.2	1.730	0.281	0.139	0.034
F4B-HRC	8.54	4/15/2014	4/28/2014	86400	129	17.0	63	12.5	2.785	0.367	0.200	0.040
F5-STB	6.92	4/15/2014	5/12/2014	86400	578	27.5	103	13.4	18.476	0.878	0.403	0.053
F6-HRC	8.52	4/28/2014	5/19/2014	86400	227	23.0	31	6.0	5.451	0.552	0.099	0.019
F7-HRC	8.27	4/28/2014	5/21/2014	86400	456	42.0	37	7.0	11.579	1.066	0.121	0.023
F8-HRC	8.08	4/28/2014	5/29/2014	86400	334	33.0	75	15.0	9.632	0.952	0.251	0.050
F9-HRC	10.16	4/28/2014	5/30/2014	86400	766	68.0	61	12.0	17.798	1.580	0.163	0.032
F10-HRC	9.32	4/28/2014	5/31/2014	85000	439	40.0	71	14.0	11.451	1.043	0.210	0.041
F11-HRC	9.27	4/28/2014	6/1/2014	86400	282	28.0	81	16.0	7.371	0.732	0.237	0.047
F12-HRC	9.14	4/28/2014	6/3/2014	84604	247	21.5	62	12.7	6.863	0.597	0.187	0.038
F13-HRC	8.89	4/28/2014	6/20/2014	86400	308	20.9	56	11.9	10.747	0.731	0.170	0.036
F14-HRC	8.96	4/29/2014	5/23/2014	86400	128	17.4	70	12.4	3.039	0.412	0.212	0.037
F15-HRC	9.09	4/29/2014	6/21/2014	86400	90	15.9	118	15.2	3.071	0.542	0.351	0.045
HWM-HRC	14.0	4/29/2014	6/19/2014	86400	53	14.98	55	13.4	1.129	0.319	0.106	0.026
F16-HRC	8.79	4/30/2014	6/22/2014	73370	62	11.0	67	13.3	2.577	0.457	0.243	0.048
F17-HRC	11.78	5/1/2014	6/23/2014	86400	65	14.2	84	14.8	1.712	0.374	0.193	0.034

VITA

Randall Paylor was born in Knoxville, Tennessee and became interested in science and the outdoors from family travel and from family members who were geologists. He attended and graduated from The Webb School in Bell Buckle, Tennessee with honors in 1982 and initially began a college program with a scholarship in astronomy and physics at Vanderbilt University. Geology became a more passionate interest, and Randy enrolled in the geology program at Tennessee Technological University, where he graduated with a Bachelor's of Science degree in geology in 1990.

Randy went on to work a variety of geology jobs before continuing school, first in the environmental consulting industry conducting site assessments and contaminant remediation. He later took a position with the U.S. Geological Survey water resources branch in Maryland, working on geographic information system projects as well as hydrology projects such as thermal remote sensing of groundwater discharge. After the USGS, Randy accepted a position with Stagg Resource Consultants in West Virginia working on mineral resource assessments and environmental issues across the U.S.

Another passion of Randy's is the world of caves and karst, in which he has been involved since a teenager. After West Virginia, he took a position as a hydrogeologist for the Kentucky Geological Survey (KGS) at the University of Kentucky working on karst groundwater and karst hazard issues across the state. He worked at KGS for 10 years and received his professional geologist certification while there, and was voted onto the management board of the National Speleological Society for six years.

Randy began attending graduate school part time at Eastern Kentucky University in 2001 to study karst hydrogeology in greater depth. He completed a Master's of Science degree at EKU in 2007, and continued to work in Kentucky through 2010, when he was accepted into the PhD program at Louisiana State University to pursue more advanced research. While in the PhD program at LSU, Randy obtained three years of funding through a competitive National Science Foundation grant for his research, and was also an instructor of record for introductory geology and environmental geology classes. Randy expects to graduate with his PhD from LSU in 2016, and is pursuing career opportunities in scientific research.